COLLEGE OF ENGINEERING

ROLLING FLOW WIND TUNNEL TESTS OF F-18 AIRCRAFT

Frederick H. Lutze

Virginia Polytechnic Institute and State University

June 1980

VIRGINIA POLYTECHNIC INSTITUTE AND STATE UNIVERSITY

BLACKSBURG, VIRGINIA

NAS1-15080

ROLLING FLOW WIND TUNNEL TESTS OF F-18 AIRCRAFT

Frederick H. Lutze

Virginia Polytechnic Institute and
State University

June 1980

ROLLING FLOW WIND TUNNEL TEST OF F-18 AIRCRAFT

Frederick H. Lutze
Virginia Polytechnic Institute
and State University

SUMMARY

The rolling flow capability of the Virginia Tech Stability Wind Tunnel was used to investigate the lateral-directional characteristics of an F-18 aircraft. The purpose of this type of testing is to obtain aerodynamic derivatives associated with pure roll rate, or the "p" derivatives. This report deals with a description of the model, the procedures used to obtain and correct the data, and a graphical presentation of the results. These results include graphs of the lateral-directional static stability derivatives versus angle of attack, and the lateral-directional force and moment coefficients versus non dimensional roll rate. Results are presented for several configurations including complete, complete without vertical tails, complete without horizontal tails, fuselage-wing and fuselage alone. Each of these configurations was tested with andwithout wing leading edge extensions. In addition results of deflecting the basic control surfaces were investigated. A brief discussion of the results is included highlighting unusual characteristics.

INTRODUCTION

Recent studies have paid particular attention to the high angle of attack region of flight. In order to fully understand the dynamic characteristics of this flight regime various methods of testing have been devised including conventional wind tunnel tests, free flight, spin tunnel, and radio controlled drop models.[1] An AGARD conference emphasized the dynamic stability problem by

being solely devoted to it.[2] A summary of this meeting calls for more testing to determine the complex flow fields encountered. This report gives the results of testing an F-18 fighter model in a unique rolling flow wind tunnel facility.

The Stability Wind Tunnel at Virginia Tech has a unique capability of being able to simulate flight in a curved or rolling path. The tunnel, located in the Department of Aerospace and Ocean Engineering, has interchangeable test sections which provide this capability. The curved flow test section provides the proper velocity distribution associated with a given curvature to simulate flight in a curved path. The rolling flow test section provides a flow which rolls about the freestream velocity vector with the proper velocity distribution to simulate rolling flight. The purpose of simulation these conditions is to provide a means to estimate the pure rotary stability derivatives known as the "p", "q" and "r" derivatives. A description of the tunnel and the curved and rolling flow test sections is given in References 3 and 4. Of particular interest in this report are the methods and procedures for obtaining the aerodynamic stability derivatives associated with pure rolling motion.

Previous results of curved flow testing of the F-18 model are presented in Reference 5. These results when combined with those given here permit the conversion of the data from the stability axes in which the data are obtained to body axes in which oscillating test data is usually measured. It should be emphasized that it is necessary to have the results of both curved and rolling flow tests for this conversion to be made.

The model and the associated equipment used were the same as those used in Reference 5, where a detailed description is given. Here a brief description of the tunnel, the rolling flow test section, and the model will be given followed by a detailed account of the rolling flow test procedure used to obtain the required data. The results of these tests are then presented in graphical

form and a brief discussion emphasizing the highlights of the graphs given.

LIST OF SYMBOLS

A_F	Projected frontal area of model perpendicular to wind tunnel axis (m^2)
A_x	Projected area perpendicular to x body axis (m^2)
A_y	Projected area perpendicular to y body axis (m^2)
A_z	Projected area perpendicular to z body axis (m^2)
b	Wing span (m)
$\bar{c}$	Wing mean aerodynamic chord (m)
$c_\ell = L/\bar{q}sb$	Roll moment coefficient
$c_m = M/\bar{q}s\bar{c}$	Pitch moment coefficient
$c_n = N/\bar{q}sb$	Yaw moment coefficient
$c_y = Y/\bar{q}s$	Side force coefficient
F	Fuselage
H	Horizontal Tail
L	Roll moment
LEX	Wing leading edge extensions
M	Pitch moment (Nm)
N	Yaw moment (Nm)
p	Pressure (N/m^2), roll rate
$\hat{p} = pb/2v$	Non-dimensional roll rate
$\bar{q}$	Dynamic pressure (N/m^2)
S	Wing area (m^2)
V	Speed (m/sec), vertical tails
W	Wing
Y	Side force (N)
α	Angle of attack (deg)
β	Angle of sideslip (deg)
δ_a	Aileron deflection, positive right aileron down (deg)
δ_d	Horizontal tail differential deflection, positive right tail trailing edge down (deg)
δ_{f,ℓ_e}	Wing leading edge flap deflection (deg)
δ_{f,t_e}	Wing trailing edge flap deflection (deg)
δ_h	Horizontal tail deflection, positive trailing edge down (deg)

δ_r Rudder deflection, positive trailing edge left (deg)

ε Blockage correction factor

θ Sting pitch angle

ρ Air density (kg/m^3)

ϕ Sting roll angle

APPARATUS, MODEL, AND TESTING TECHNIQUE

Wind Tunnel

The tests were conducted in the round or rolling flow test section(1.83m (6 ft.) in diameter) of the Virginia Tech Stability Wind Tunnel. A sketch of the rolling flow test section is shown in Figure 1. At the upstream end of the test section there is a motor driven rotor device which can impart a rotary or helical motion to the airstream as it passes through the test section. The vanes in the rotor, shown in Figure 2, are shaped to provide a velocity distribution similar to that of a solid vortex. Consequently the flow field that the fixed model experiences is the same as that experienced by an aircraft rolling about its velocity vector in still air. Details concerning the rolling test section and its calibration are given in Reference 4.

Balance

For these tests a lateral-directional force and moment internal strain gage balance was used. No longitudinal data was taken. The balance, #FF06 (roll and yaw moments and side force) was supplied by NASA Langley Research Center and was compatible with the model. A nominal 5 volt power supply was used to power the balances. The calibrations used for these tests are the same as those used for the curved flow tests in Reference 5. Details of the calibration procedure are presented there.

Data Aquisition System

Data was obtained using a Hewlett Packard HP 3052A Data Aquisition System which includes an HP 3455A digital voltmeter, an HP 3495A forty channel scanner and an HP 9825A calculator. Data was obtained according to the procedures

described below, reduced to coefficient form and stored on tape. Subsequently it was transferred to the University's IBM 370/168 computer where it was sorted for the purposes of plotting the results.

Model

The investigation was conducted with a 0.07 scale model of the F-18 aircraft. It is the same model that was used in collecting the data in Reference 5. A three view sketch of the model is shown in Figure 5. The model was constructed in a manner that allowed various parts to be easily removed to permit build up tests of several configurations to be performed. In addition several control surfaces could be set in deflected positions. These include wing leading and trailing edge flaps, ailerons and rudders on the twin vertical tails. In addition the horizontal tail surfaces could be deflected together or in a differential manner. The configurations tested along with their identifying numbers are given in Table 1. It should be noted that the base configuration (#1) was the full configuration with the leading edge flaps deflected down 25 degrees. Unless otherwise stated, the leading edge flaps were in the deflected position for all configurations.

The geometric properties of the model, including those used for blockage corrections, are presented in Table 2. All moments are referenced to the 0.24 mean aerodynamic chord point.

Test Procedure

The model was mounted in the rolling flow test section using a pylon supported sting mount, similar to that described in Reference 5. By using a double dog leg support for the sting it was possible to obtain angles of attack from 0 to 45 degrees. Unlike the arrangement for the curved flow test section, here the pylon is rigidly fastened to the top and bottom of the test section so that arbitrary yaw angles could not be set. The sting however could roll through any angle so that artibrary combinations of roll angle and sting angle of attack

could be achieved. By comparing the orientation of the model with respect to the wind vector using the angle of attack, α, and sideslip angle, β with that obtained using the sting pitch angle, θ, and the sting roll angle, θ, the relationships among the angles can be determined. They are given by

$$\tan\alpha = \tan\theta \cos\phi \qquad \text{or} \qquad \cos\theta = \cos\alpha \cos\beta$$

$$\sin\beta = \sin\theta \sin\phi \qquad\qquad \tan\phi = \tan\beta/\sin\alpha$$

From the latter equations the value of θ and ϕ can be determined for each desired α and β. Since the roll angle was not easily set it was determined that certain selected roll angles would be used and the pitch angle set so that the equivalent angle of attack was exactly at the five degree angle of attack increments, 0, 5, 10, 15, ..., 45 degrees and that the sideslip angle would be as near as possible to the nominal values of -10, -5, 0, and 10 degrees. The values determined in this manner and used in these tests are given in Table 3.

In order to simulate a spectrum of rolling rates, the rotor is powered by a variable speed reversible d.c. motor. Calibration of the rolling flow test section indicated an asymmetry in equivalent roll rate with rotor speed. In an attempt to generate the desired symmetry the tests were done with the rotor motor tachometer set at values which would give equivalent positive and negative aerodynamic roll rates. The values used in these tests are presented in Table 4. Furthermore since this asymmetry is apparently caused by the vanes themselves, it was observed that readings with zero rotor speed readings were taken with the rotor in the same arbitrarily selected position.

The tests were performed in the following general sequence. Initially a preselected sting roll angle was set and a configuration selected. For each configuration and roll angle the appropriate sting pitch angles were selected. Finally for each sting angle the full range of roll rates was examined. At each sting angle one wind-off reading was taken. Hence the

complete range of roll rates was obtained without shutting the tunnel off. Roll rate settings always started at zero and increased (decreased) in steps to the maximum positive (negative) roll rate, returned to zero and then decreased (increased) in the opposite direction until maximum negative (positive) roll rate was achieved. The tunnel speed was selected so that the dynamic pressure, as measured by the upstream nozzle contraction pressure ratio, was that of the desired dynamic pressure in the unoccupied test section with the rotor at rest. For these tests the pressure ratio was 0.036m (1.39 in). of water which corresponds to a test section dynamic pressure of $\bar{q}$ = 766.08 N/m^2 (16 lbs/ft^2) in the unoccupied test section. This speed gives a Reynolds number of 6 x 10^5 based on the model mean aerodynamic chord.

At each test point, roll rate, configuration, pitch angle, and roll angle were observed and entered into the data acquisition system. The static pressure, temperature, tunnel dynamic pressure, and the six components of the strain gage balance were read on command by the data acquisition system. These readings were obtained by taking the average of 15 samples taken over an 8 second time interval.

It was observed during the tests that the rotor created considerable vibration to occur in the test section itself. The model, being supported by the pylon which was attached in the test section also vibrated considerably. Consequently there was a high noise to signal ratio in these rolling flow tests. The averaging procedure described above helped to reduce these effects but not eliminate them. Hence some scatter in the results is expected and indeed observed. In the future the use of filters to eliminate tunnel vibration frequencies may be in order.

TESTS

Lateral-directional data were obtained for all the configurations in Table 1. Test were run for angles of attack from 0 to 45 degrees in 5 degree

increments and for side slip angles nominally from -10 to +5 degrees in 5 degree increments. The actual values of sideslip are given in Table 3. At each angle of attack and sideslip angle the nine roll rates given in Table 4 were tested. Exceptions to the above test schedule occured for configurations 16, 17, and 18, which were tested at the zero sideslip condition only.

DATA REDUCTION

The data recorded for each test were run number, roll rate, configuration, sting pitch angle, sting roll angle, local pressure, local temperature, contraction ratio pressure drop and the three component outputs from the strain gage balance wind on and wind off. This data was reduced and printed out in the form of run number, configuration number, non-dimensional roll rate, angle of attack, sideslip angle, corrected tunnel dynamic pressure, speed, Reynolds number, and the non-dimensional force and moment coefficients in both body and stability axes. Included in this reduction is a correction to the tunnel dynamic pressure due to the blockage effects.

The blockage correction used is the same as that used in Reference 5 and is given by[6]

$$\overline{q}_c = \overline{q}(1 + 2\varepsilon)$$

where

$$\varepsilon = \frac{1}{4}\frac{\text{frontal area}}{\text{tunnel area}}$$

The frontal area depends upon the angle of attack and sideslip and is given by

$$A_F = (A_x \cos\alpha + A_z \sin\alpha)\cos\beta + A_y |\sin\beta|$$

where A_x, A_y, and A_z are the projected areas perpendicular to the x, y, and z body axes and are given in Table 2.

RESULTS AND DISCUSSION

The results of the rolling flow tests are presented graphically in Figures 4 through 24. These figures include the standard lateral-directional static stability derivatives as well as results in the steady state rolling flow. All results are presented in stability axes since the roll rate is simulated about the relative wind vector which is approximately the same as the x stability axes. In the following discussion the significance of each figure will be discussed and the highlights associated with it emphasized.

Figure 4 presents the lateral-directional static stability derivatives and how they change with angle of attack. These were obtained from the rolling flow tests for the special case where the rotor speed was zero and with the rotor stopped so that the vanes were in the same position each time. The stability derivatives plotted were calculated by taking the difference between the coefficients at the nominal values of sideslip of ± 5 degrees and dividing the results by the actual difference in sideslip angles. The results therefore are in units "per degree." These graphs should compare with similar data taken in the curved flow test section at zero curvature.[5] Comparisons are quite good with the overall curve shapes being the same. At angles of attack above 15 degrees some scatter is observed but the same trends are maintained. One phenomena observed in previous curved and rolling flow tests[7,8] is that the yaw static stability parameter, C_{n_β} is slightly lower (0.0014) in the rolling flow test section than in the curved flow test section (0.0018) at the lower angles of attack. In these tests however a similar shift in the sideforce static stability parameter, C_{y_β}, is observed with the value at zero degrees angle of attack being -0.017 for the curved flow test section and -0.014 for the rolling flow test

section. No difference is observed in the roll moment stability parameter, C_{ℓ_β}. Other than this shift at the low angles of attack all configurations showed good agreement between the two test sections.

Figures 5 through 9 show the effects of roll rate and sideslip on lateral stability. These are non-traditional plots which are obtained by calculating the lateral stability coefficients in three different methods. The three methods used as numbered in the figures are:

1. The standard method as used in the previous figures where the derivative is obtained by using the values at $\pm$ 5 degrees (nominal) and dividing by the difference in sideslip angle.
2. The use of just the positive sideslip values where the difference used in between +5 and 0 degrees (nominal) sideslip.
3. The use of just the negative sideslip values where the difference used is between 0 and -5 degrees (nominal) sideslip.

It is clear the first method is the average of the last two and always falls between them. In general at low angles of attack the three methods coincide. However as the angle of attack (AOA) increases the differences can become quite large, indicating some asymmetric behavior in the flow field. One cause for this difference has been shown to be the asymmetric vortex shedding from the nose coupled with the interaction of these vortices with the wing and tail structures.[9,10]

In viewing these graphs, the key feature to observe is the separation of the curves associated with the three methods described above. Such a separation indicates strong dependence on the direction of sideslip. Furthermore if this separation causes the lines from methods 2 and 3 to straddle the line where the static stability parameter is zero, then the static stability depends on the

direction of sideslip. For the purposes of discussion we will refer to such a situation as being bistable. A vehicle has even bistable behavior if positive sideslip yields positive stability and negative sideslip yields negative or unstable behavior. Odd bistable behavior is the opposite of the above. The best example of this type of behavior is illustrated by the fuselage alone configuration. For this case bistable behavior occurs in both yaw and roll derivatives. From Figures 5 through 9 we can see that for negative roll rates the fuselage alone exhibits even bistability in yaw and odd bistability in roll for AOA between 20 and 30 degrees. This characteristic is exactly reversed for the positive roll rates. Hence a yaw with nose into the roll is stabilizing in yaw and destabilizing in roll indicating the dominant contributions most likely come from the aft portion of the fuselages.

In the discussion which follows the curves from Figures 5 through 9 will be considered for each configuration examined. Graphs for the two extreme roll rates ($\hat{r} = \pm 0.058$) were also generated but are not included here. In most cases the differences between the extreme roll rate curves and those shown here are small. Exceptions to these general trends, if they occur, will be indicated in the discussion.

The wing-fuselage combination exhibits some bistable behavior at the lower AOA in roll. At higher AOA the bistable behavior is virtually eliminated in roll. Although it still occurs for the case of the yaw parameter, the strength of the bistability is considerably reduced. Unlike the fuselage alone curves, these curves do not show the appropriate asymmetry with direction of roll. Adding the wing leading edge extensions (LEX) to the fuselage wing combination eliminates completely any bistable behavior in yaw except at zero roll rate where it is not well defined. The yaw stability parameter curves show good asymmetry with

direction of roll with the relative positions of the three curves reversed. The roll stability parameter does not show this asymmetry since there is an indication of strong odd bistable behavior for negative roll rates at high AOA while none occurs for positive roll rate. The relative positions of the three curves appears to be somewhat asymmetric with respect to roll rate at the highest AOA but not convincingly so at lower AOA. In general the addition of the LEX tends to destabilize the vehicle in roll and yaw at the higher AOA from the stability level observed for fuselage and wing.

The fuselage, wing and vertical tail configuration shows similar behavior to the fuselage alone configuration with the yaw stability parameter curves shifted upward and the roll stability curves shifted downward. The separation of the various curves occurs in the same sense as the fuselage alone case indicating the dominant force changes with sideslip occur at the tail. In addition good asymmetric behavior with roll direction is observed for both the yaw and roll stability parameter curves. Adding the LEX to this configuration tends to reduce the separation between the curves for the yaw stability parameter and shift the beginning of separation between the curves of the roll parameter to a higher AOA. The roll curves still show asymmetry with roll rate while the yaw curves do not. Odd bistable behavior is observed in yaw in the high AOA and negative roll rate. For positive roll rate mixed bistable behavior is observed in yaw in the high AOA range.

The fuselage, wing and horizontal tail configuration curves show a considerable reduction of separation between the curves for both the yaw and roll rate stability parameters. For this case the extreme roll rates cause considerably more separation at AOA above 30 degrees and in the opposite sense

then that at r = $\pm$ 0.046. The addition of LEX increase the separation of curves for the roll stability parameter with little change to the yaw stability parameter curves. The roll stability parameter curves show asymmetric behavior with roll direction while the yaw stability parameter curves do not for all roll rates.

For the full configuration without LEX, both the roll and yaw stability curves show good asymmetric behavior with roll direction. The roll stability parameter exhibits odd bistable behavior for negative roll rates and even bi-stable behavior for positive roll rates. Hence a nose yawed into the roll direction is destabizing in roll. The yaw stability parameter, on the other-hand exhibits even bistable behavior for intermediate AOA and odd bistable behavior for high AOA for the case of negative roll and vice versa for the case of positive roll. Adding the LEX generally reduces the separation between the yaw stability parameter curves. They also tend to destroy the asymmetry with roll direction in both roll and yaw parameters. The roll stability parameter curves show a large separation at a higher AOA then for the configuration with no LEX for negative roll rate. The relative positions of the curves is the same for both cases however. For positive roll rate, the LEX seem to reduce the separation of the roll stability curves. The sense of the separation is not necessarily the same for the two configurations. For the extreme positive roll rate the roll stability parameter curves show some separation of AOA above 30 degrees in a sense asymmetric with that shown by the negative roll rates.

The most dramatic effects of the LEX can be seen for the full configuration with leading edge flaps undeflected. A large separation of curves occurs for both roll and yaw stability parameters at the intermediate AOA. In the case of

yaw there is strong bistable behavior at 20 degrees AOA. It is even bistable behavior for negative roll rate and odd bistable behavior for positive roll rate. Fairly good asymmetry with roll direction is displayed which improves as roll rate increases. The addition of the LEX reduces the separation of all curves considerably. It is particularly clear from these curves that the LEX tend to destabilize both roll and yaw of 25 degrees AOA. In fact the 25 degree AOA point represents the largest difference between the curves with the LEX and those without.

The remaining plots, figures 10 thru 25 represent roll rate plots where the side force, yaw and roll moment coefficients are plotted vs. the nondimensional roll rate. A considerable amount of information can be obtained from these plots, including much of the material presented in Figures 5 thru 9. In interpreting these graphs the following observations can be made. Lines which appear parallel indicate the rolling rate derivative, C_{X_p} is independent of sideslip angle. Lines that are equally spaced indicate the sideslip derivatives C_{X_β} are independent of roll rate. Finally lines that are straight indicate the roll rate derivative is independent of roll rate. If lines on a graph cross, it is likely that the sideslip derivative changes sign indicating a possible bistable behavior as found in the previous graphs. In this set of graphs, however, we can examine behavior beyond the -5 degree sideslip case. Each figure presents one configuration for AOE from 0 to 45 degrees in 5 degree increments. Here only highlights of a figure will be discussed. The results are presented in a "build up" order with the fuselage only results as a starting point.

Figure 10 is for the fuselage only configuration. At zero AOA the curves are indeed straight and parallel with some exception in side forces at high roll rates. Some of these points may represent scatter in the data due to the

vibration of the support as noted earlier in the test procedure section. The first unusual behavior occurs at 20 degrees AOA where it can be observed that the lines in the yaw coefficient plot cross. In particular bistable behavior occurs at large positive and negative roll rates since the zero sideslip line is below both ±5 degree sideslip lines at the negative roll rates and above both at the positive roll rates. Hence we have even bistable behavior in yaw for negative roll rates and the opposite for positive roll rates. At -10 degrees sideslip the fuselage is unstable in yaw for all roll rates. The roll situation is difficult to interpret here since the lines are so close. At 25 degrees AOA the zero sideslip line can be readily traced in both yaw and roll plots and is seen to clearly cross over the appropriate curves leading to bistable behavior in both yaw and roll. This same trend is increased at 30 degrees AOA to include the -10 degree sideslip as well. The behavior of the side force at 30 degrees AOA would seem to indicate the dominate force acts at the aft end of the fuselage and saturates at some level. Recall the roll rate is about the wind axes so increasing the AOA puts the extremes of the fuselage in a cross flow proportional to the roll rate. Here the force is in the same direction as the crossflow on the tail.

Figure 11 gives fuselage-wing results. The zero AOA plots show effect of wings on roll due to roll rate. Furthermore some yaw dependence on roll rate occurs. As angle of attack increases the change in roll due to roll rate diminishes. Again changes in the yaw curves occur at about 25 to 30 degrees AOA. Adding LEX to the previous configuration improves the behavior of the curves for the higher AOA. It is not until 30 degrees AOA that significant changes are observed. In roll bistable behavior appears at negative roll rates but not at positive roll rates. The behavior is the same at 35 degrees AOA.

At 40 and 45 degrees AOA the trend is back to normal.

Figure 13 shows the behavior of the fuselage, wing and vertical tails with roll rate. Curves start to cross at 20 degrees AOA but bistable behavior does not occur until 25 degrees AOA. Such behavior occurs at the larger roll rates in both yaw and roll. In all cases of roll the yaw stability coefficient indicates instability between -5 and -10 degrees sideslip but is not always unstable between 0 and -5 degrees sideslip. The addition of LEX (Figure 14) improves the roll behavior at 25 degrees AOA over the same situation without LEX. At 30 degrees AOA the roll behavior becomes bistable at the extreme roll rates. At 40 and 45 degrees AOA the differences in configurations with and without LEX are small.

Figures 15 and 16 show the behavior of the fuselage, wing and horizontal tail without and with LEX respectively. The two configurations behave similarly up to 15 degrees AOA. Here the lines for the rolling moment are further apart indicating a contribution to roll stability in sideslip due to LEX. At 25 degrees AOA the configuration with the LEX retains the roll damping property for all sideslip while without the LEX negative sideslip displays roll damping properties while the positive sideslip curve has negative roll damping on the average. At 30 degrees AOA the LEX maintains a negative yaw stability parameter while reversing the bistable behavior observed in roll at the negative roll rates. At 30 to 40 degrees AOA with LEX a bistable behavior is observed in roll for negative roll rates but not for positive roll rates as observed in the previous set of figures (5-9).

Results for the full configuration with and without LEX are given in Figures 18 and 17 respectively. At low AOA the results are very similar, as expected.

At 10 degrees AOA the distance between the roll moment curves starts to widen for the case of the full configuration with LEX. This trend is continued through 20 degrees AOA. At 25 degrees AOA the LEX appear to be destabilizing in both yaw and roll for small sideslip but not for large sideslip. At higher AOA the roll moment behavior improves while the yaw moment behavior becomes confused showing few systematic trends.

Figure 18 and 19 show the results for the leading edge flaps at zero deflection. As noted previously this case shows the largest difference for LEX on or off. The characteristics without flap deflection change at an earlier AOA then when the flaps are deflected. In this case, without LEX, significant changes appear at 15 degrees AOA. With the LEX these changes are postponed until 20 degrees AOA. Without LEX at 20 degrees AOA definite strong bistable behavior is noted in yaw. With LEX this type of behavior is still noted but considerably weaker and reversed for positive roll rates. At higher AOA the roll moment becomes better behaved for both cases while the yaw moment behavior continues to show no trend.

The remaining figures show full configuration with various control surfaces deflected. Basically the results are similar as those for the full configuration and will not be discussed here.

The above discussion emphasized the characteristics of the various curves but put little emphasis on the cause of such behavior, this aspect will be discussed elsewhere after further study.

ACKNOWLEDGEMENTS

In order to obtain the large amount of data associated with this project many people were involved. For their committment to the project and long hours of work, the following people deserve special mention: Don DeGutz, Howard Gofus, Joyce Hoffman, Sharon Janeczek, and Tom Trimbath. Without their help compilation of the data for this report would not have been possible. The funds for this research were provided by NASA Langley Research Center under Contract NAS1-15080 Task Authorization Number 8.

REFERENCES

1. Chambers, J. R. and Grafton, S. B., "Aerodynamic Characteristics of Airplanes at High Angles of Attack," NASA TM 74097, December 1977.

2. AGARD Conference Proceedings No. 235, Dynamic Stability Parameters, November, 1978.

3. Lutze, F. H., and Cliff, E. M., "New Calibration and Corrections for the VPI&SU Stability Wind Tunnel Curved Flow Test Section," Dept. of Aerospace and Ocean Engr., Report, VPI-Aero-069, August 1977.

4. Lutze, F. H., "Calibration of the VPI&SU Stability Wind Tunnel Rolling Flow Test Section," Dept. of Aerospace and Ocean Engr. Report, VPI-Aero-070, August 1977.

5. Lutze, F. H., "Curved Flow Wind Tunnel Tests of F-18 Aircraft," Dept. of Aerospace and Ocean Engr. Report, VPI-Aero-108, April, 1980

6. Pope, A. and Harper, J., Low Speed Wind Tunnel Testing, John Wiley, 1966.

7. Lutze, F. H., "Rolling Flow Tests of a Spin Resistant Aircraft Configuration," Dept. of Aerospace and Ocean Engr. Report, VPI-Aero-075, December,1977.

8. Lutze, F. H., "Curved Flow Wind Tunnel Tests of a Spin-Resistant Aircraft Configuration," Dept. of Aerospace and Ocean Engr. Report, VPI-Aero-067, August, 1977.

9. Lutze, F. H., "Experimental Determination of Pure Rotary Stability Derivatives Using a Curved and Rolling Flow Wind Tunnel," 19th Aerospace Science Meeting, AIAA-80-0309, January 1980.

10. Steidle, C. E., "Analysis and Application of Curved and Rolling Flow Wind Tunnel Testing," Masters Thesis, VPI&SU, Dec. 1979.

TABLE 1 Configurations

Number	Symbol	Number	Symbol
1	FWVHL	10	FWVL
2	FWVHL $\delta_h = -12$	11	FWH
3	FWVHL $\delta_f, \ell_e = 0$	12	FWV
4	FWVHL $\delta_f, t_e = 20$	13	FWL
5	FWVHL $\delta_h = -24$	14	FW
6	FWVH	15	F
7	FWVH $\delta_f, \ell_e = 0$	16	FWVHL $\delta_r = 30$
8	-	17	FWVHL $\delta_a = 25$
9	FWHL	18	FWVHL $\delta_d = 10$

where the following symbols are defined

F = fuselage

W = wing

V = vertical fins

H = horizontal tail

L = leading edge extensions (LEX)

δ_h = horizontal tail deflection (positive trailing edge down)

δ_f, ℓ_e = wing leading edge flap (nominally down 25 deg.)

δ_f, t_e = wing trailing edge flap

δ_r = rudder deflection (positive trailing edge left)

δ_a = aileron deflection (positive right aileron down = δ_a)

δ_d = differential tail deflection (positive right horizontal tail down $\delta_d/2$)

TABLE 2 Model Geometry

Reference Geometry	Wing Span = 0.798m (2.619 ft.)		Wing chord (MAC) = 0.245m (0.805 ft.)			
	Wing Area = 0.597m (1.960 ft.)		Center of Mass = 0.24 MAC			
Configurations	1,2,3,4,5,16,17,18		6,7		9	
Frontal area	0.028m^2	(0.300 ft^2)	0.028m^2	(0.300 ft^2)	0.028m^2	(0.300 ft^2)
Planform area	0.322m^2	(3.464 ft^2)	0.300m^2	(3.234 ft^2)	0.313m^2	(3.374 ft^2)
Profile area	0.120m^2	(1.294 ft^2)	0.120m^2	(1.294 ft^2)	0.097m^2	(1.040 ft^2)
Volume	0.013m^3	(0.476 ft^3)	0.013m^3	(0.476 ft^3)	0.013 m^3	(0.476 ft^3)
Configurations	10		11		12	
Frontal area	0.028m^2	(0.300 ft^2)	0.028m^2	(0.300 ft^2)	0.028m^2	(0.300 ft^2)
Planform area	0.284m^2	(3.058 ft^2)	0.292m^2	(3.144 ft^2)	0.263m^2	(2.828 ft^2)
Profile area	0.120m^2	(1.294 ft^2)	0.097m^2	(1.040 ft^2)	0.120m^2	(1.294 ft^2)
Volume	0.013m^3	(0.476 ft^3)	0.013m^3	(0.476 ft^3)	0.013m^2	(0.476 ft^3)
Configurations	13		14		15	
Frontal area	0.028m^2	(0.300 ft^2)	0.028m^2	(0.300 ft^2)	0.020m^2	(0.210 ft^2)
Planform area	0.276m^2	(2.968 ft^2)	0.254m^2	(2.738 ft^2)	0.112m^2	(1.210 ft^2)
Profile area	0.097m^2	(1.040 ft^2)	0.097m^2	(1.040 ft^2)	0.097m^2	(1.040 ft^2)
Volume	0.013m^3	(0.476 ft^3)	0.013m^3	(0.476 ft^3)	0.013m^3	(0.459 ft^2)

TABLE 3 Angle Relations

Angle of Attack	Sideslip Angle (deg)		Sting Angles (deg)	
	Nominal (±)	Actual (±)	Pitch	Roll (±)
0	5	5.00	5.00	90
0	10	10.00	10.00	90
5	5	4.98	7.05	45
5	10	11.70	10.59	65
10	5	4.63	11.01	25
10	10	9.85	4.00	45
15	5	5.38	15.91	20
15	10	10.27	18.11	35
20	5	5.24	20.65	15
20	10	9.06	21.88	25
25	5	4.26	25.34	10
25	10	11.15	27.23	25
30	5	5.03	30.38	10
30	10	10.31	31.57	20
35	5	5.77	35.41	10
35	10	11.79	36.69	20
40	5	5.16	40.28	8
40	10	9.77	40.98	15
45	5	5.67	45.28	8
45	10	10.73	45.99	15

TABLE 4 Roll Rates

Motor Tach	pb/2V*
-1120	-0.058
- 800	-0.046
- 530	-0.032
- 260	-0.015
0	0
300	0.015
600	0.032
900	0.046
1250	0.058

* Based on 0.798m (2.619 ft.) model wing span

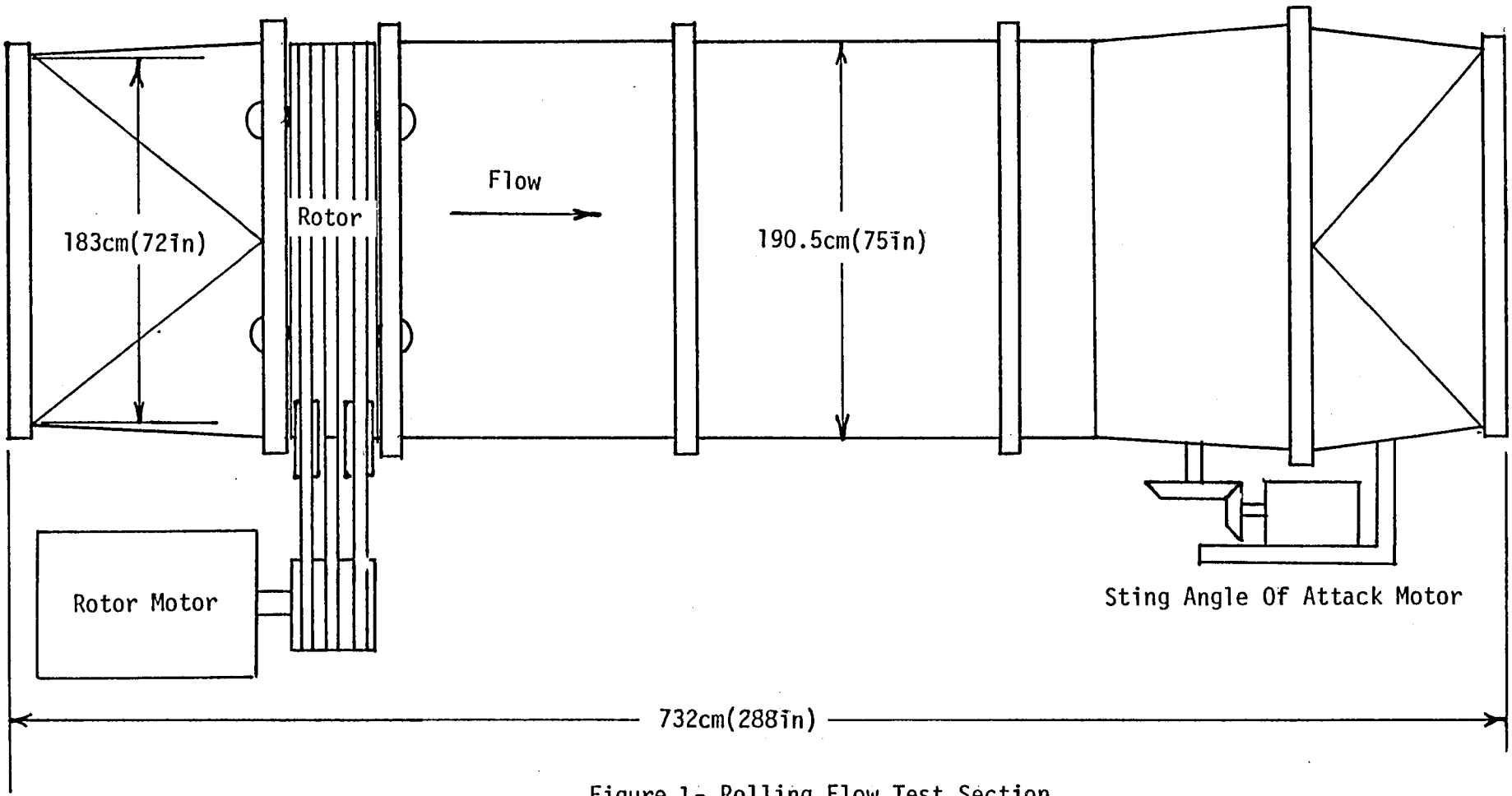

Figure 1- Rolling Flow Test Section

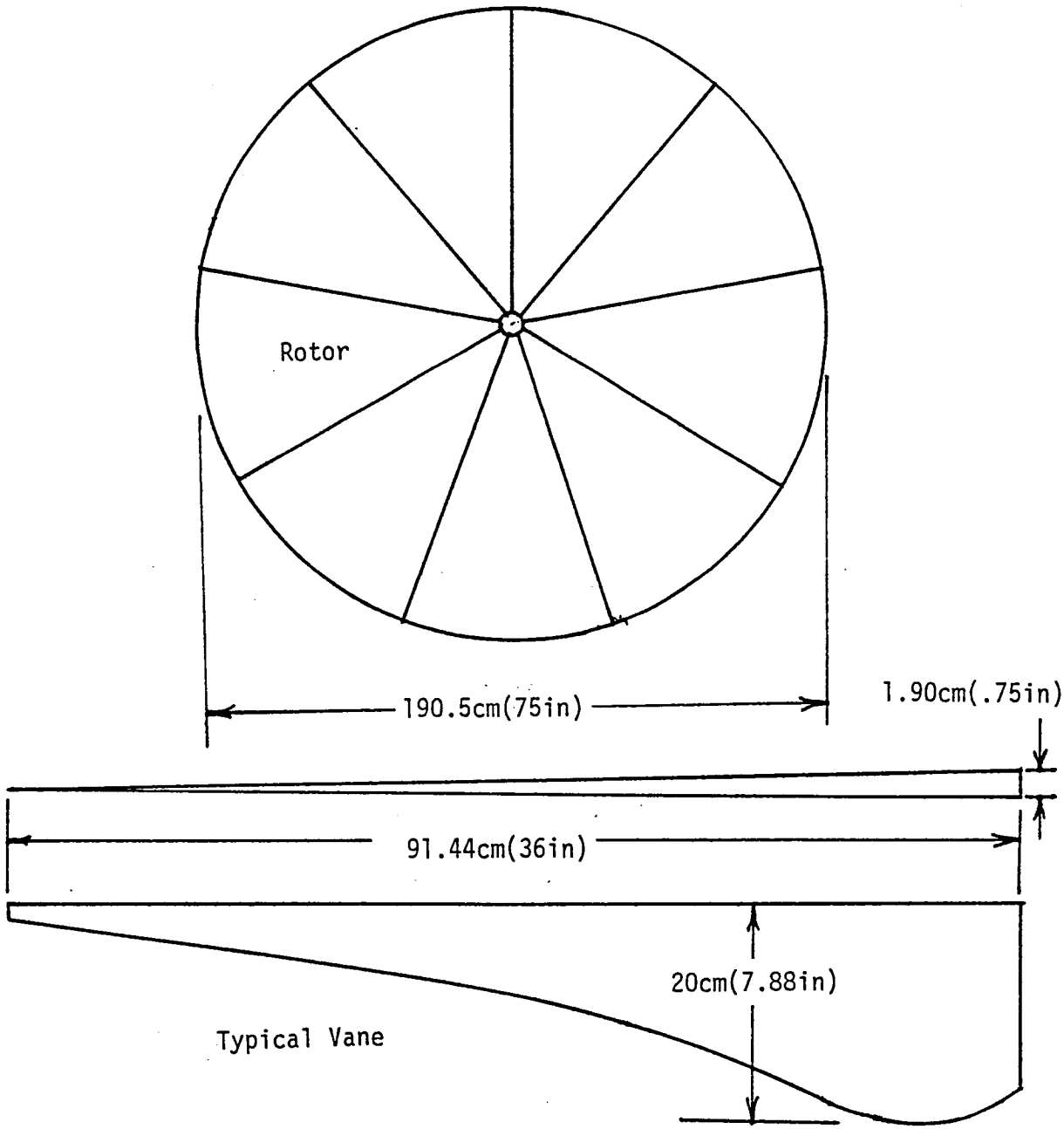

Figure 2- Rolling Flow Rotor and Vane

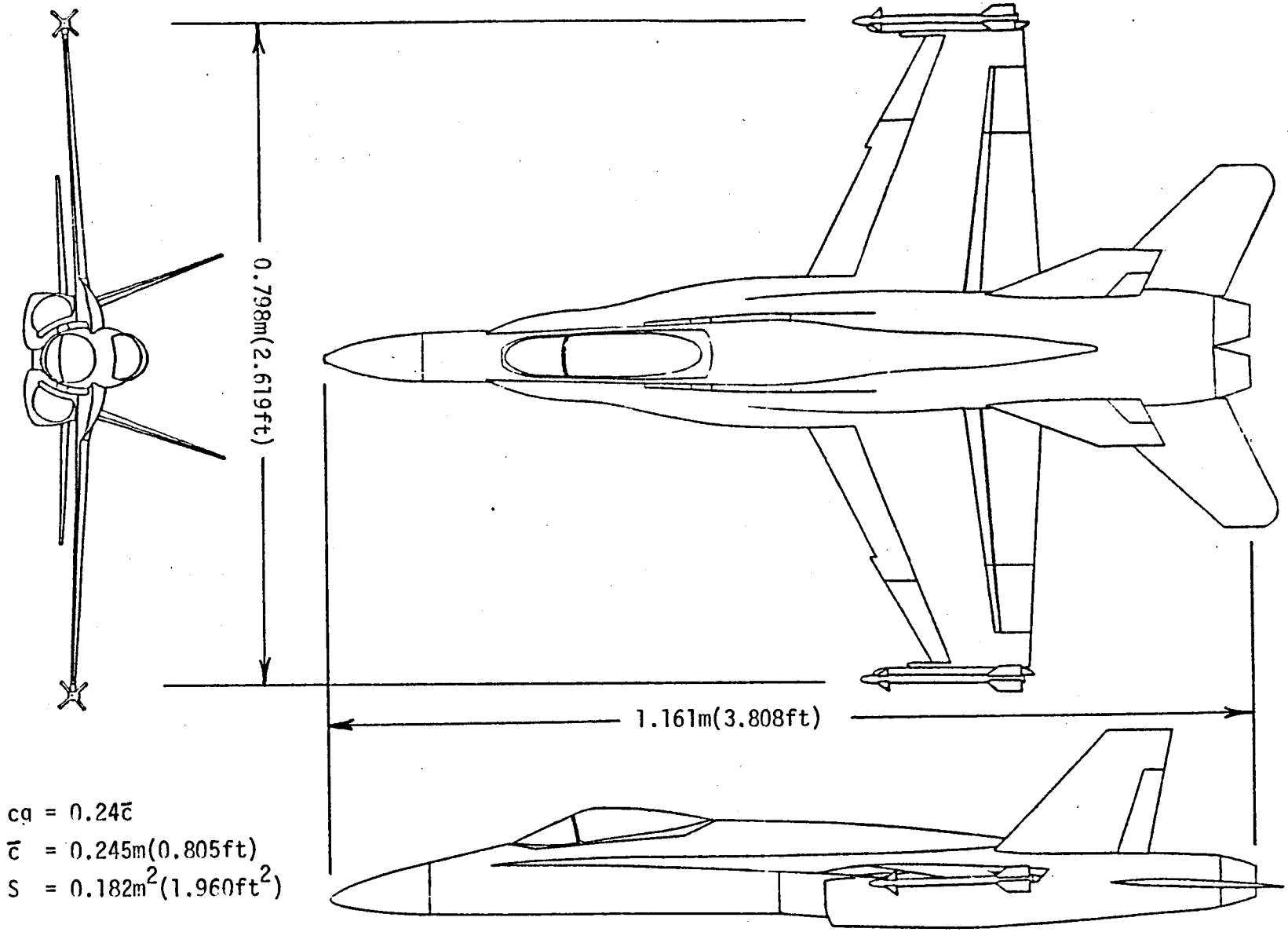

Figure 3 Sketch of Basic Model

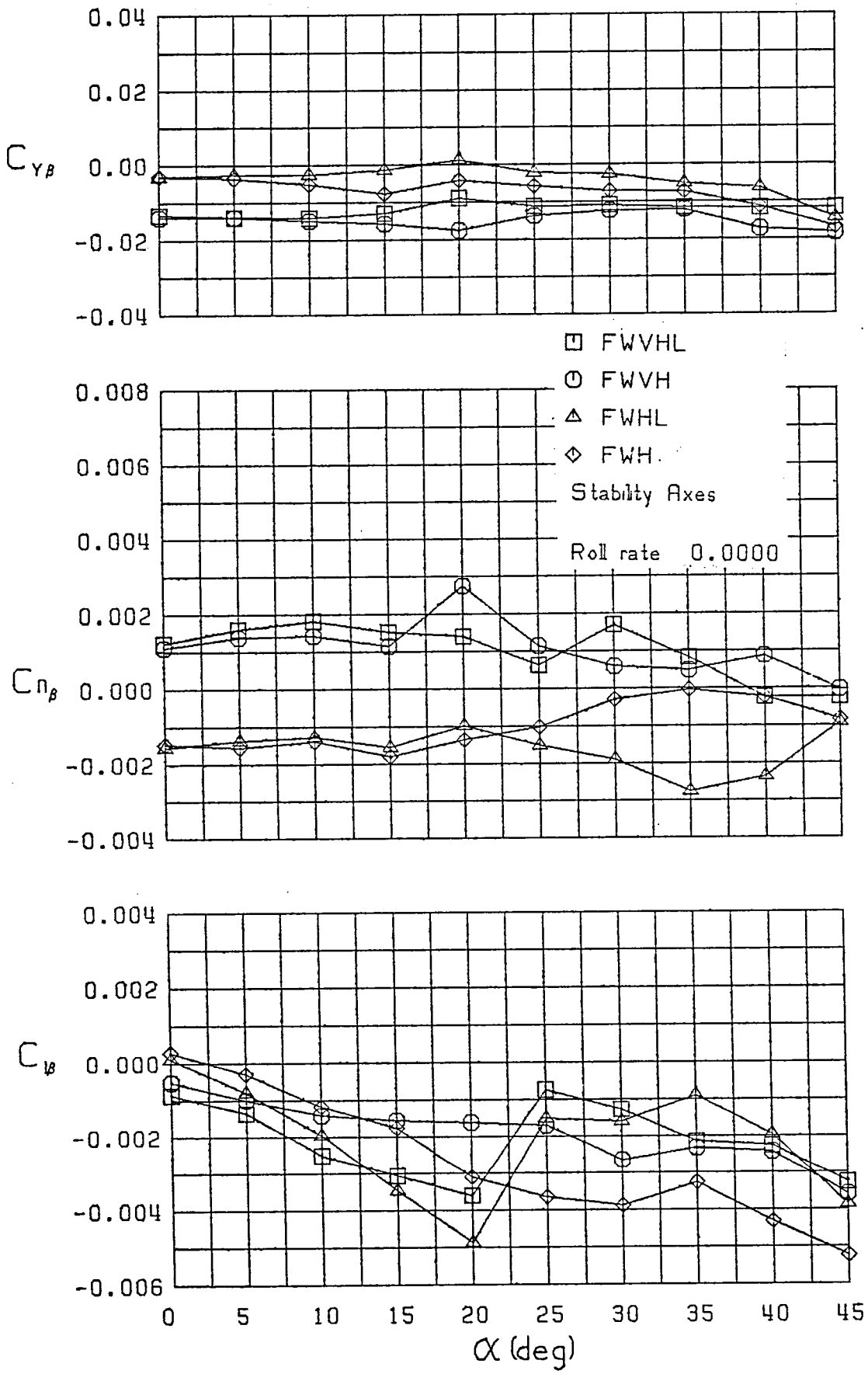

Figure 4 - Variation of Lateral-Directional Static Stability Derivatives with Angle of Attack, p = 0.0

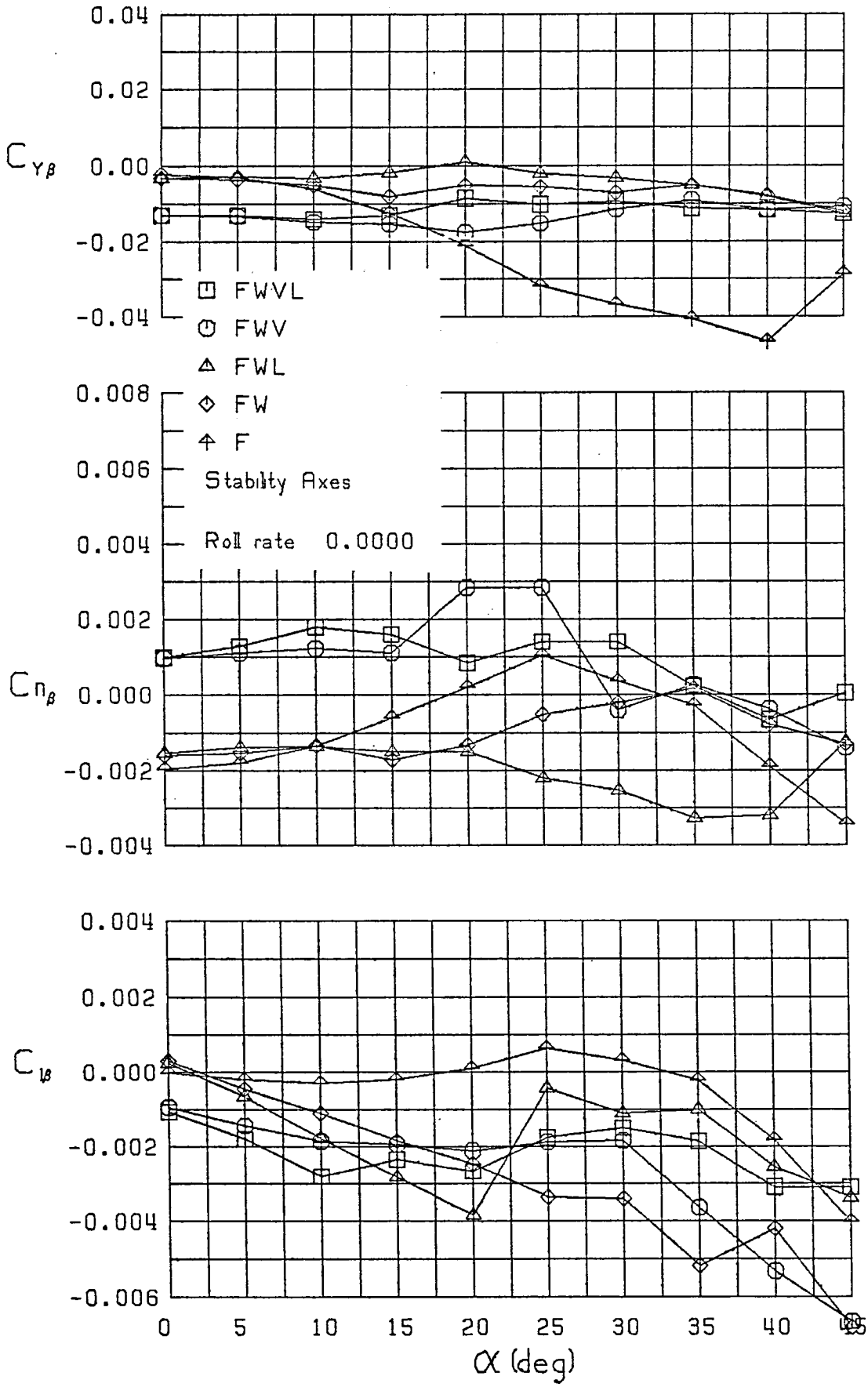

Figure 4 (Continued)

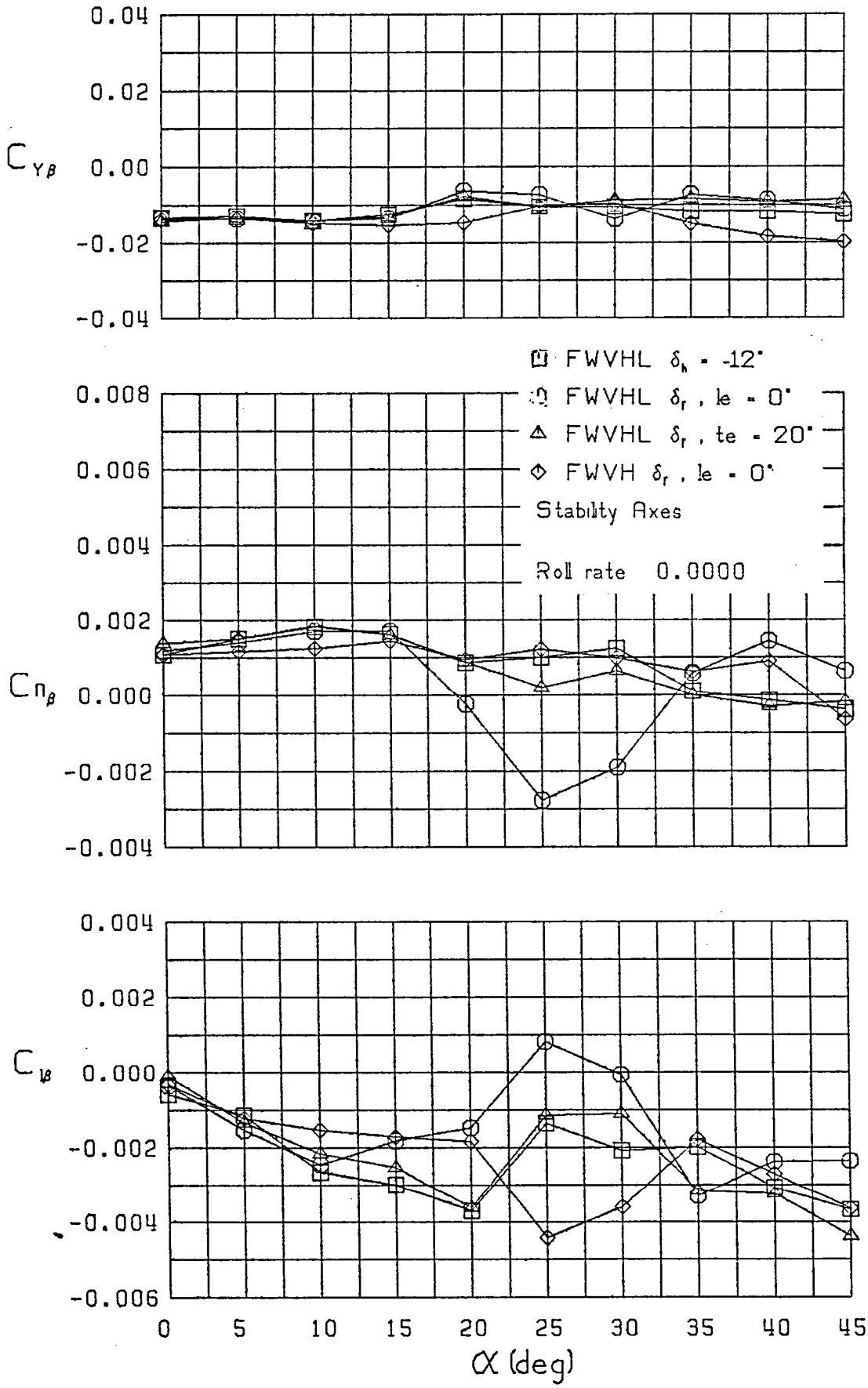

Figure 4 (Continued)

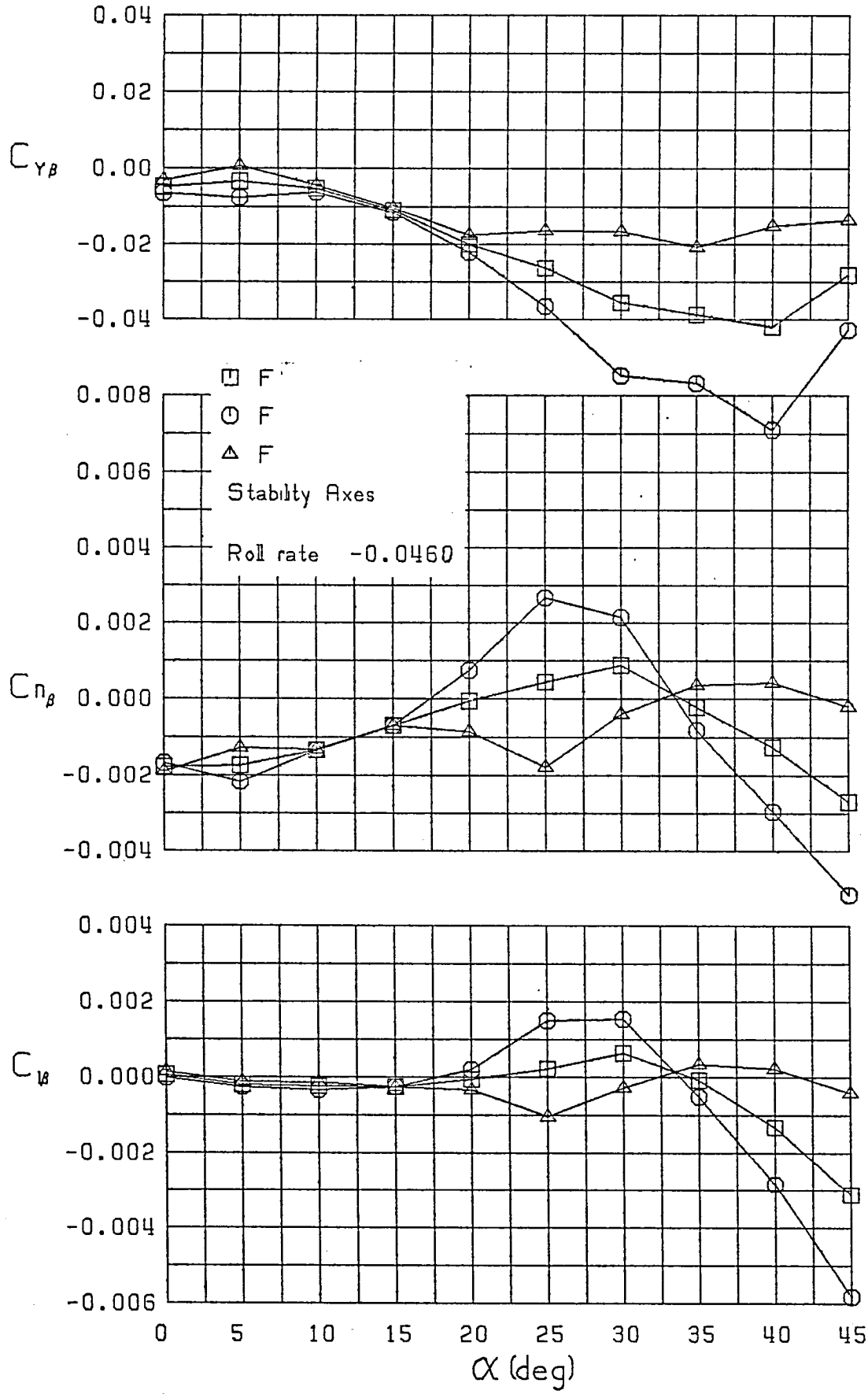

Figure 5 - Variation of Lateral-Directional Static Stability Derivatives with Angle of Attack and Sideslip, $\hat{p}$ = -0.0460

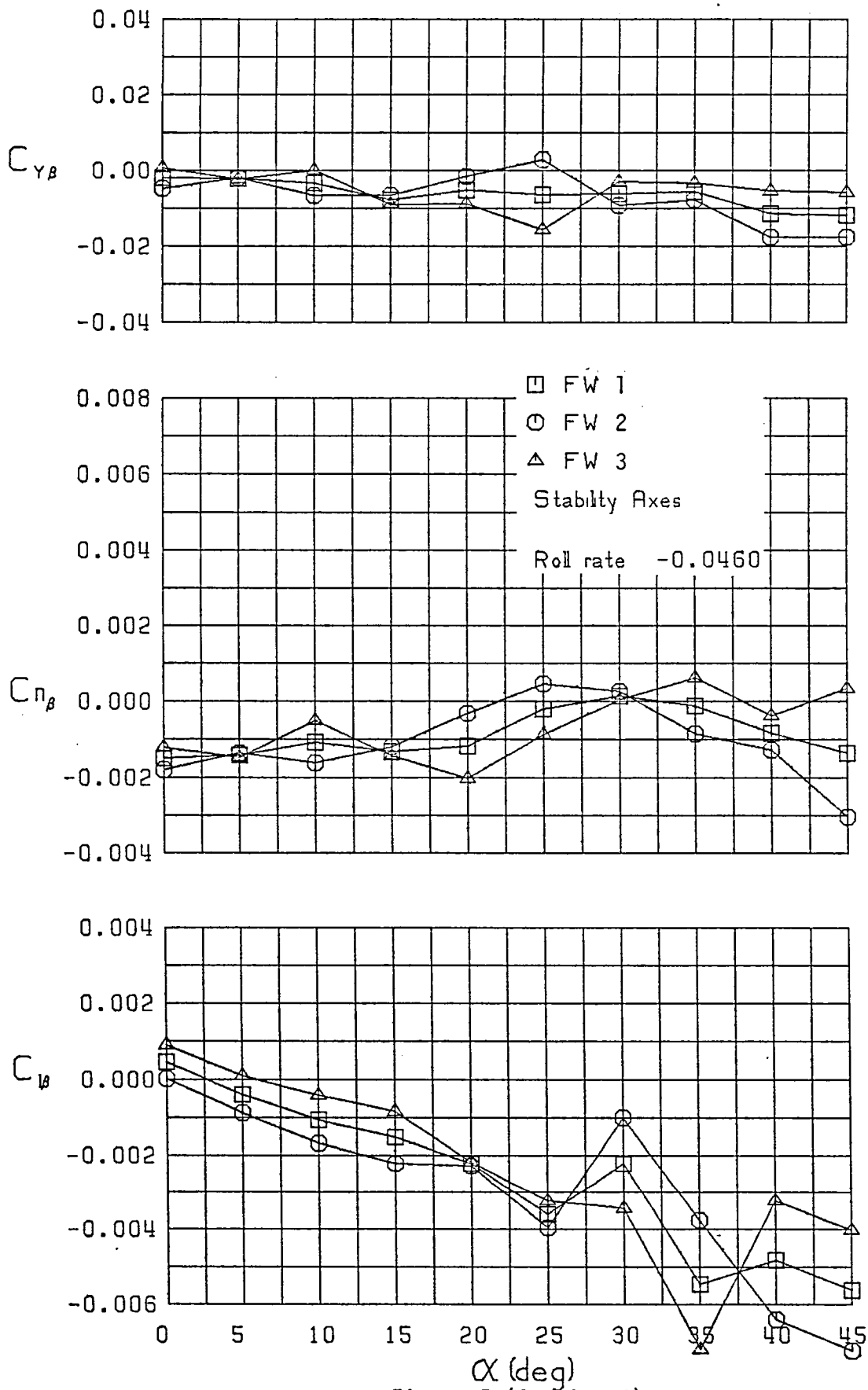

Figure 5 (Continued)

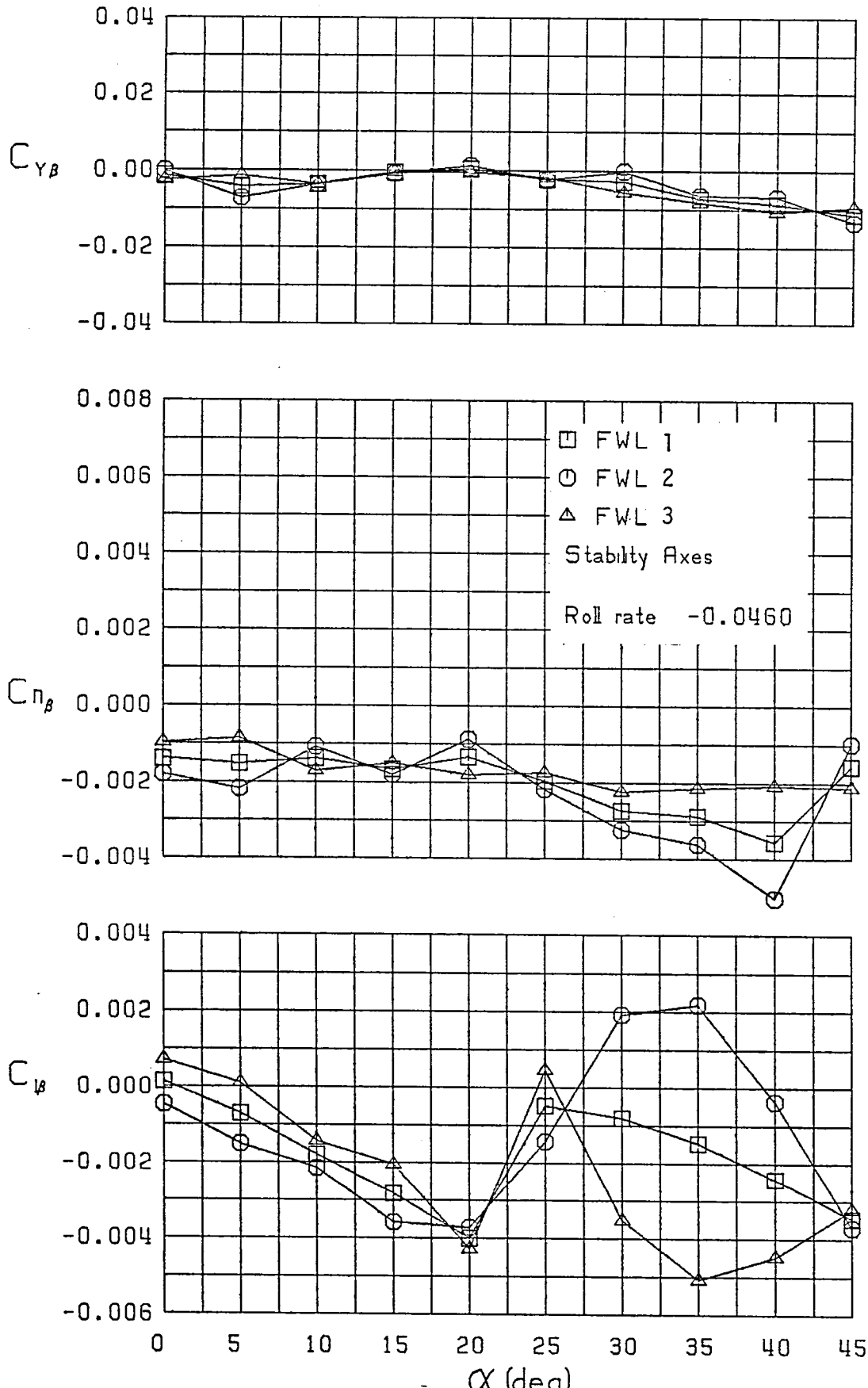

Figure 5 (Continued)

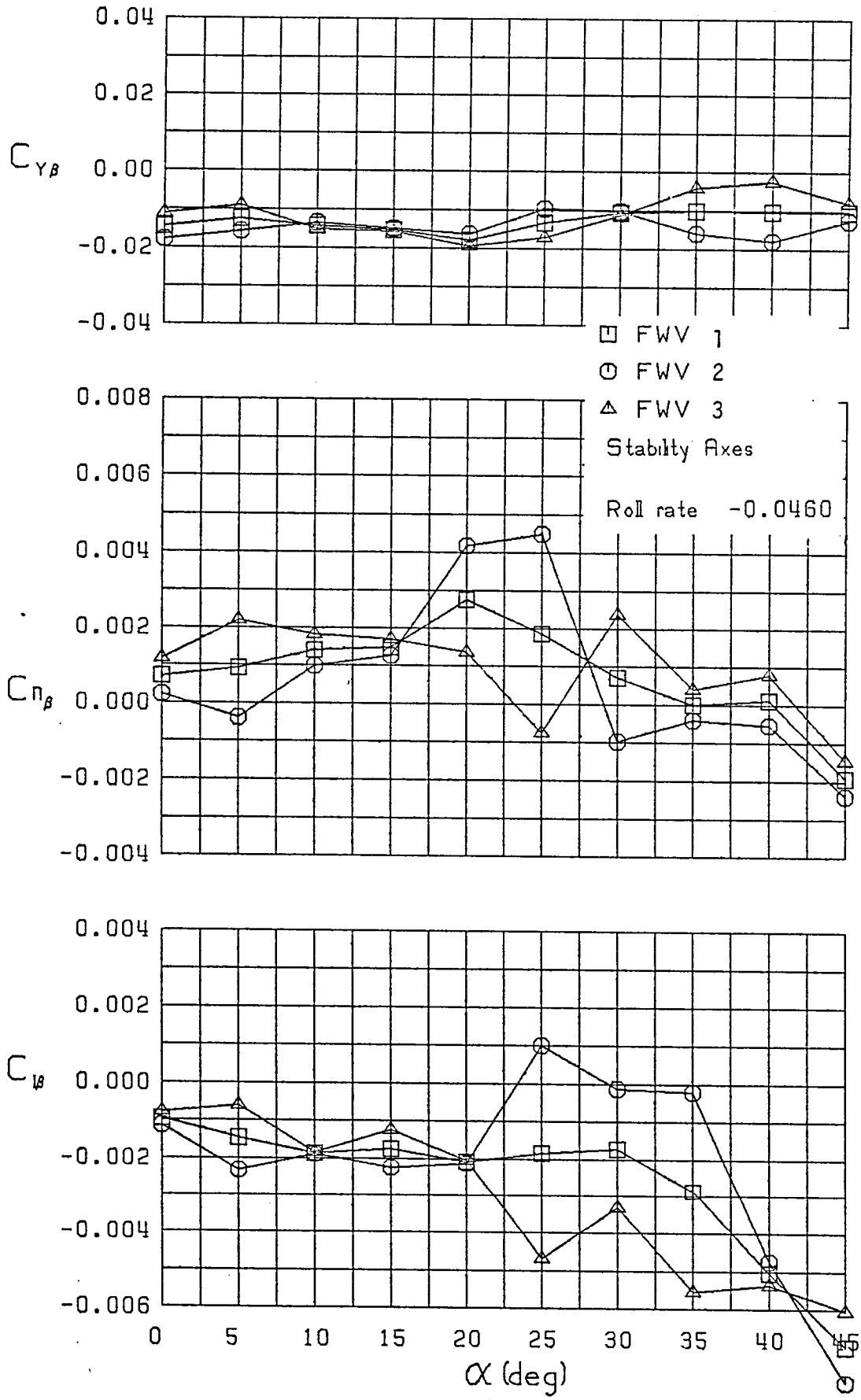

Figure 5 (Continued)

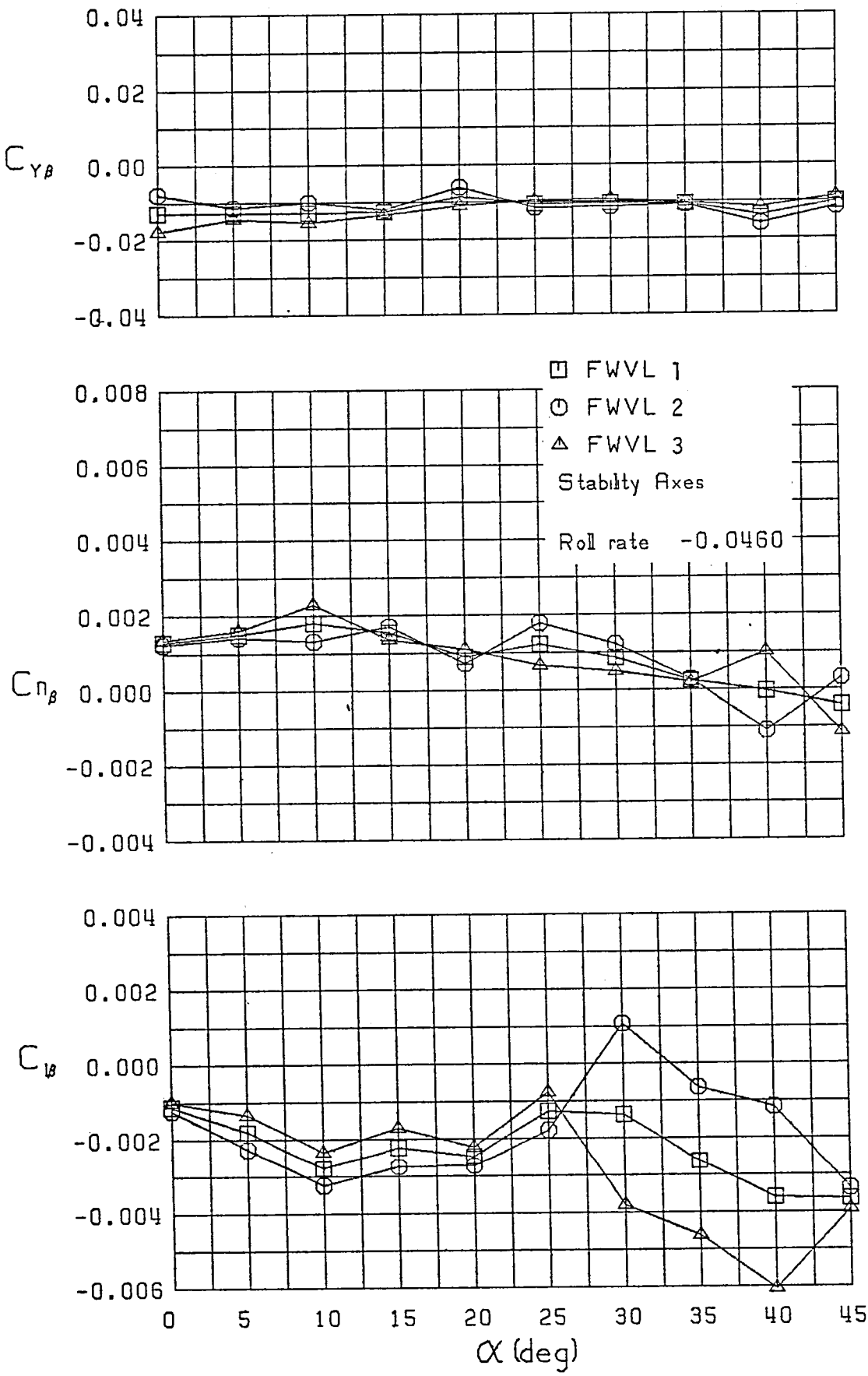

Figure 5 (Continued)

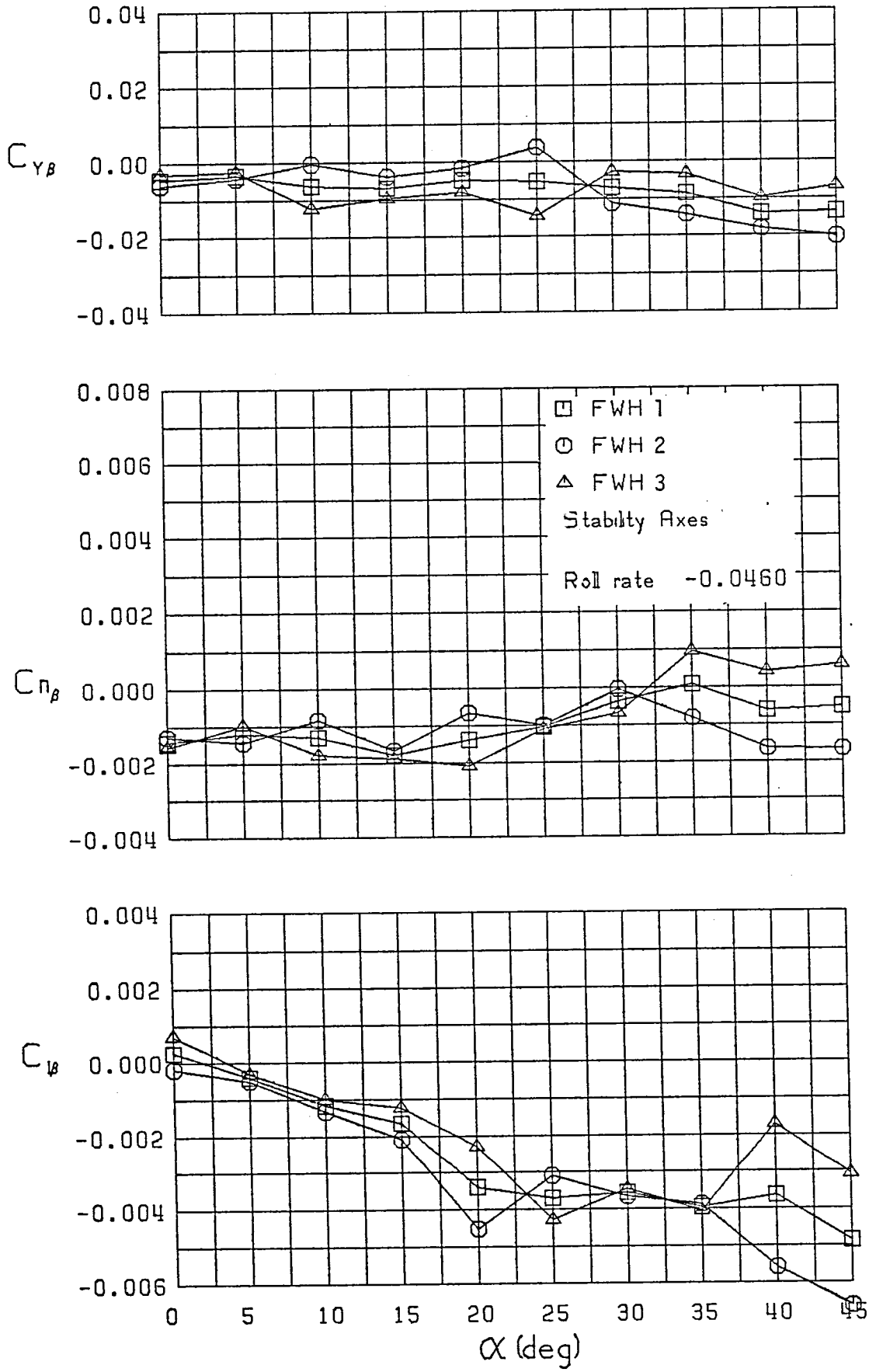

Figure 5 (Continued)

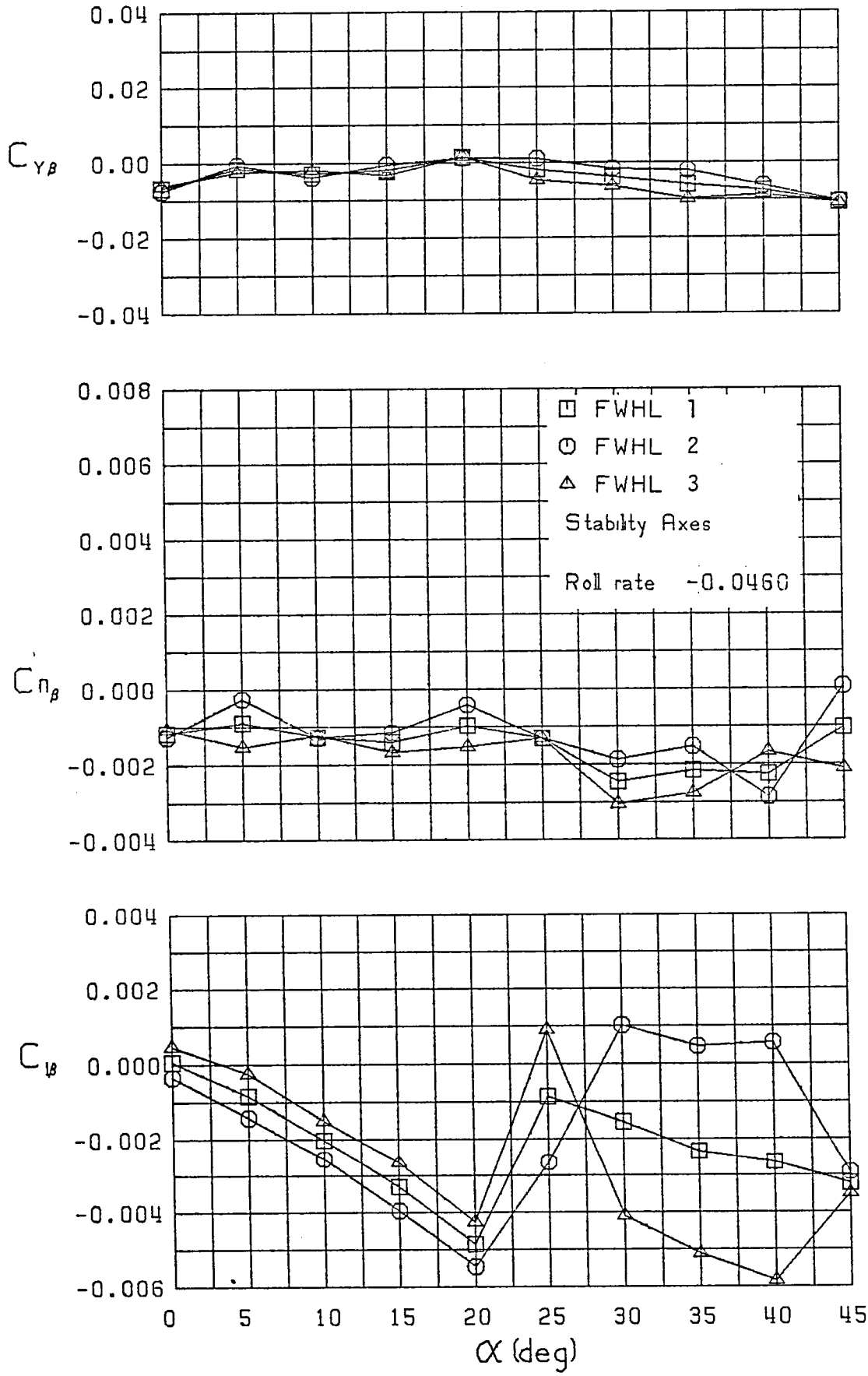

Figure 5 (Continued)

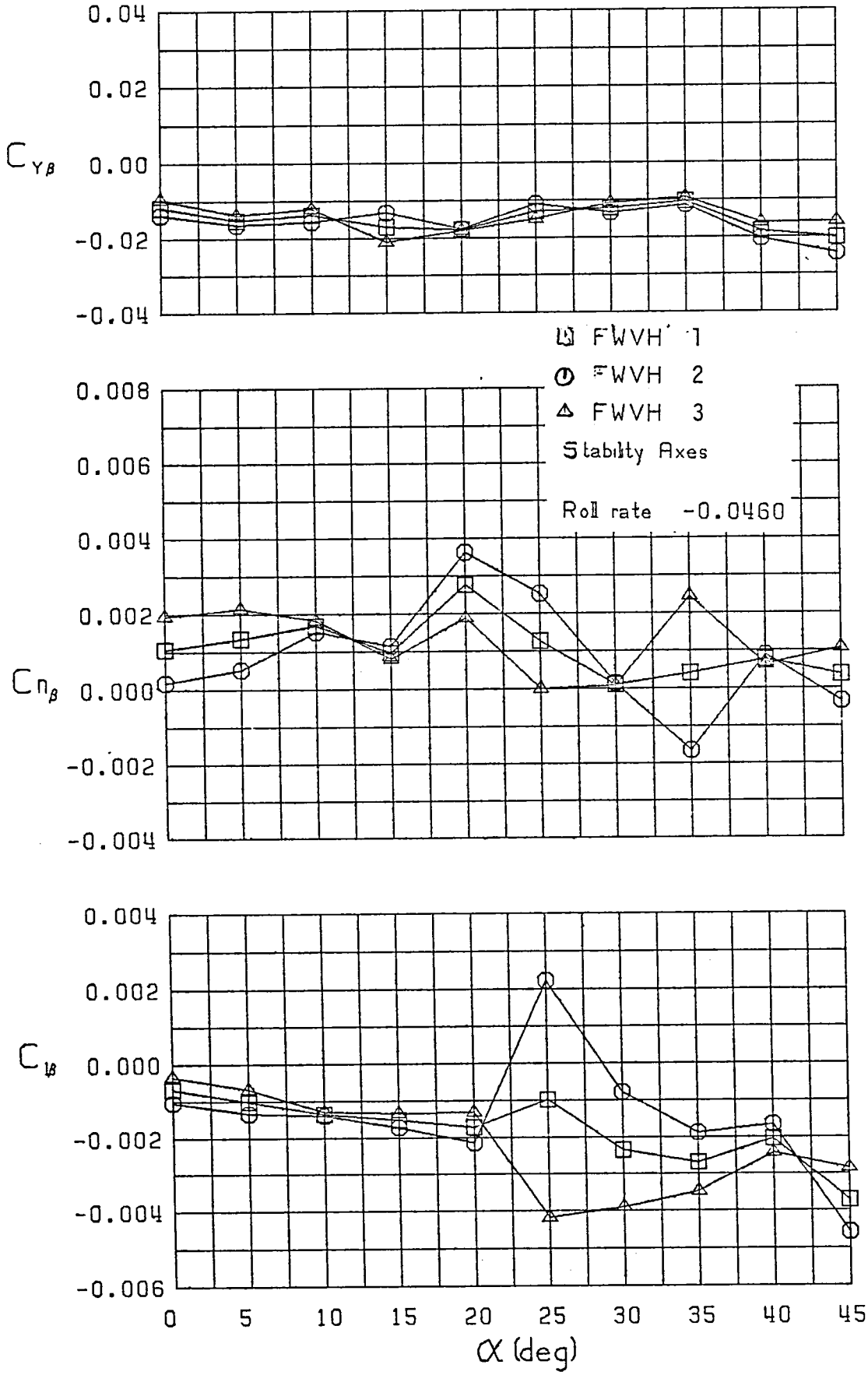

Figure 5 (Continued)

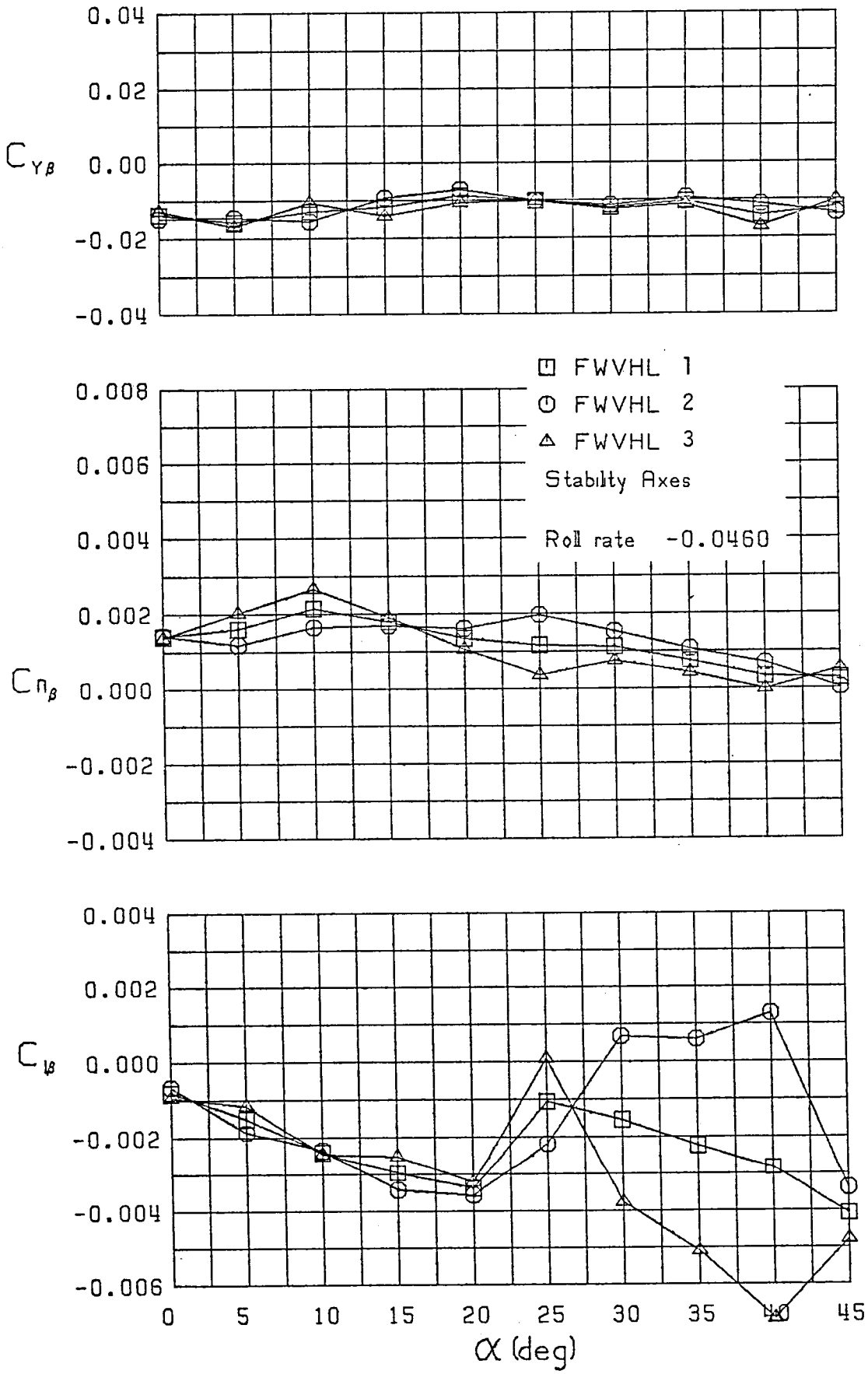

Figure 5 (Continued)

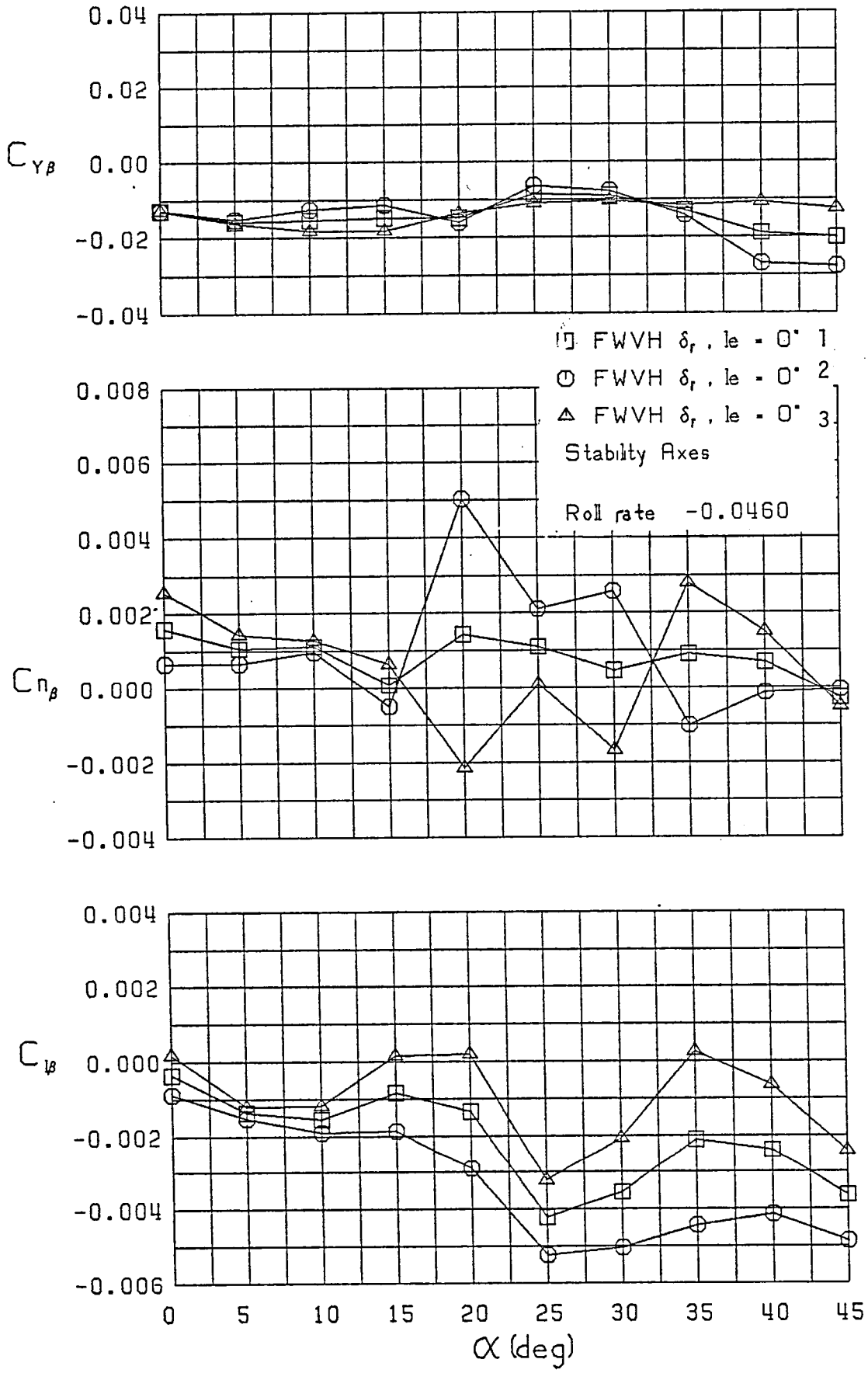

Figure 5 (Continued)

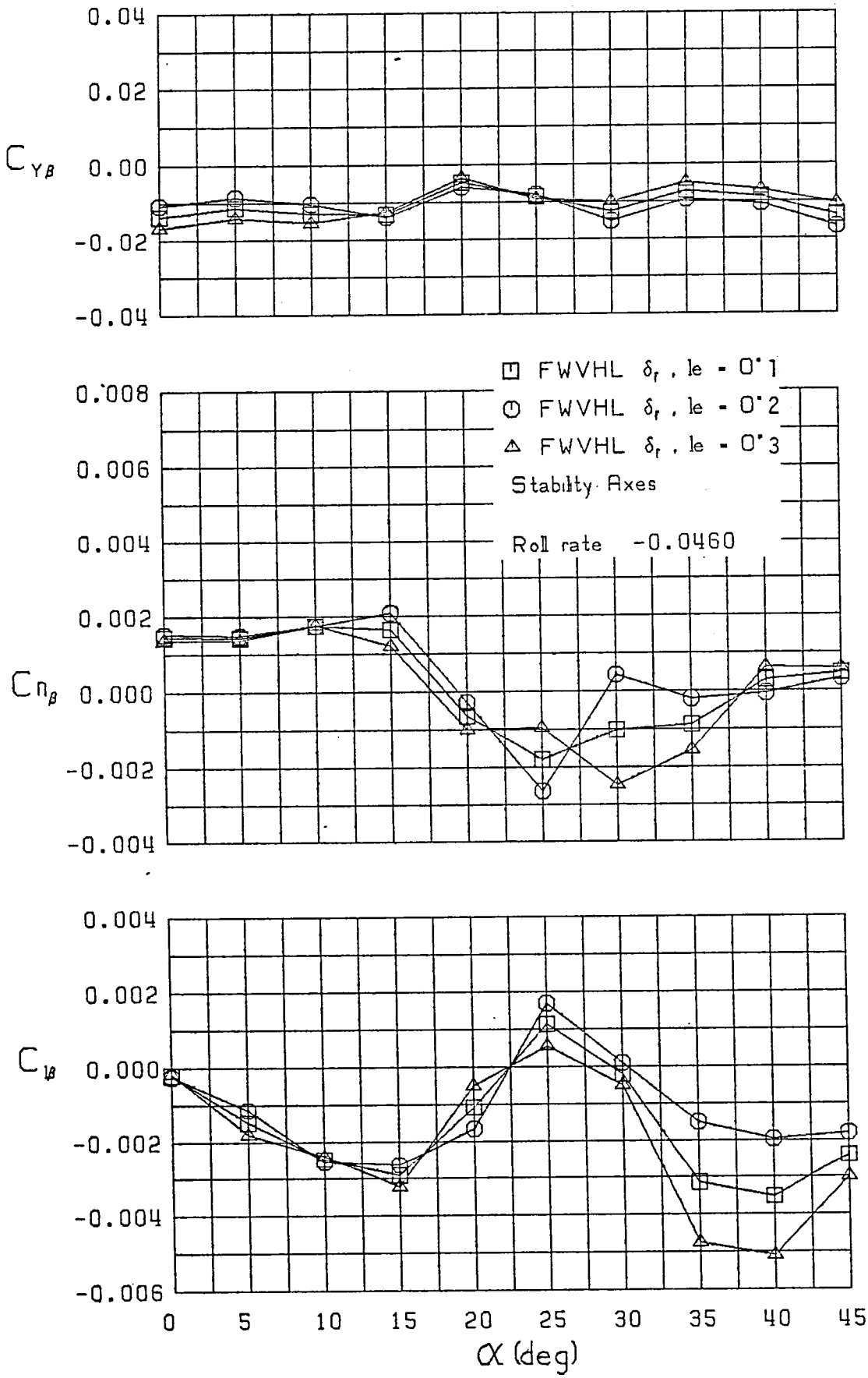

Figure 5 (Continued)

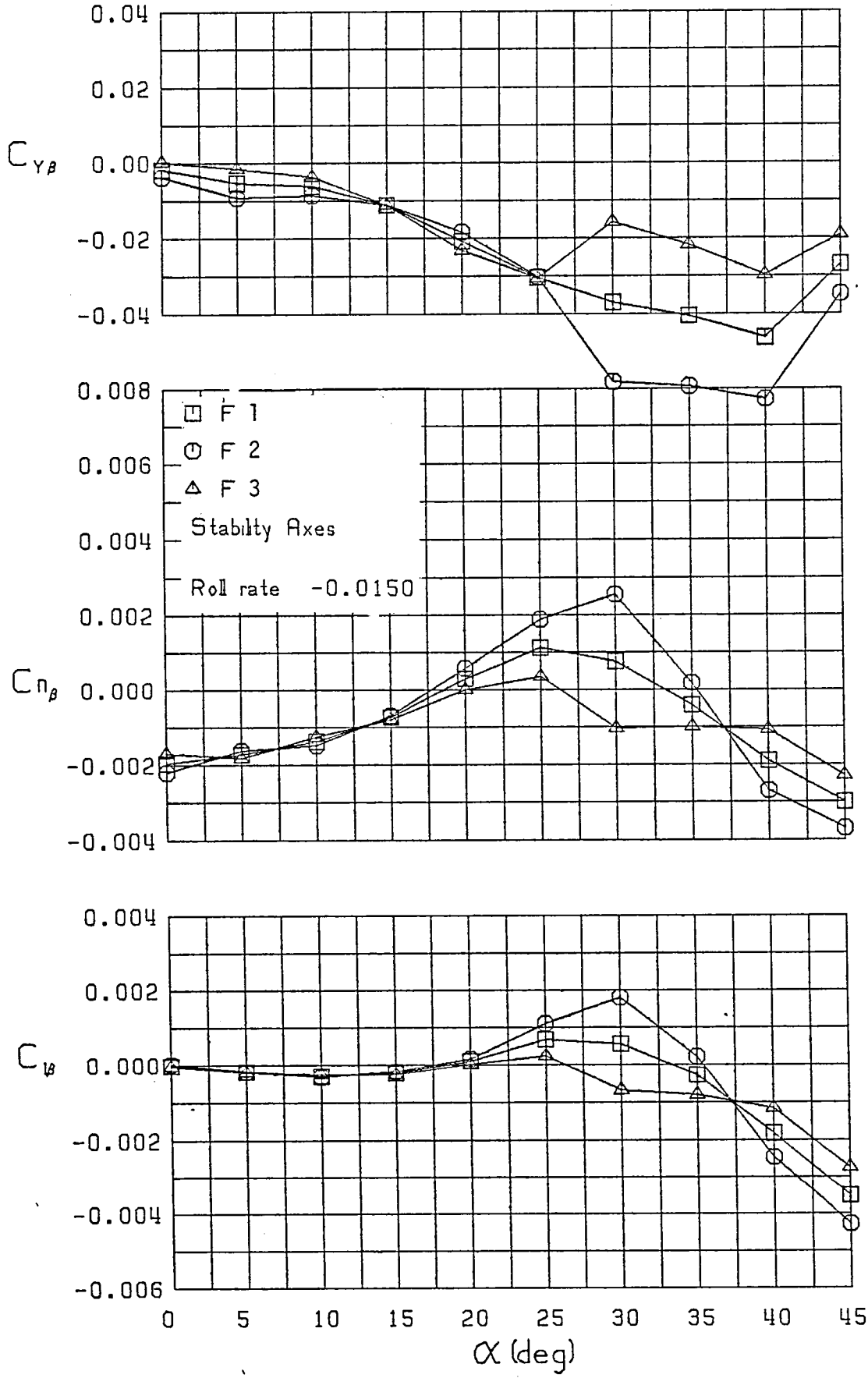

Figure 6 - Variation of Lateral-Directional Static Stability Derivatives with Angle of Attack and Sideslip, $\hat{p}$ =-0.0150

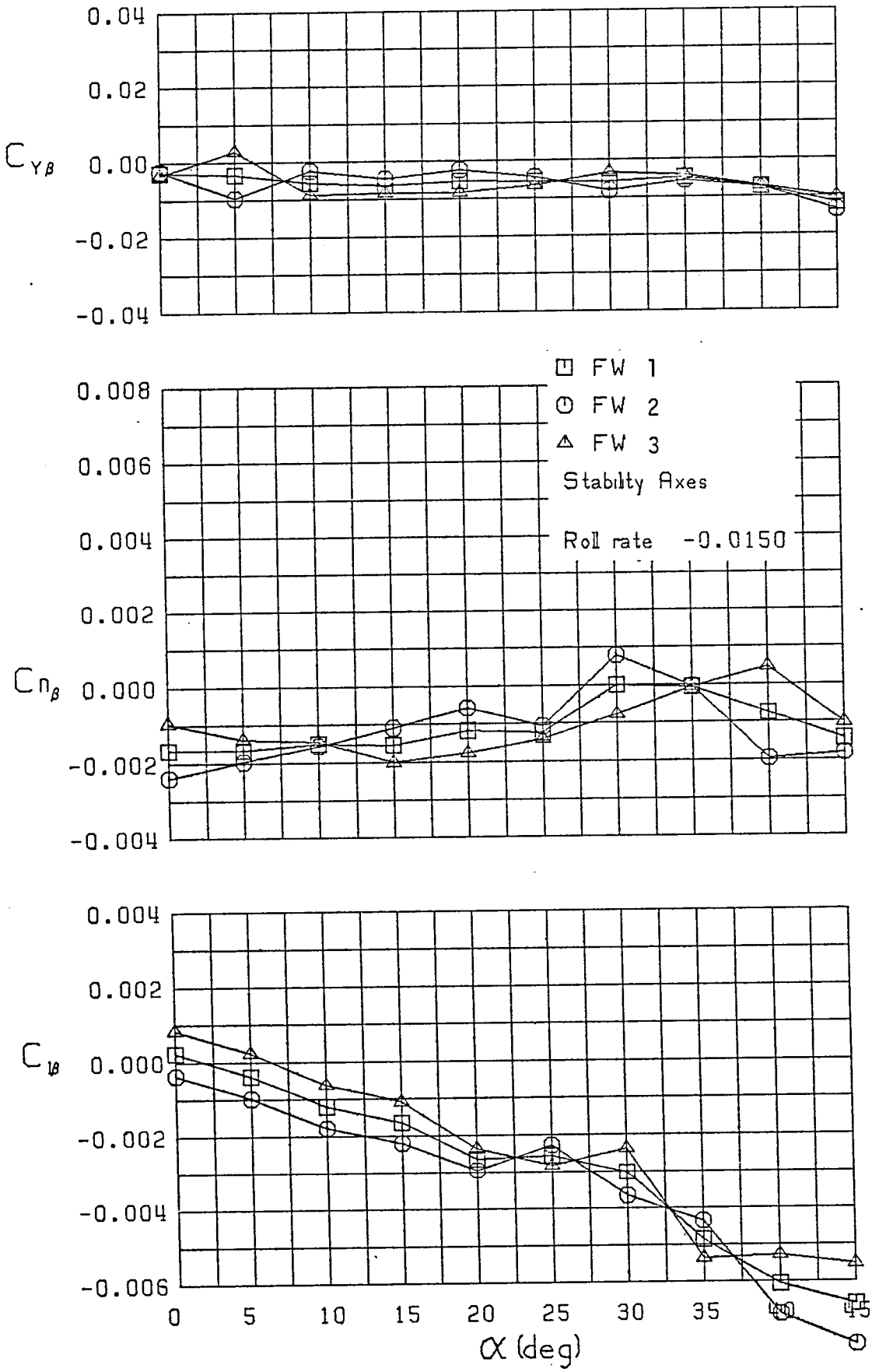

Figure 6 (Continued)

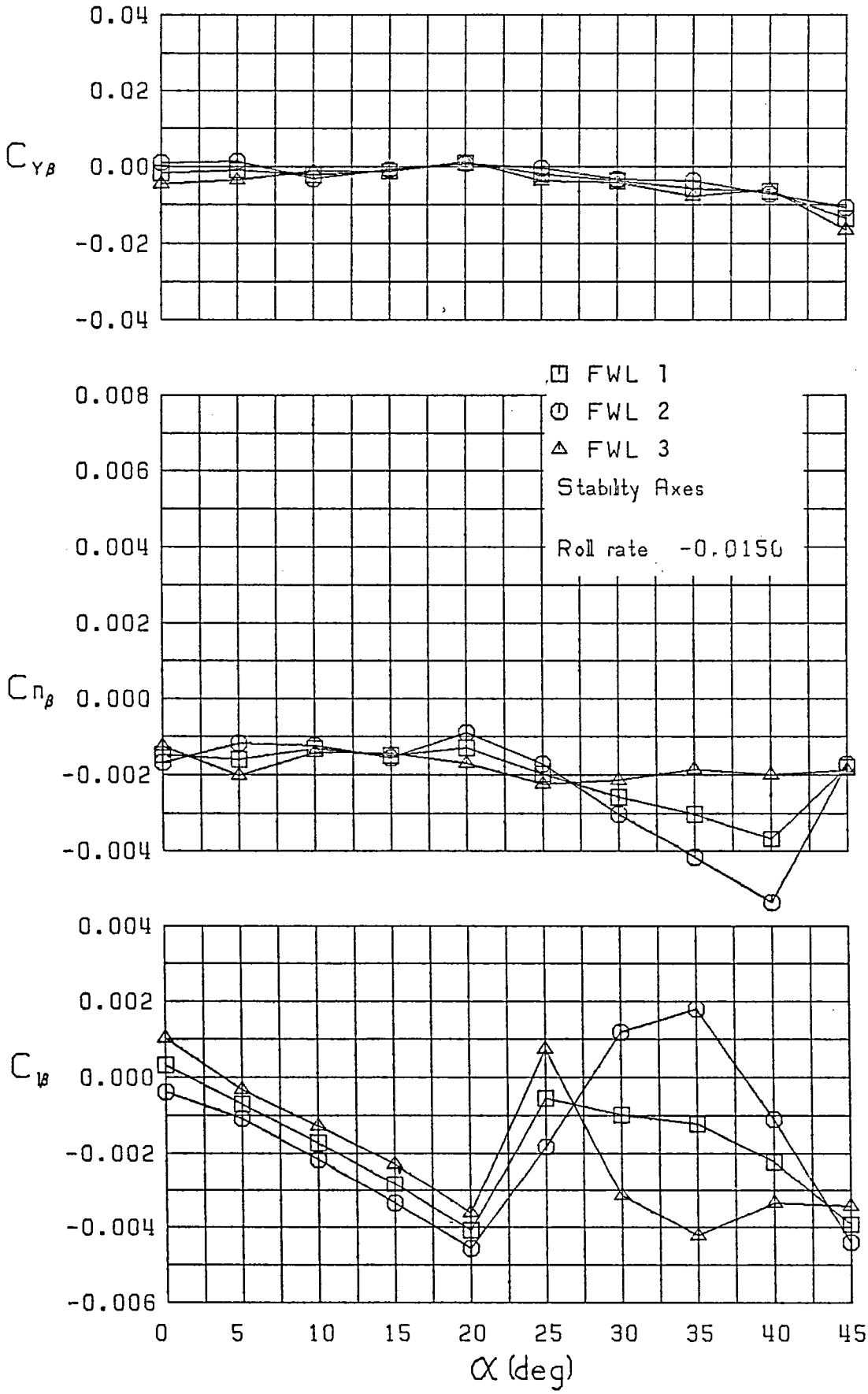

Figure 6 (Continued)

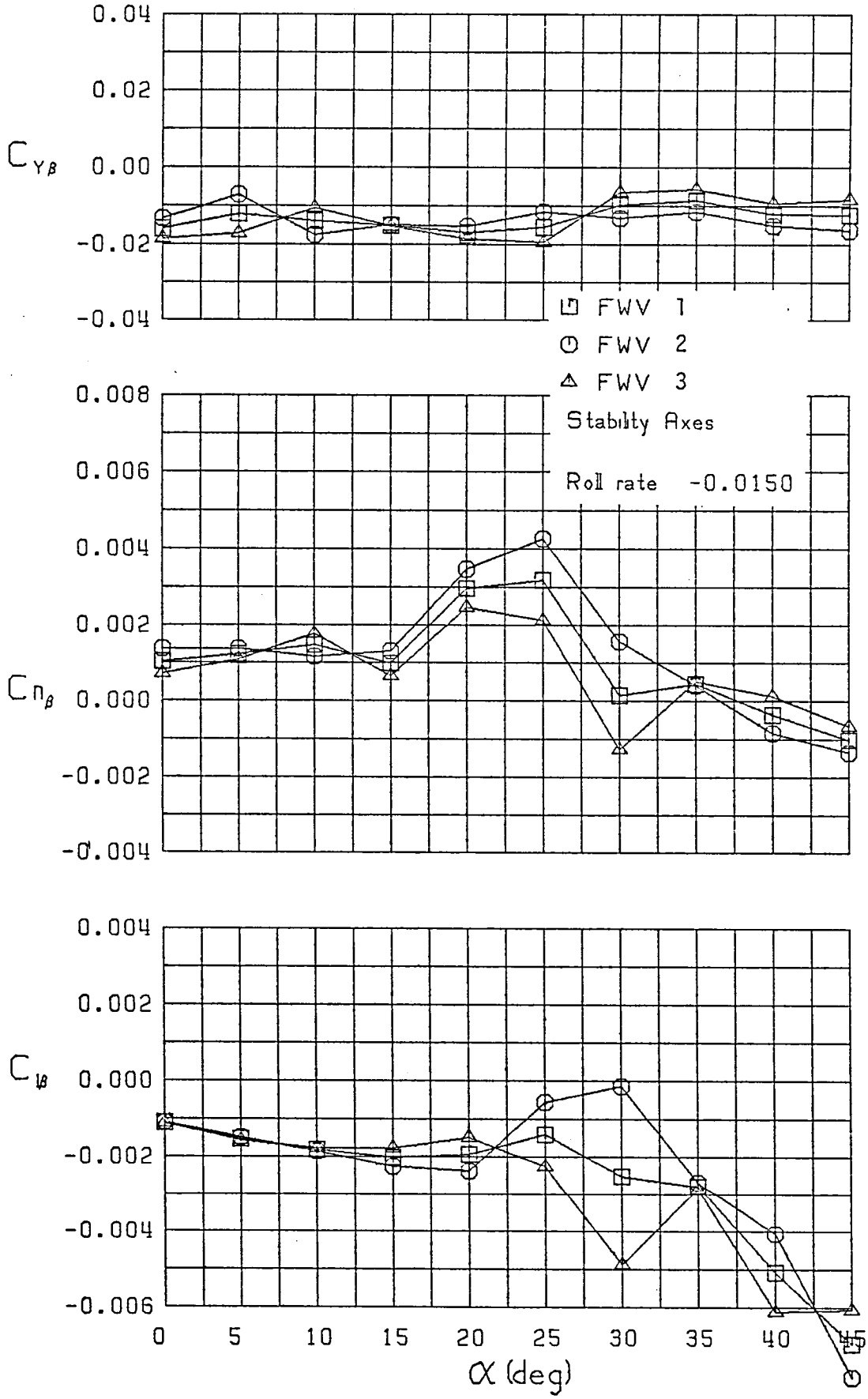

Figure 6 (Continued)

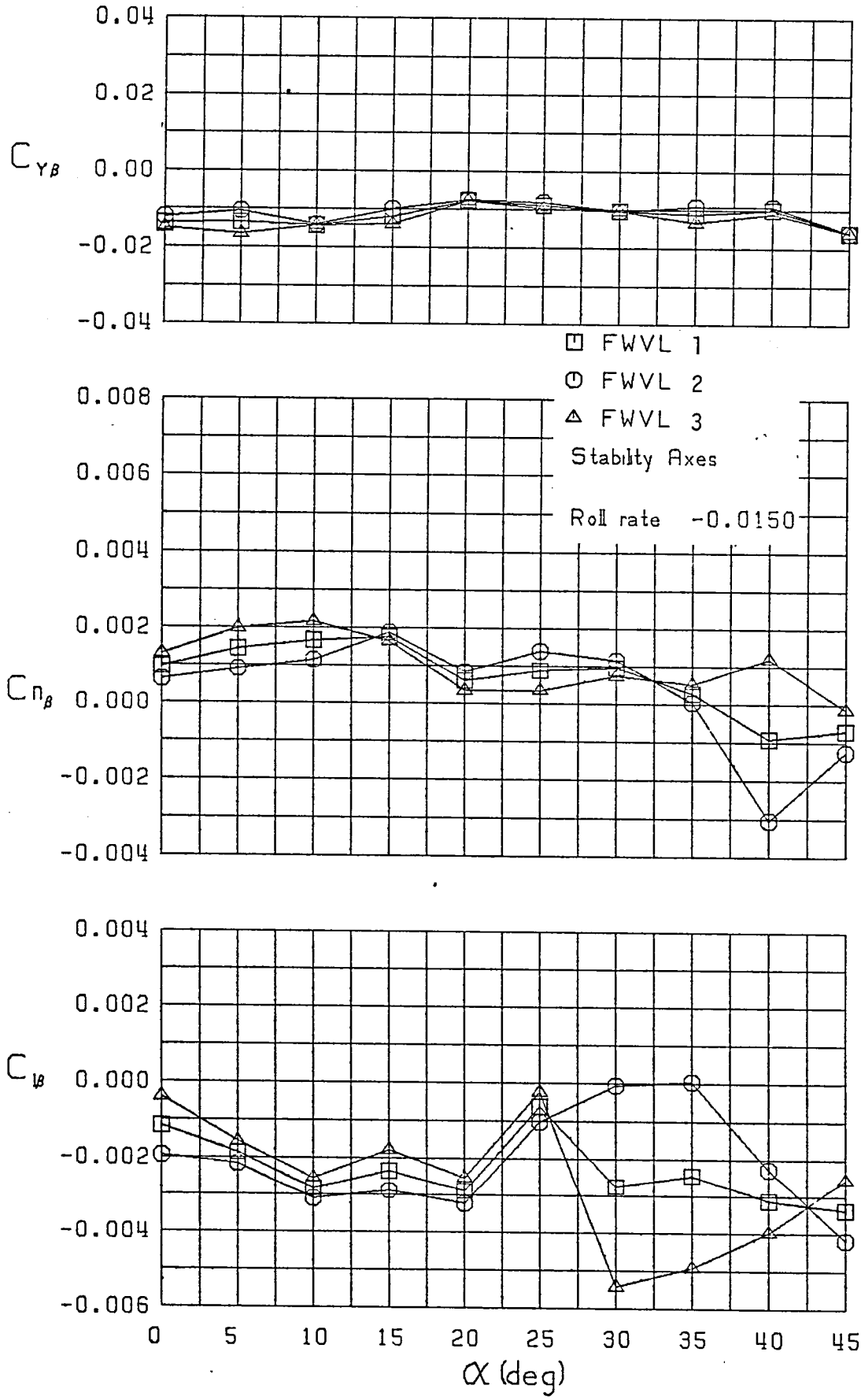

Figure 6 (Continued)

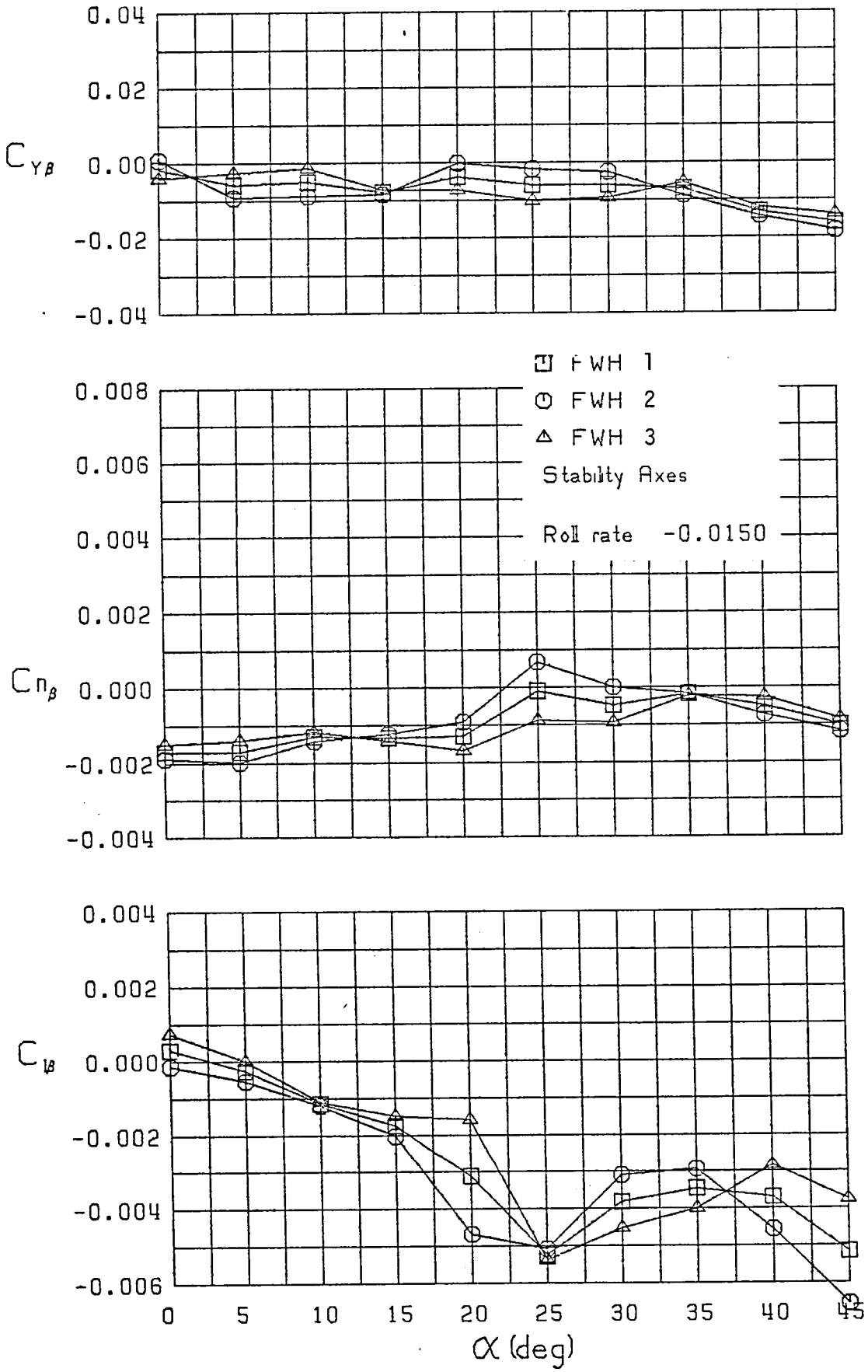

Figure 6 (Continued)

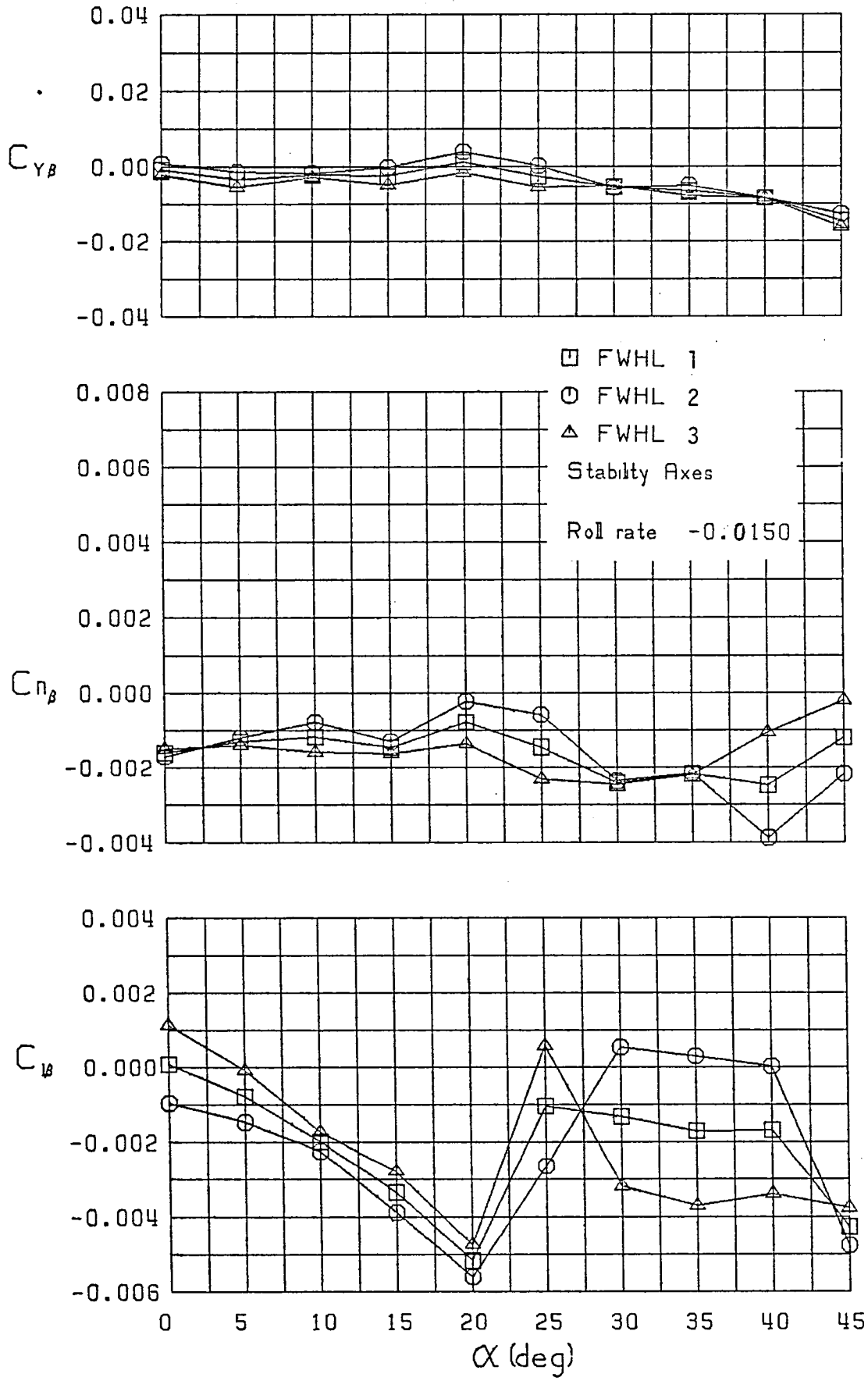

Figure 6 (Continued)

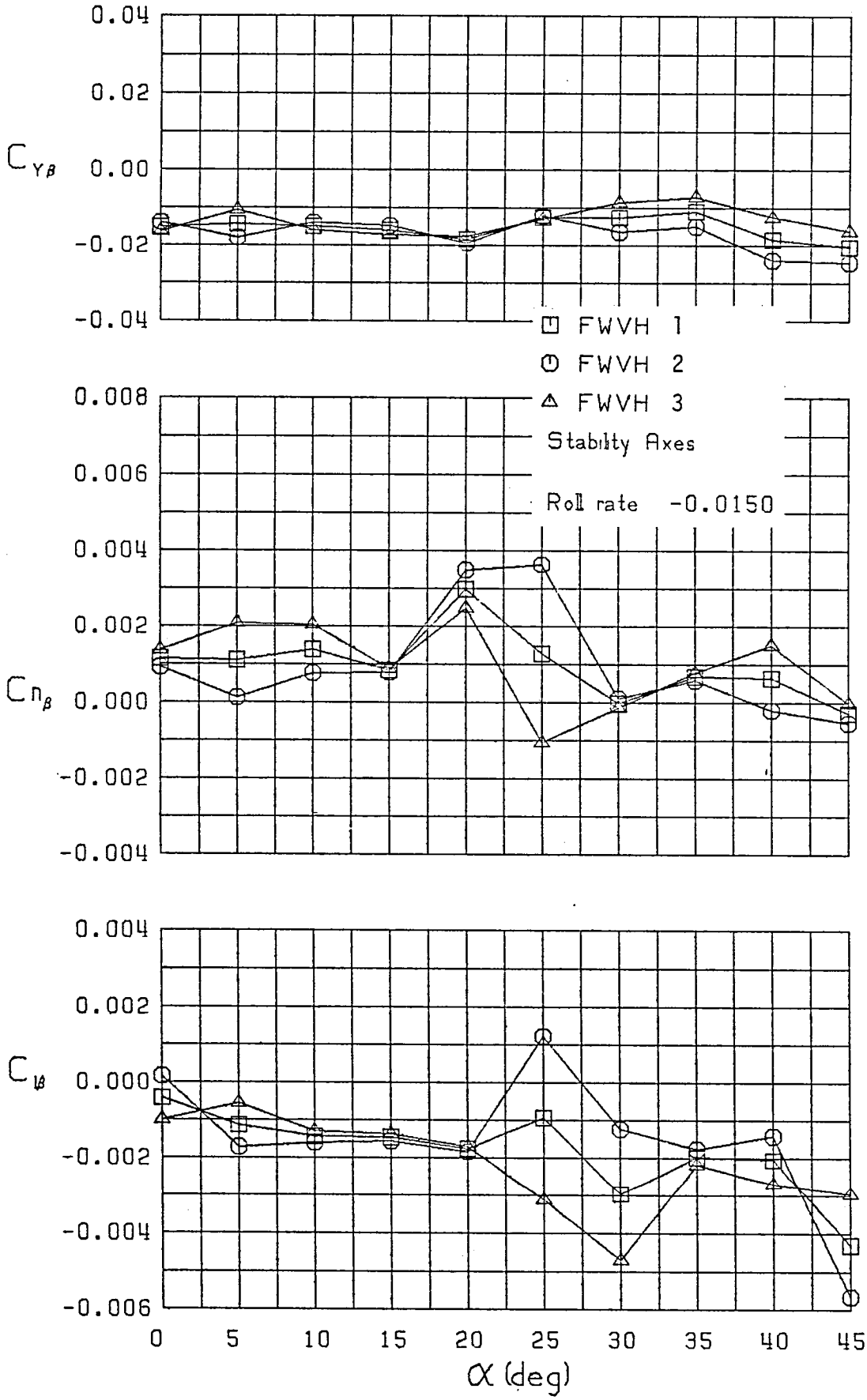

Figure 6 (Continued)

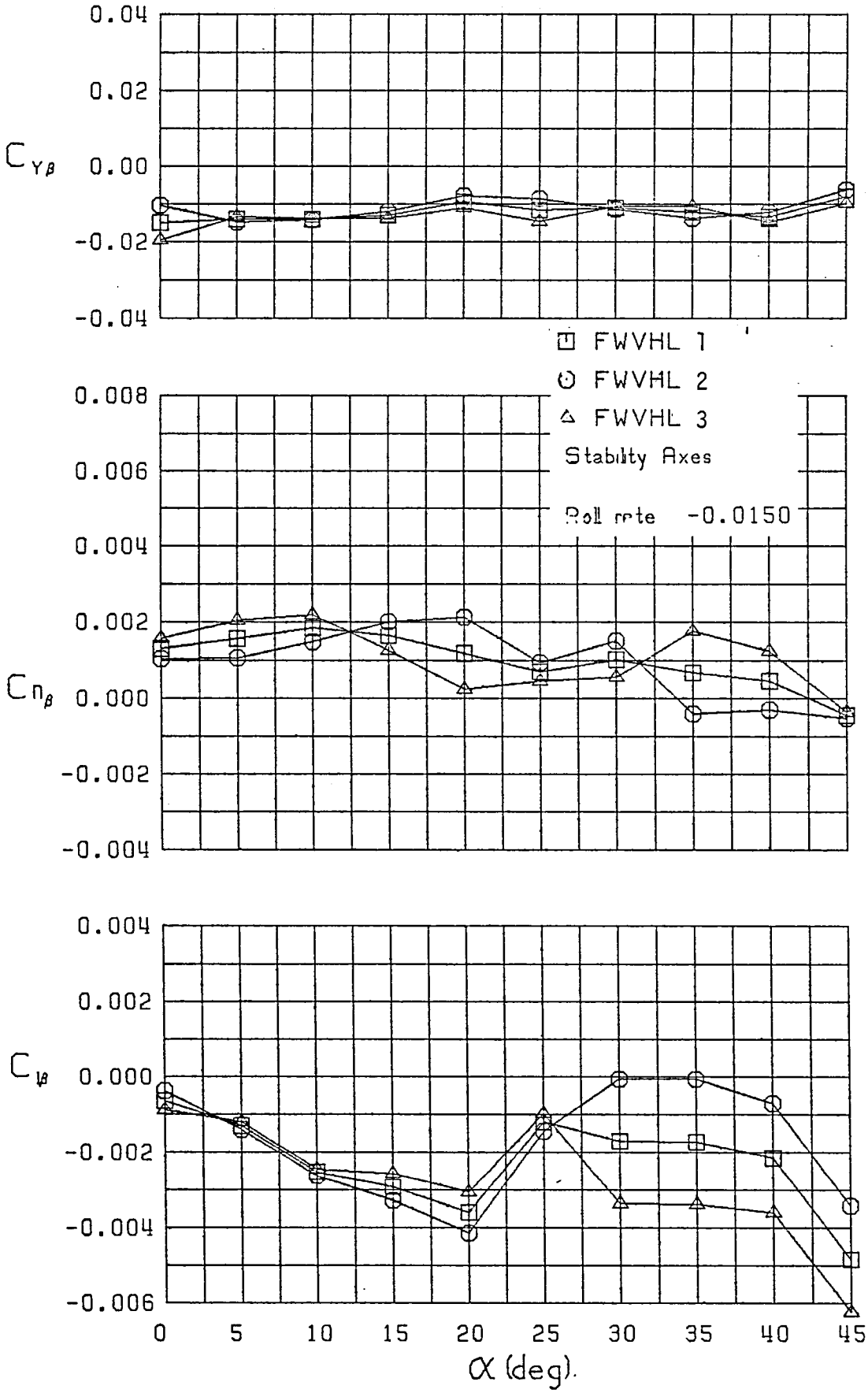

Figure 6 (Continued)

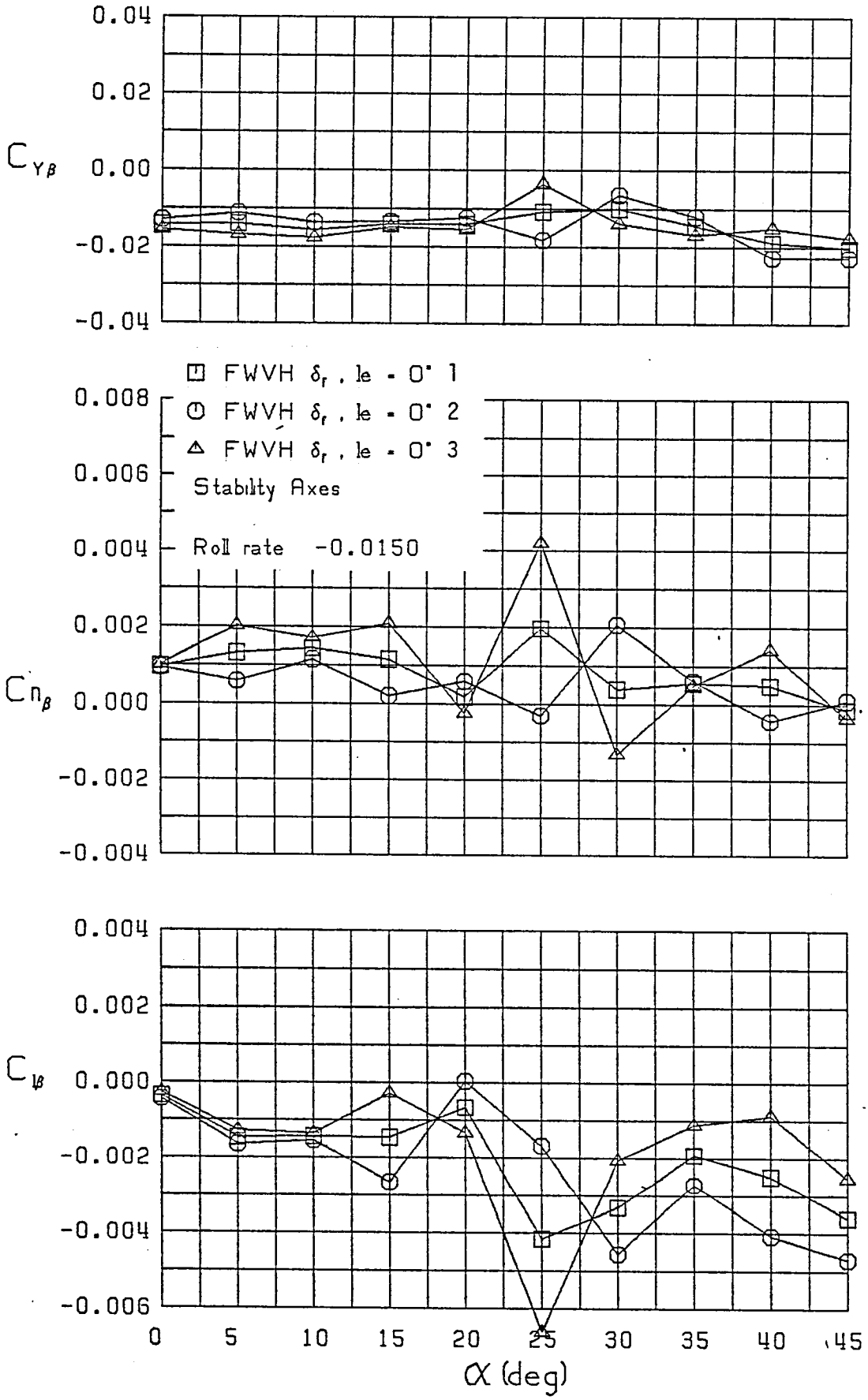

Figure 6 (Continued)

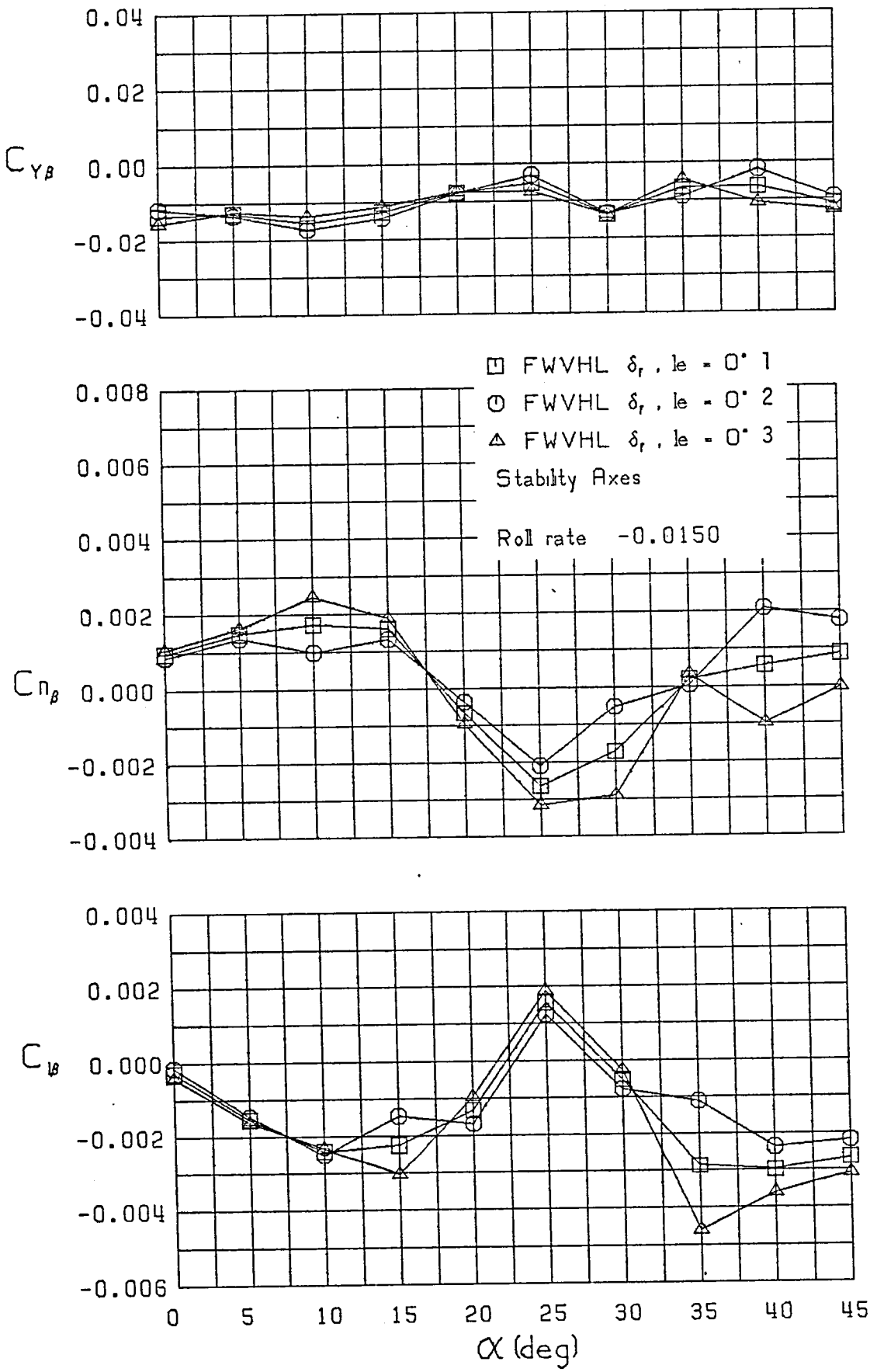

Figure 6 (Continued)

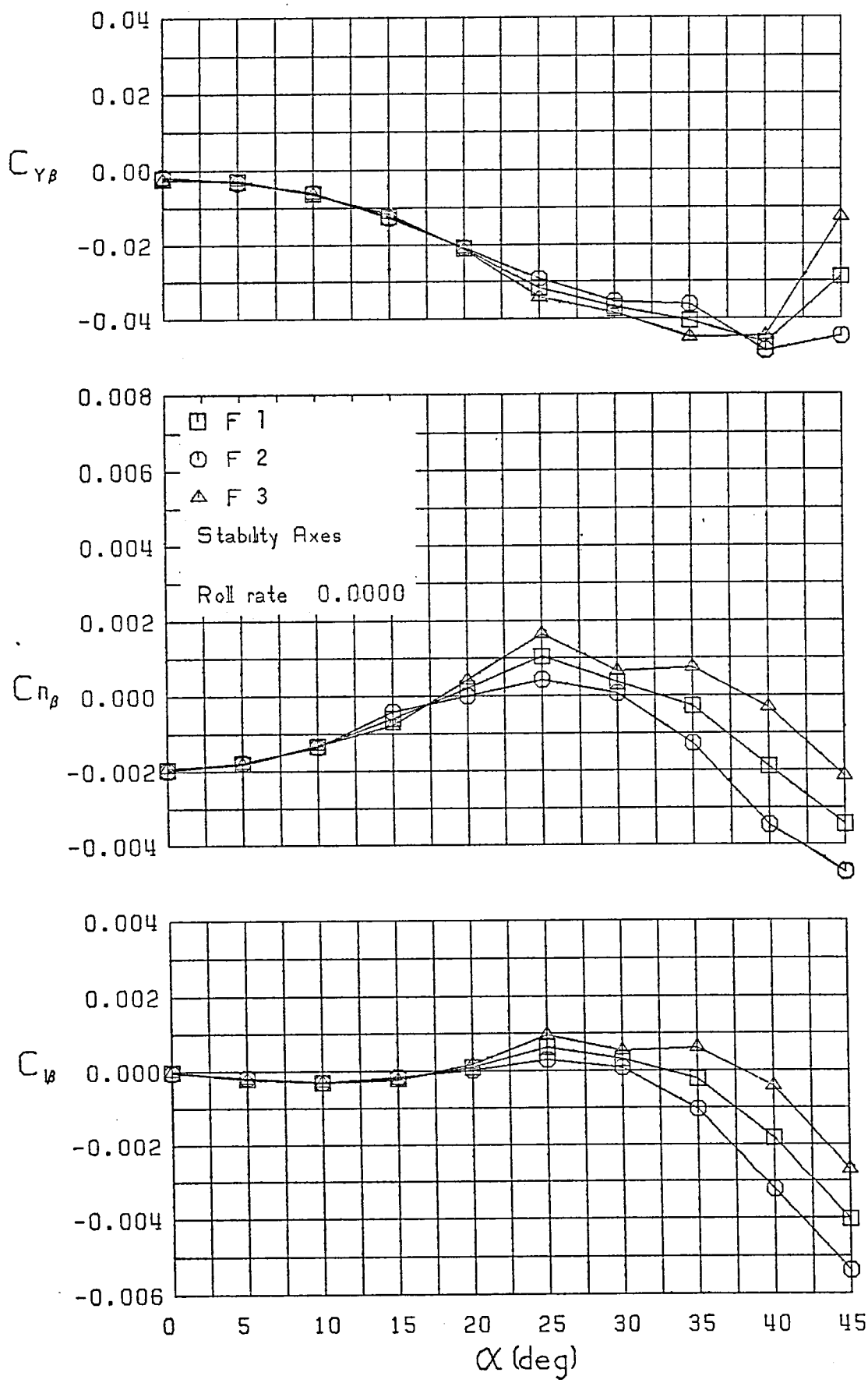

Figure 7 - Variation of Lateral-Directional Static Stability Derivatives with Angle of Attack and Sideslip, $\hat{p}$ = 0.0000

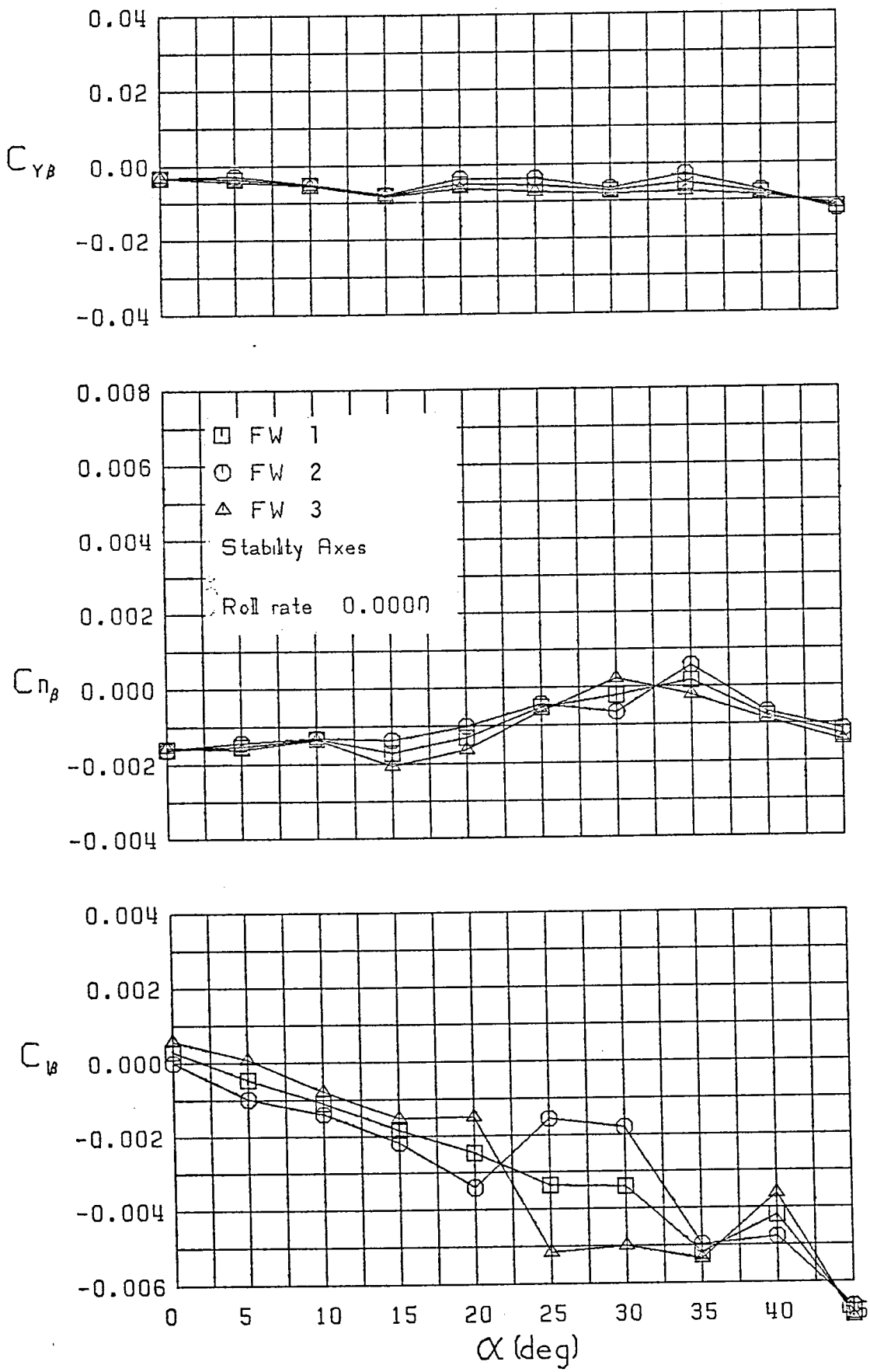

Figure 7 (Continued)

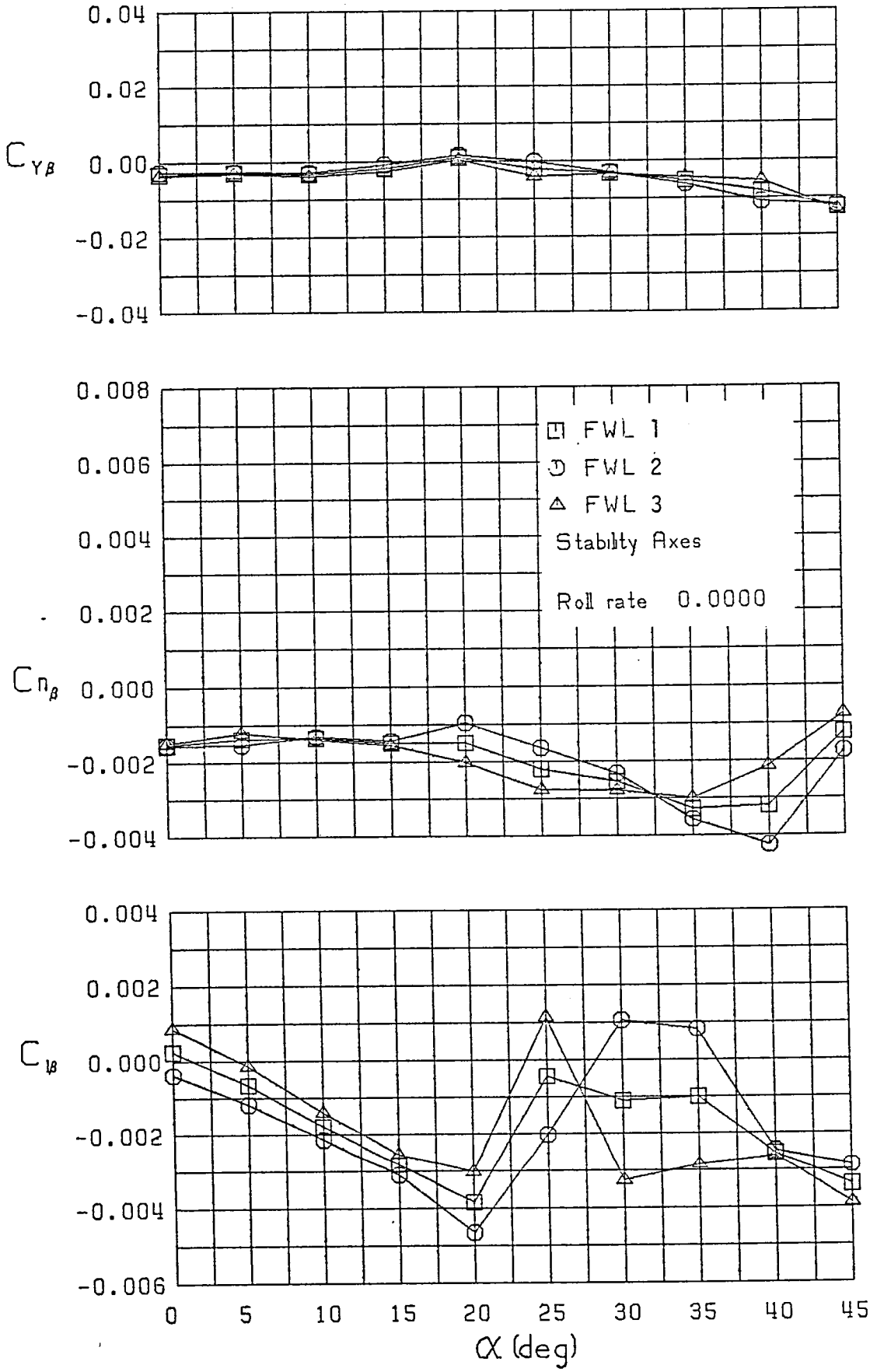

Figure 7 (Continued)

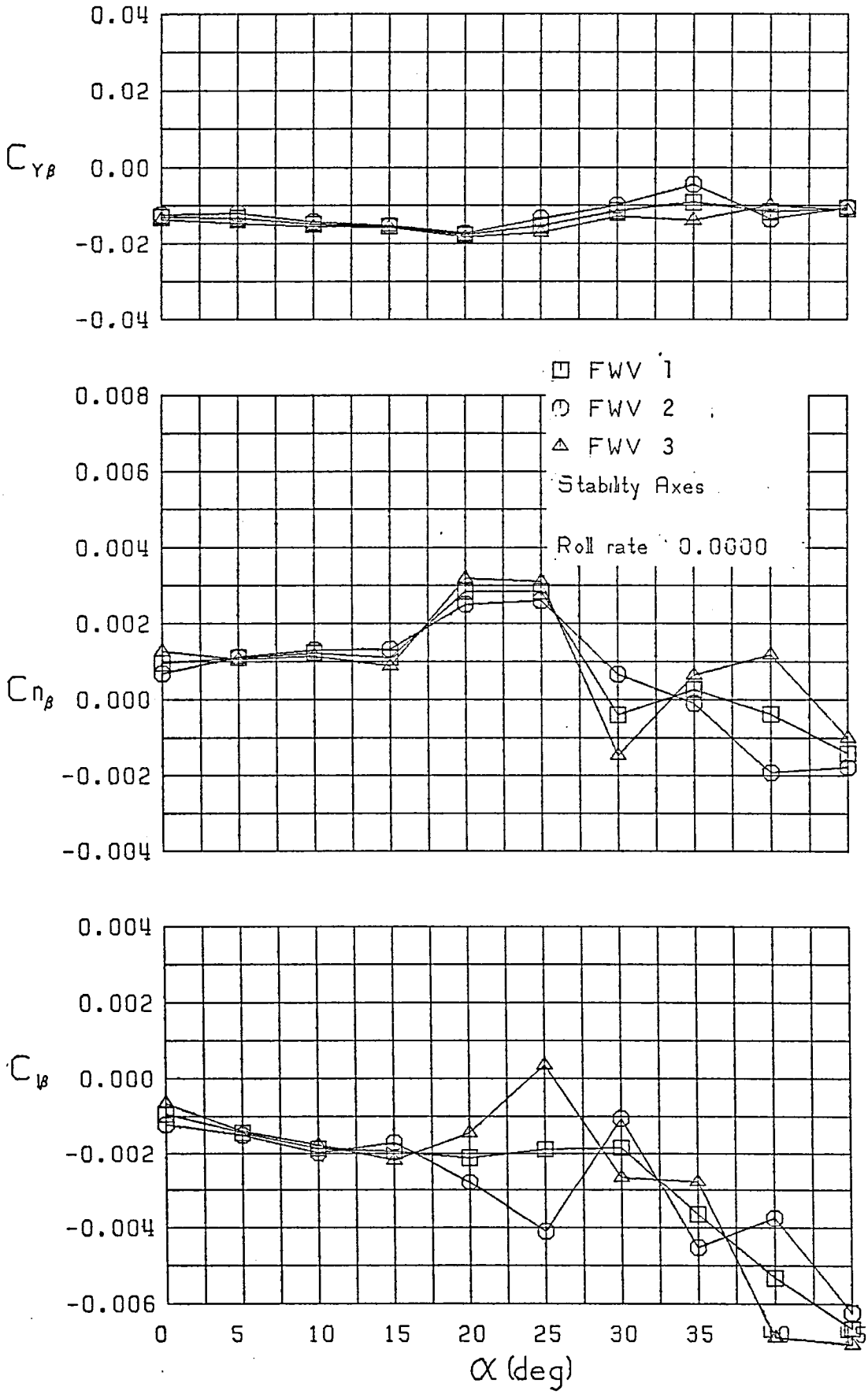

Figure 7 (Continued)

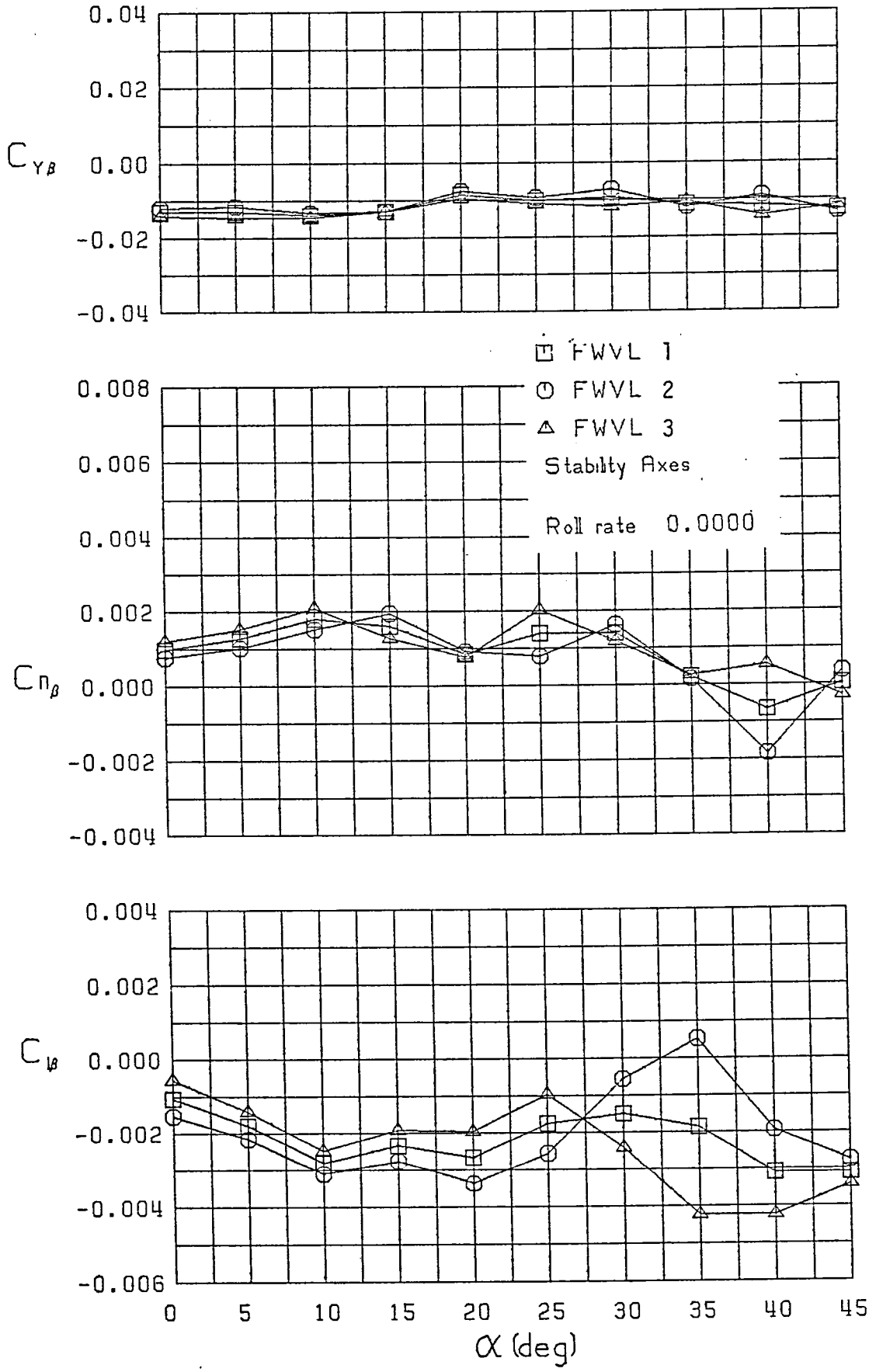

Figure 7 (Continued)

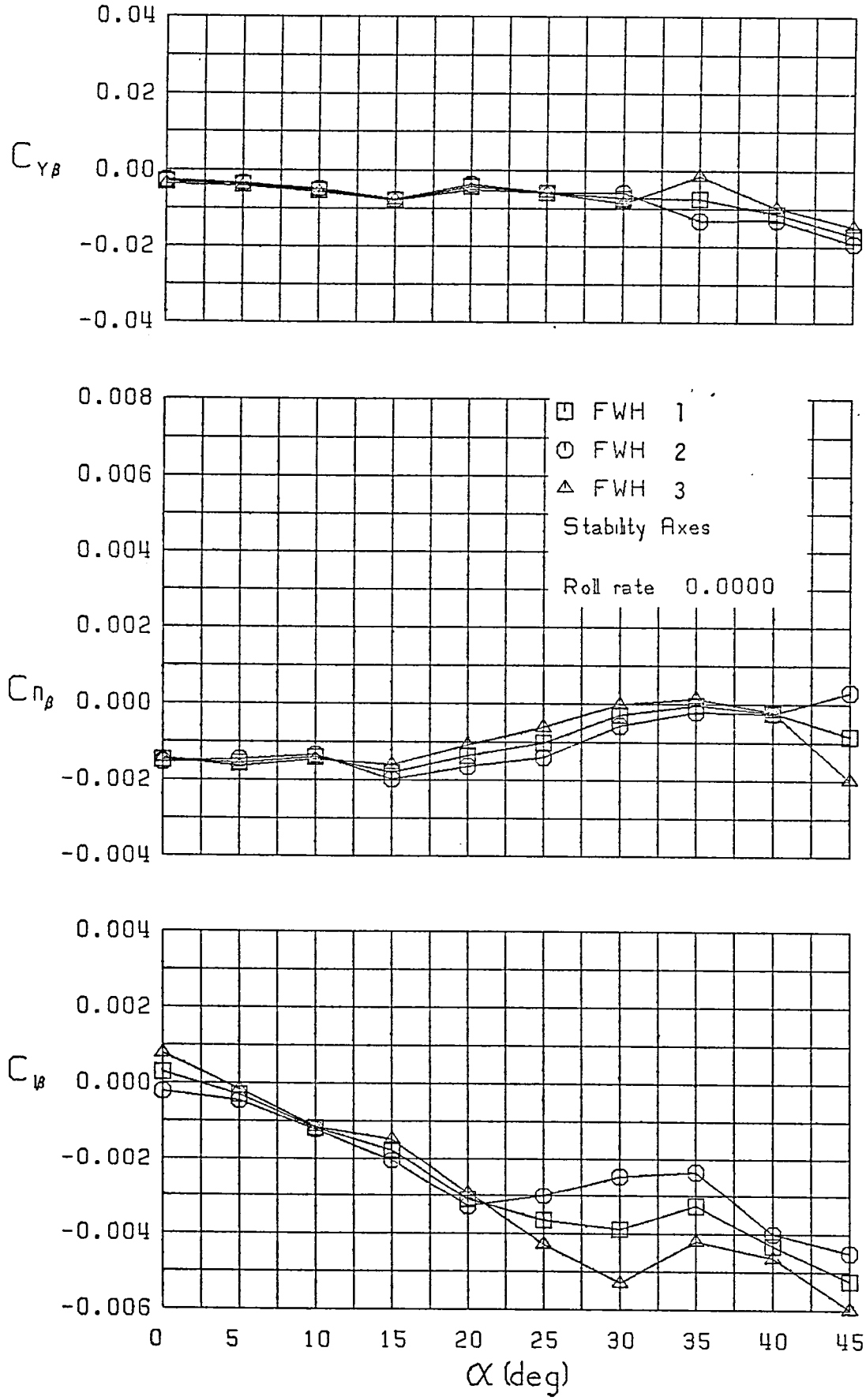

Figure 7 (Continued)

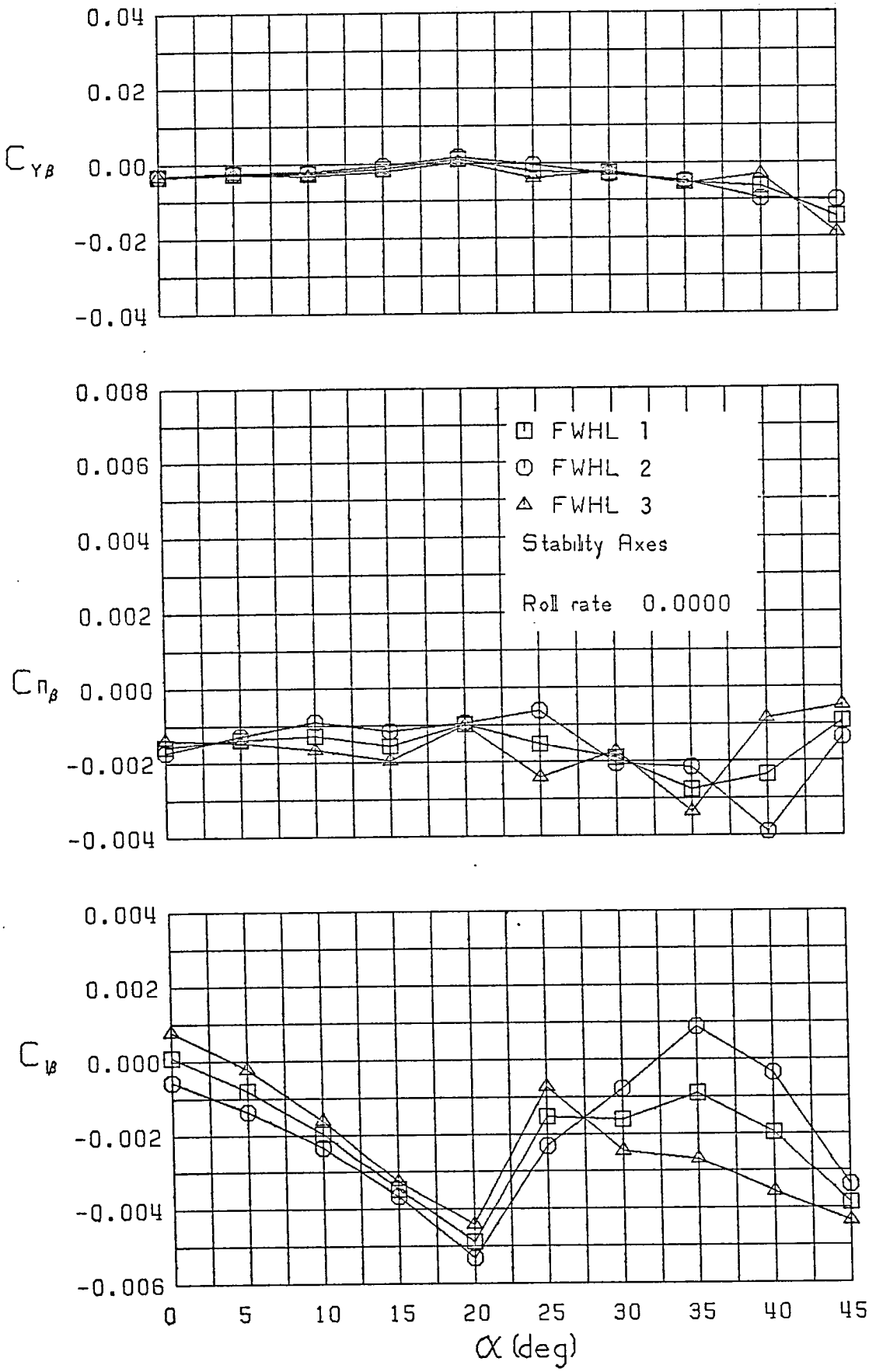

Figure 7 (Continued)

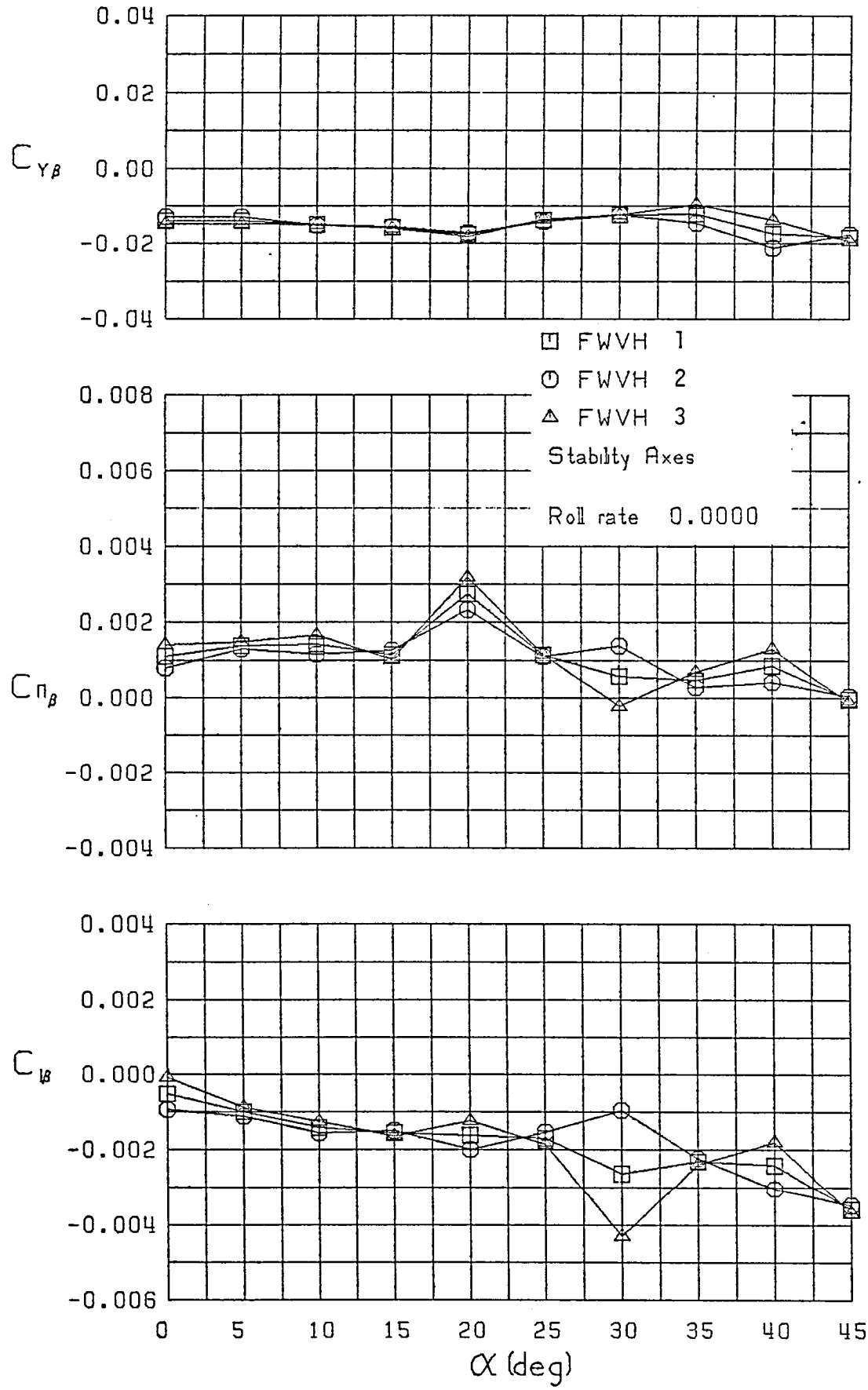

Figure 7 (Continued)

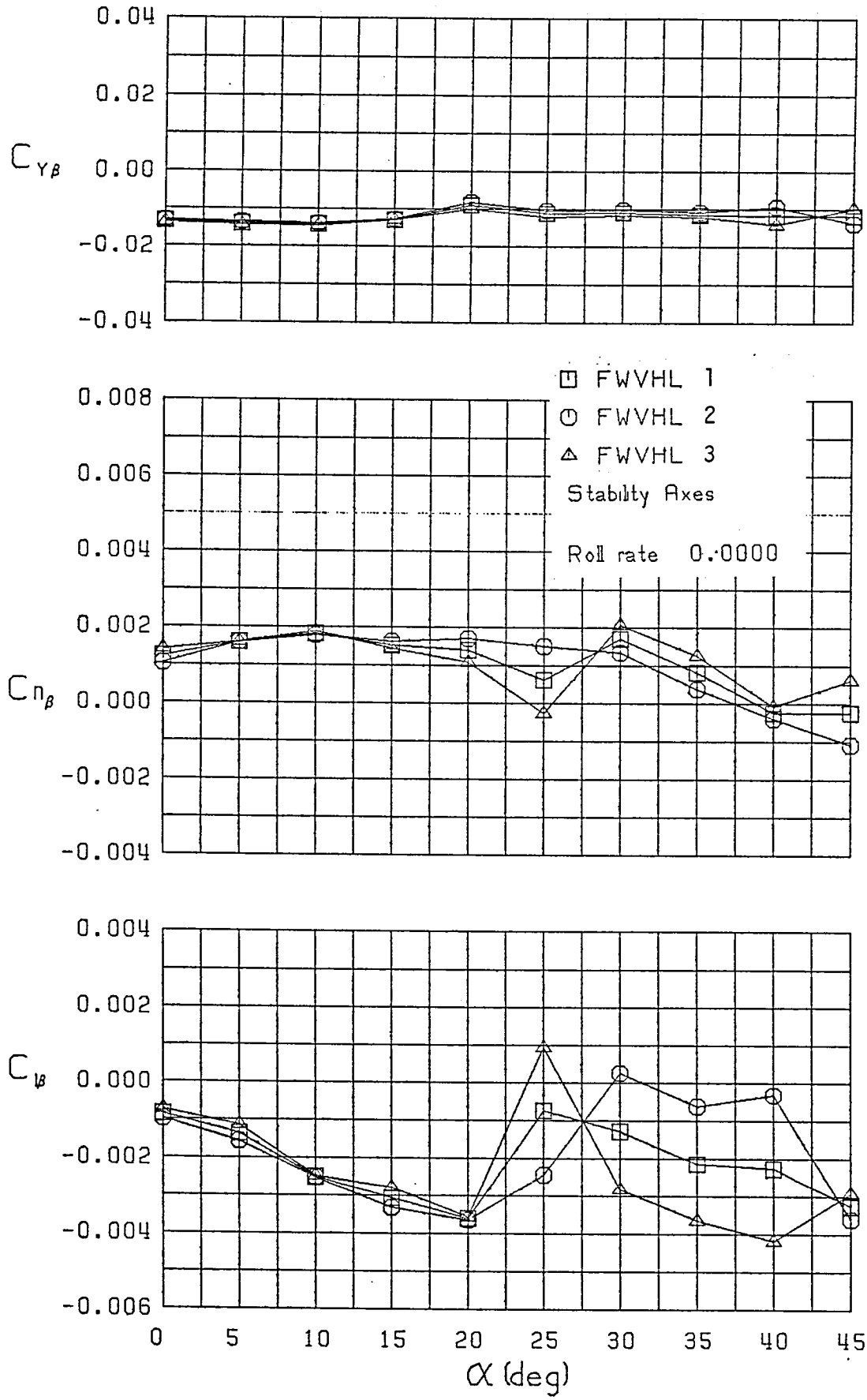

Figure 7 (Continued)

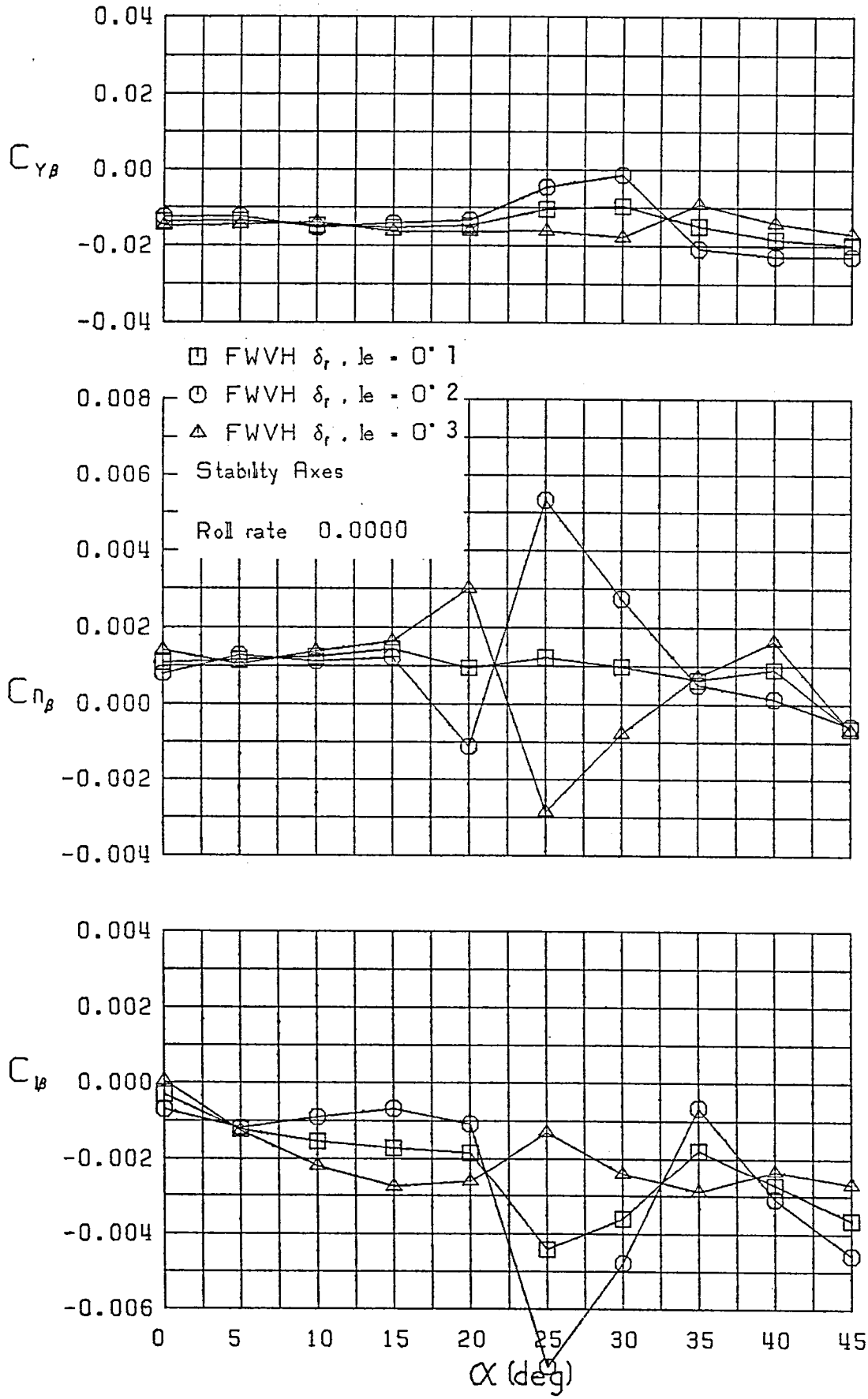

Figure 7 (Continued)

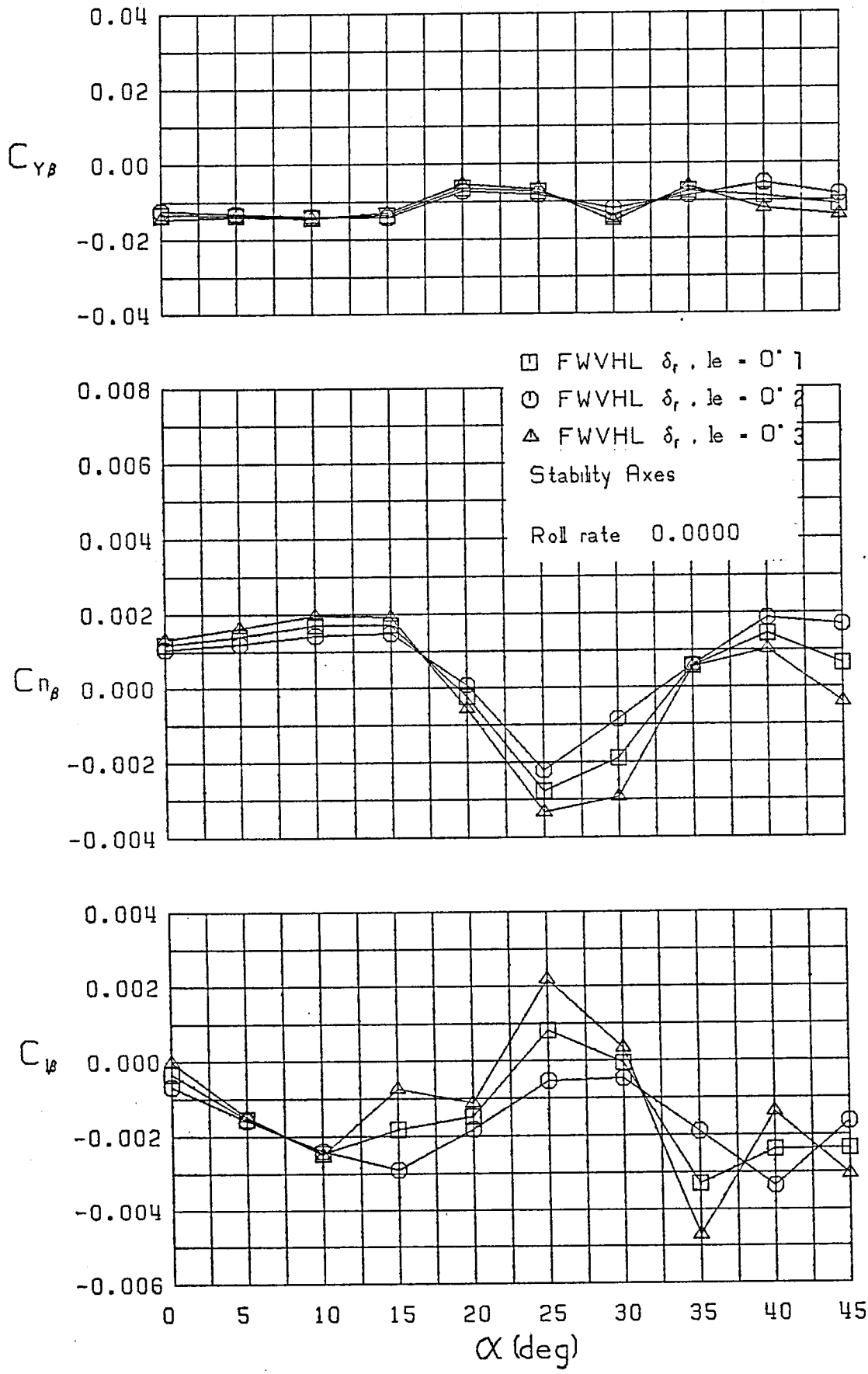

Figure 7 (Continued)

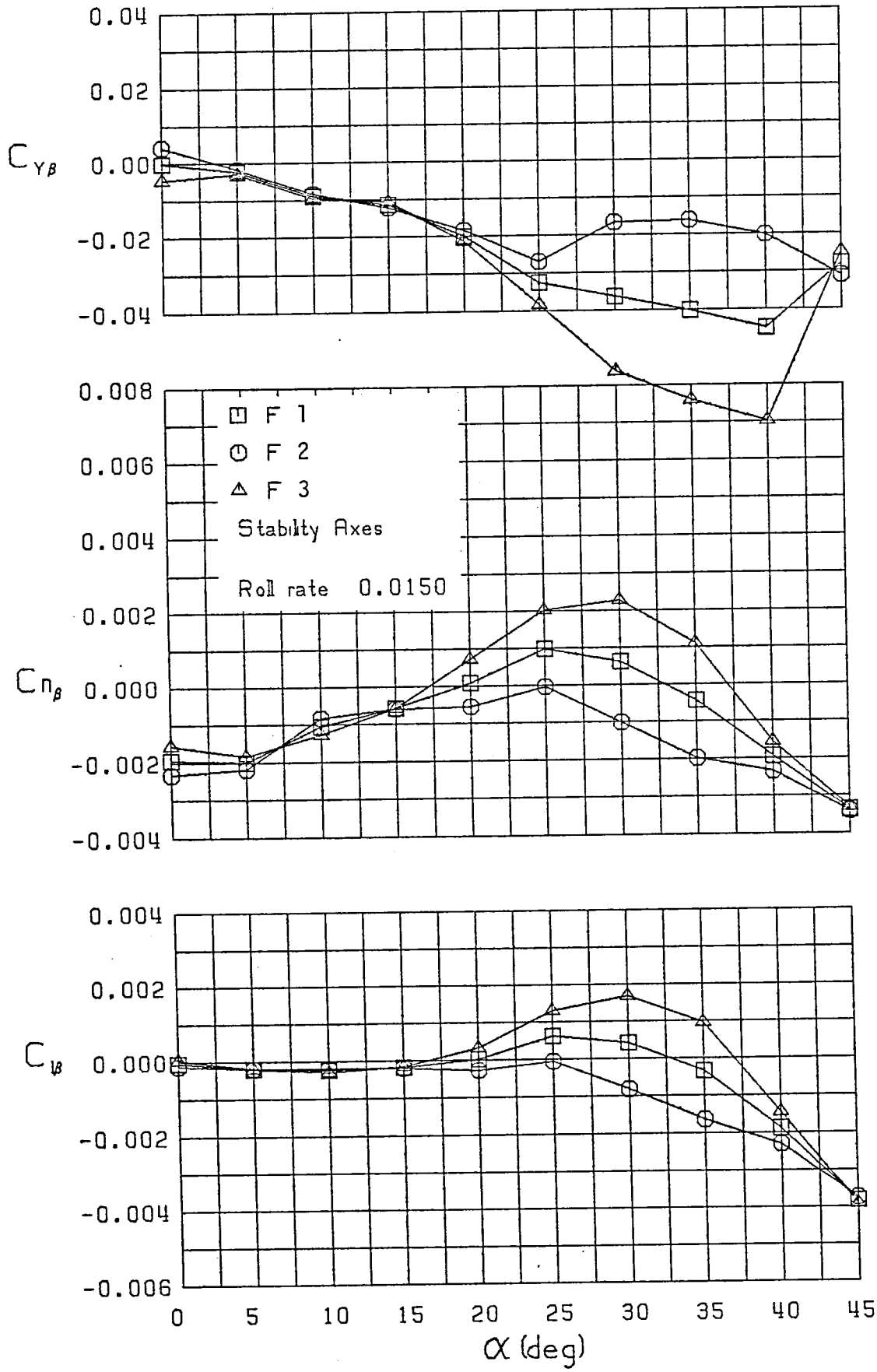

Figure 8 - Variation of Lateral-Directional Static Stability Derivatives with Angle of Attack and Sideslip, $\hat{p} = 0.0150$

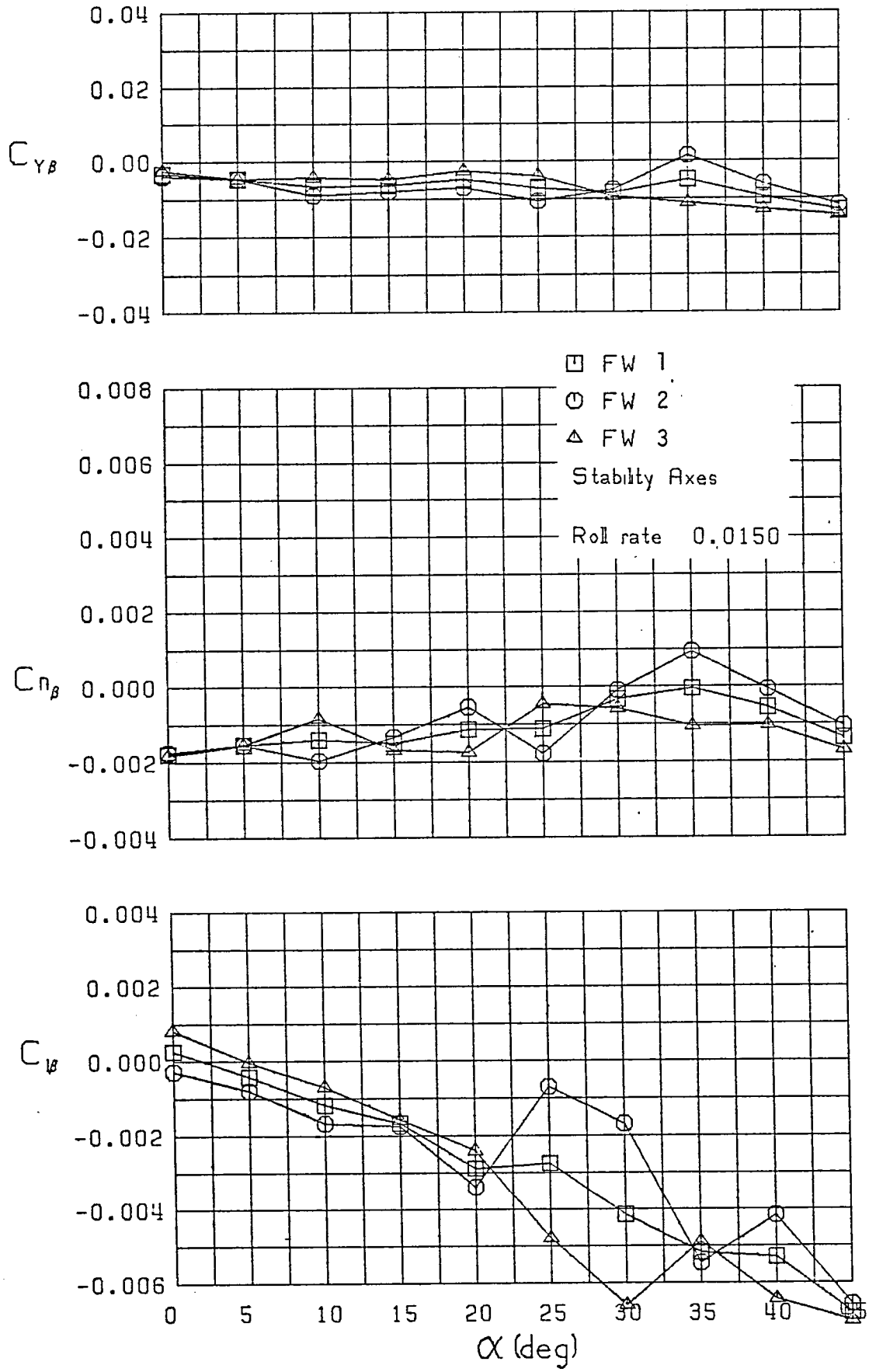

Figure 8 (Continued)

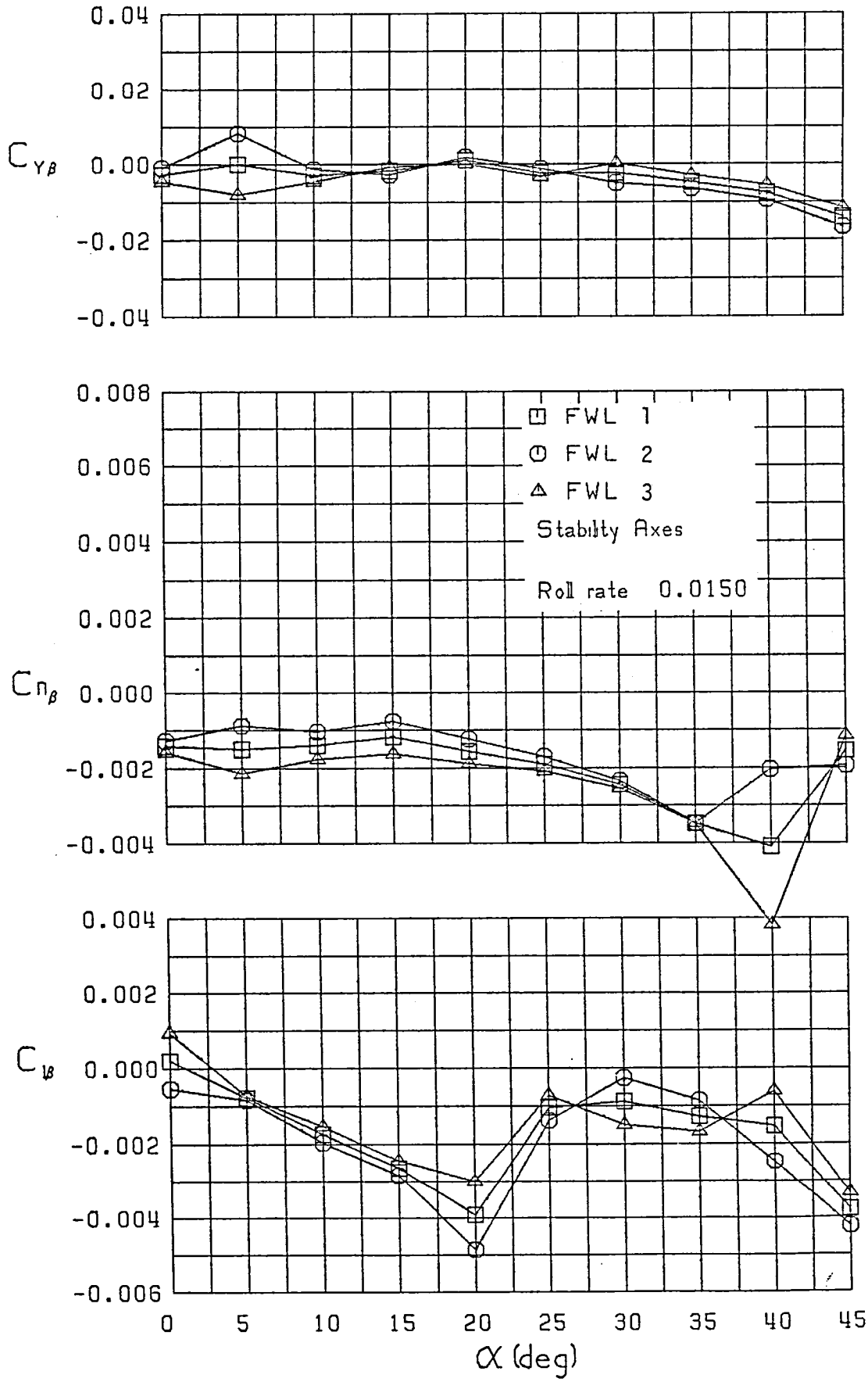

Figure 8 (Continued)

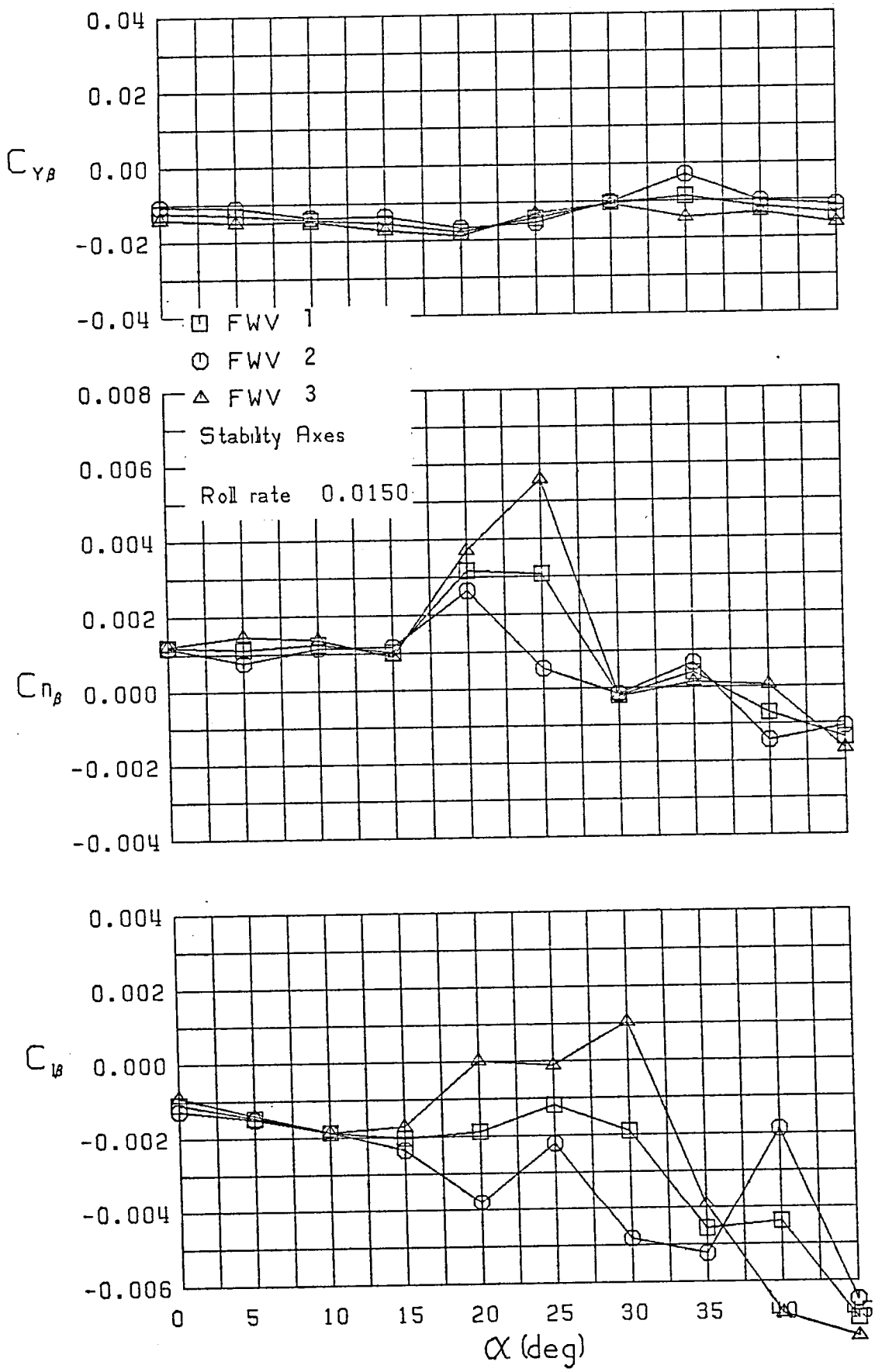

Figure 8 (Continued)

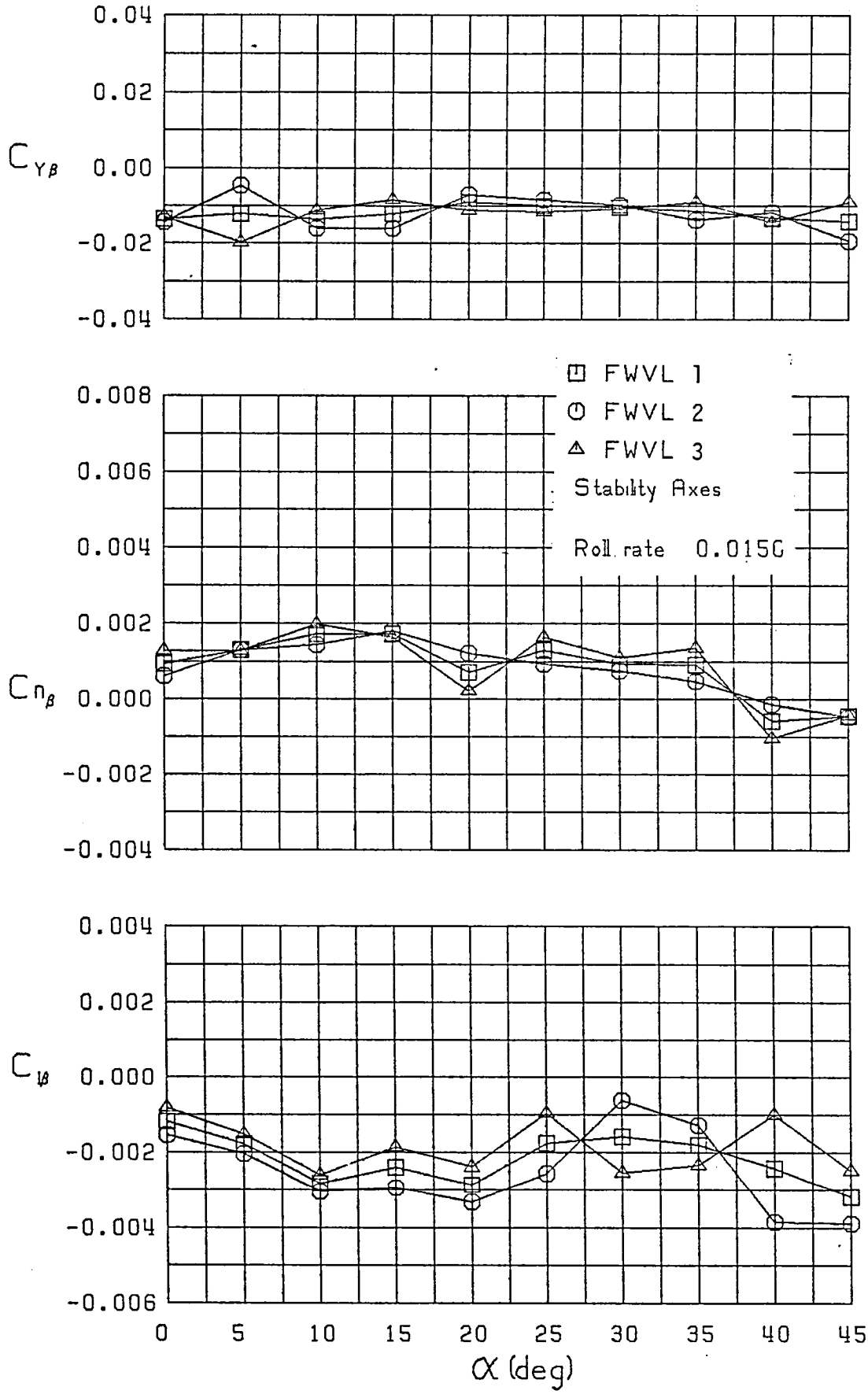

Figure 8 (Continued)

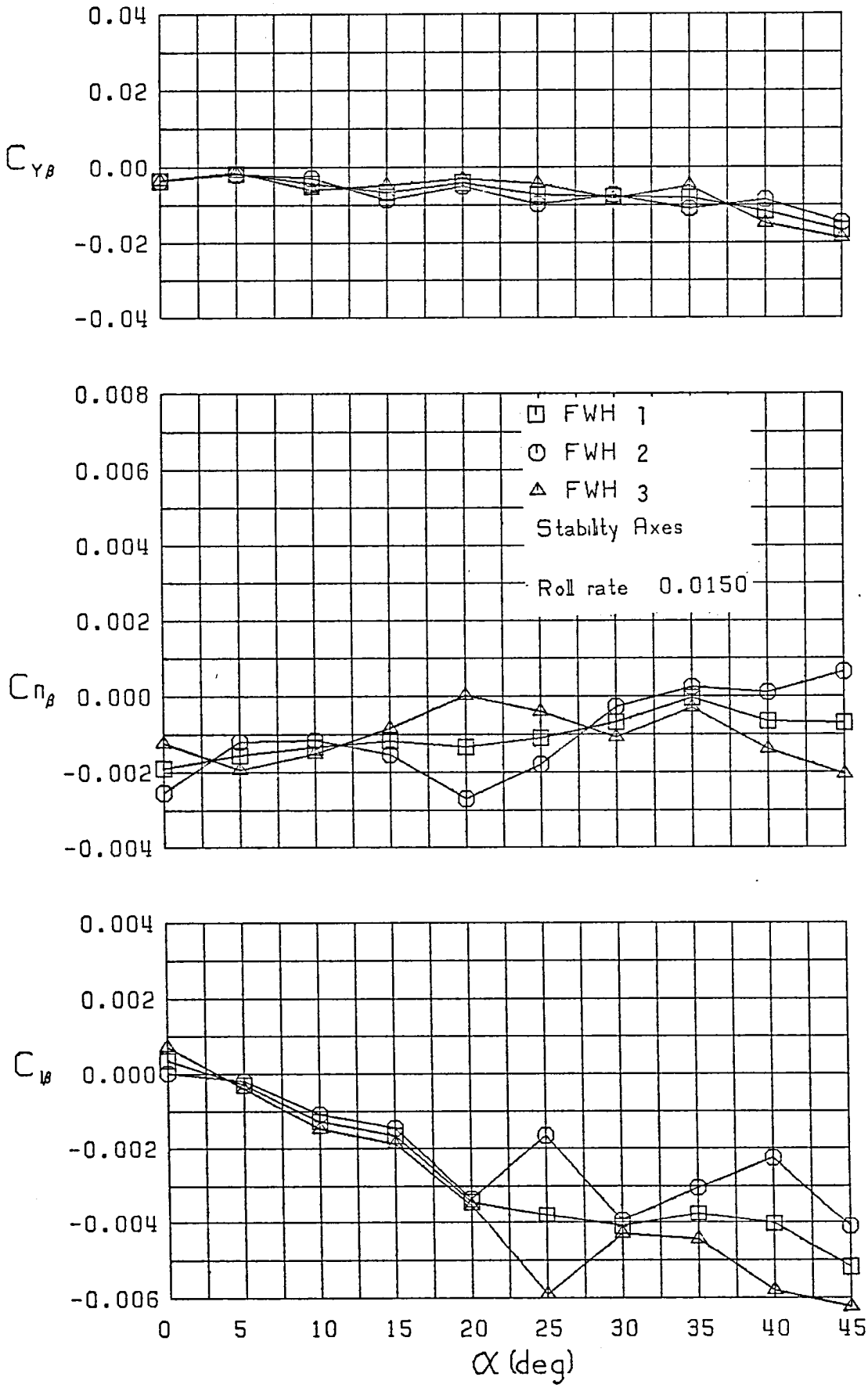

Figure 8 (Continued)

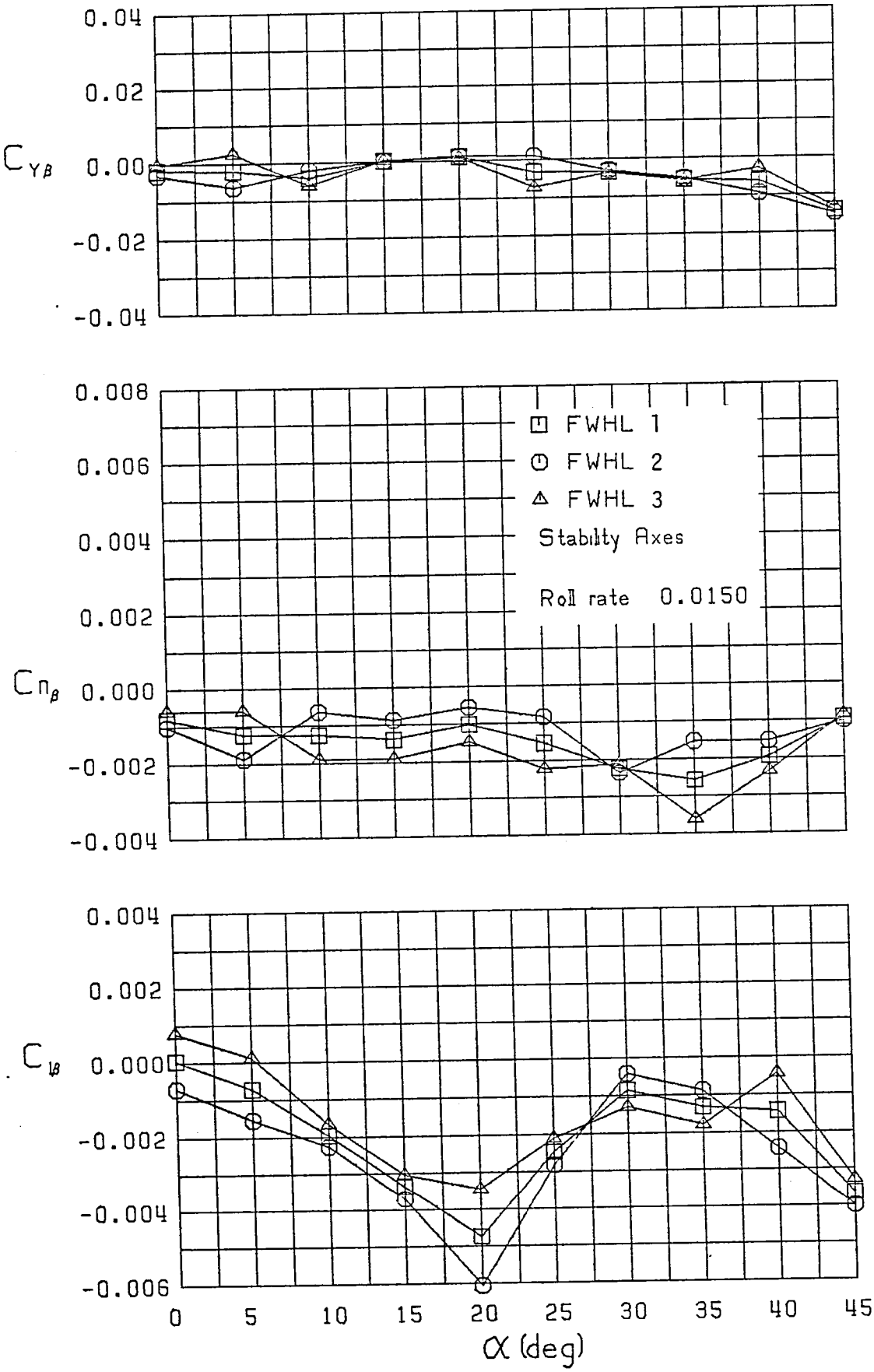

Figure 8 (Continued)

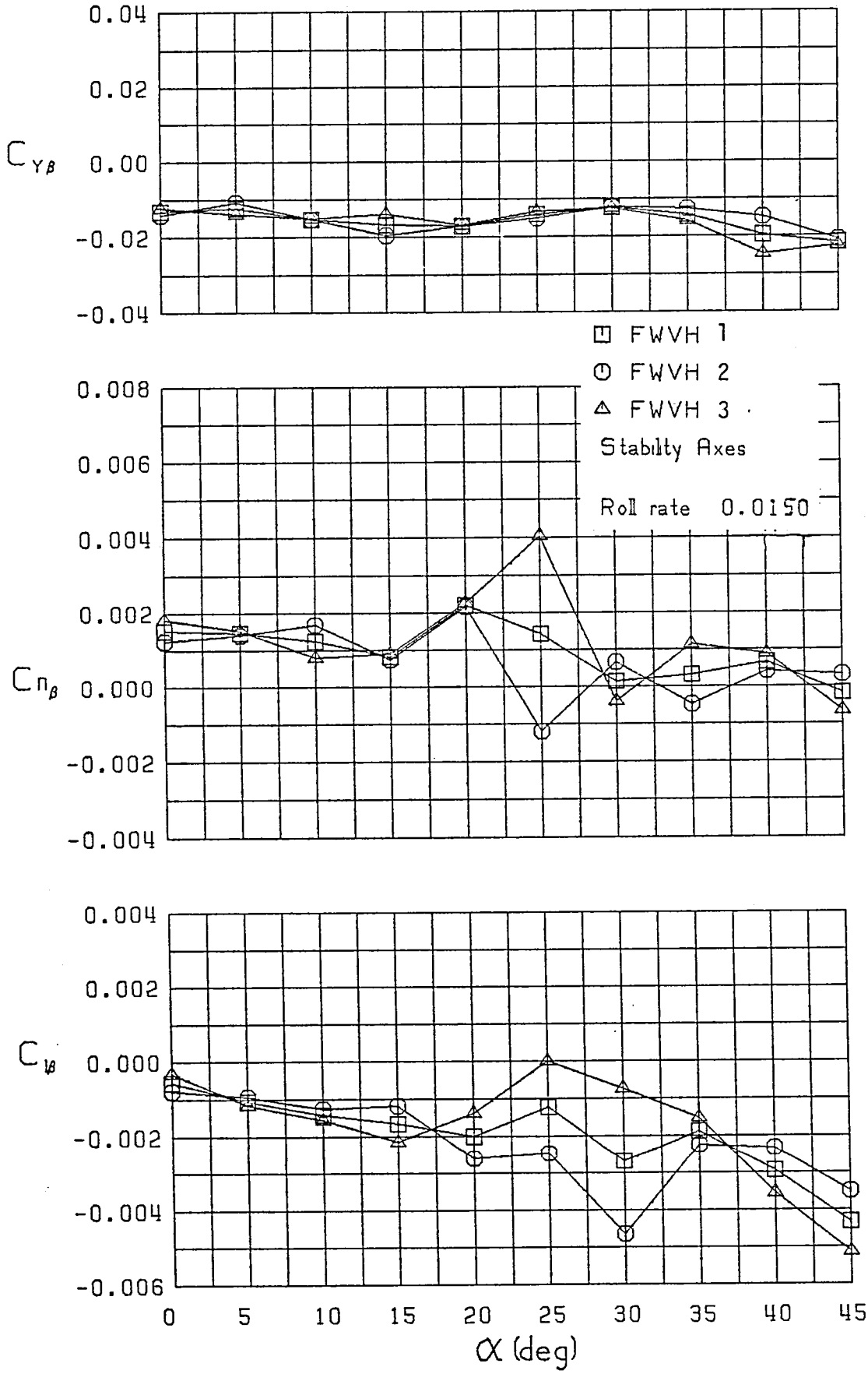

Figure 8 (Continued)

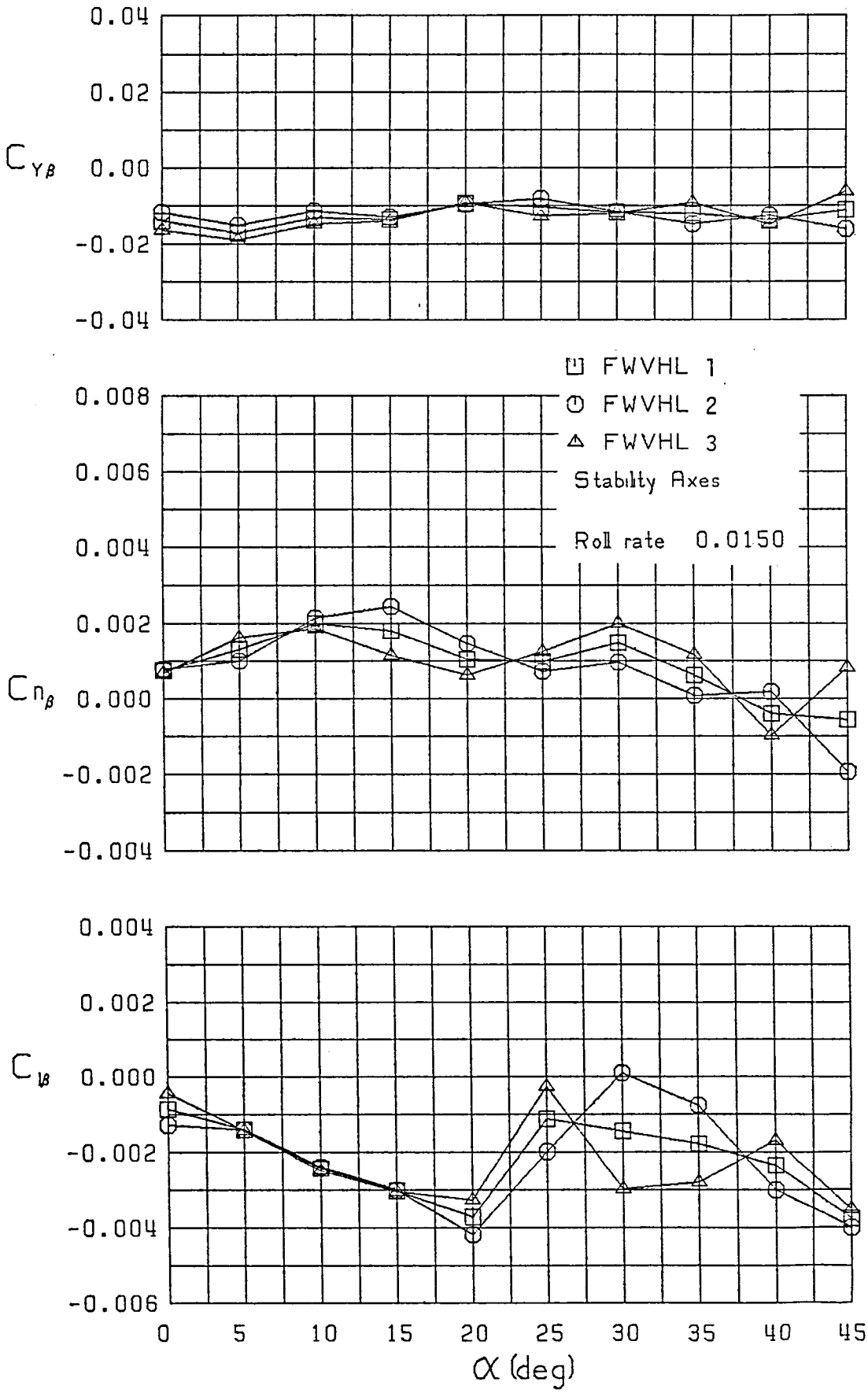

Figure 8 (Continued)

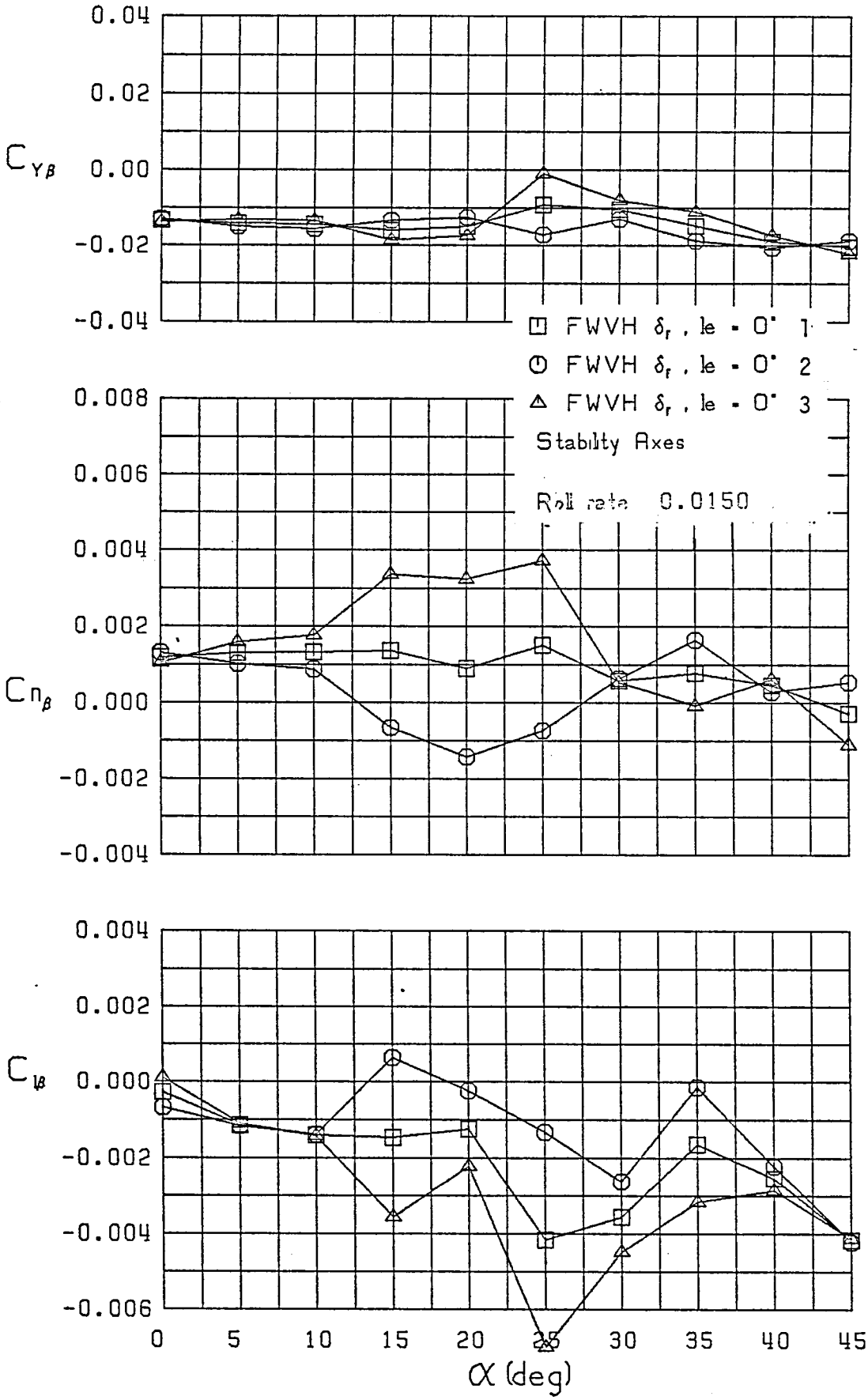

Figure 8 (Continued)

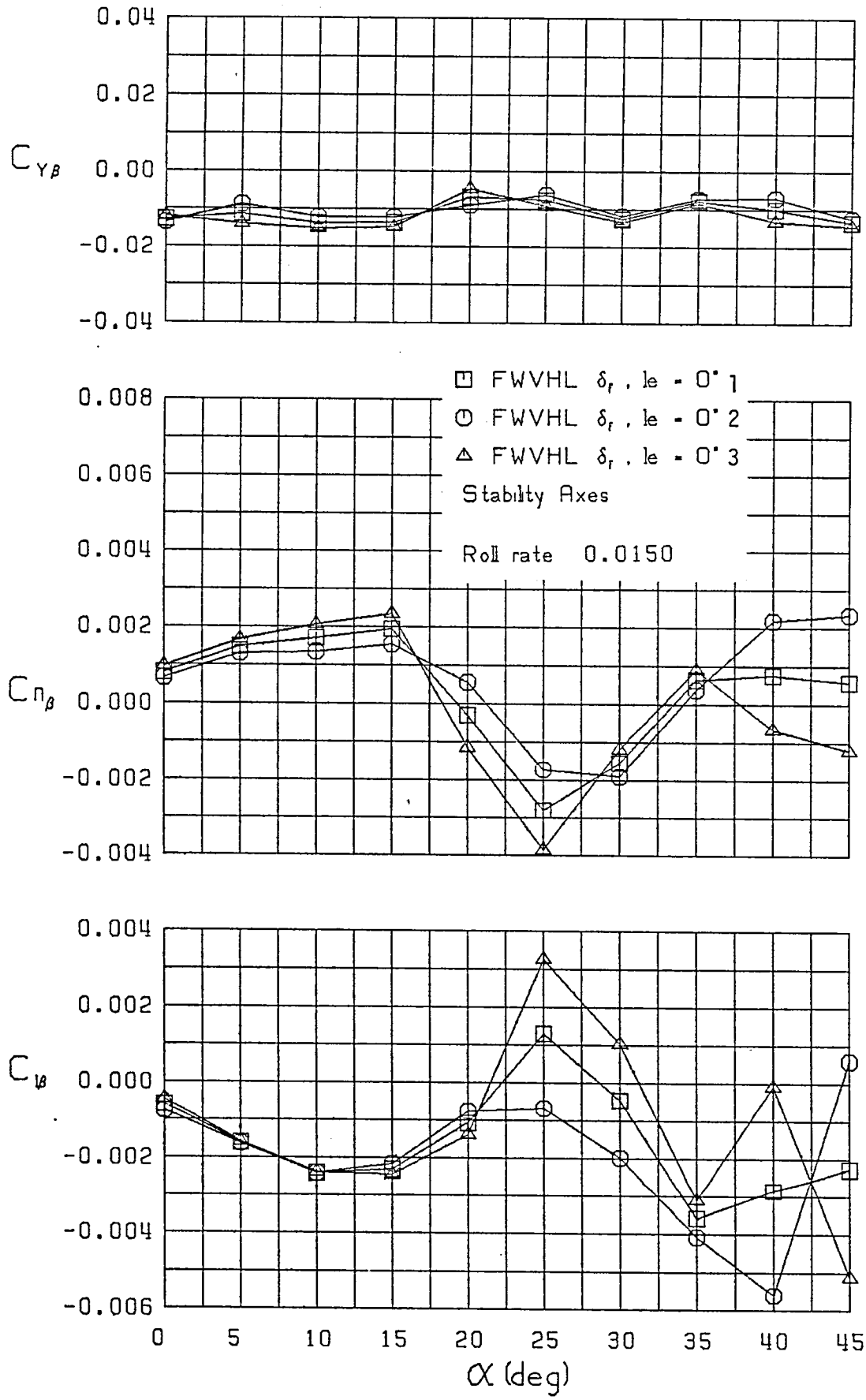

Figure 8 (Continued)

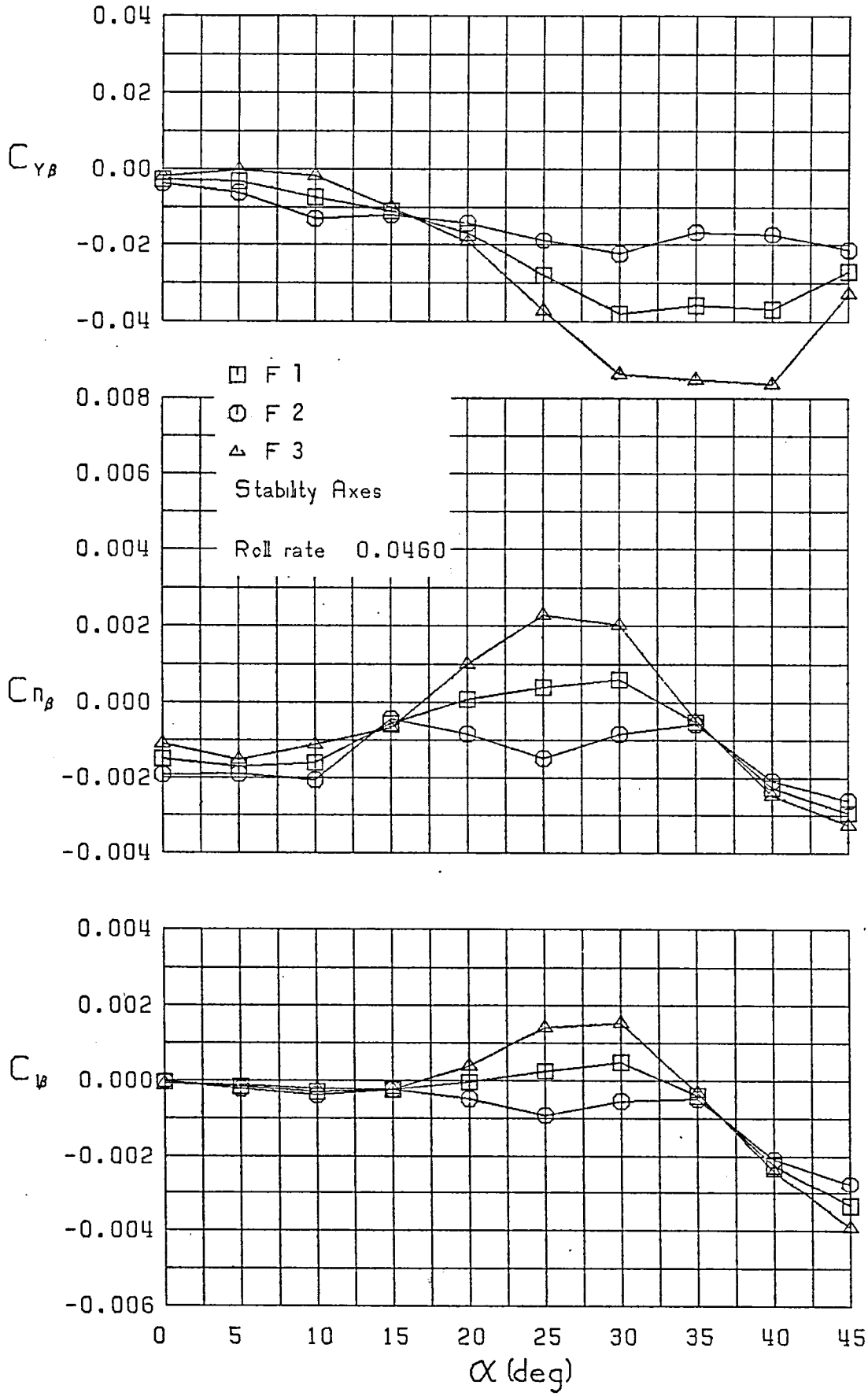

Figure 9 - Variation of Lateral-Directional Static Stability Derivatives with Angle of Attack and Sideslip, $\hat{p}$ = 0.0460

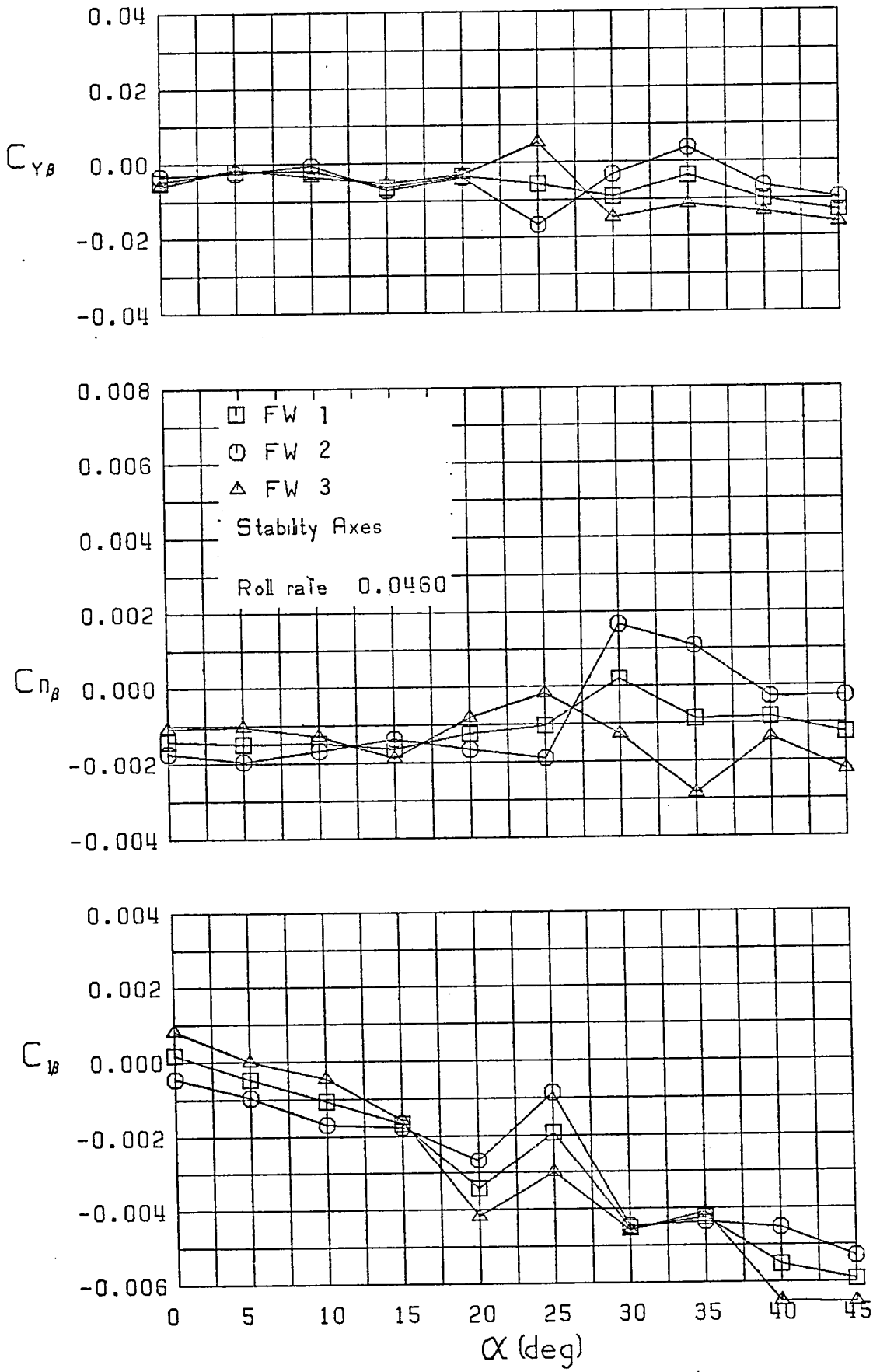

Figure 9 (Continued)

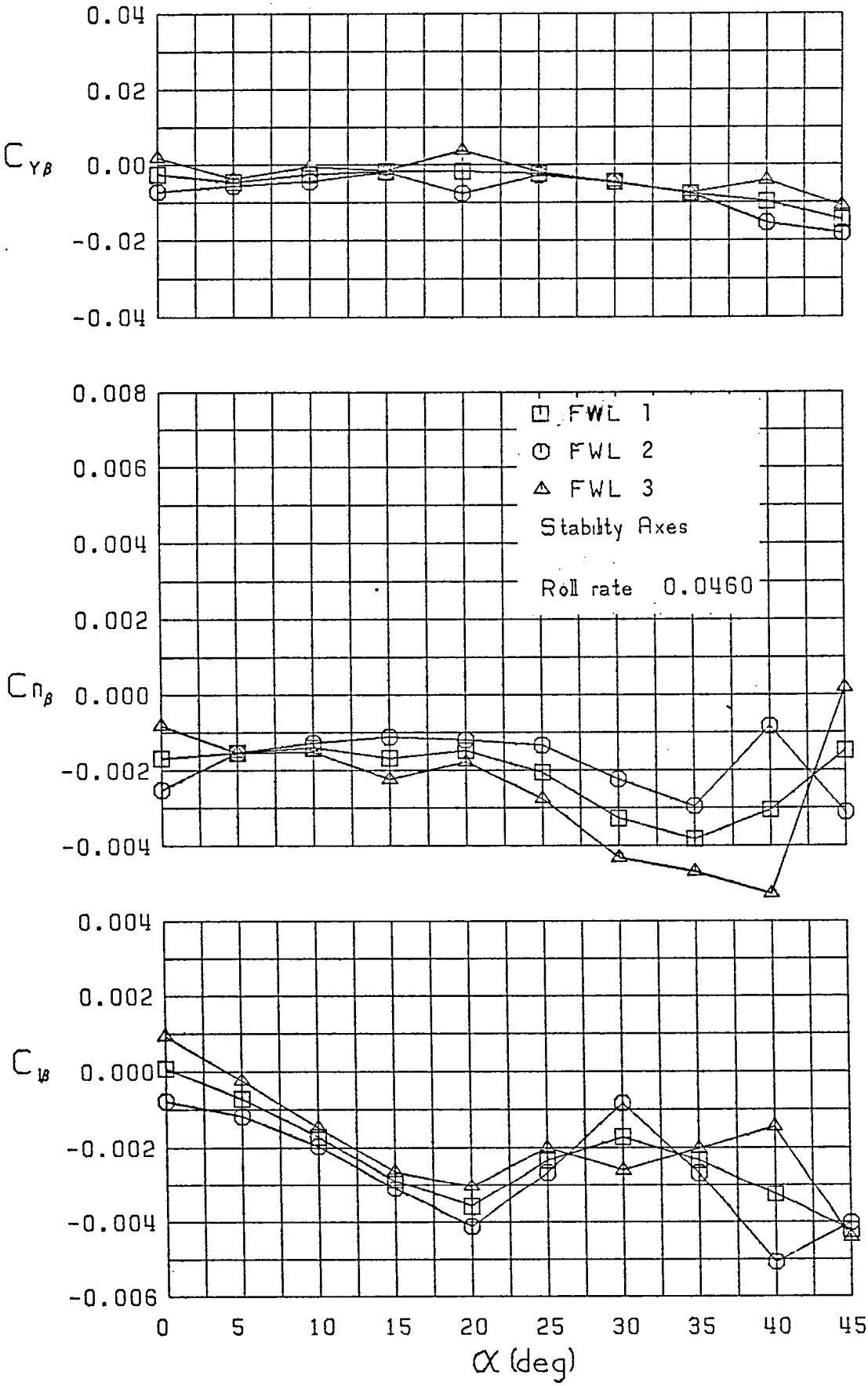

Figure 9 (Continued)

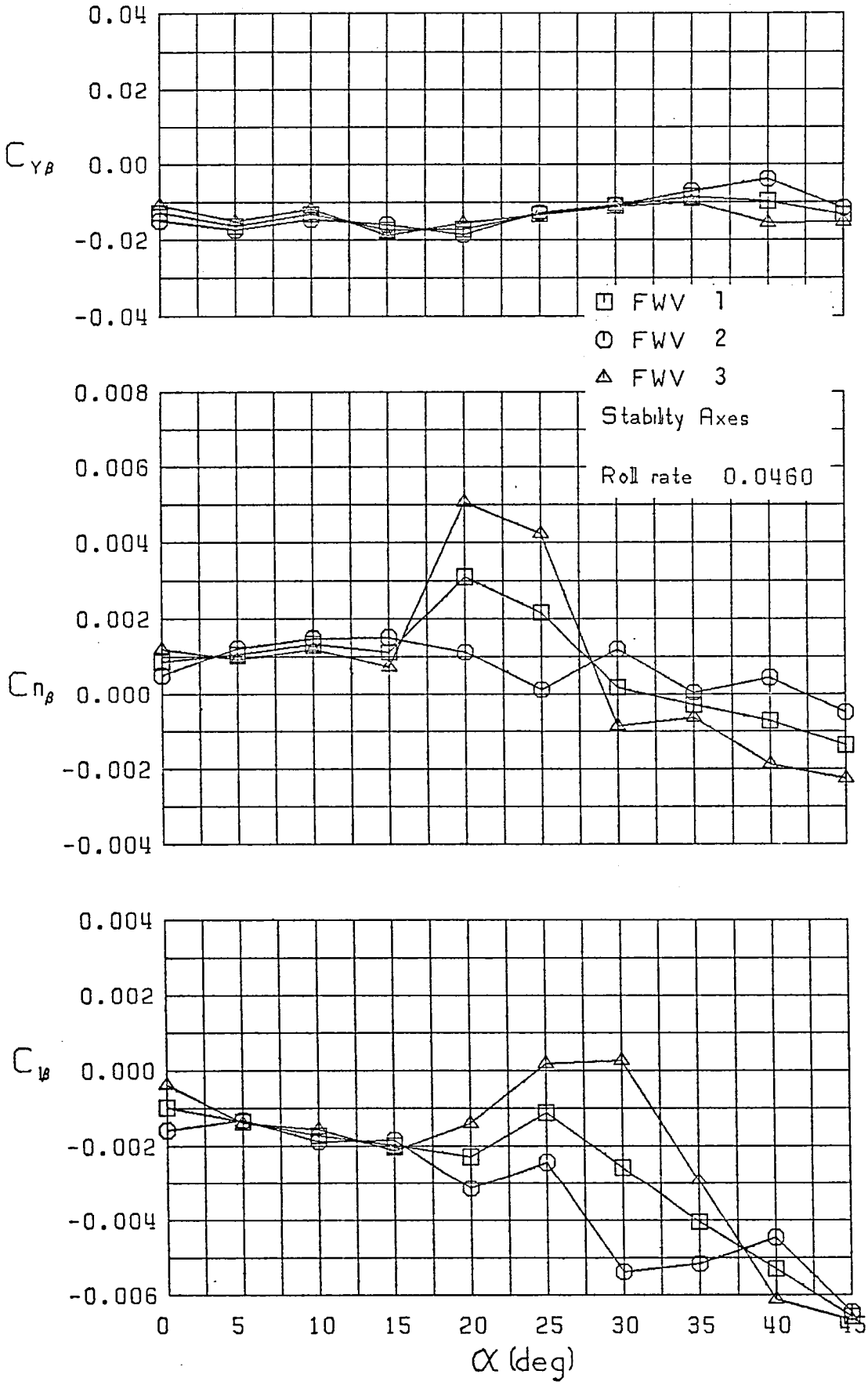

Figure 9 (Continued)

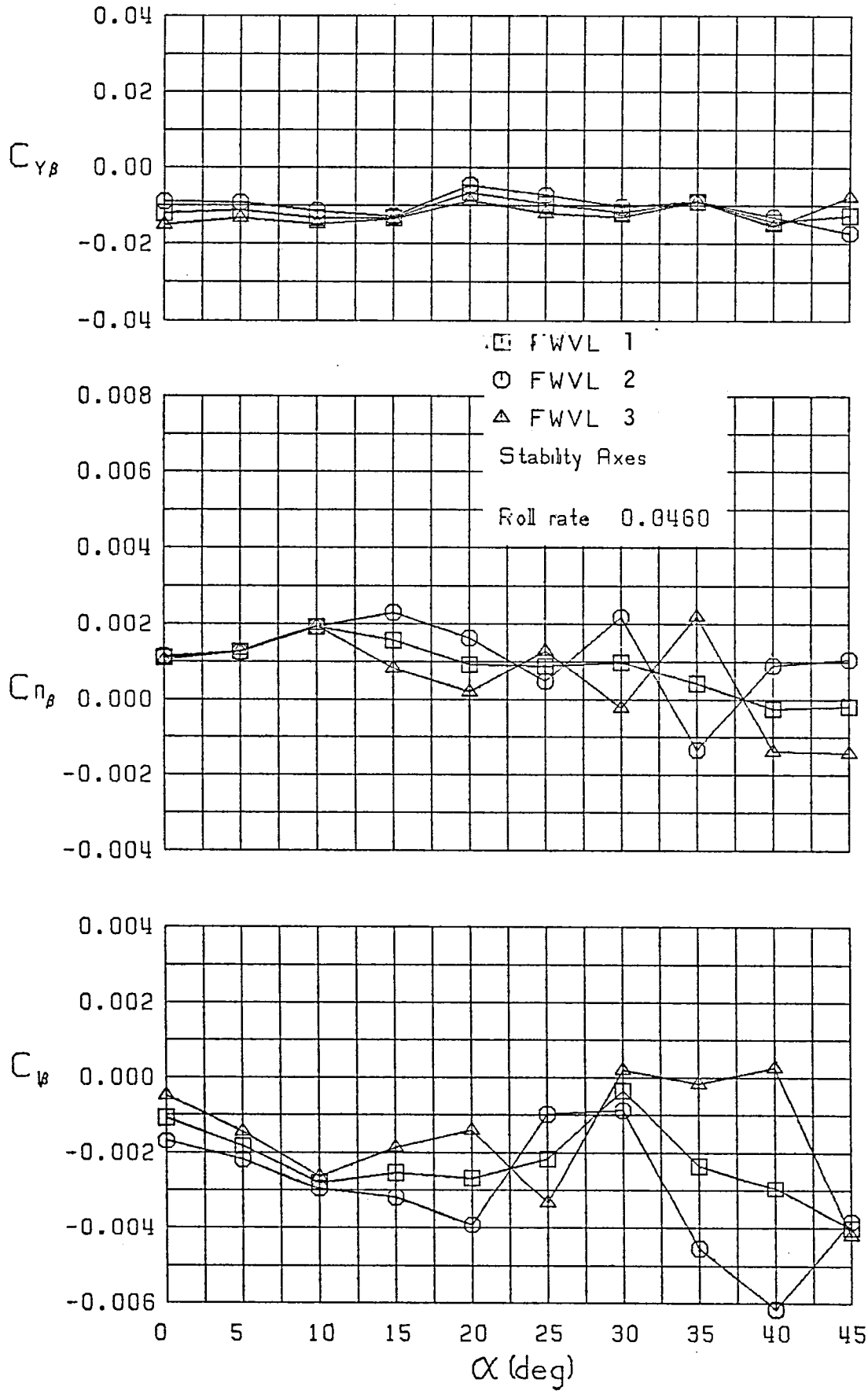

Figure 9 (Continued)

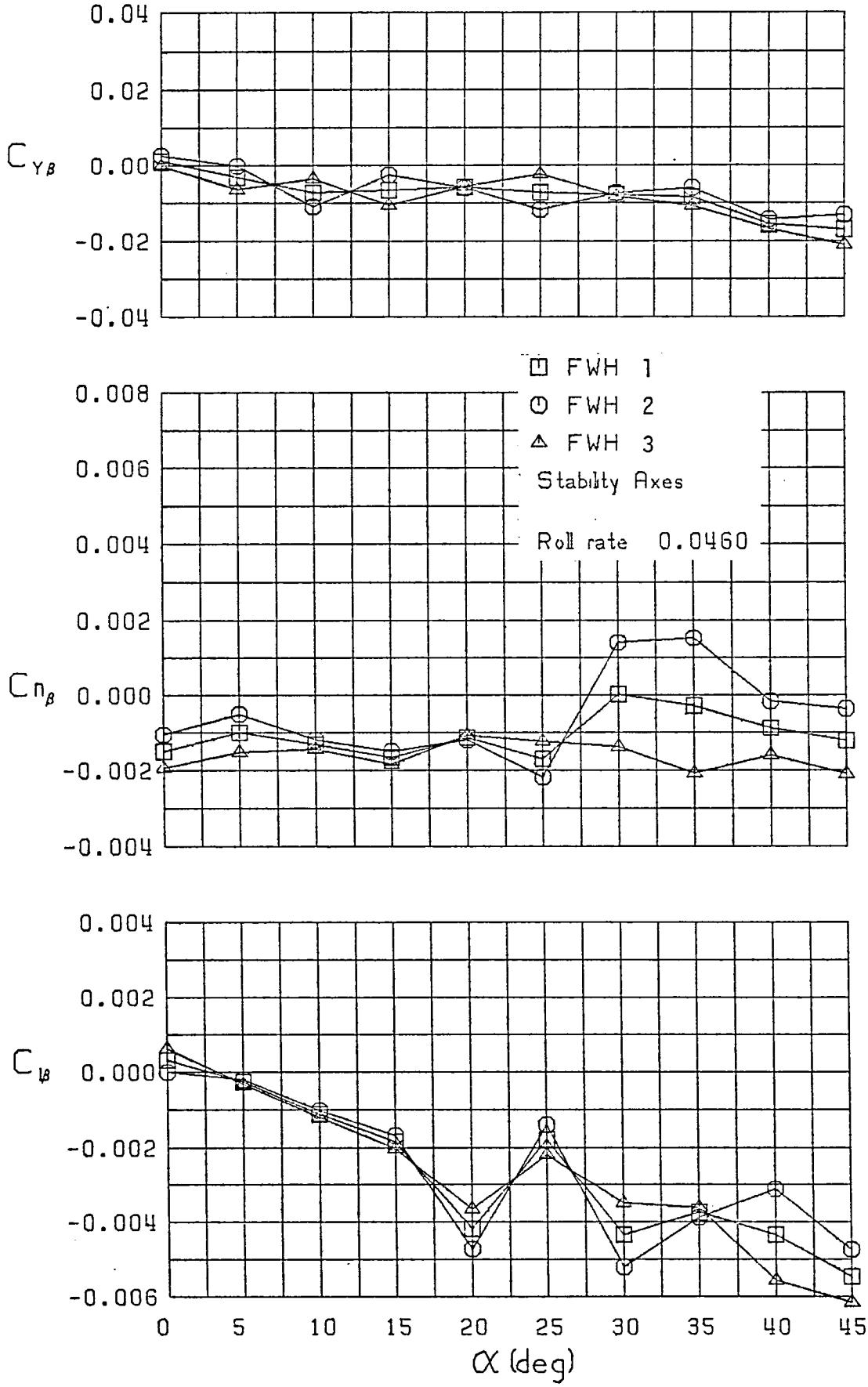

Figure 9 (Continued)

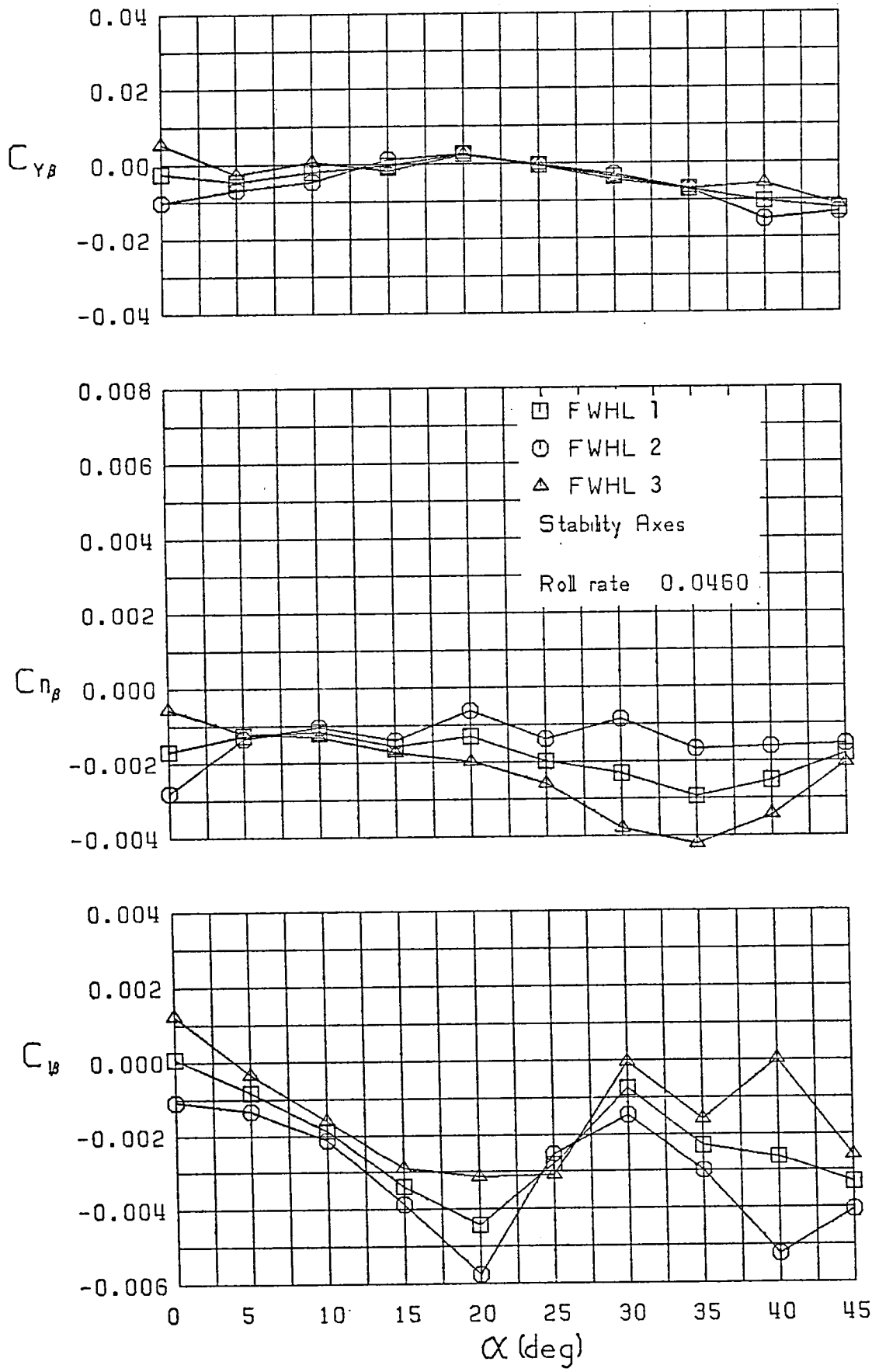

Figure 9 (Continued)

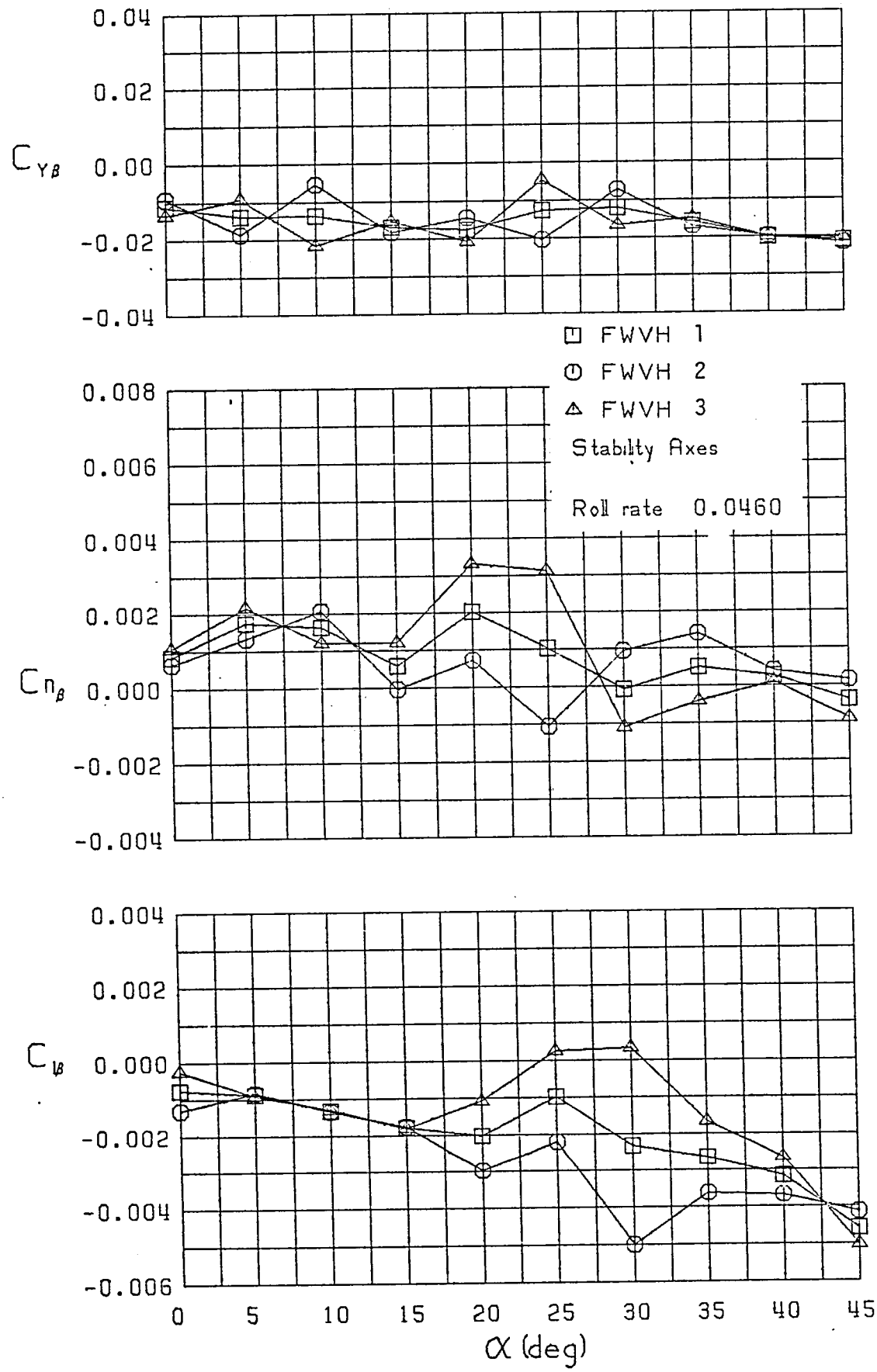

Figure 9 (Continued)

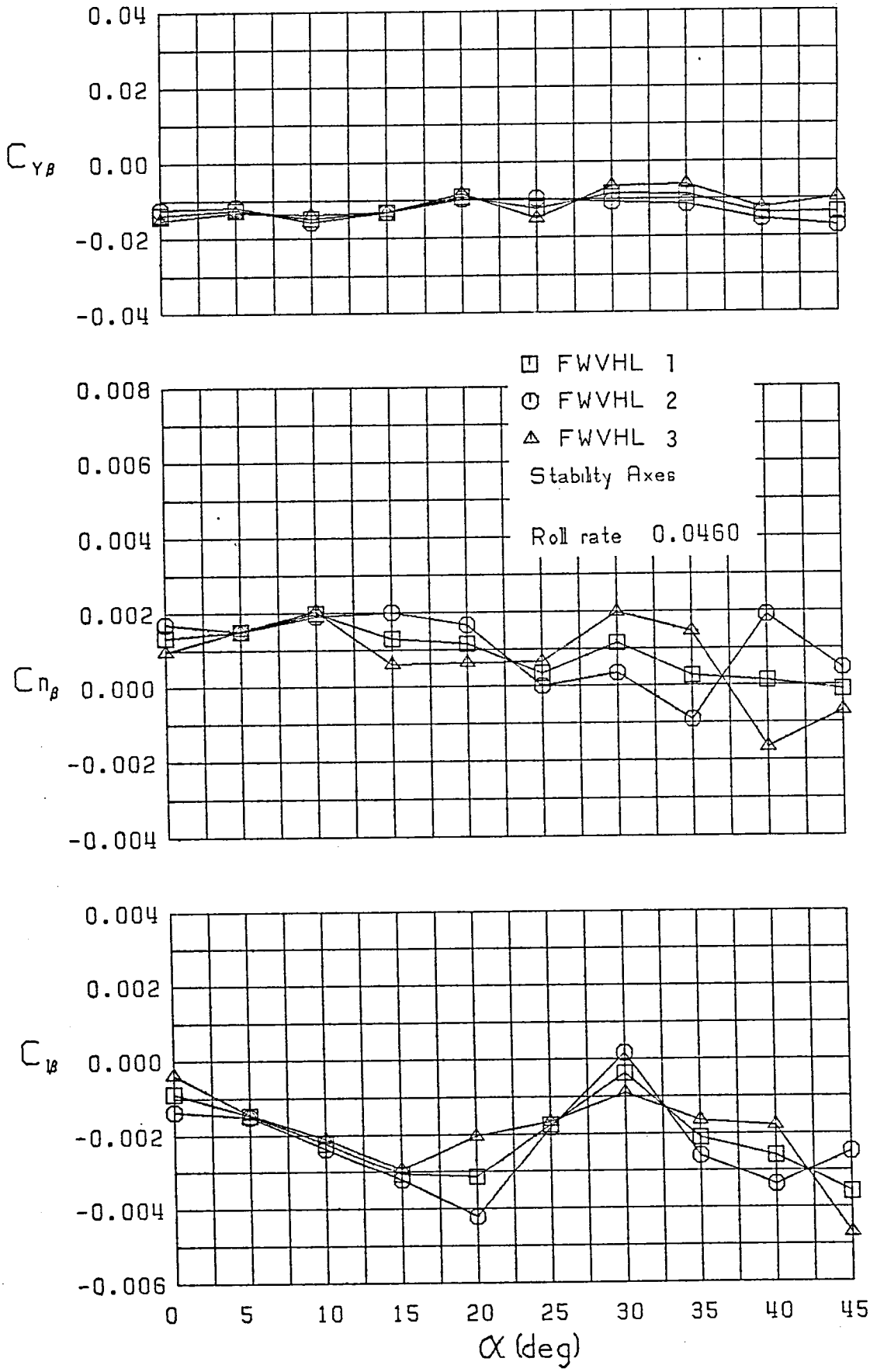

Figure 9 (Continued)

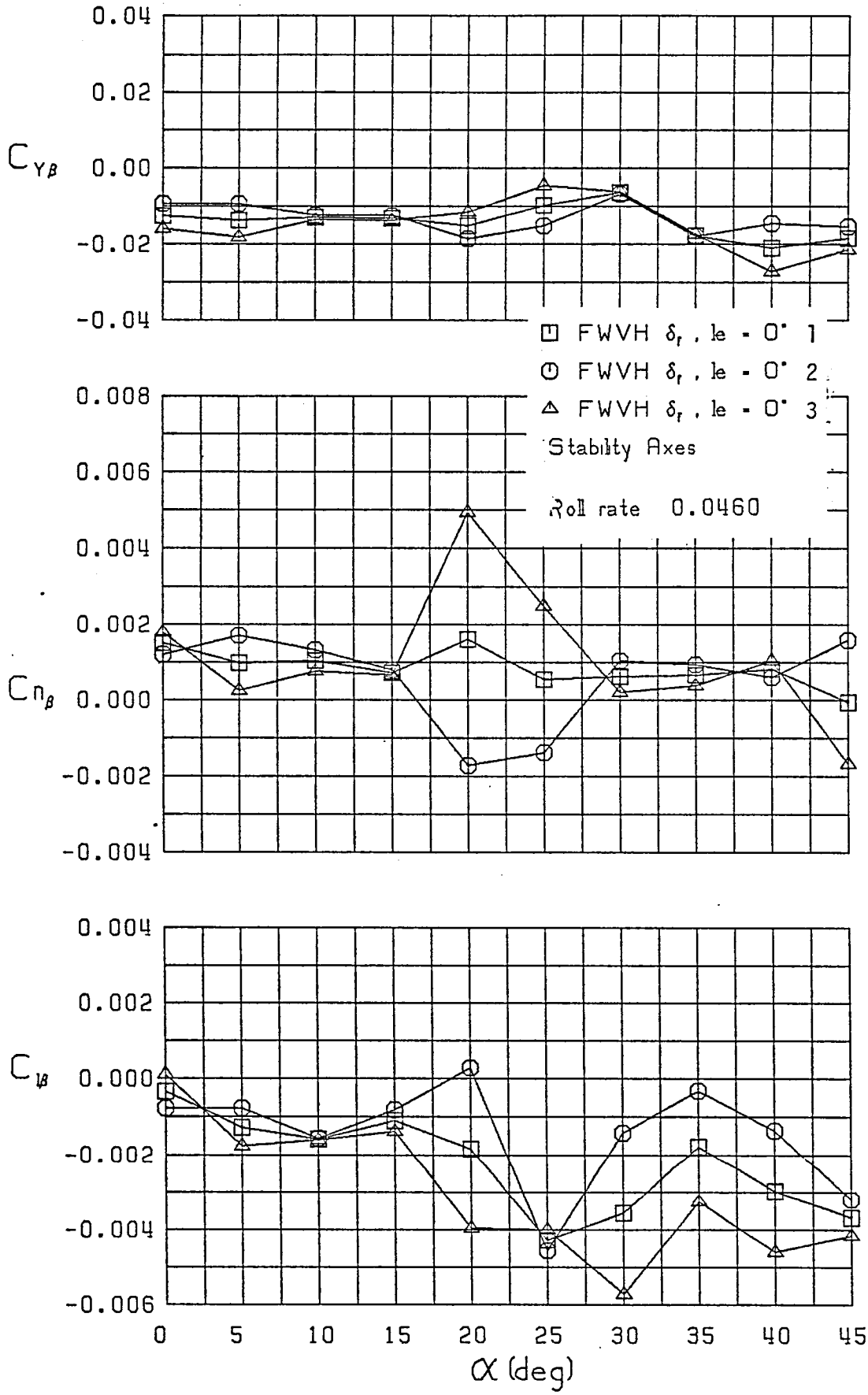

Figure 9 (Continued)

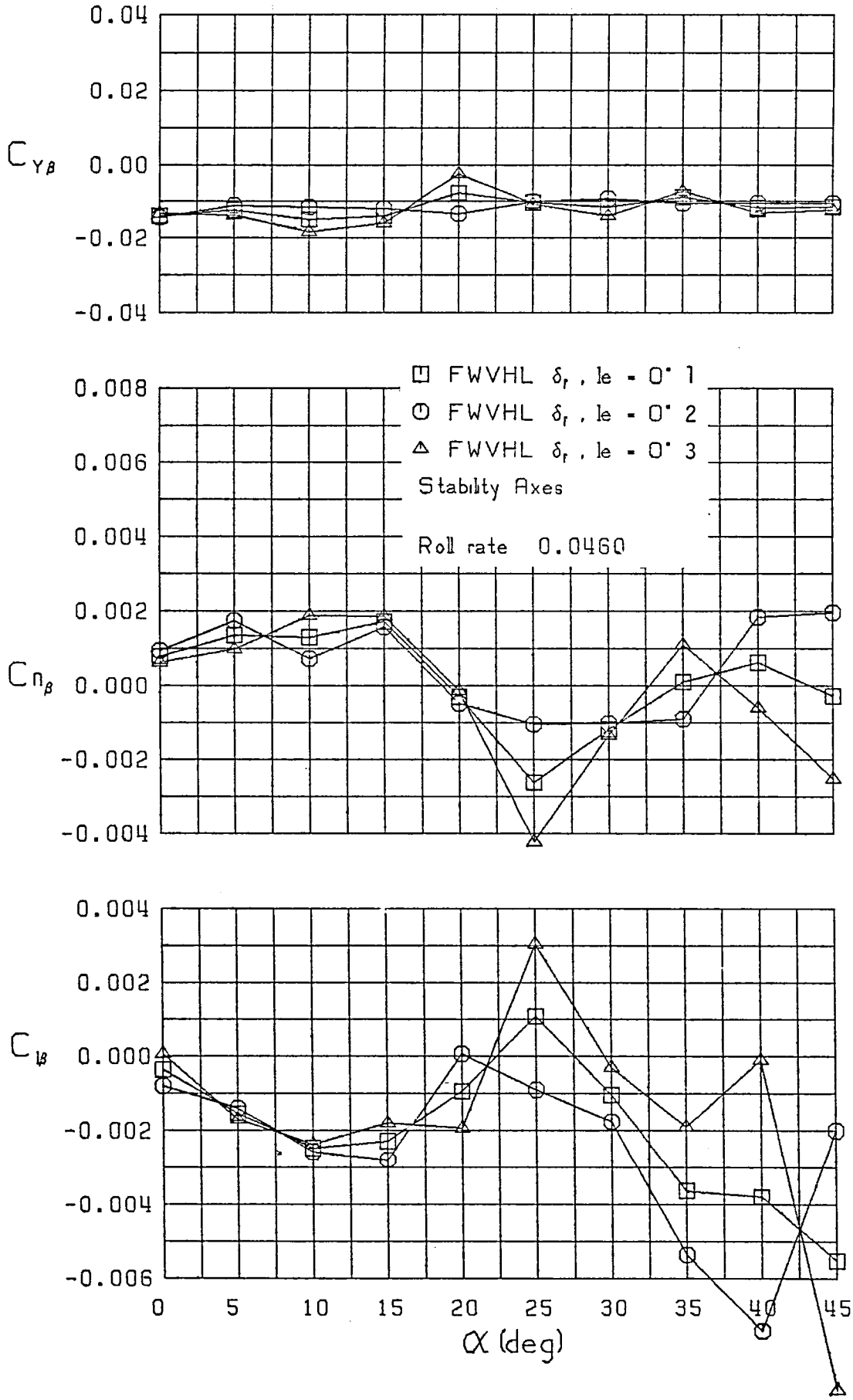

Figure 9 (Continued)

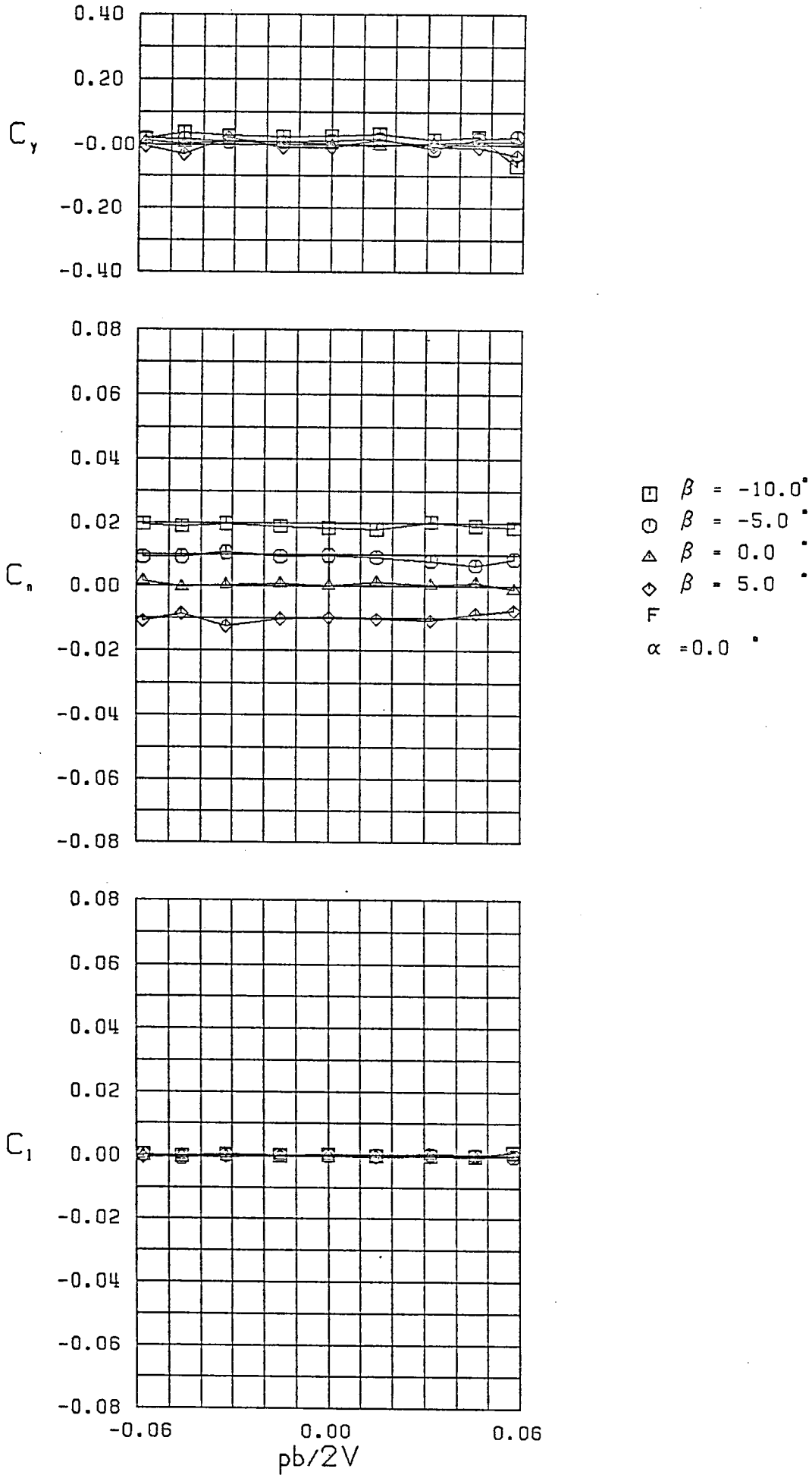

Figure 10 - Variation of Lateral-Directional Characteristics with Roll Rate-Configuration 15

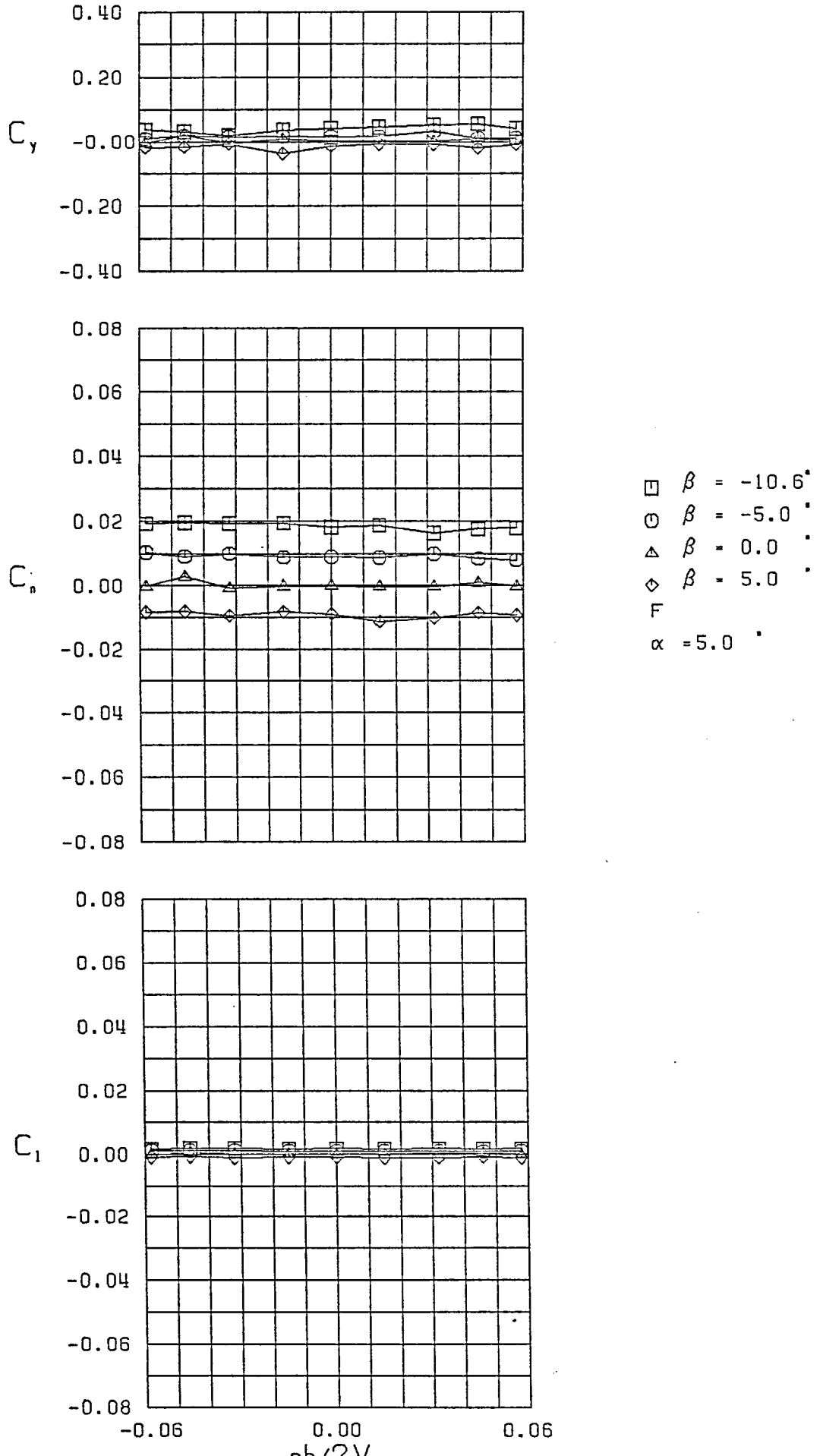

Figure 10 (Continued)

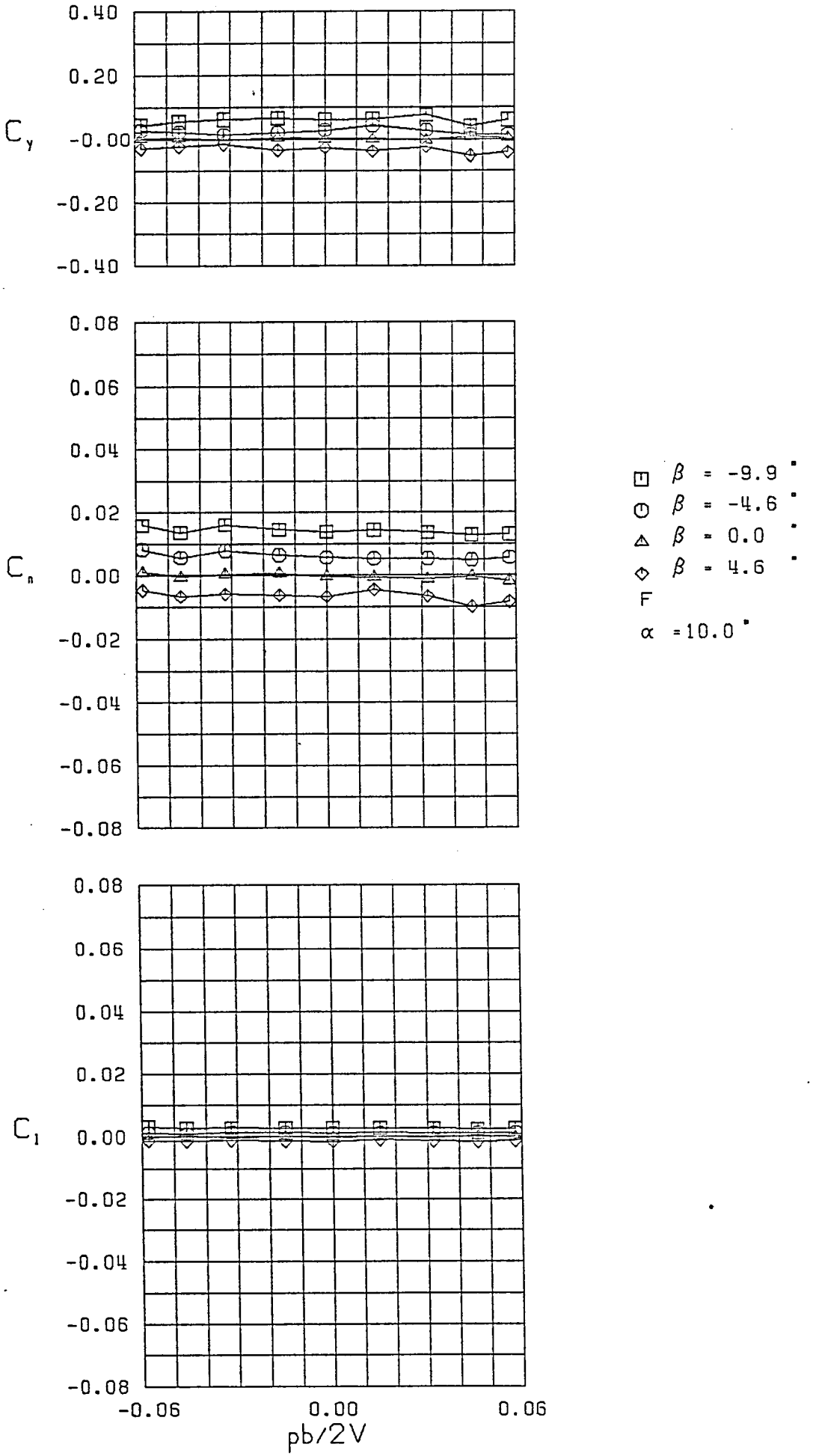

Figure 10 (Continued)

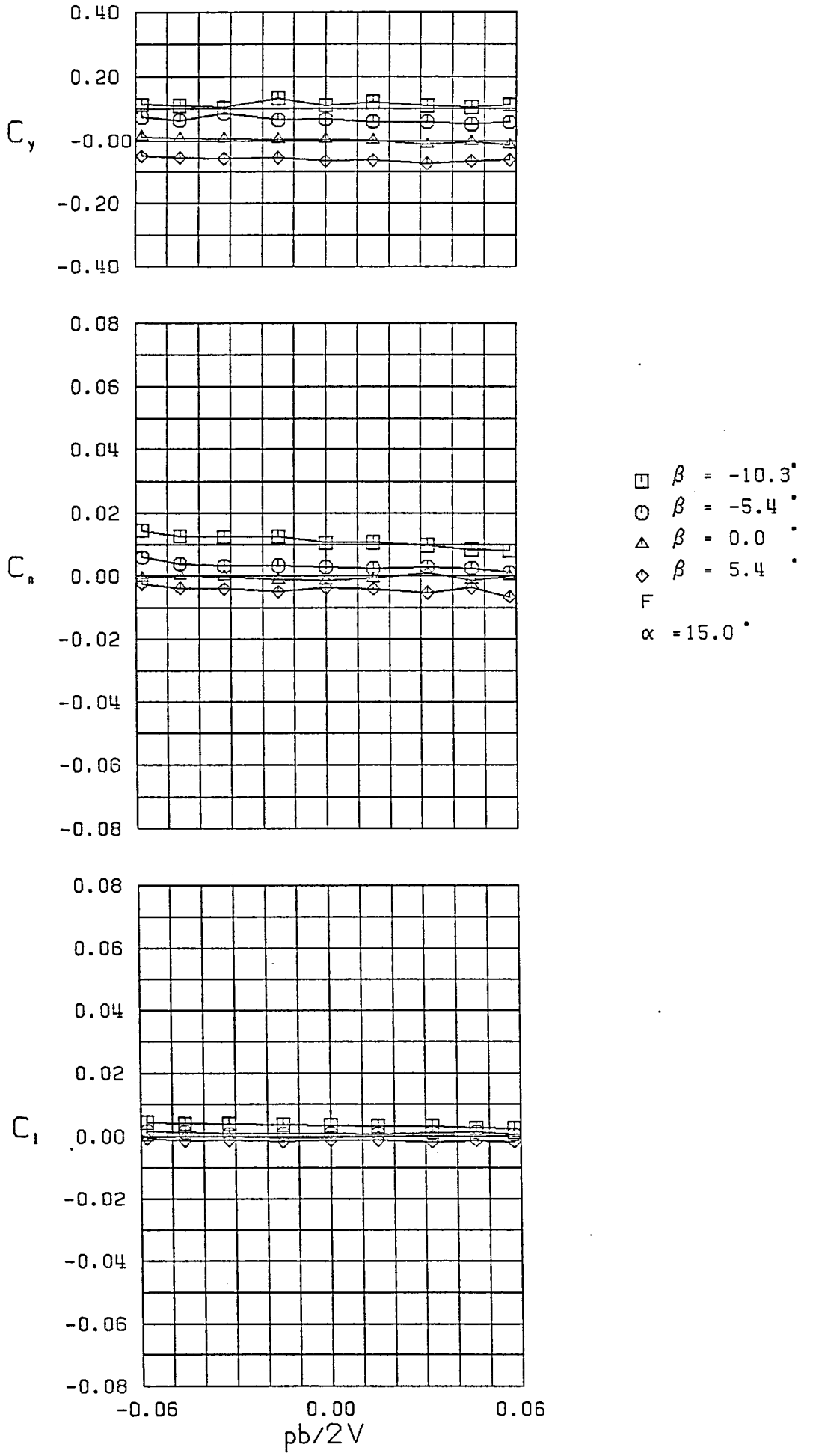

Figure 10 (Continued)

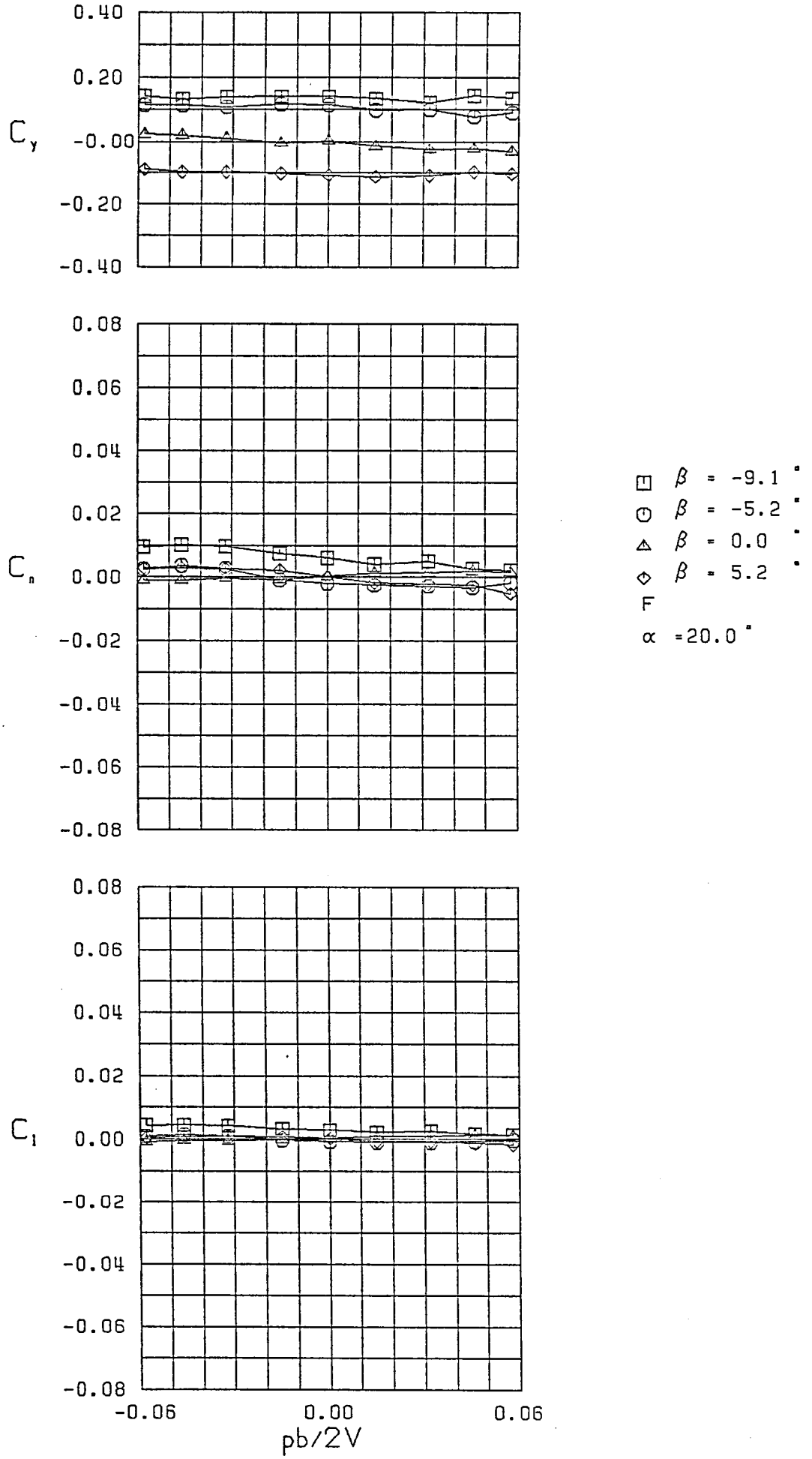

Figure 10 (Continued)

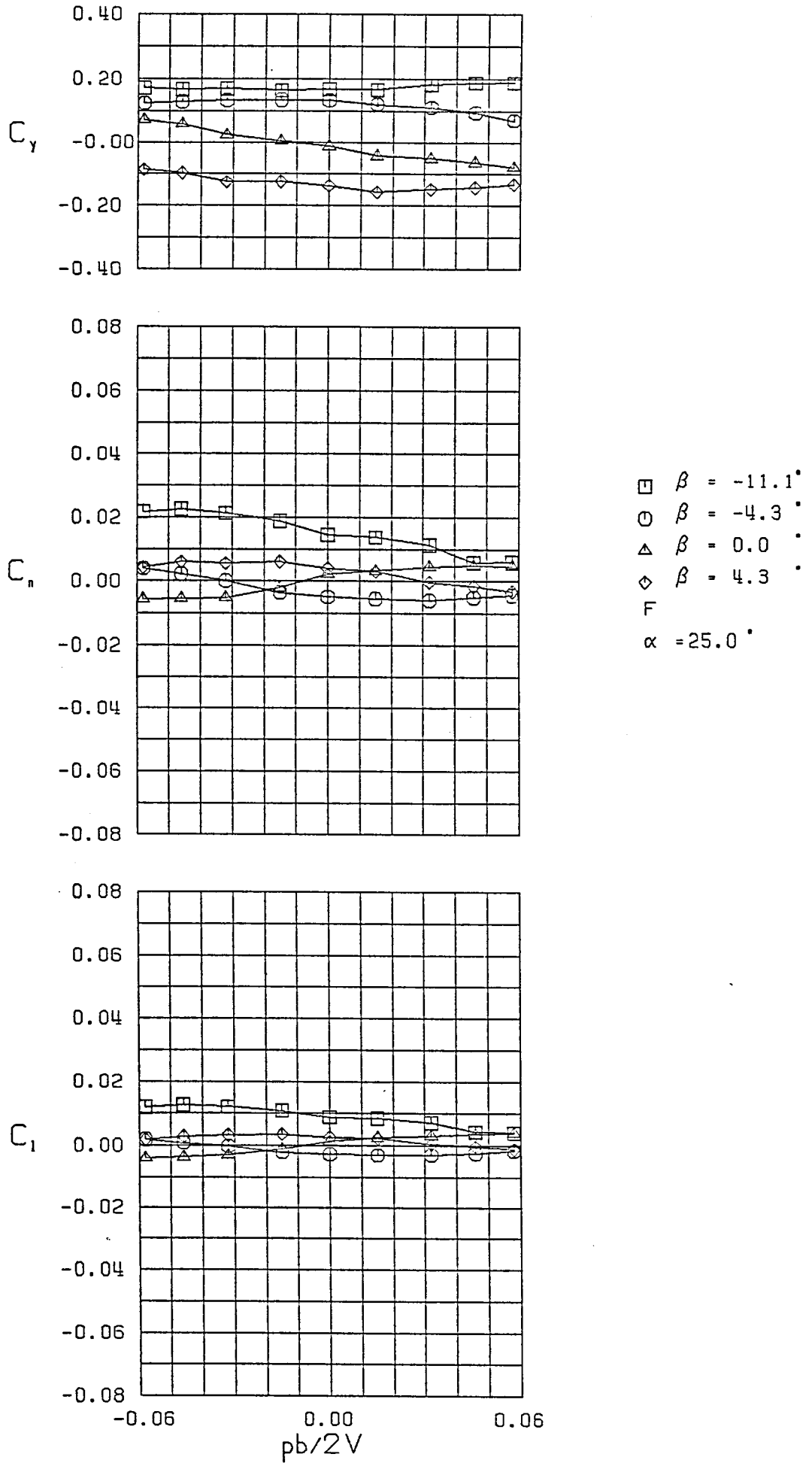

Figure 10 (Continued)

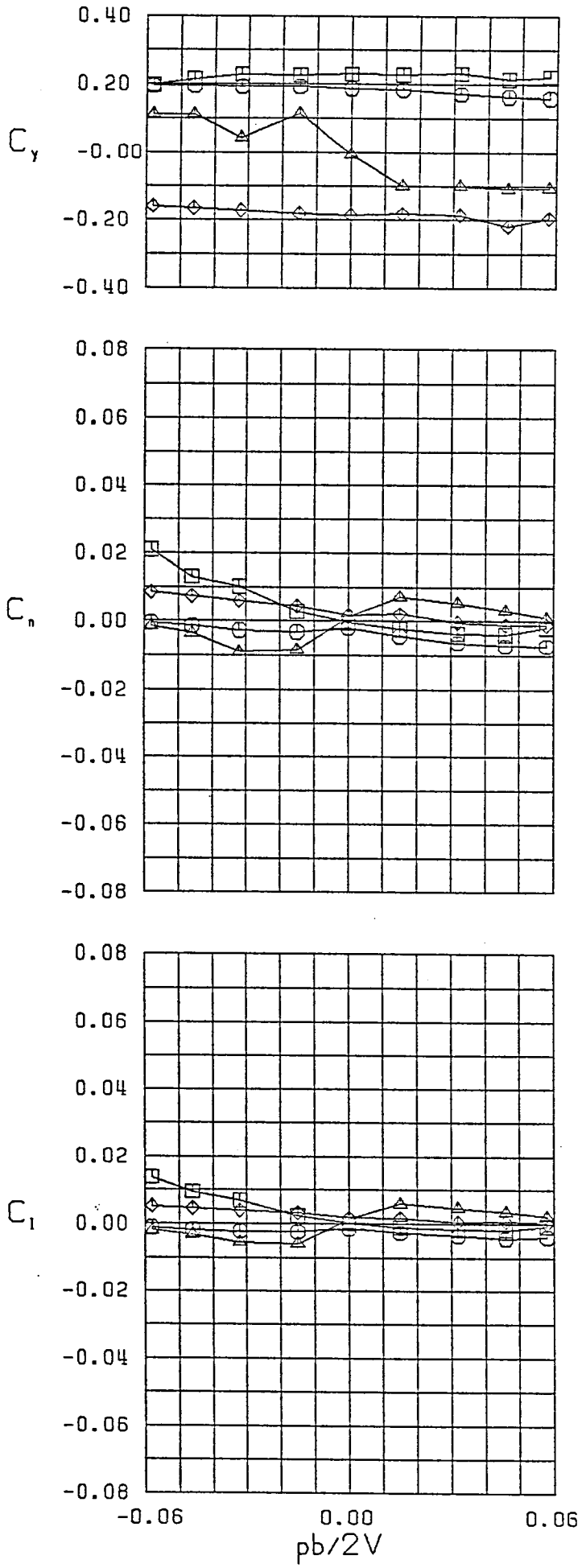

Figure 10 (Continued)

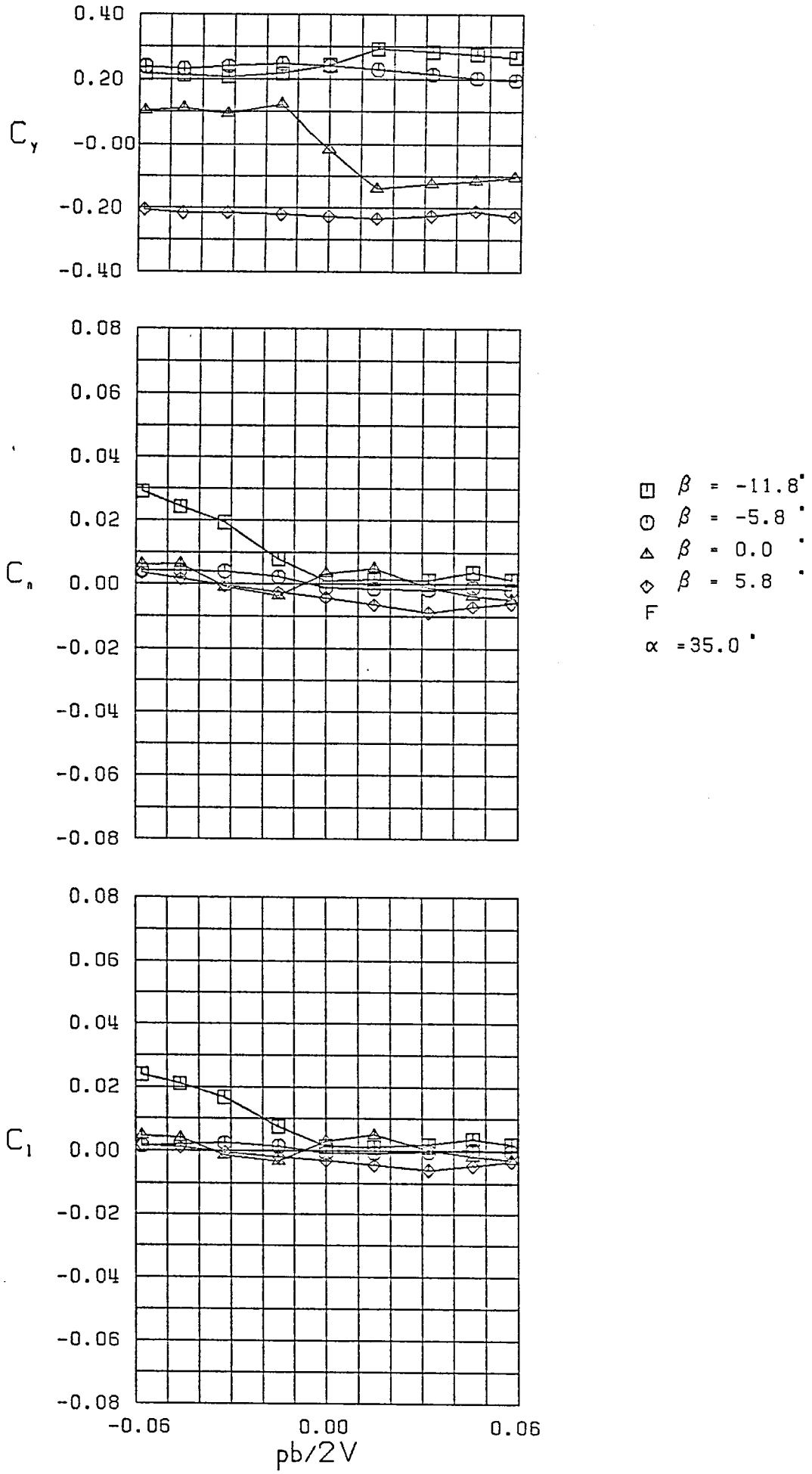

Figure 10 (Continued)

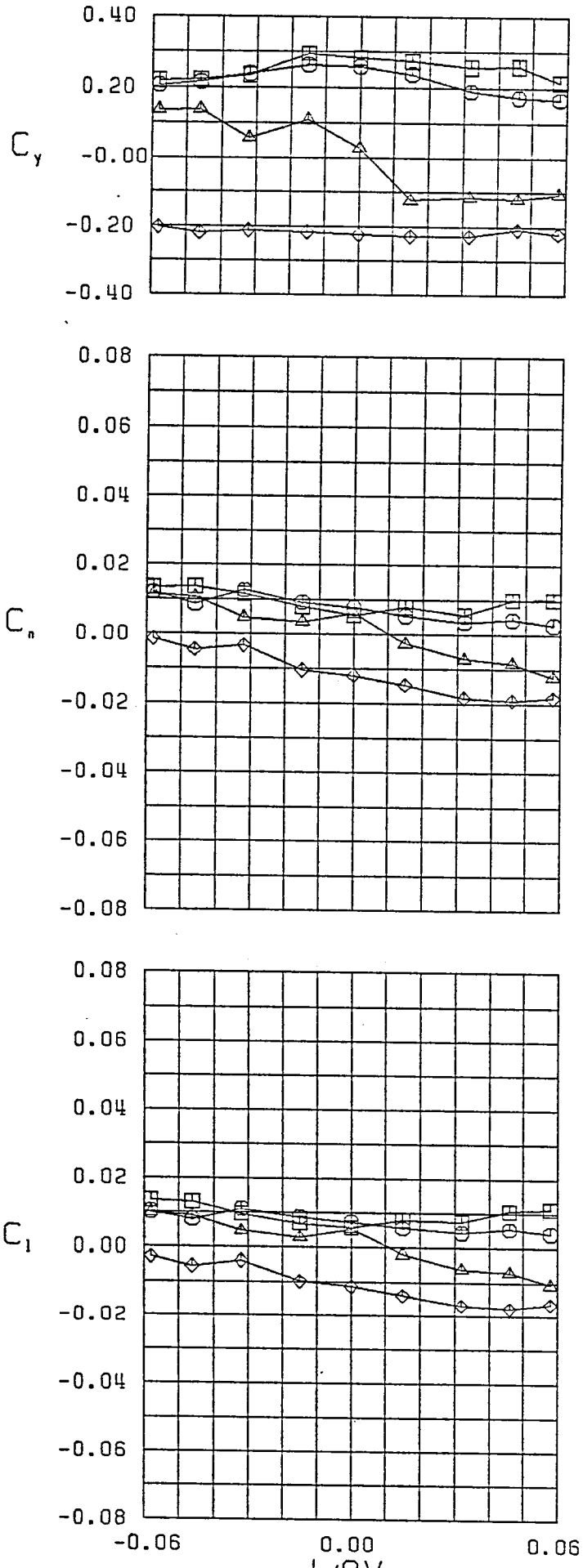

Figure 10 (Continued)

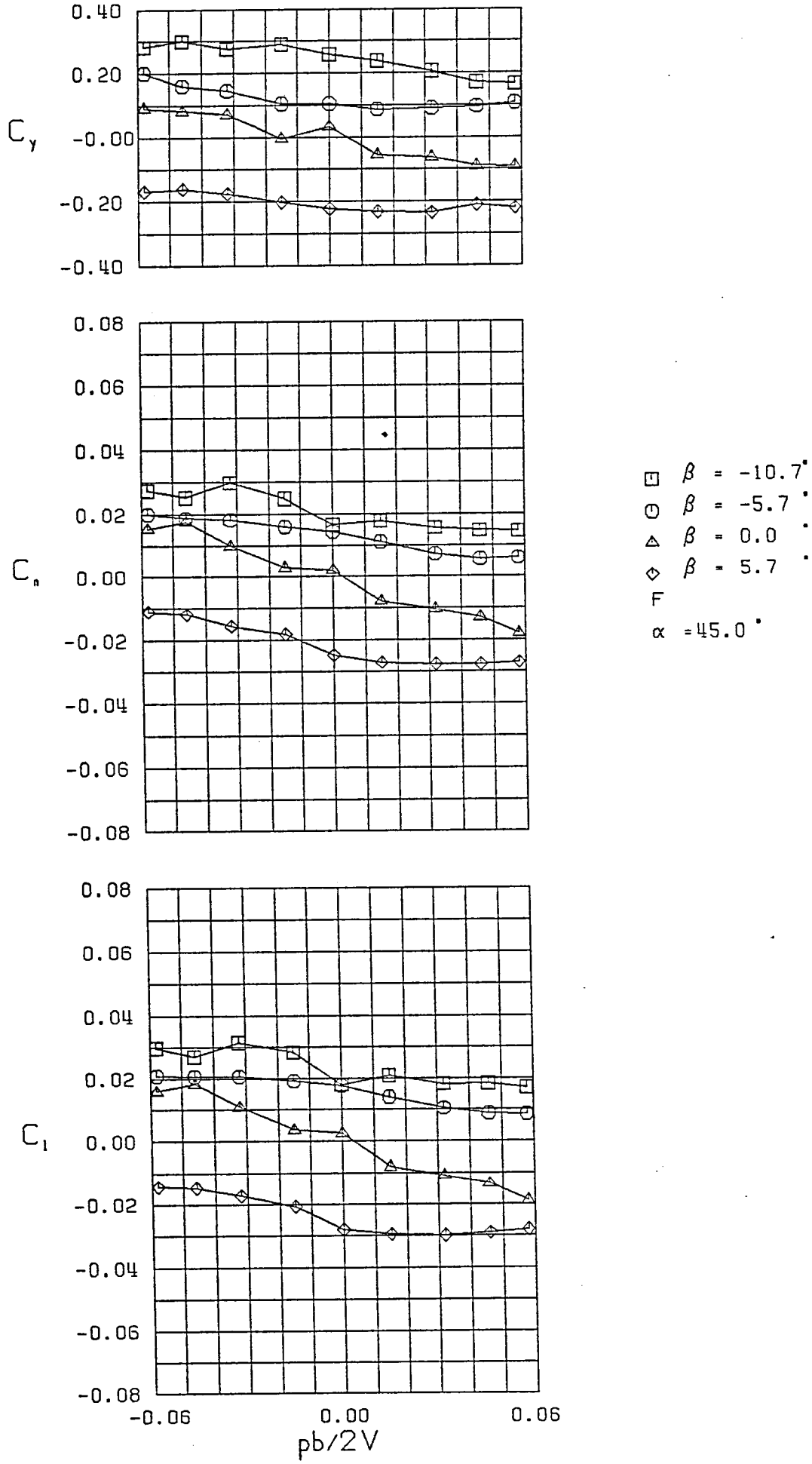

Figure 10 (Continued)

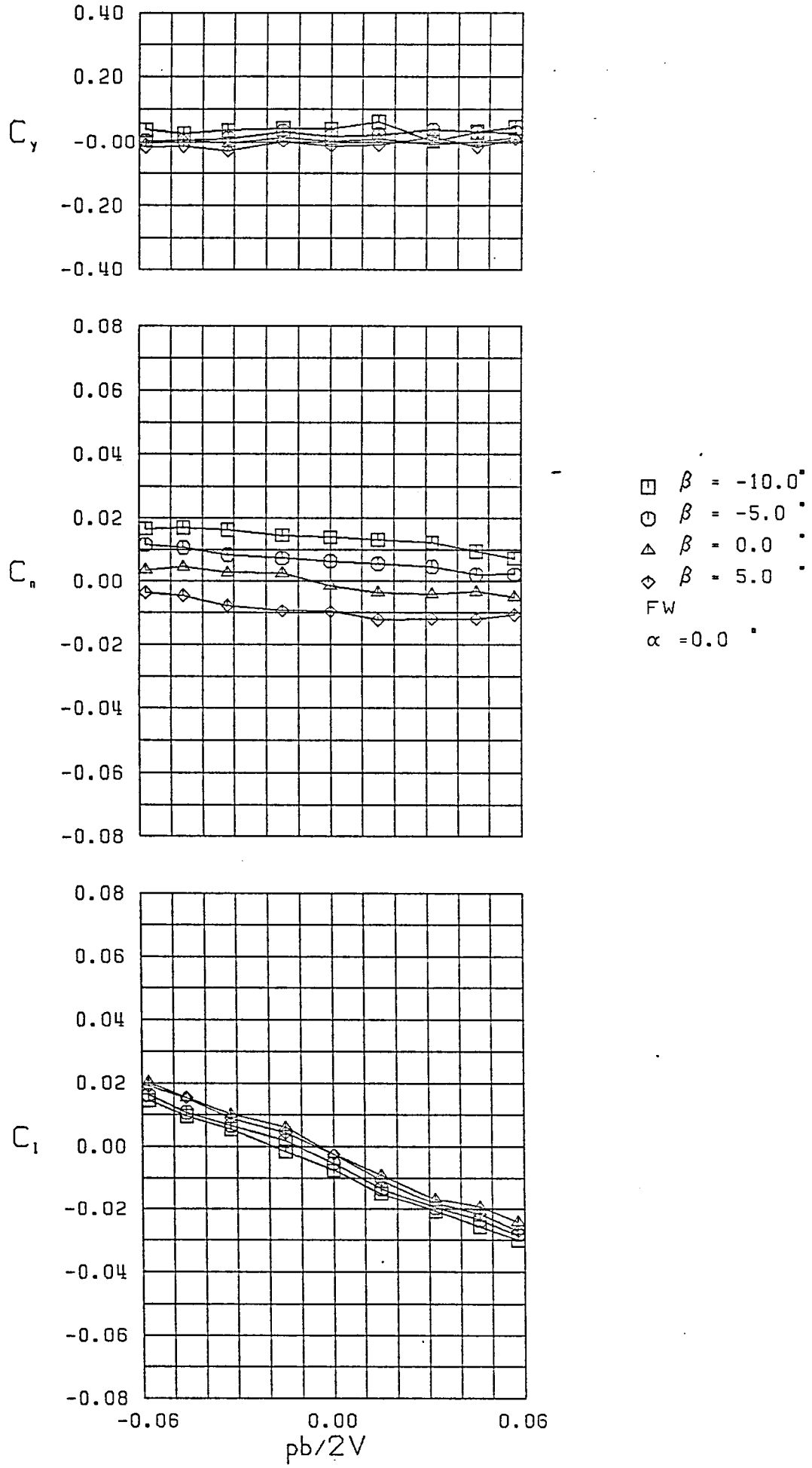

Figure 11 - Variation of Lateral-Directional Characteristics with Roll Rate-Configuration 14

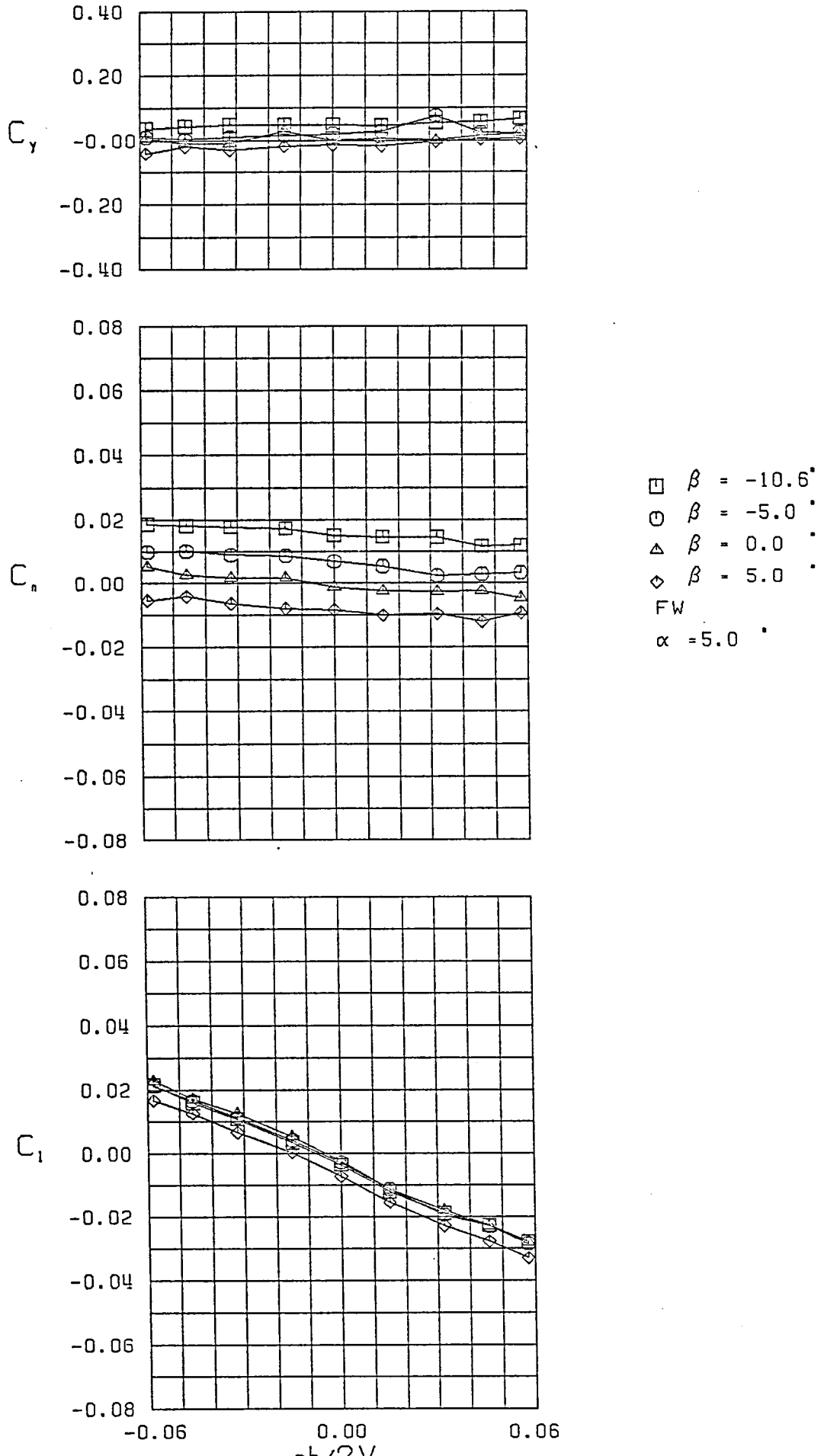

Figure 11 (Continued)

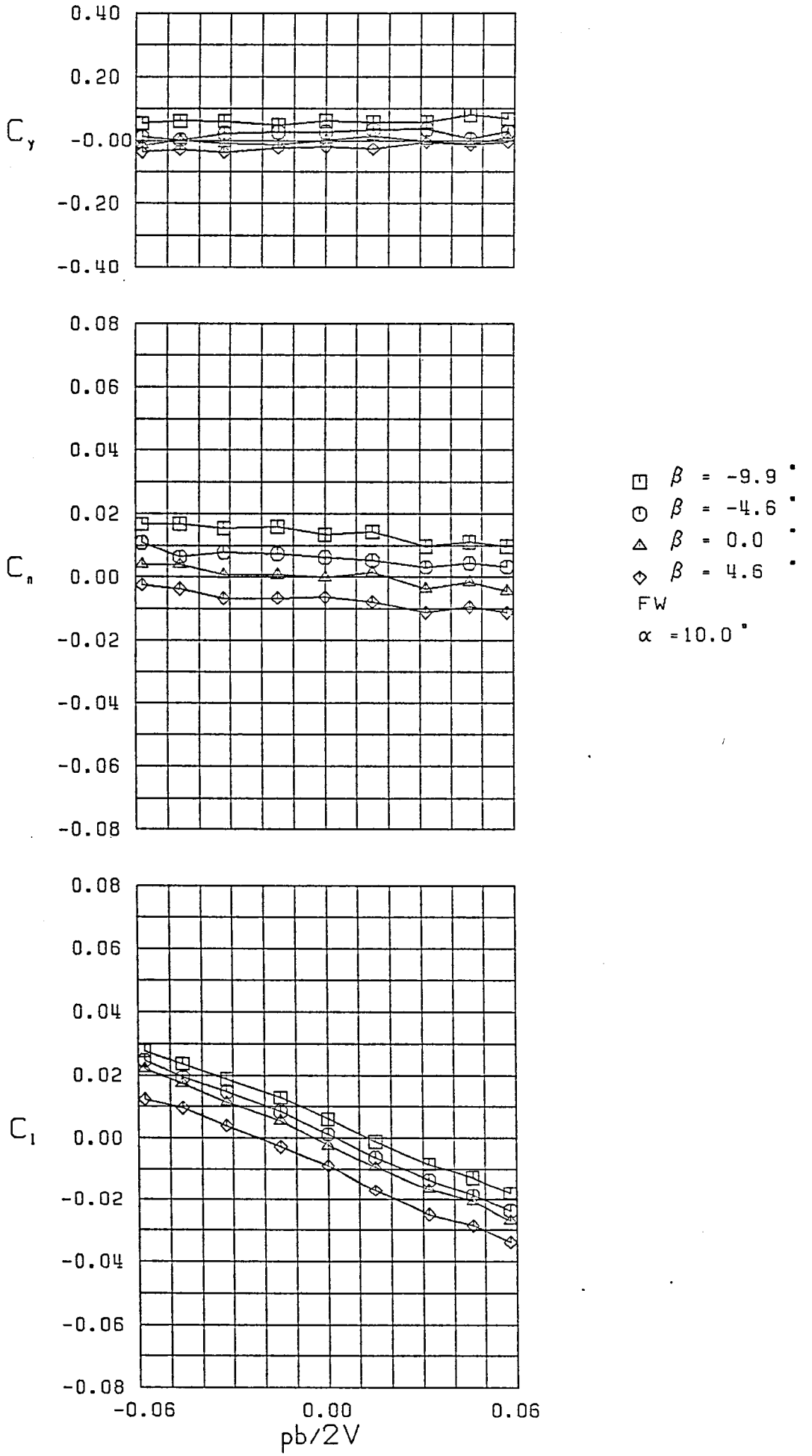

Figure 11 (Continued)

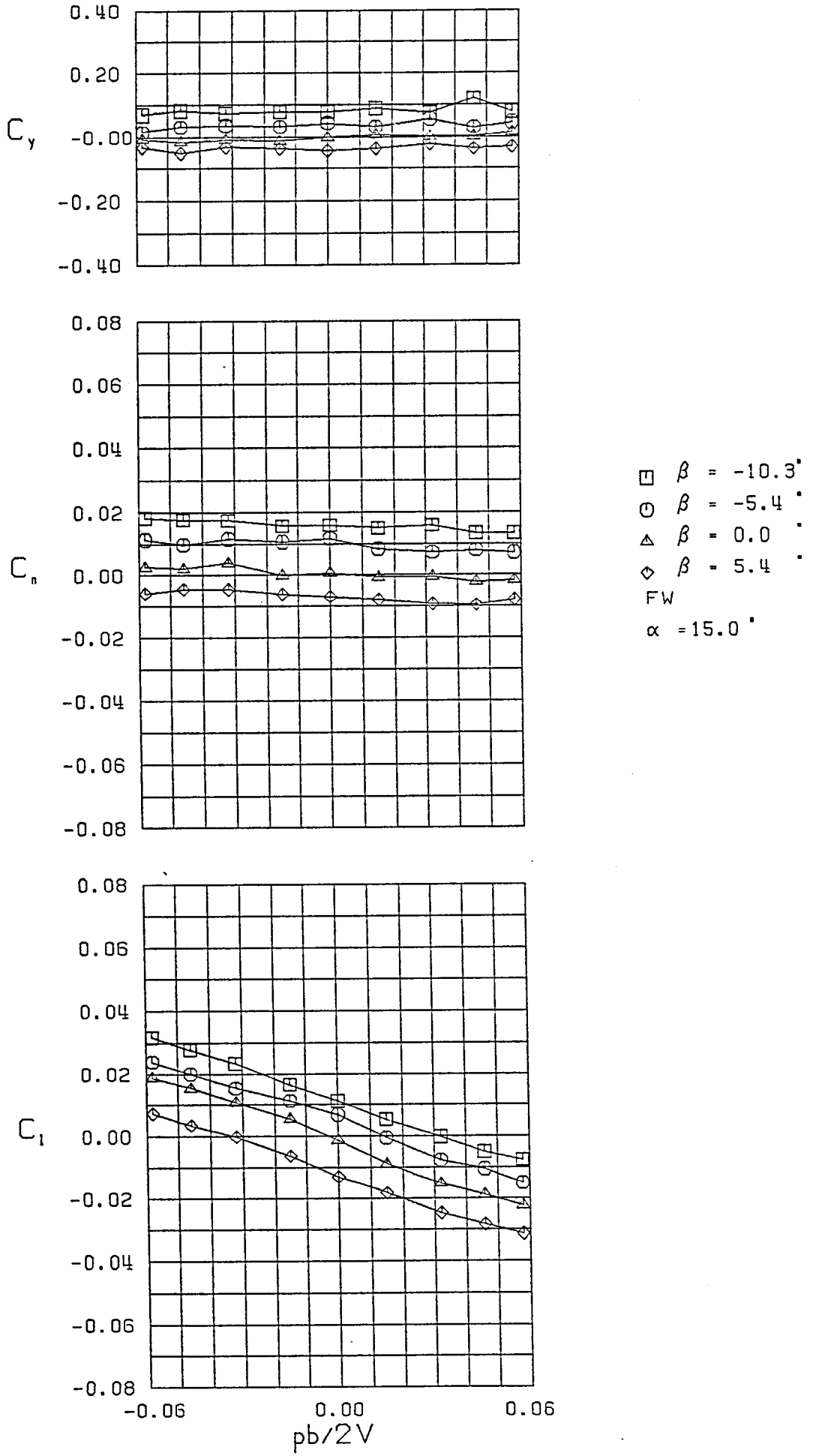

Figure 11 (Continued)

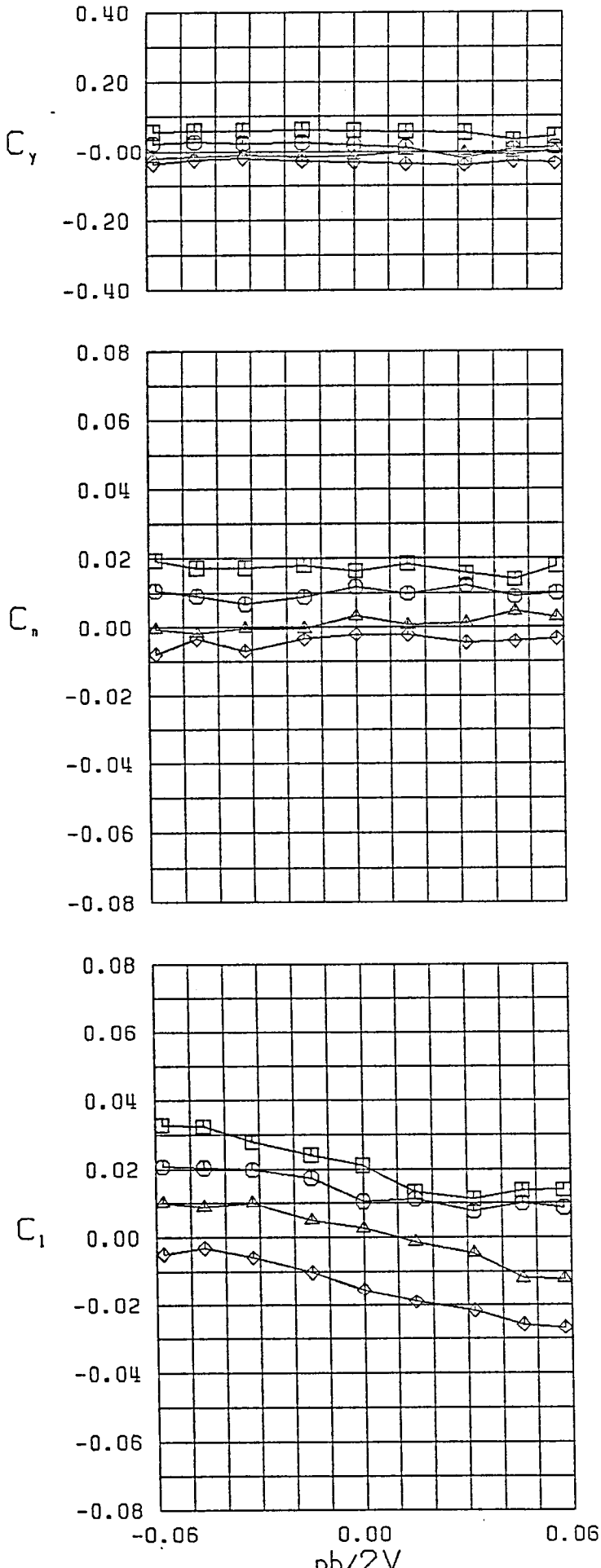

Figure 11 (Continued)

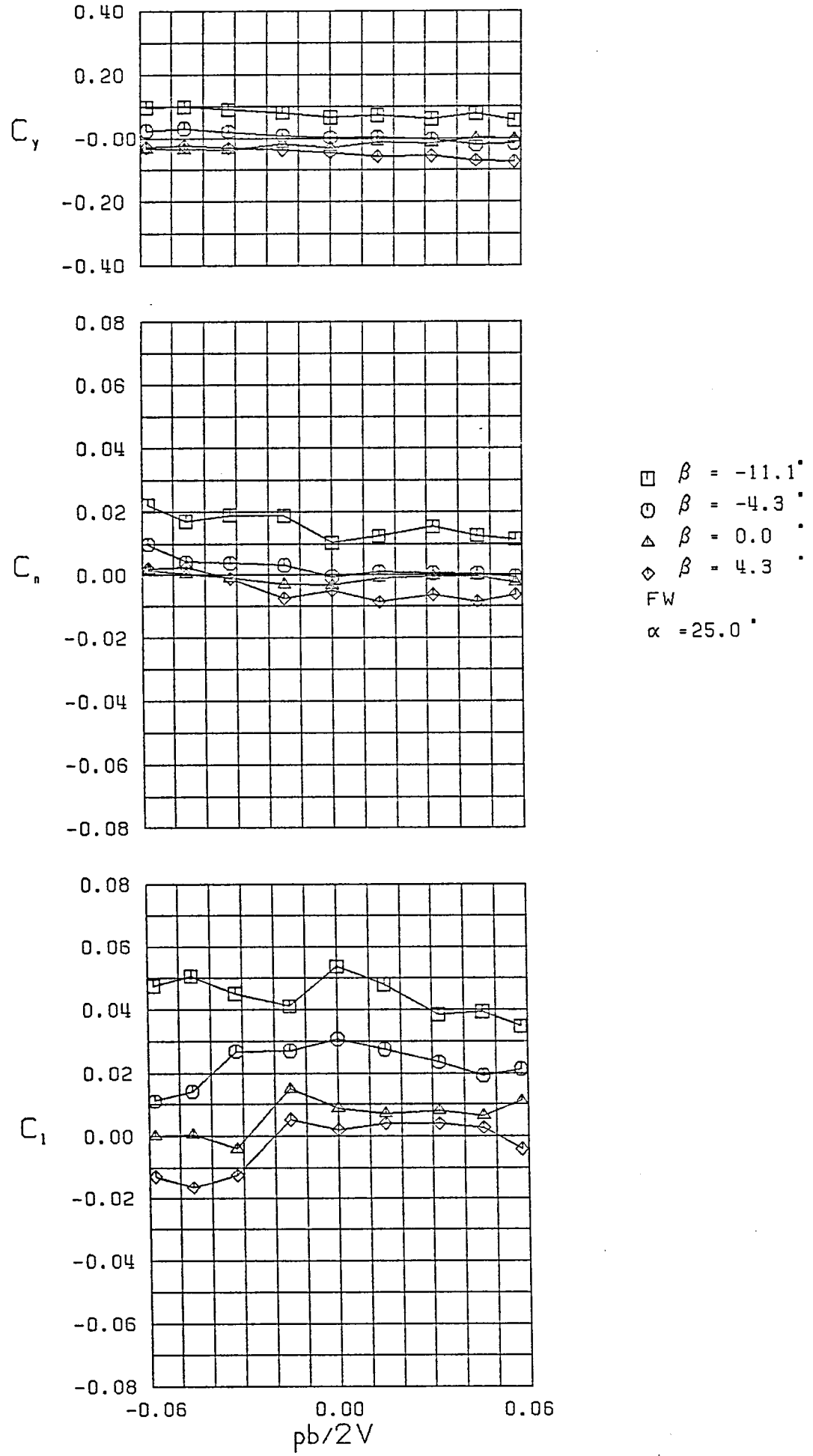

Figure 11 (Continued)

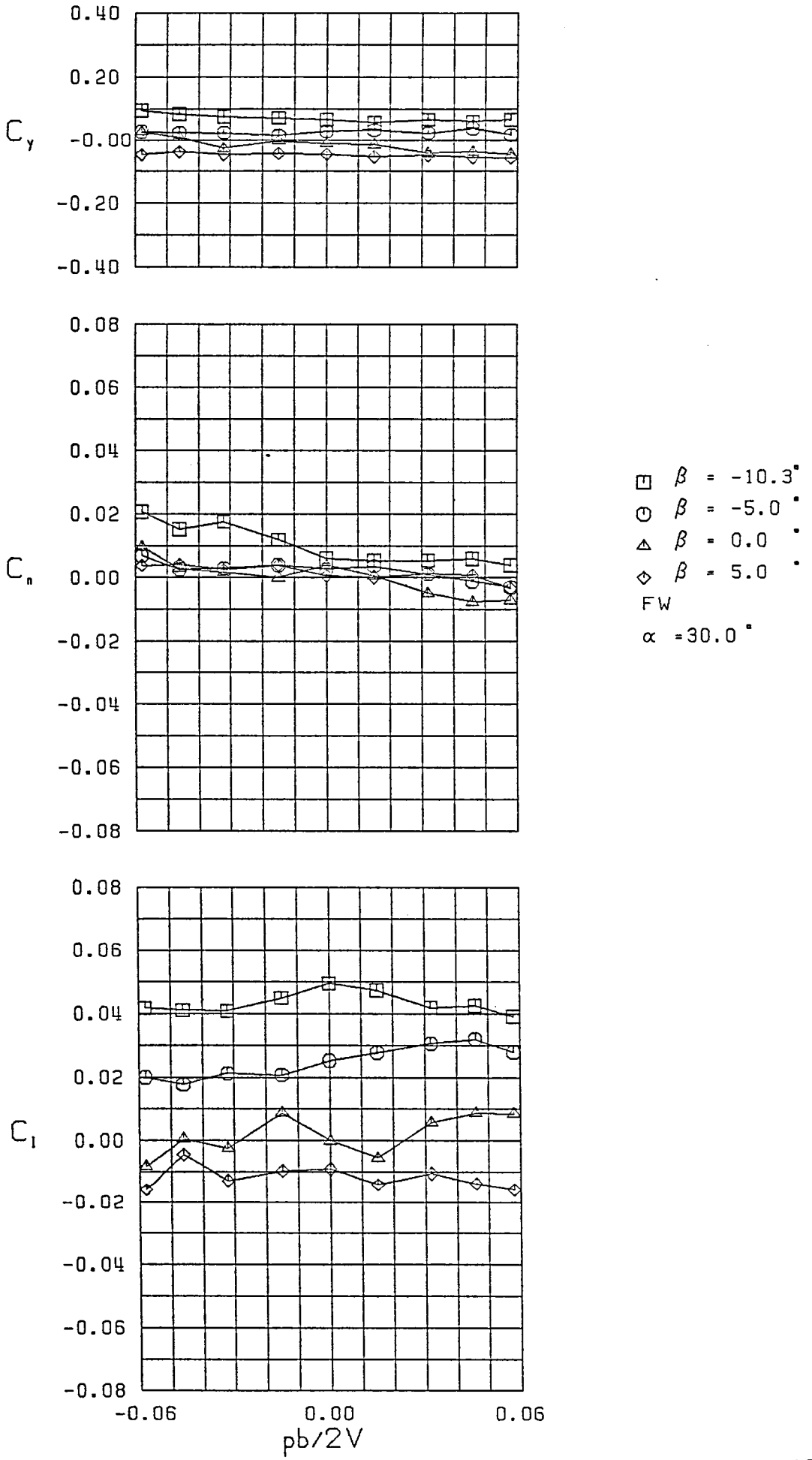

Figure 11 (Continued)

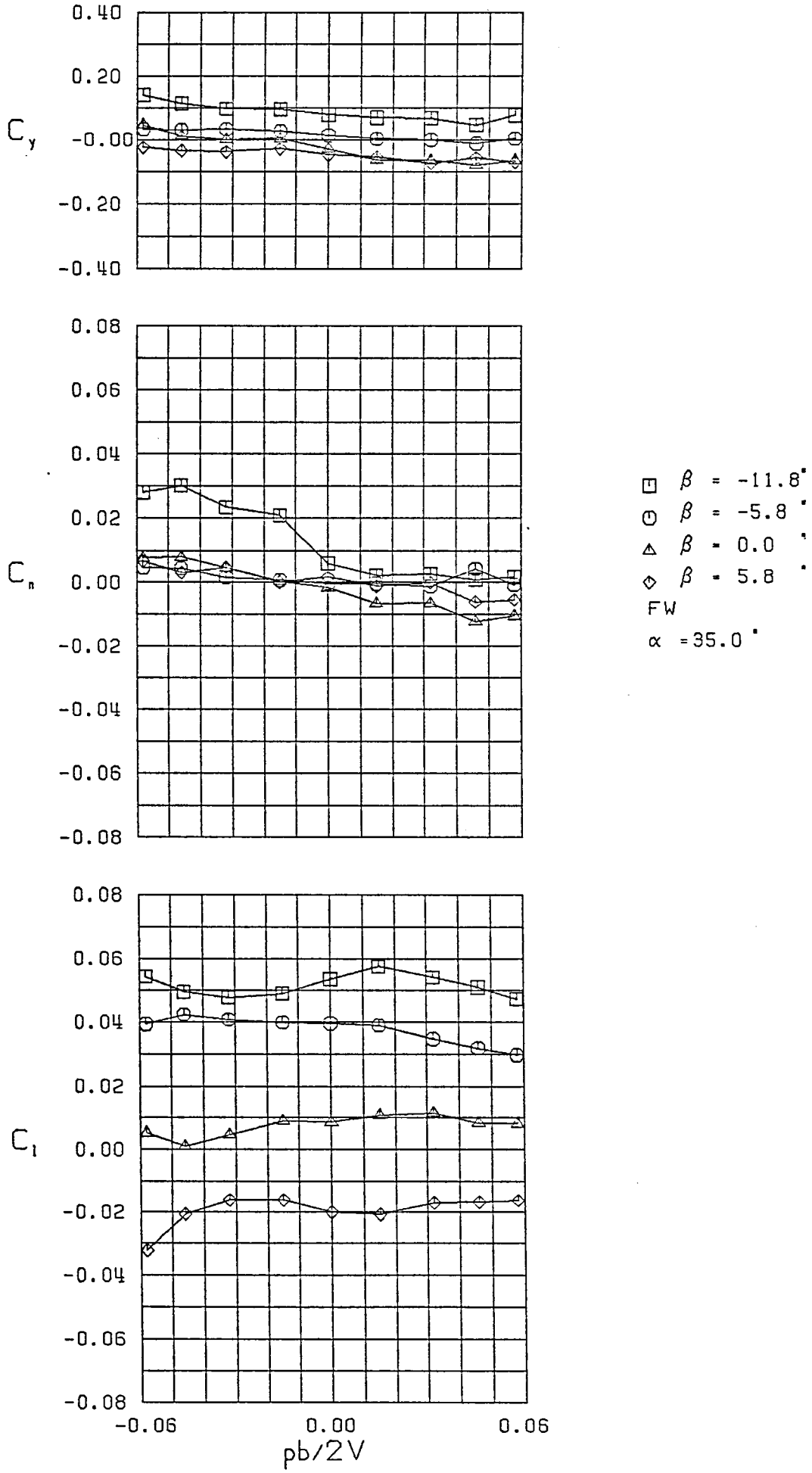

Figure 11 (Continued)

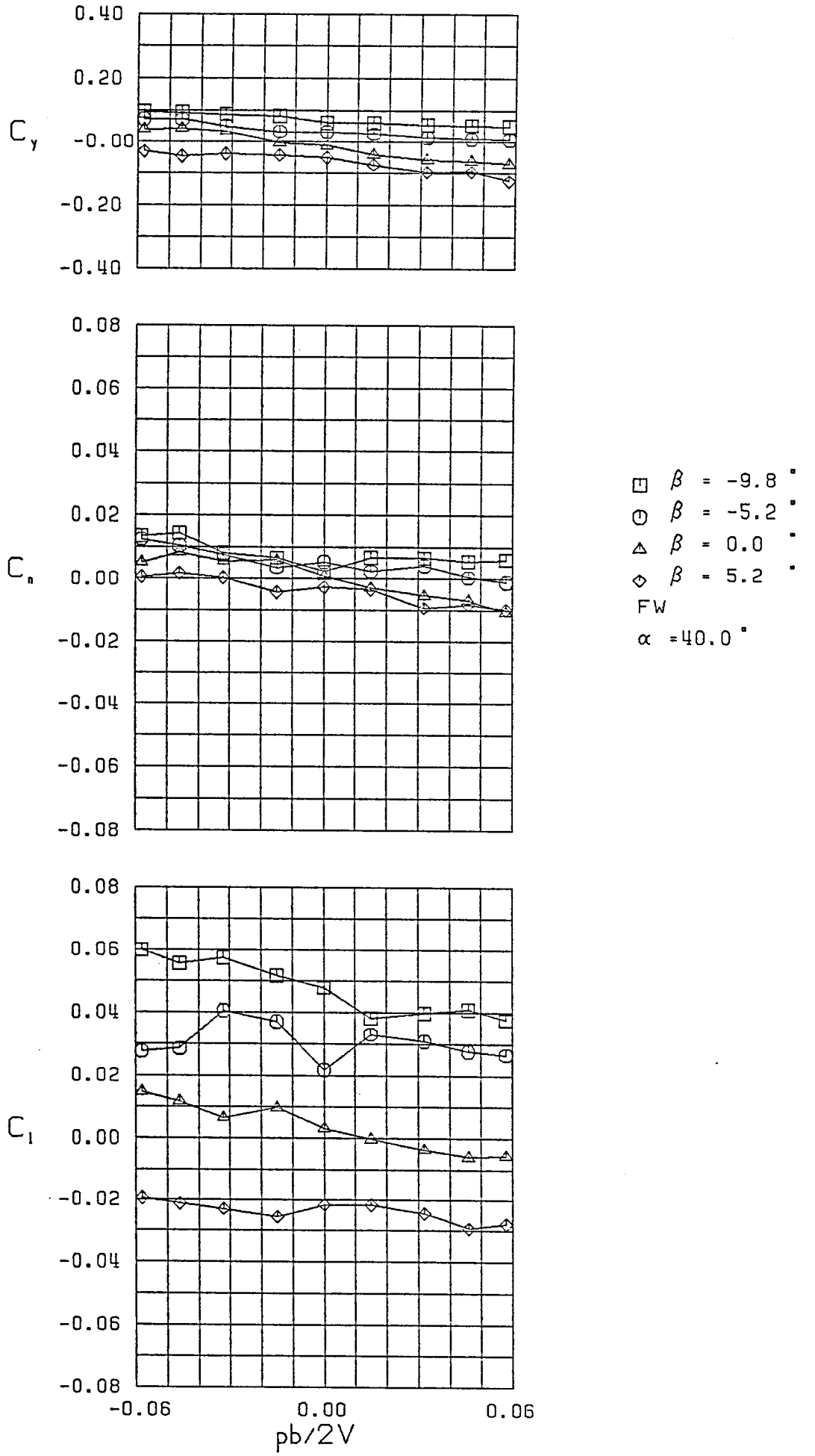

Figure 11 (Continued)

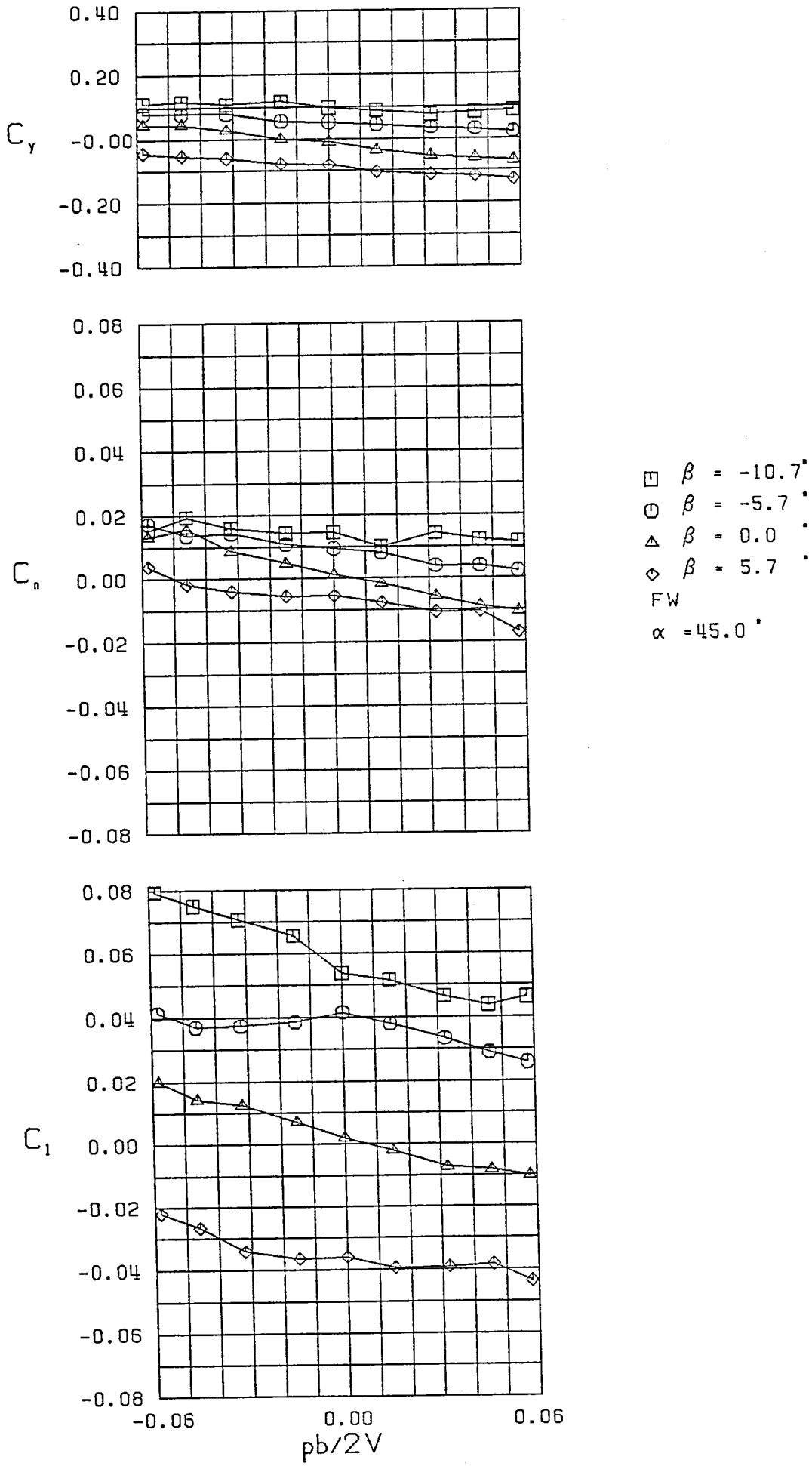

Figure 11 (Continued)

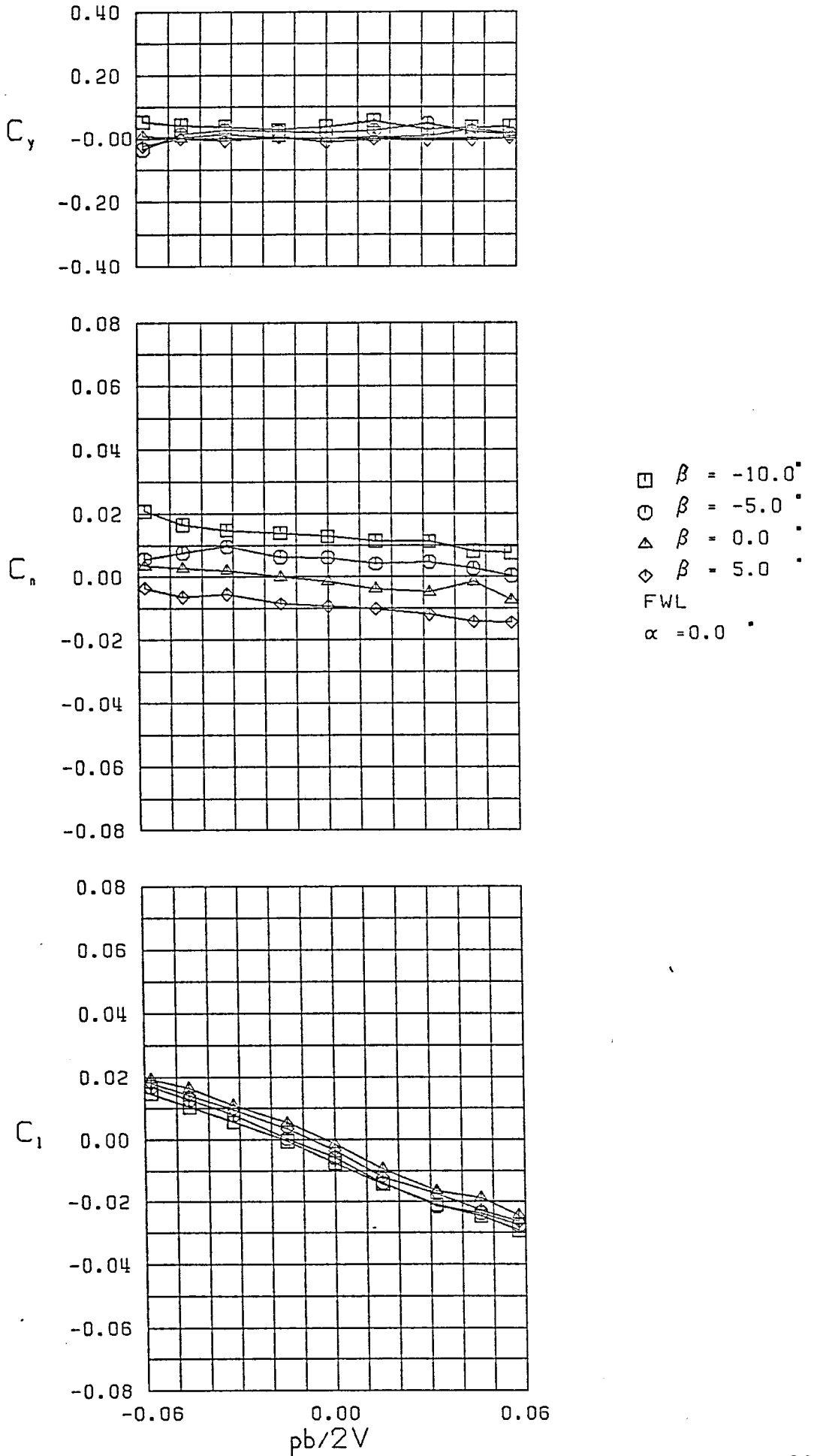

Figure 12 - Variation of Lateral-Directional Characteristics with Roll Rate-Configuration 13

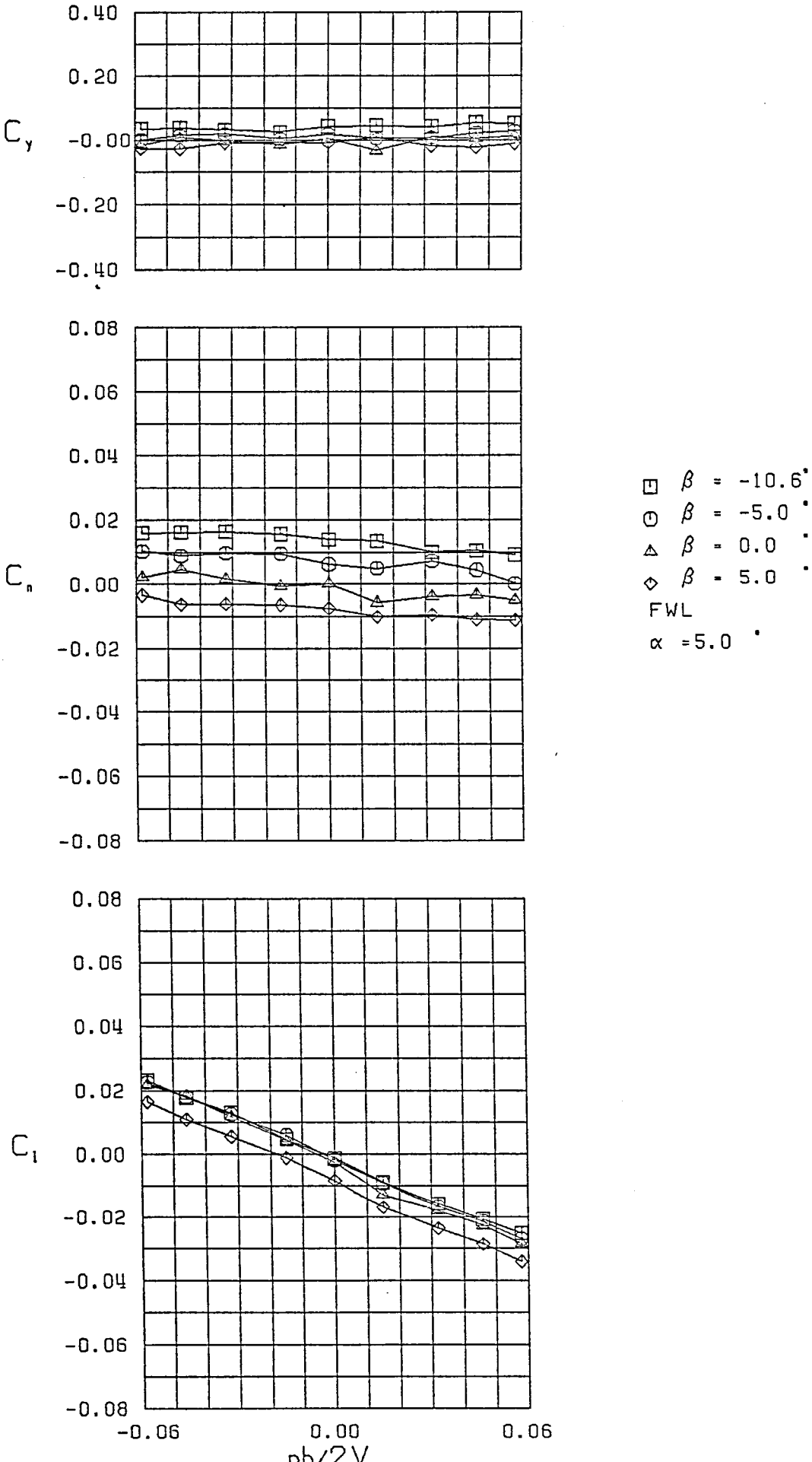

Figure 12 (Continued)

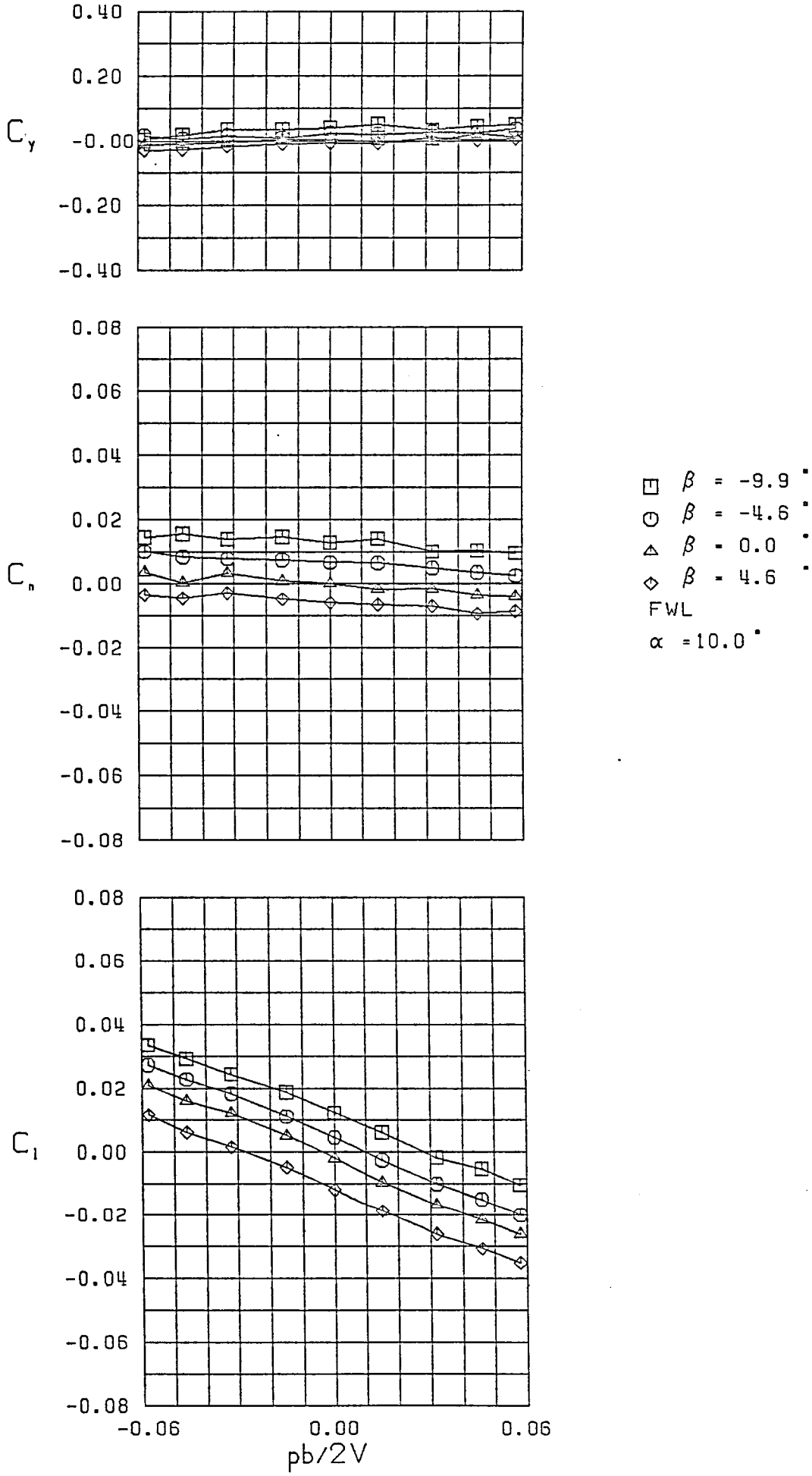

Figure 12 (Continued)

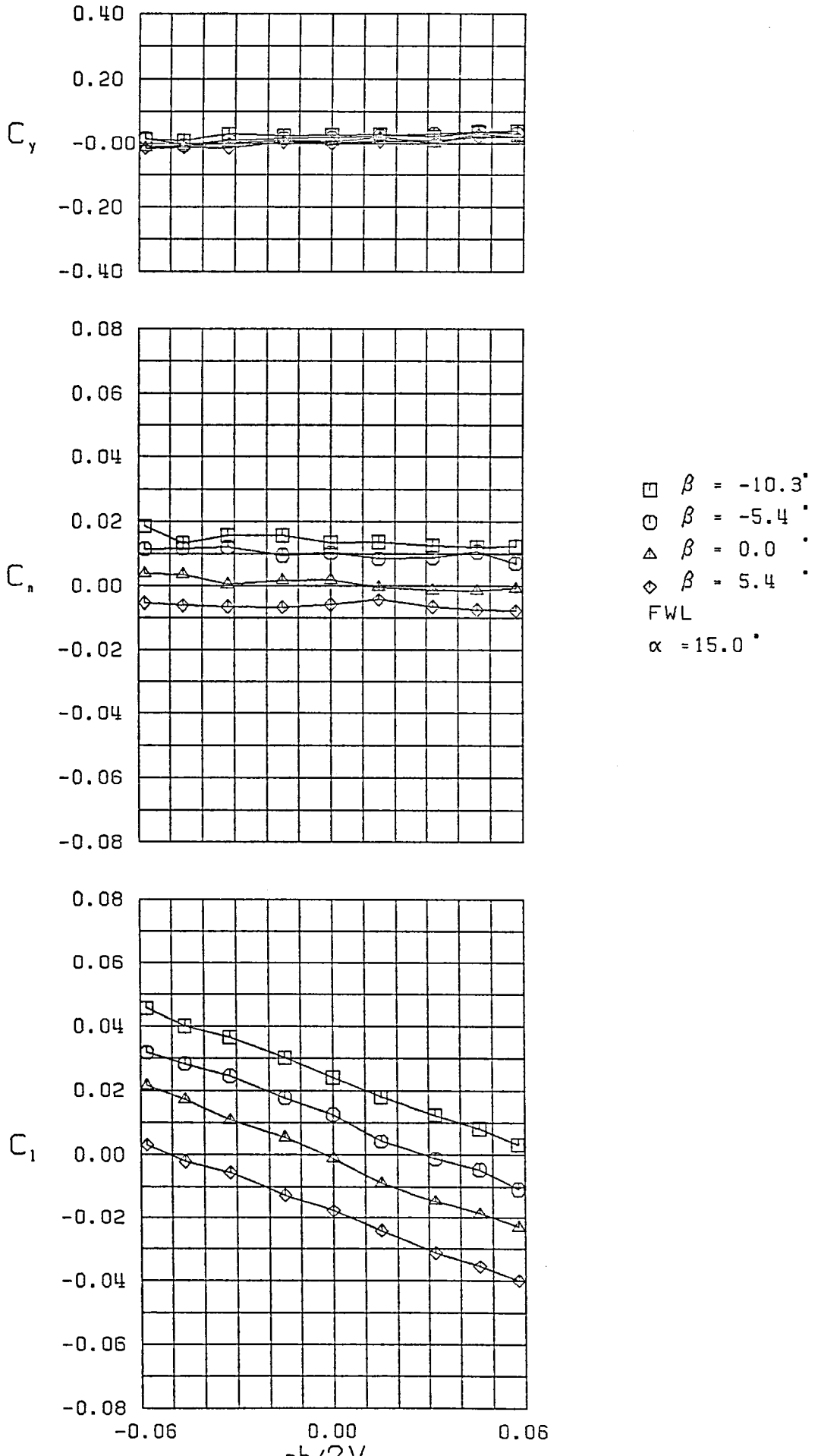

Figure 12 (Continued)

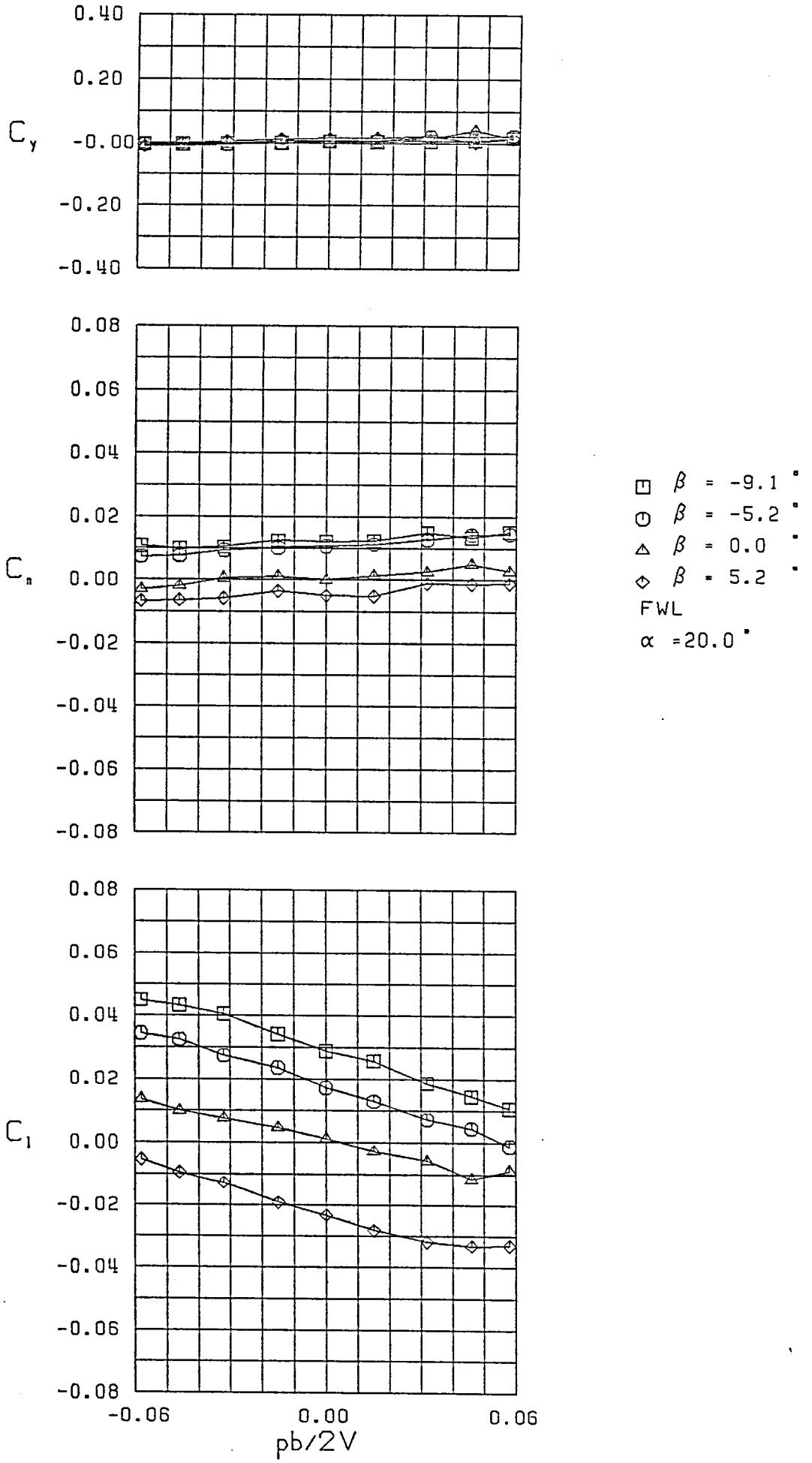

Figure 12 (Continued)

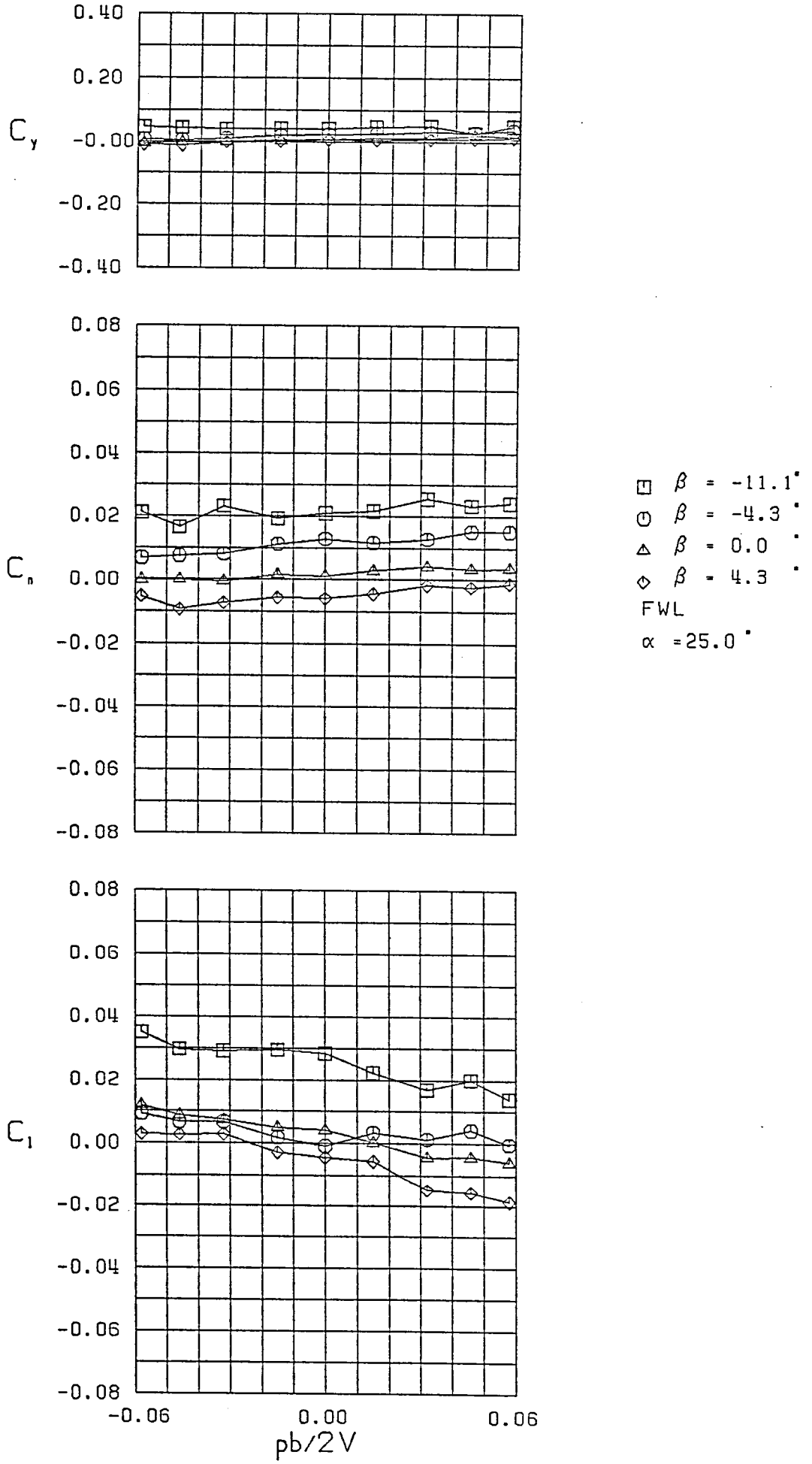

Figure 12 (Continued)

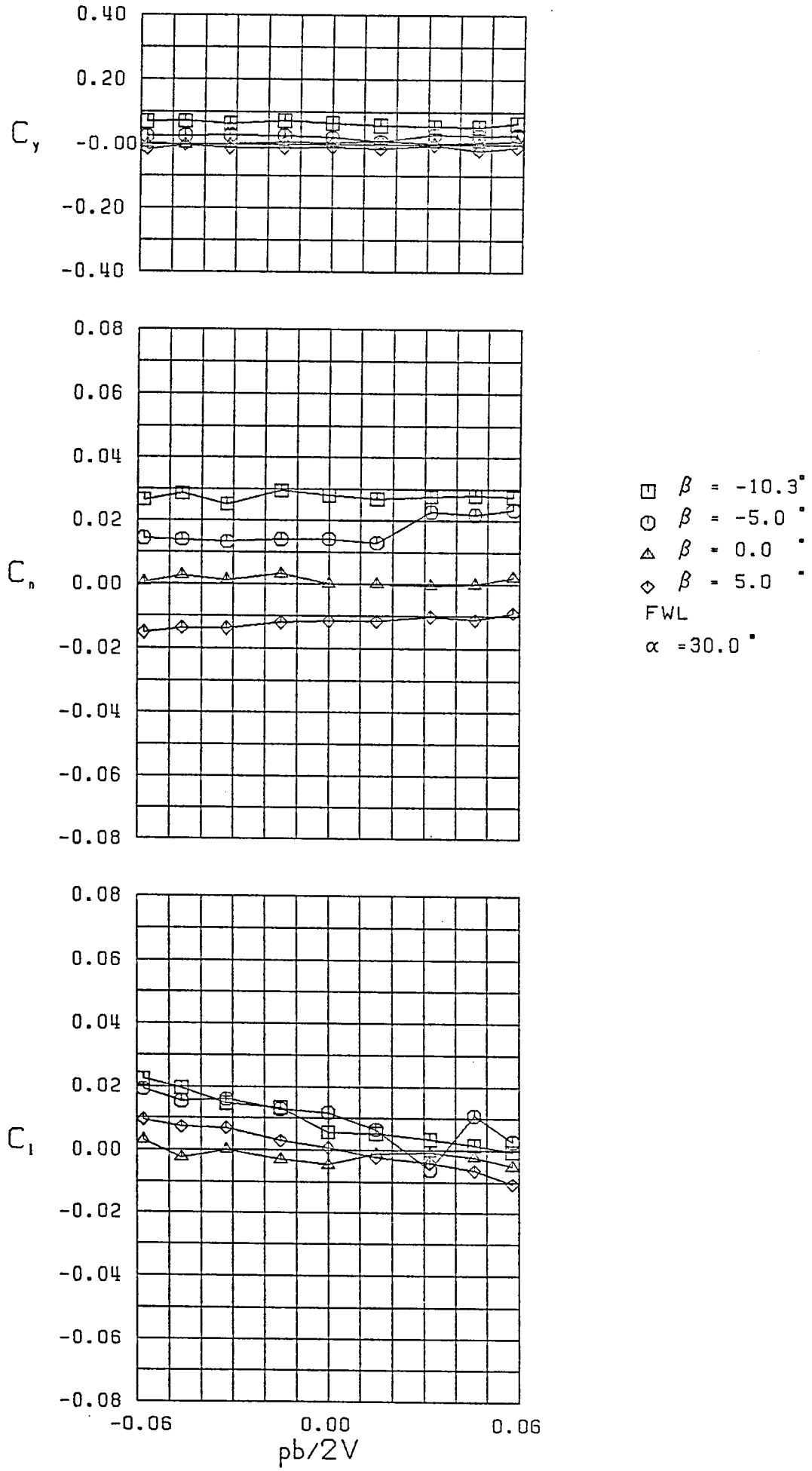

Figure 12 (Continued)

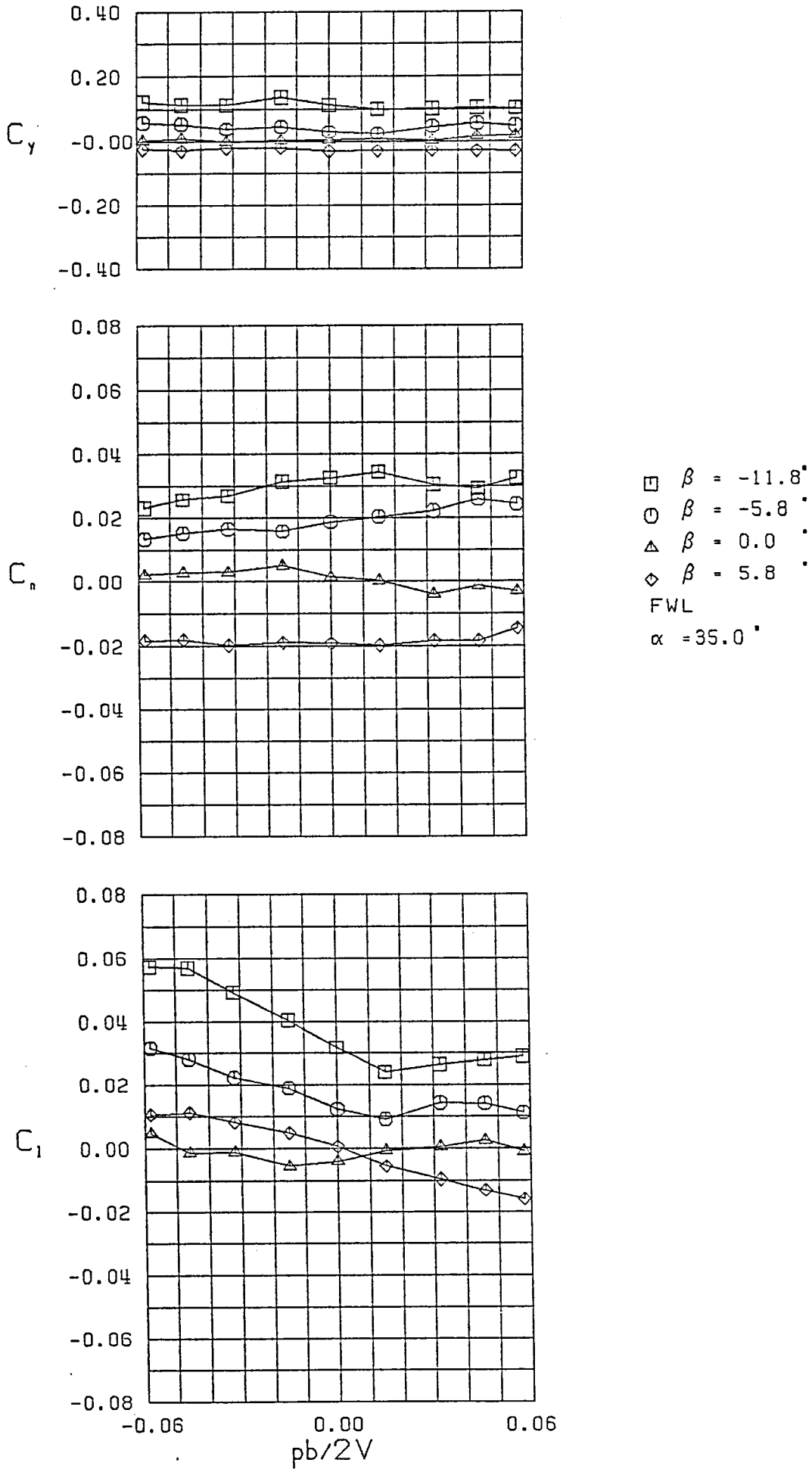

Figure 12 (Continued)

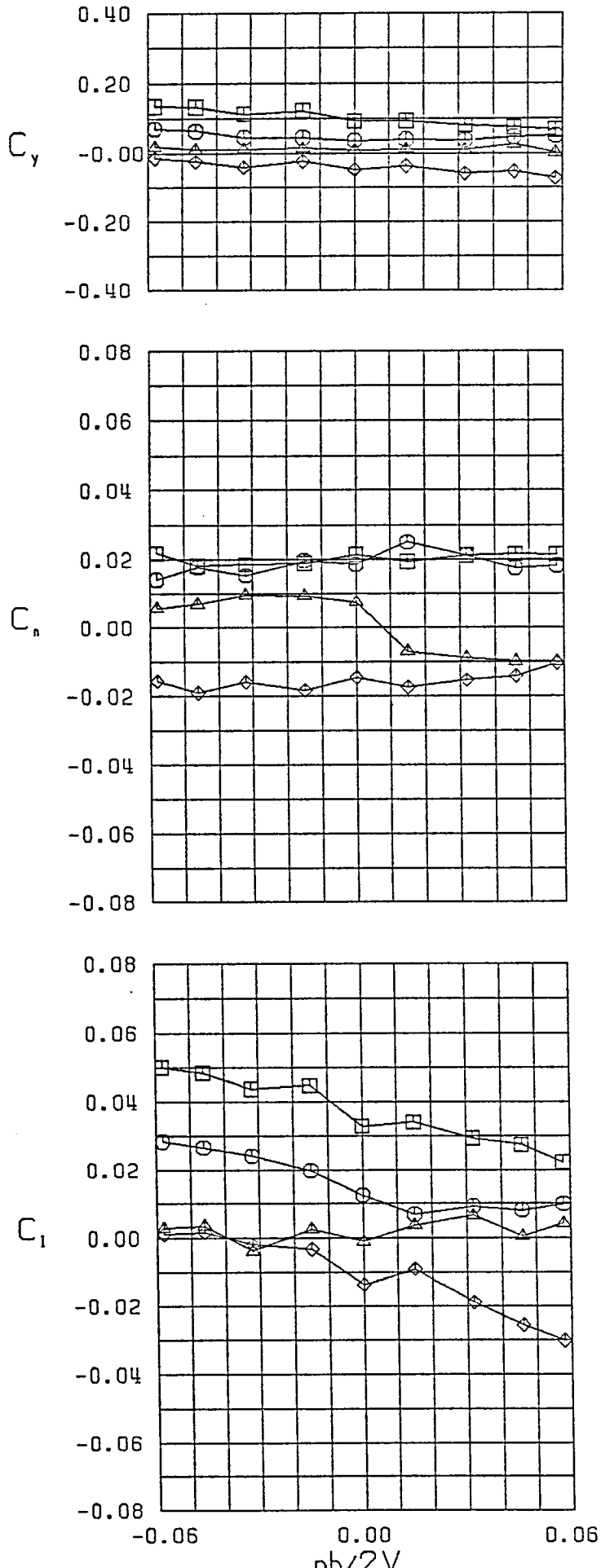

Figure 12 (Continued)

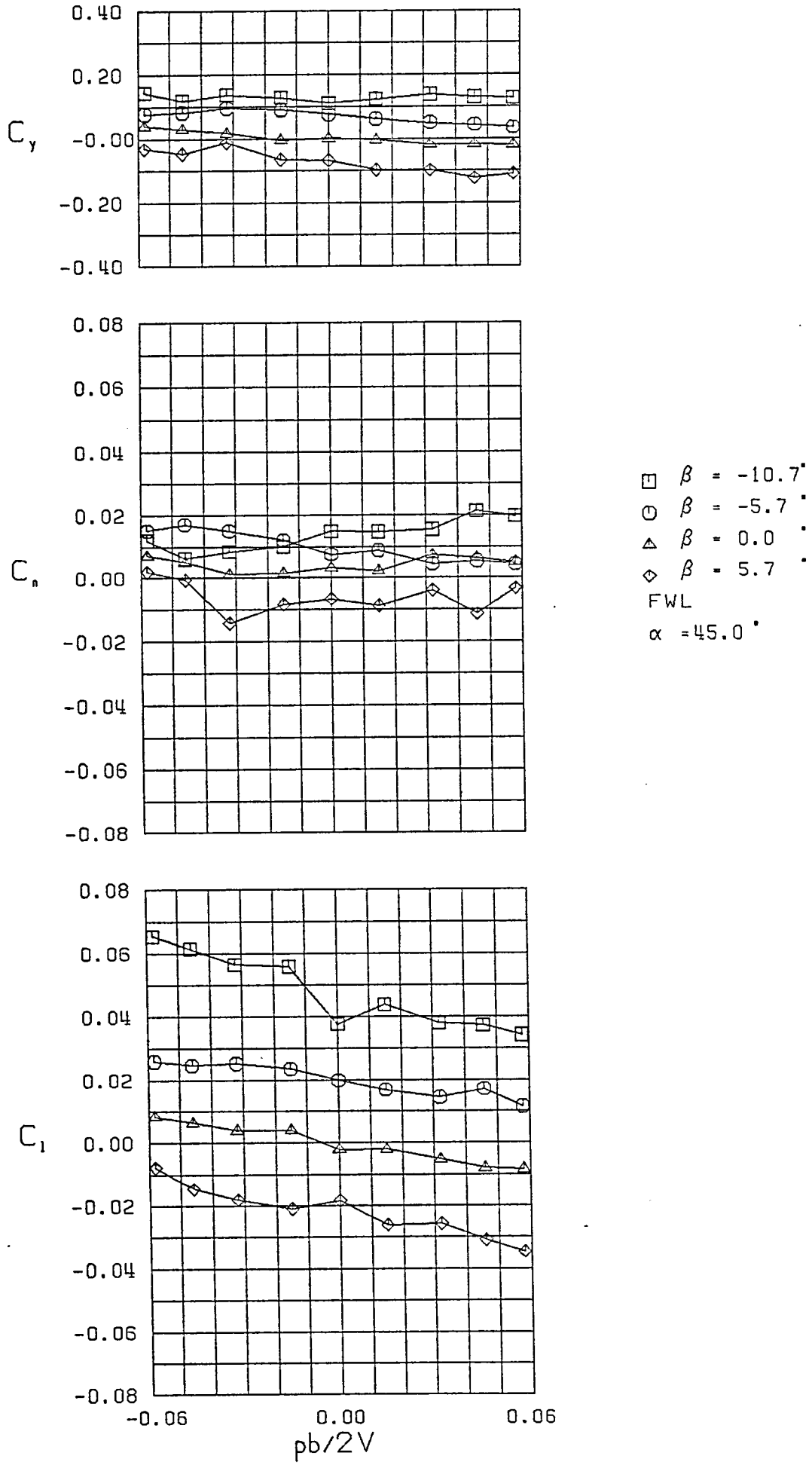

Figure 12 (Continued)

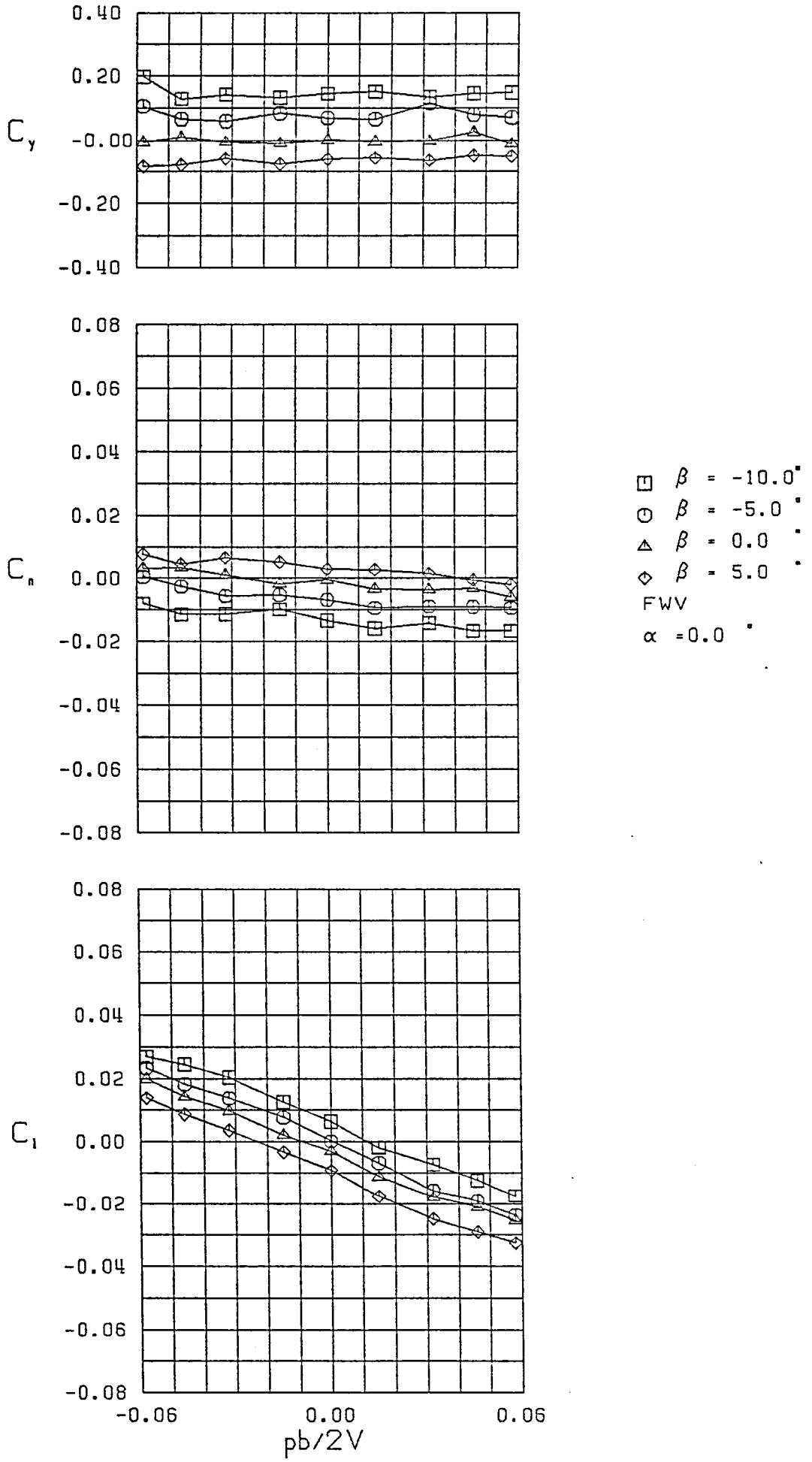

Figure 13 - Variation of Lateral-Directional Characteristics with Roll Rate-Configuration 12

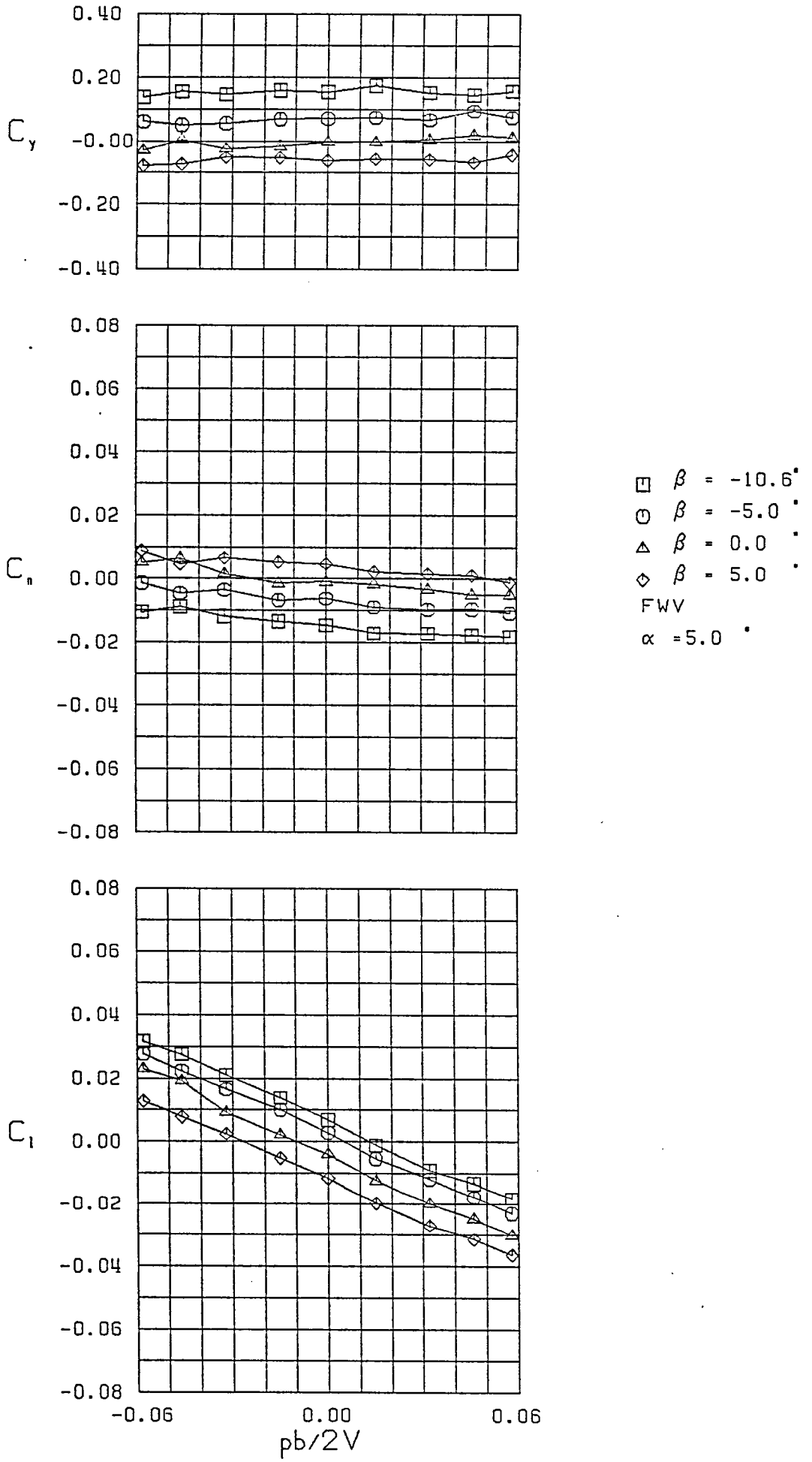

Figure 13 (Continued)

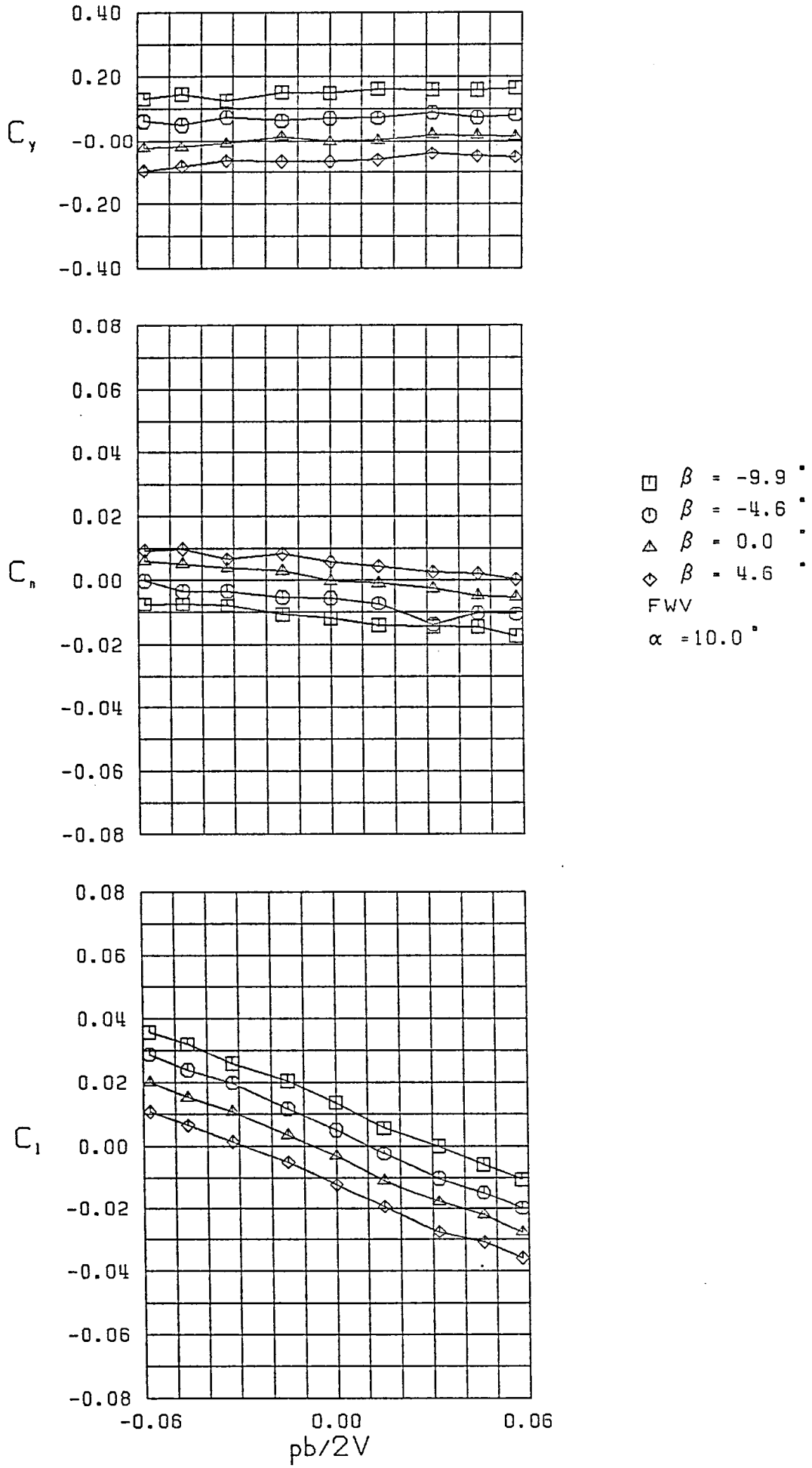

Figure 13 (Continued)

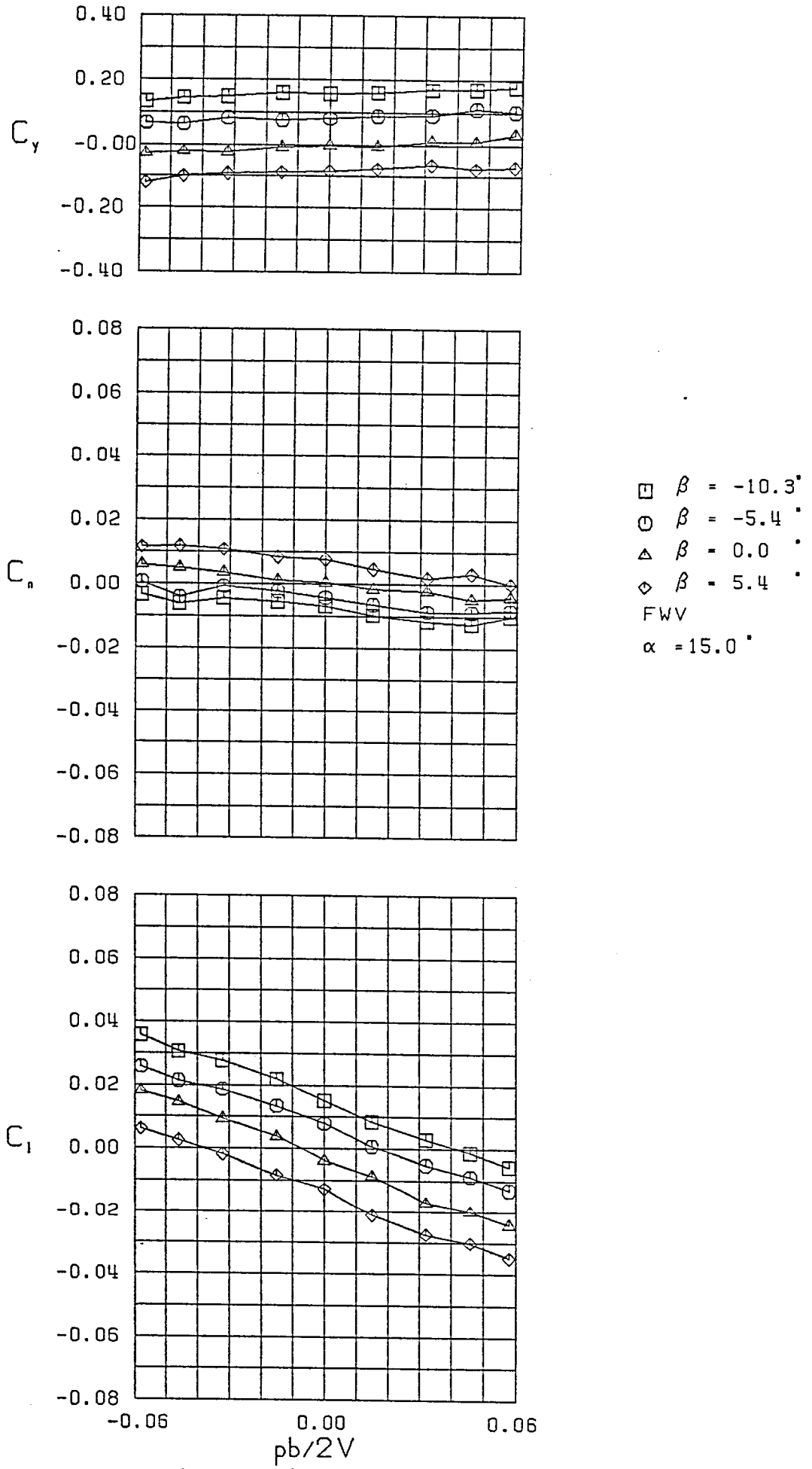

Figure 13 (Continued)

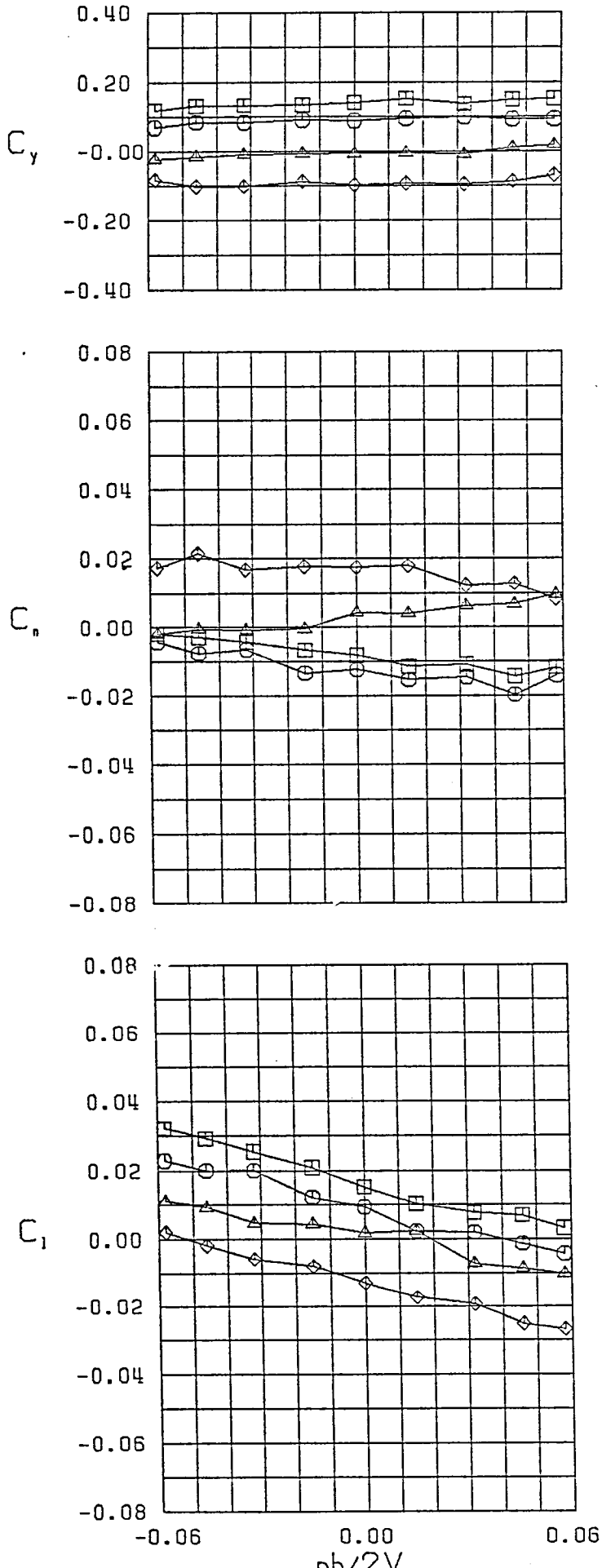

Figure 13 (Continued)

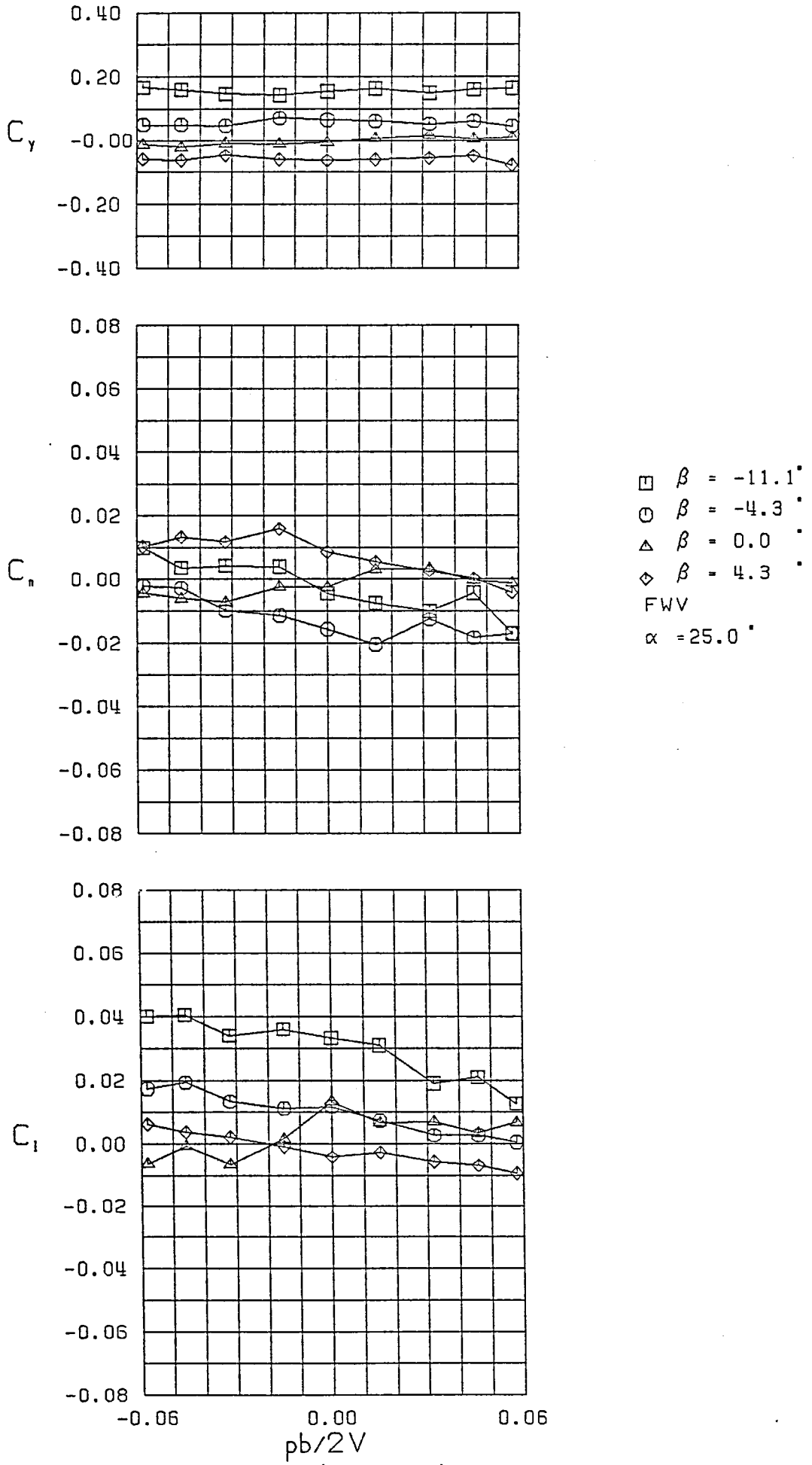

Figure 13 (Continued)

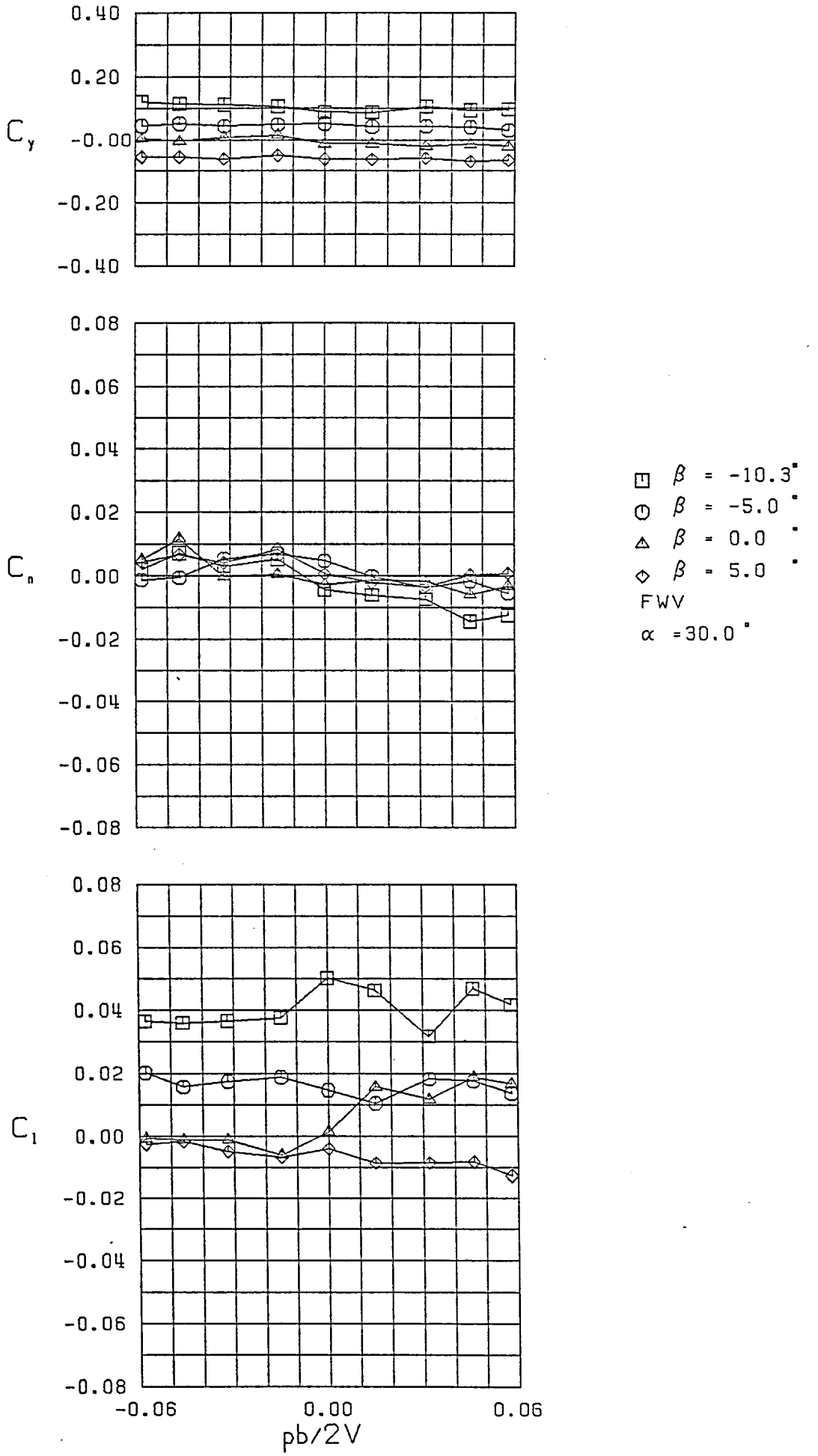

Figure 13 (Continued)

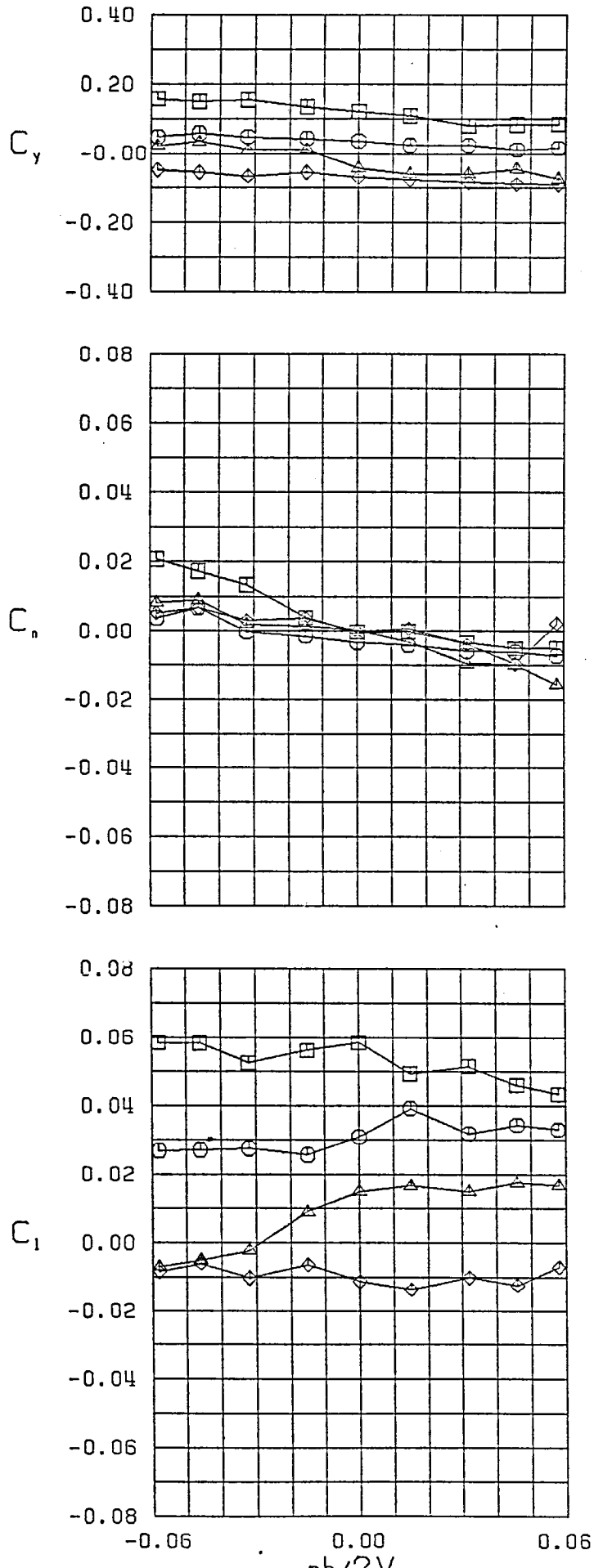

Figure 13 (Continued)

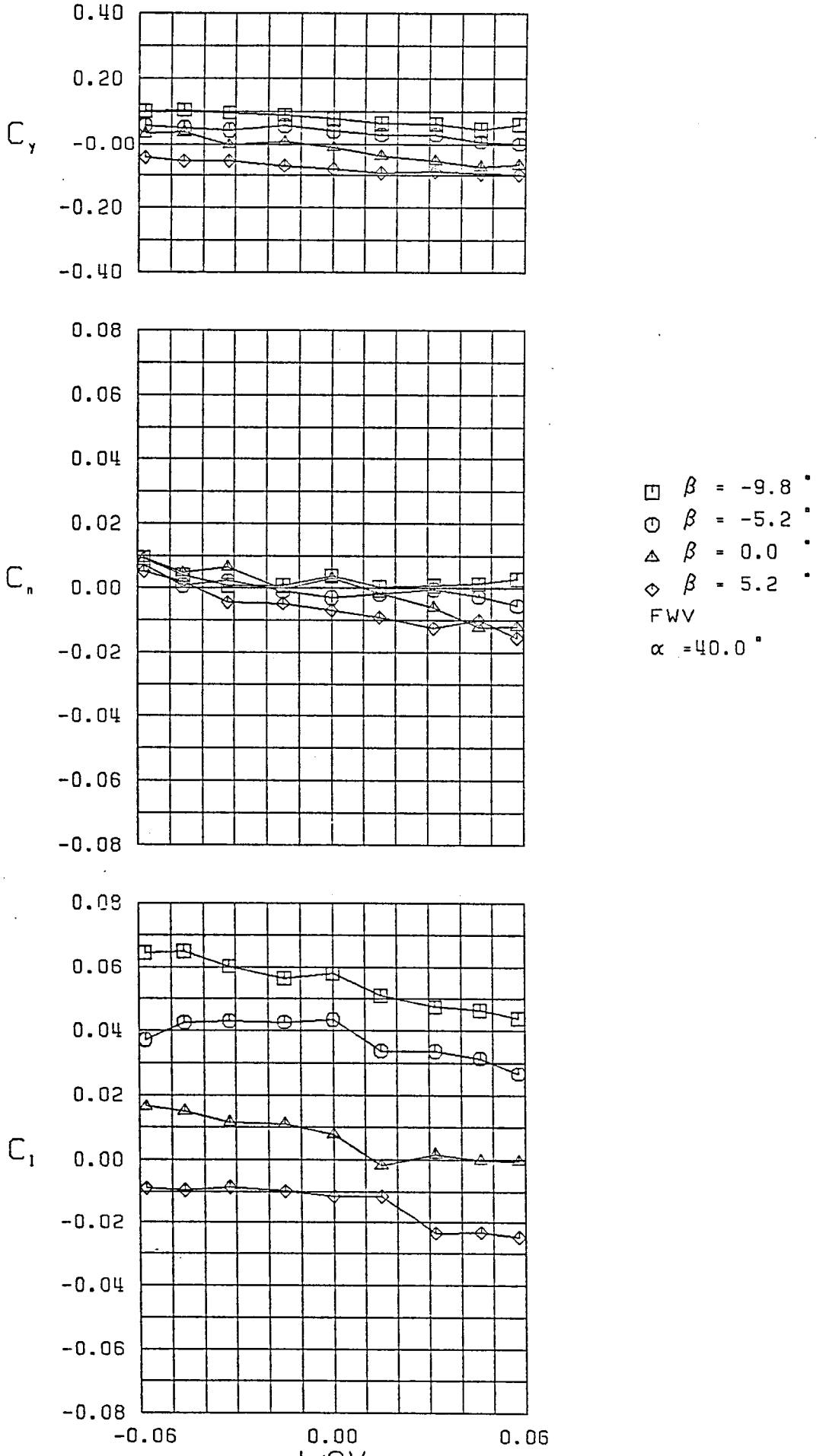

Figure 13 (Continued)

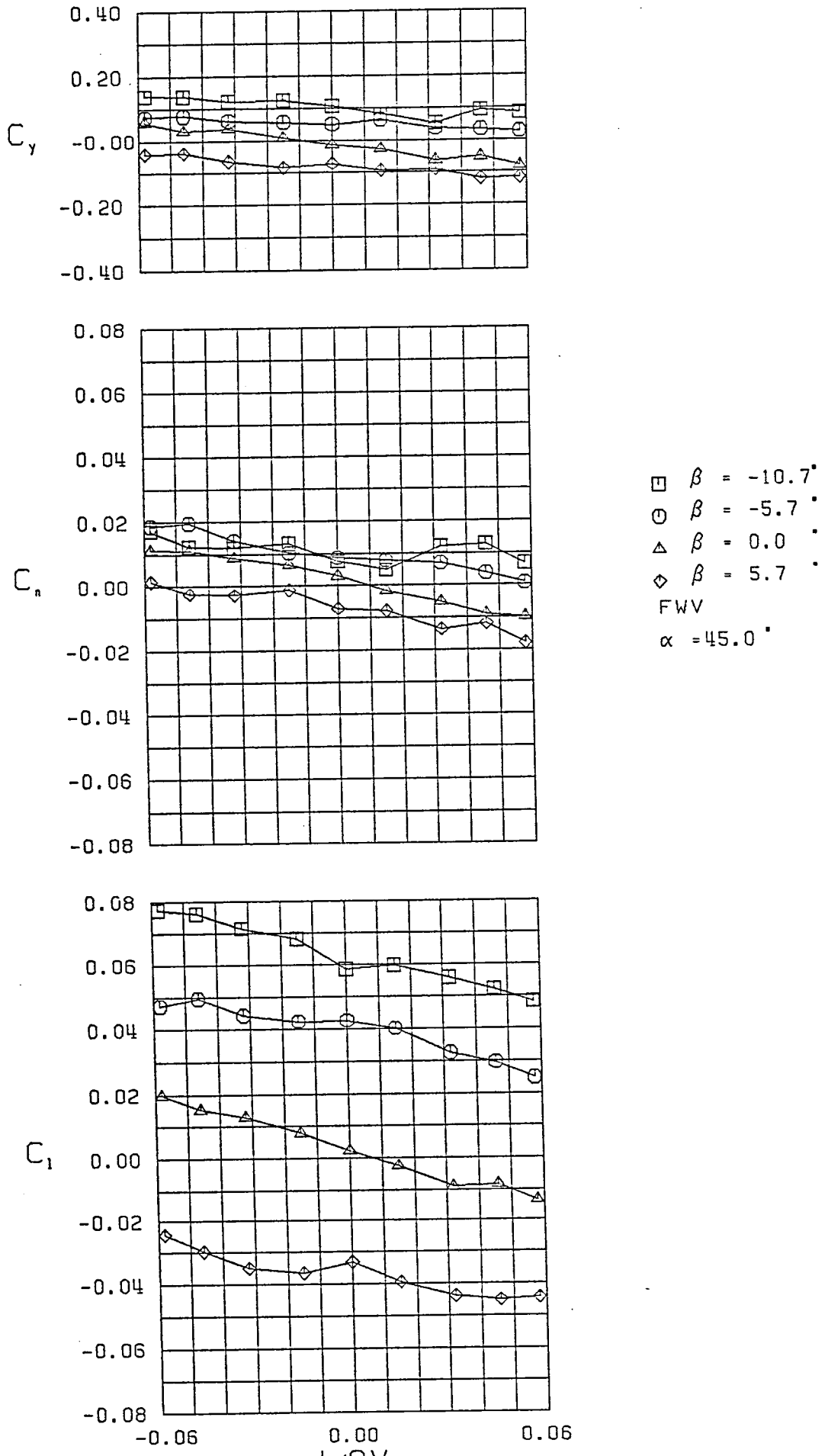

Figure 13 (Continued)

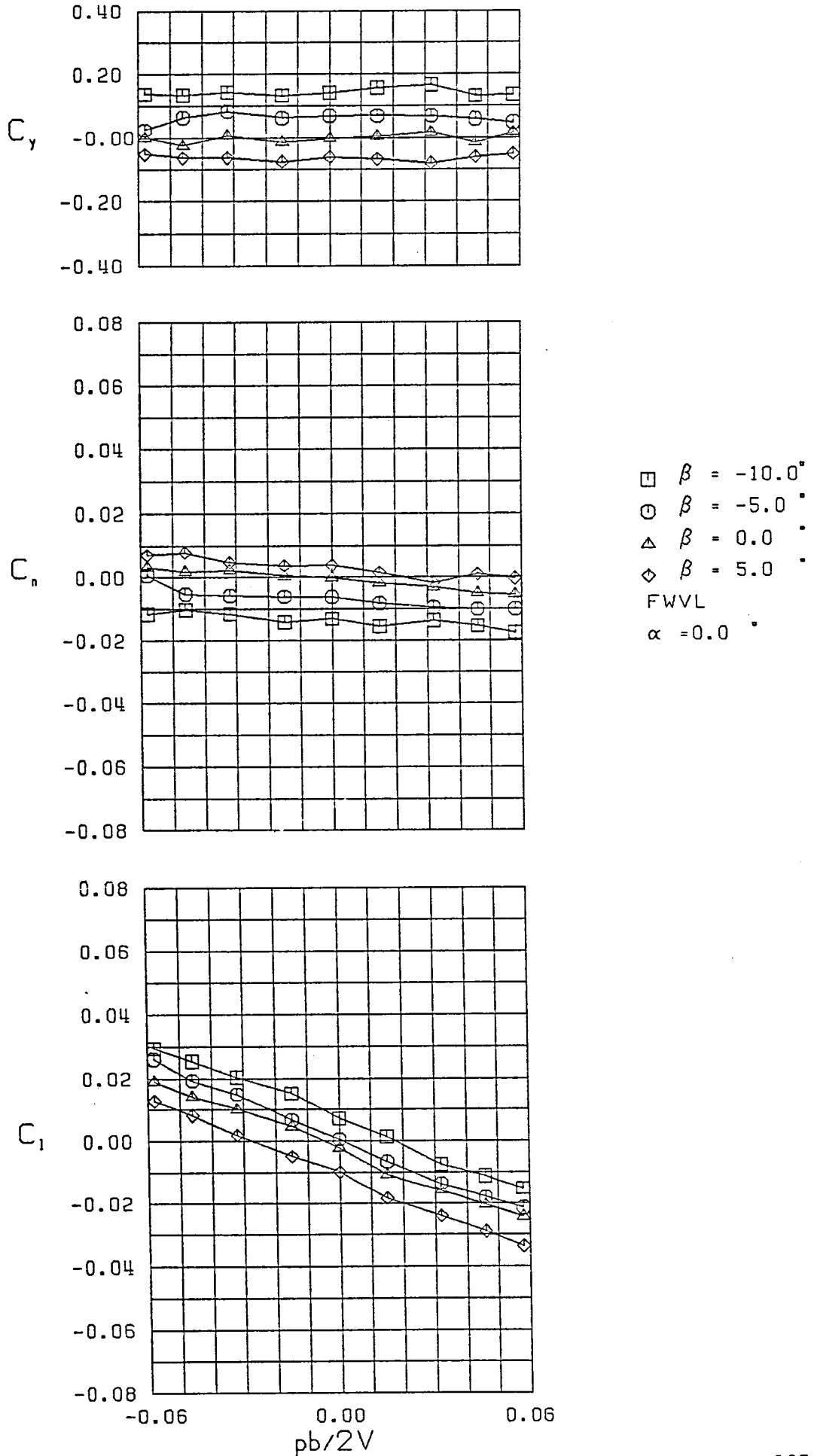

Figure 14 - Variation of Lateral-Directional Characteristics with Roll Rate-Configuration 10

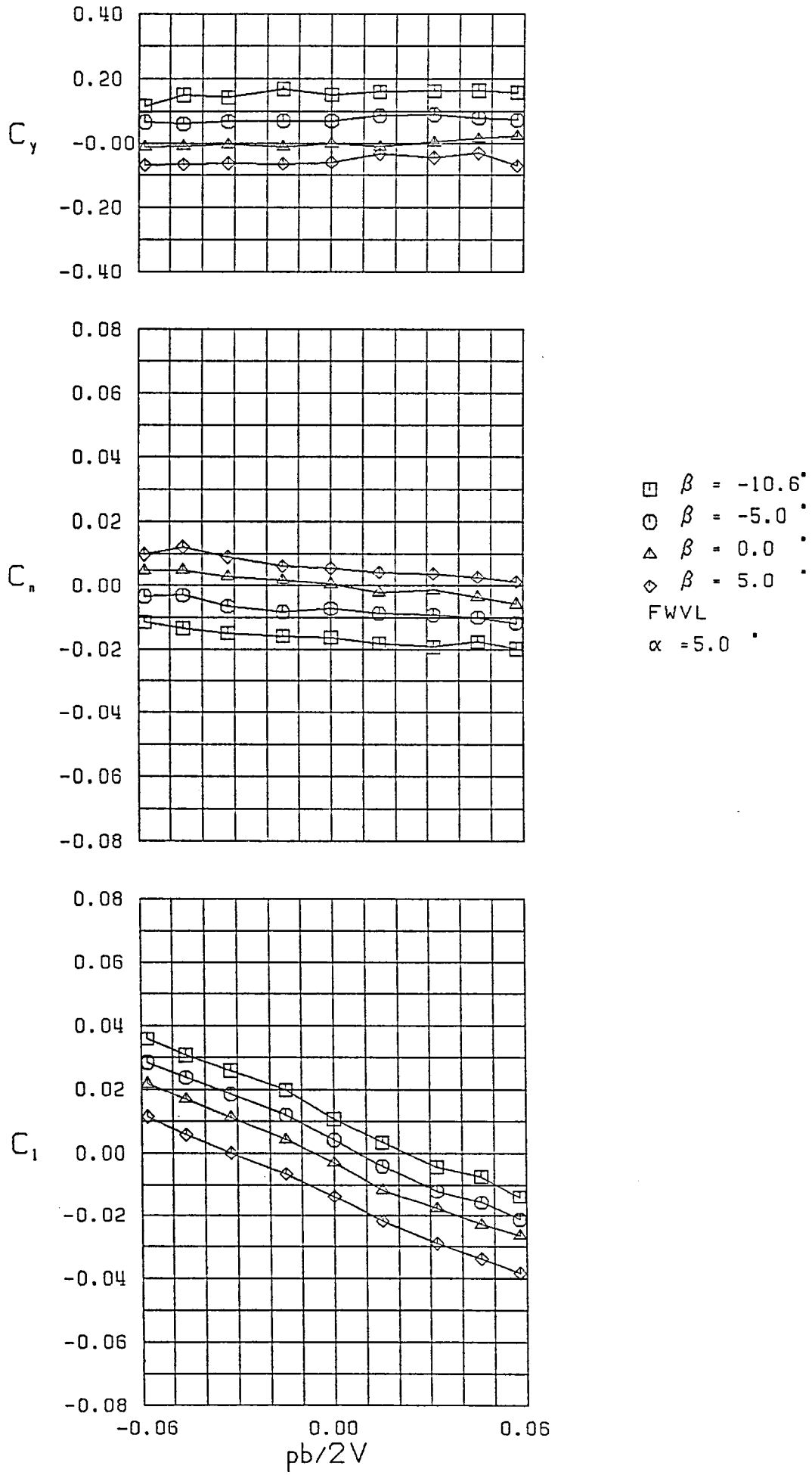

Figure 14 (Continued)

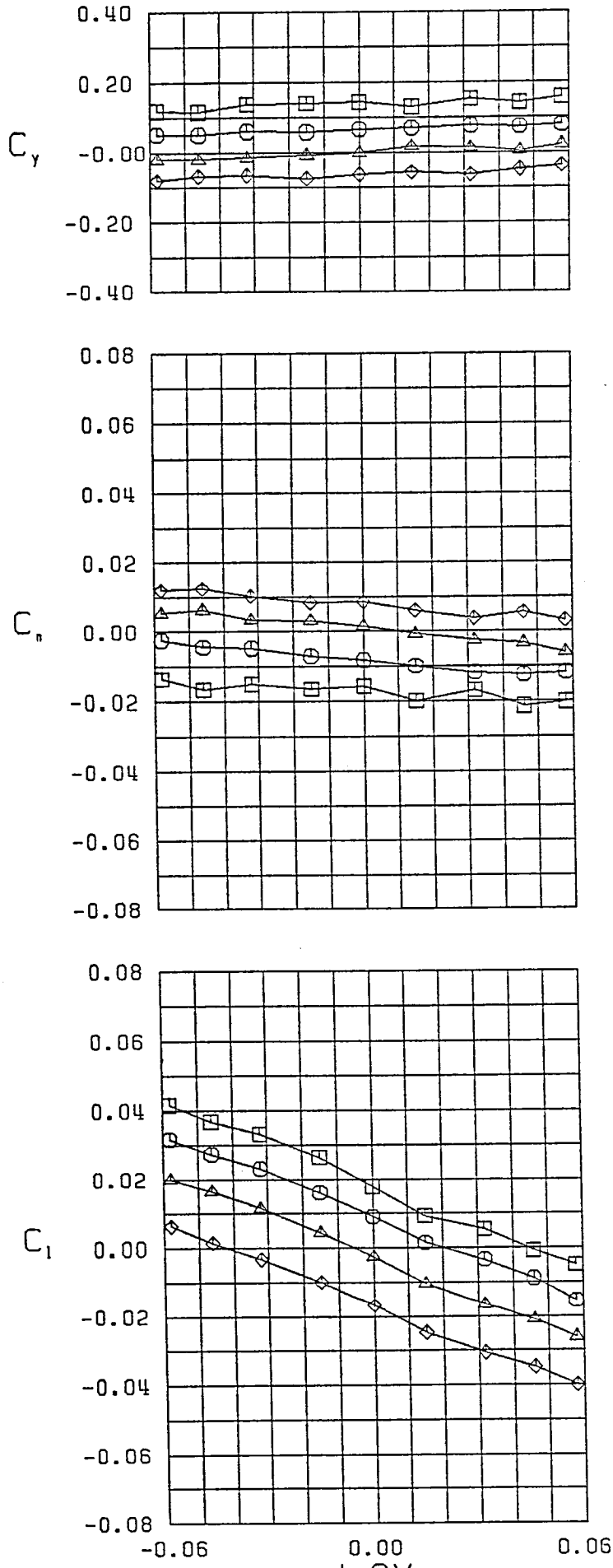

Figure 14 (Continued)

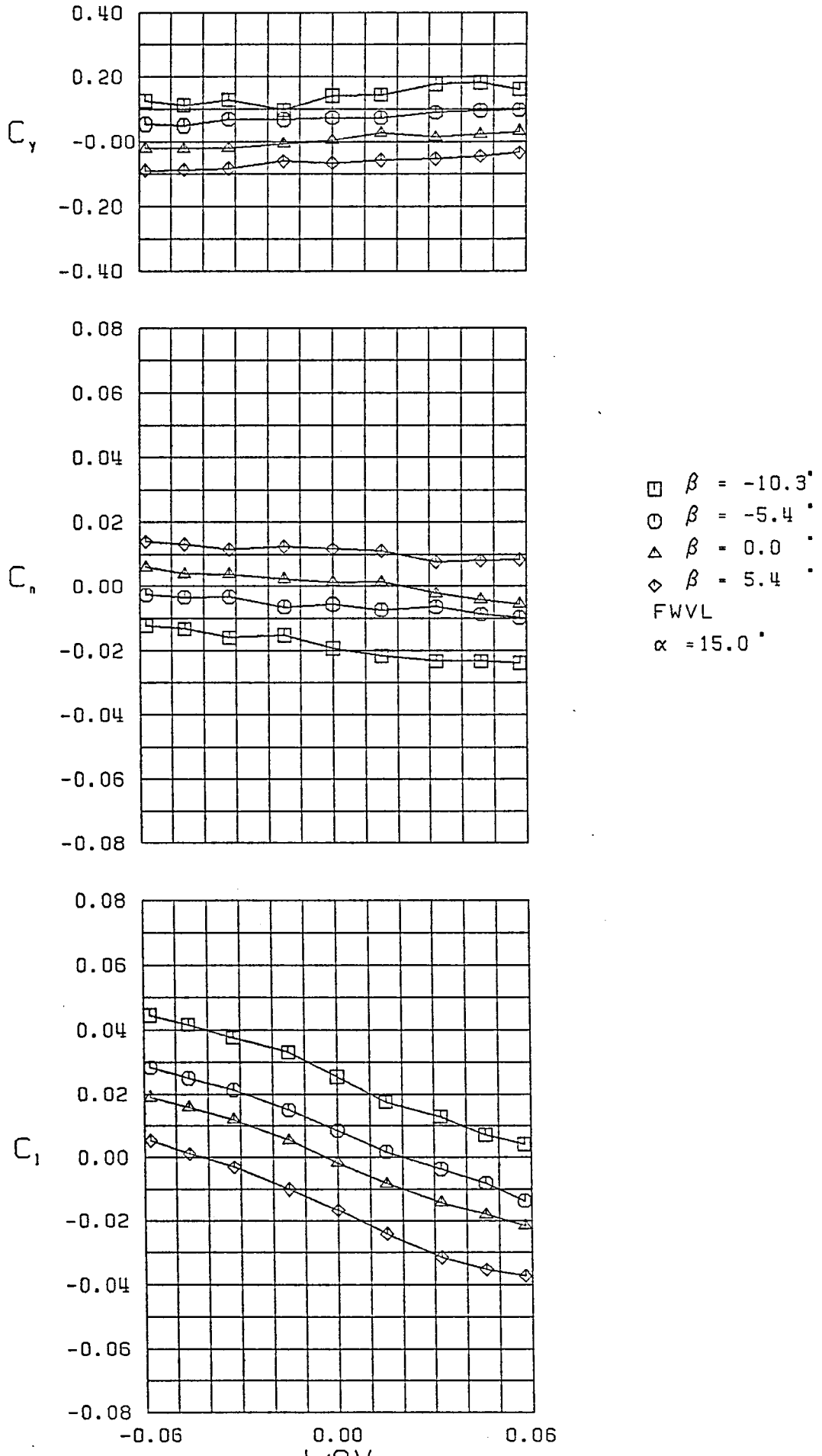

Figure 14 (Continued)

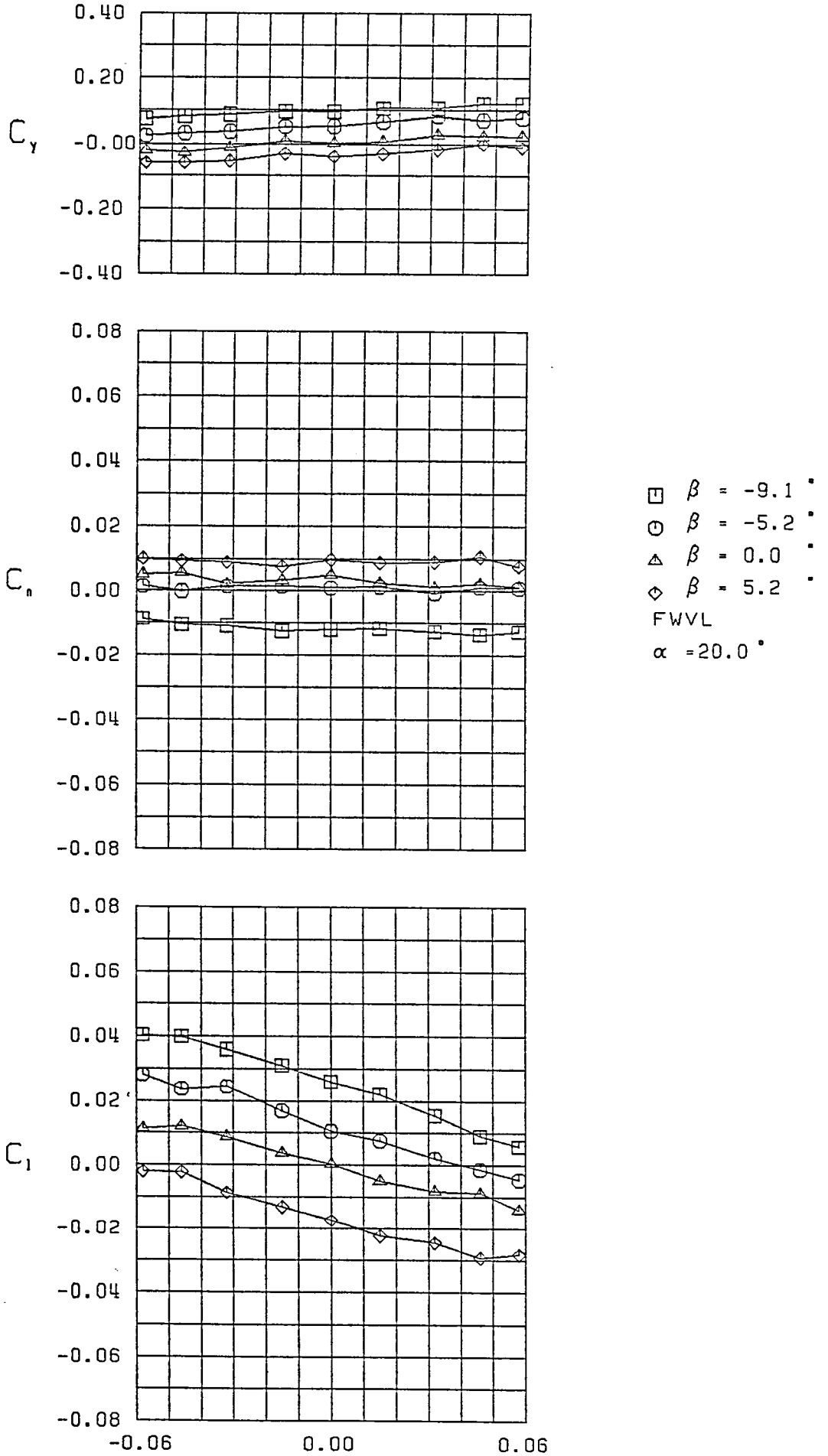

Figure 14 (Continued)

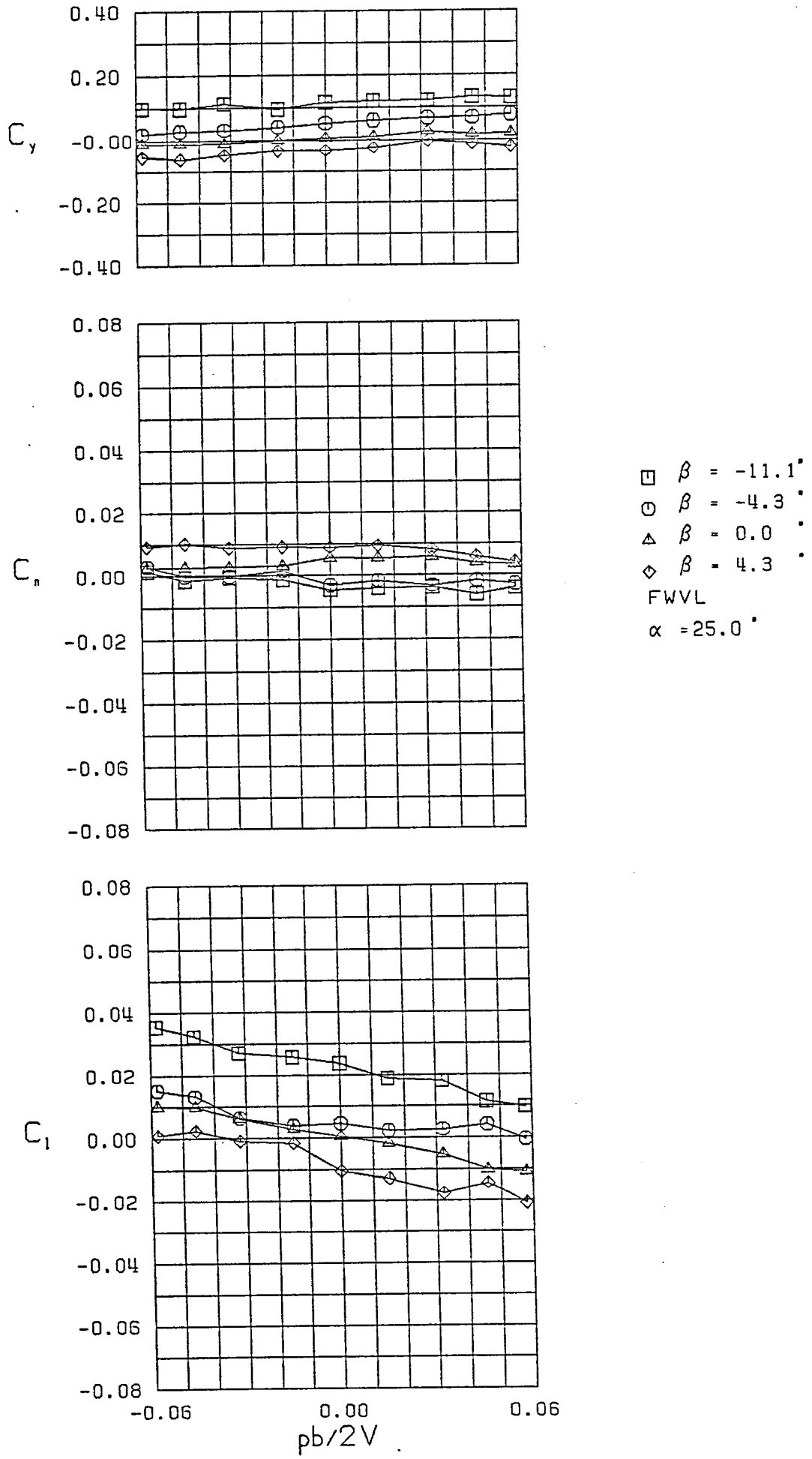

Figure 14 (Continued)

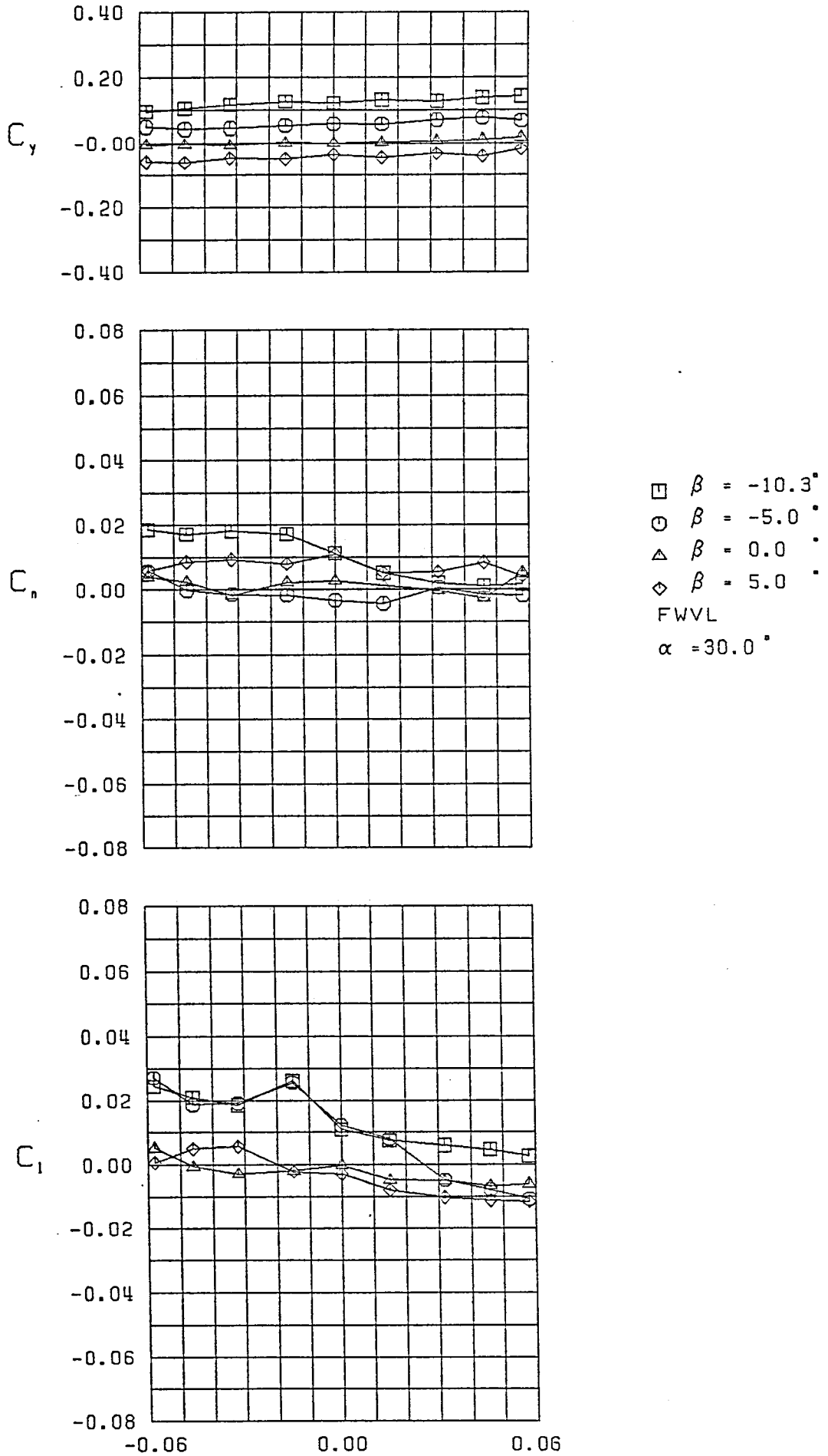

Figure 14 (Continued)

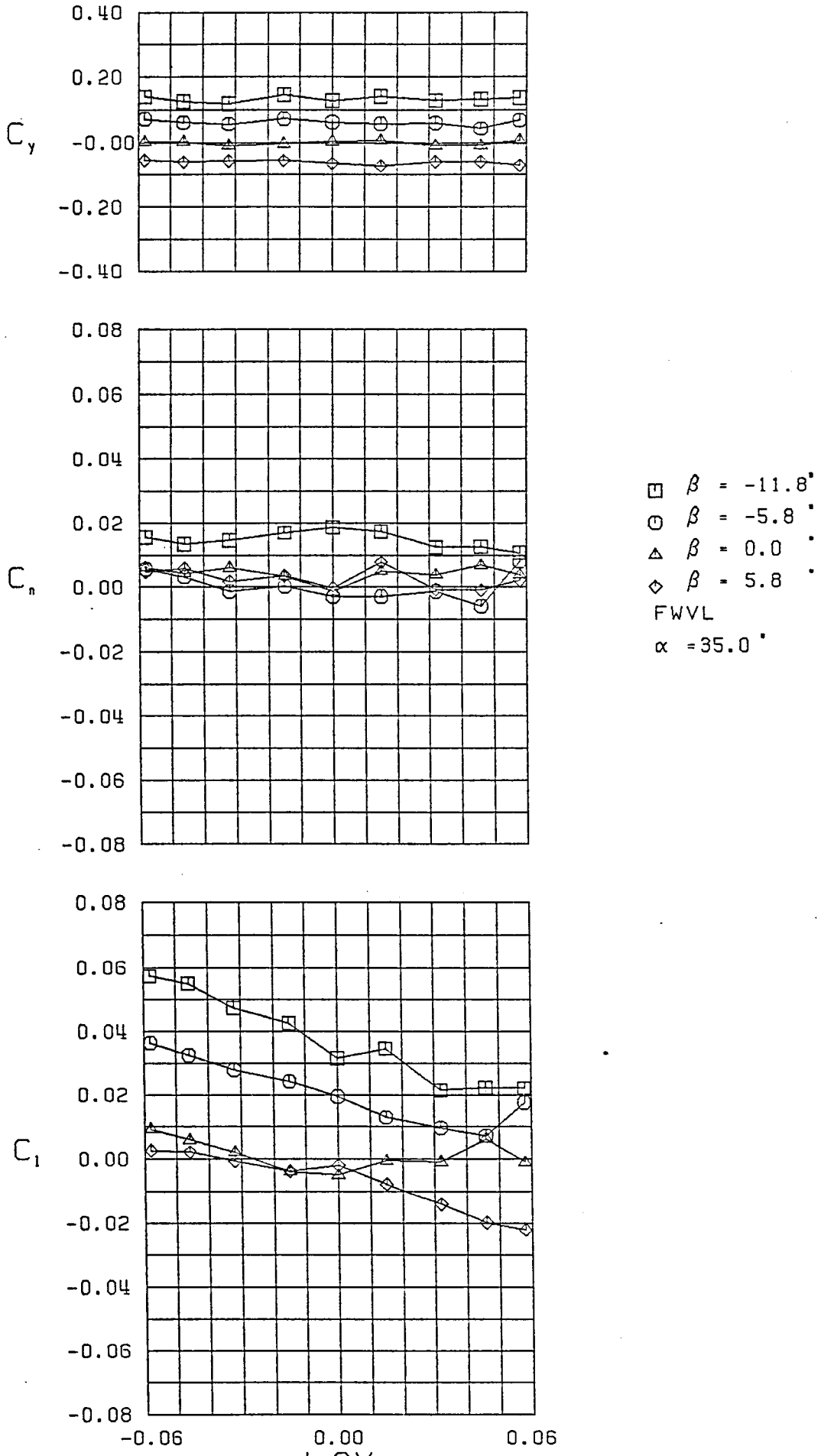

Figure 14 (Continued)

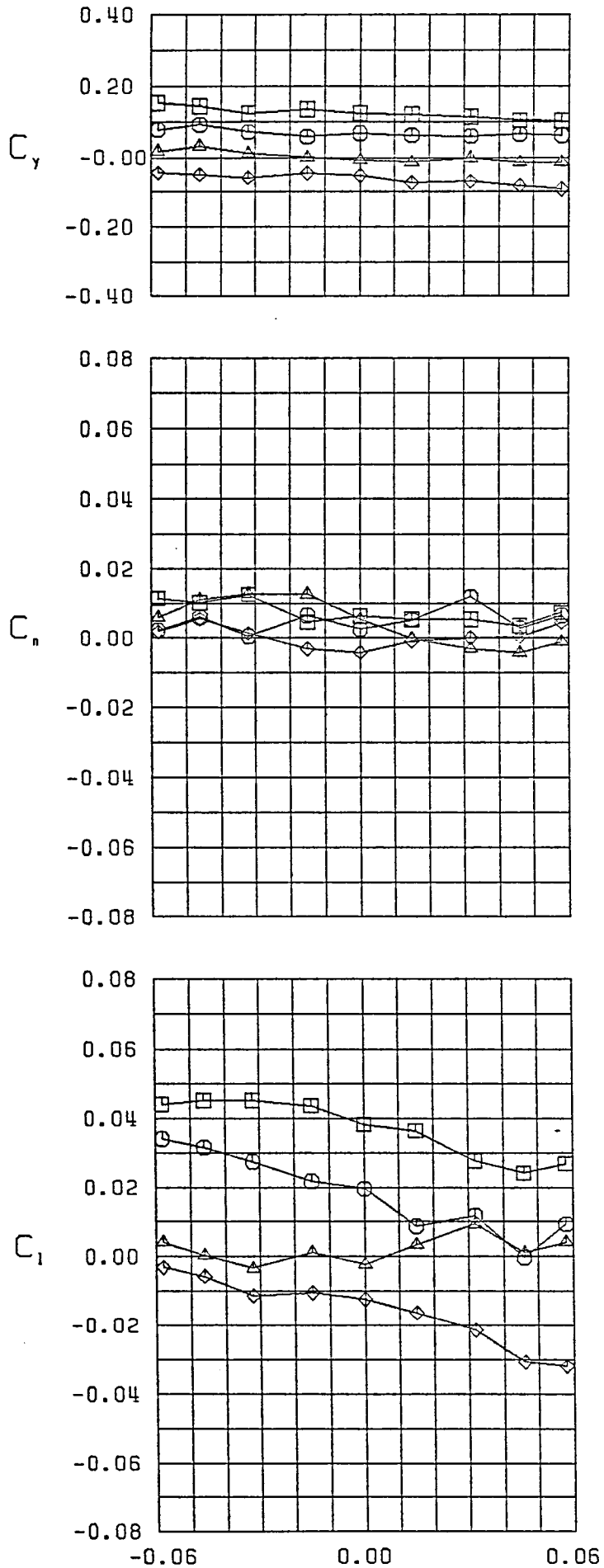

Figure 14 (Continued)

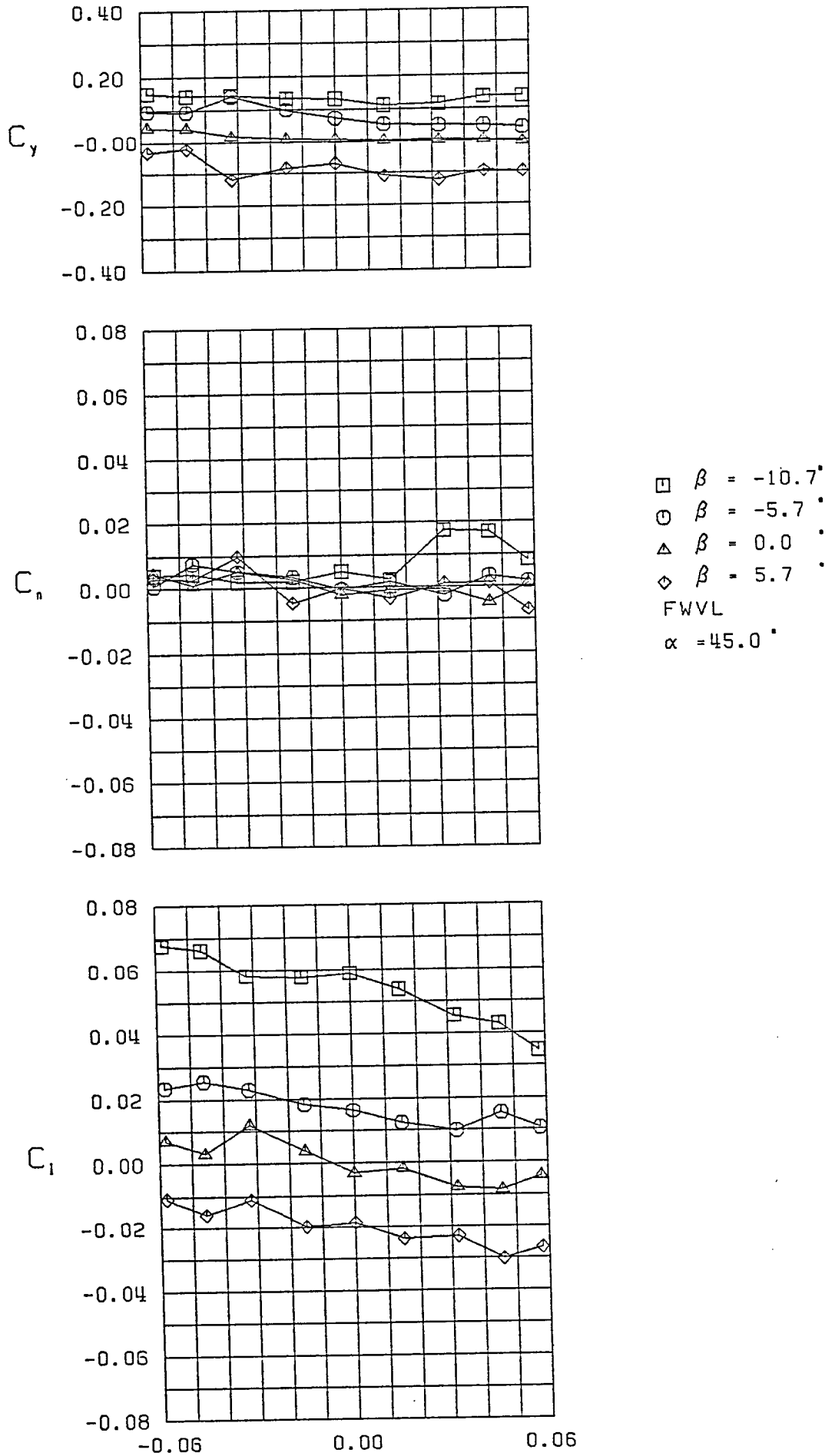

Figure 14 (Continued)

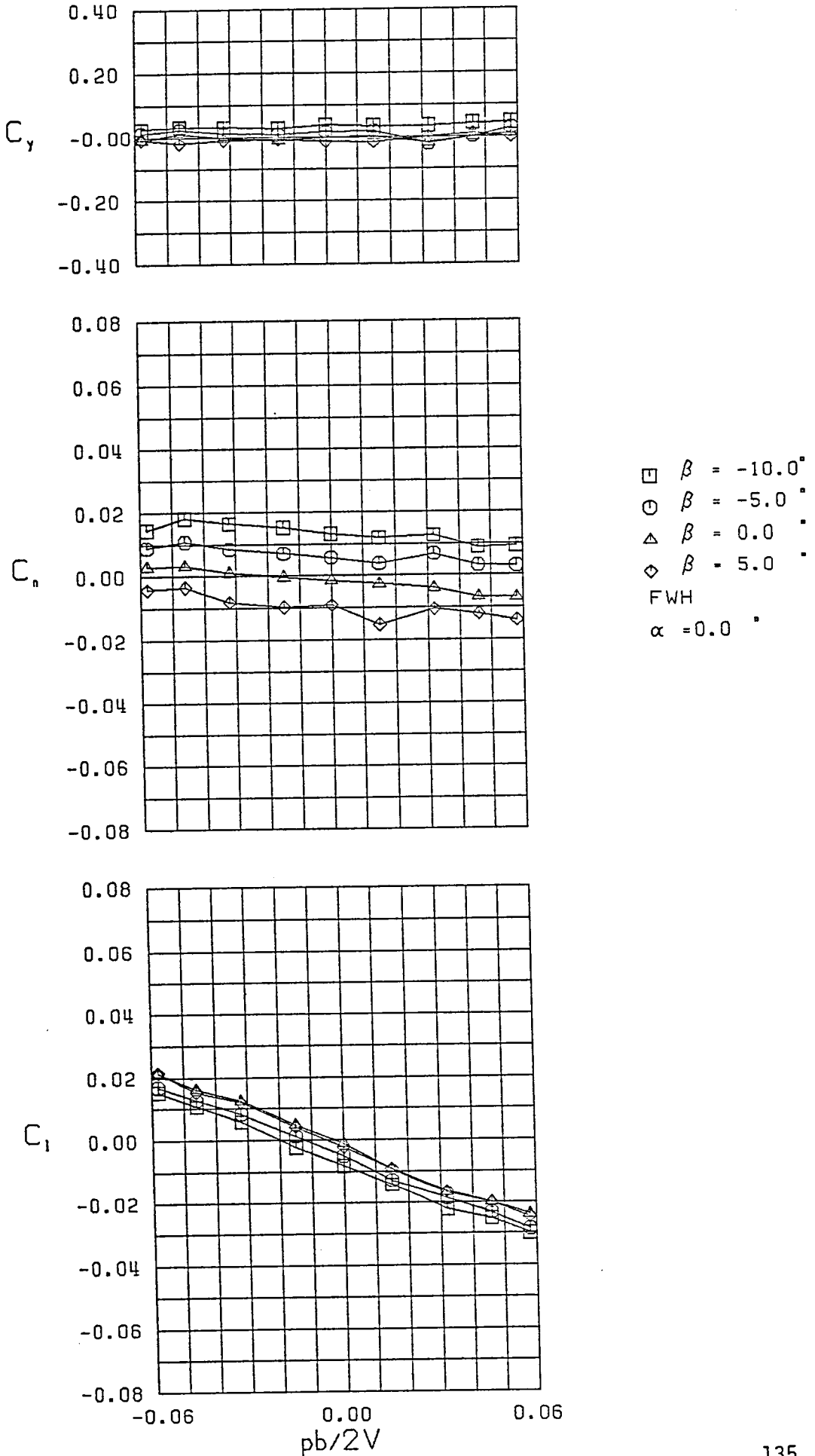

Figure 15 - Variation of Lateral-Directional Characteristics with Roll Rate-Configuration 11

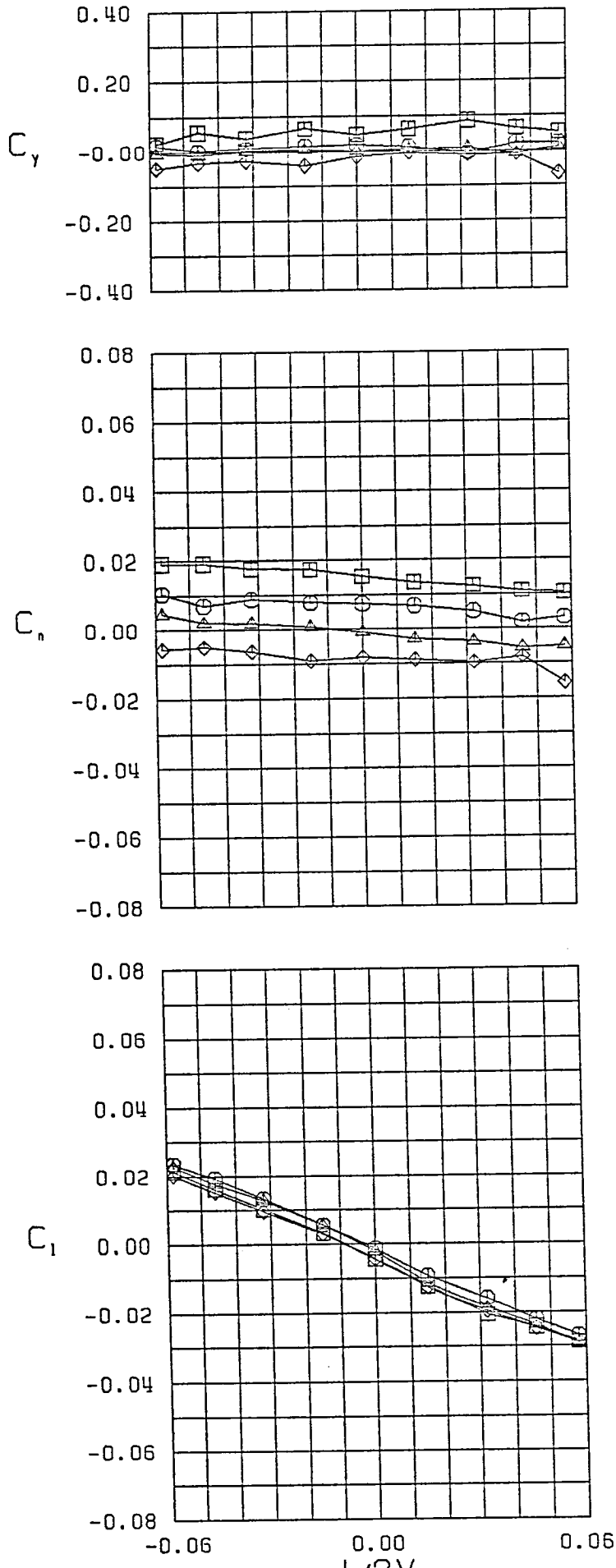

Figure 15 (Continued)

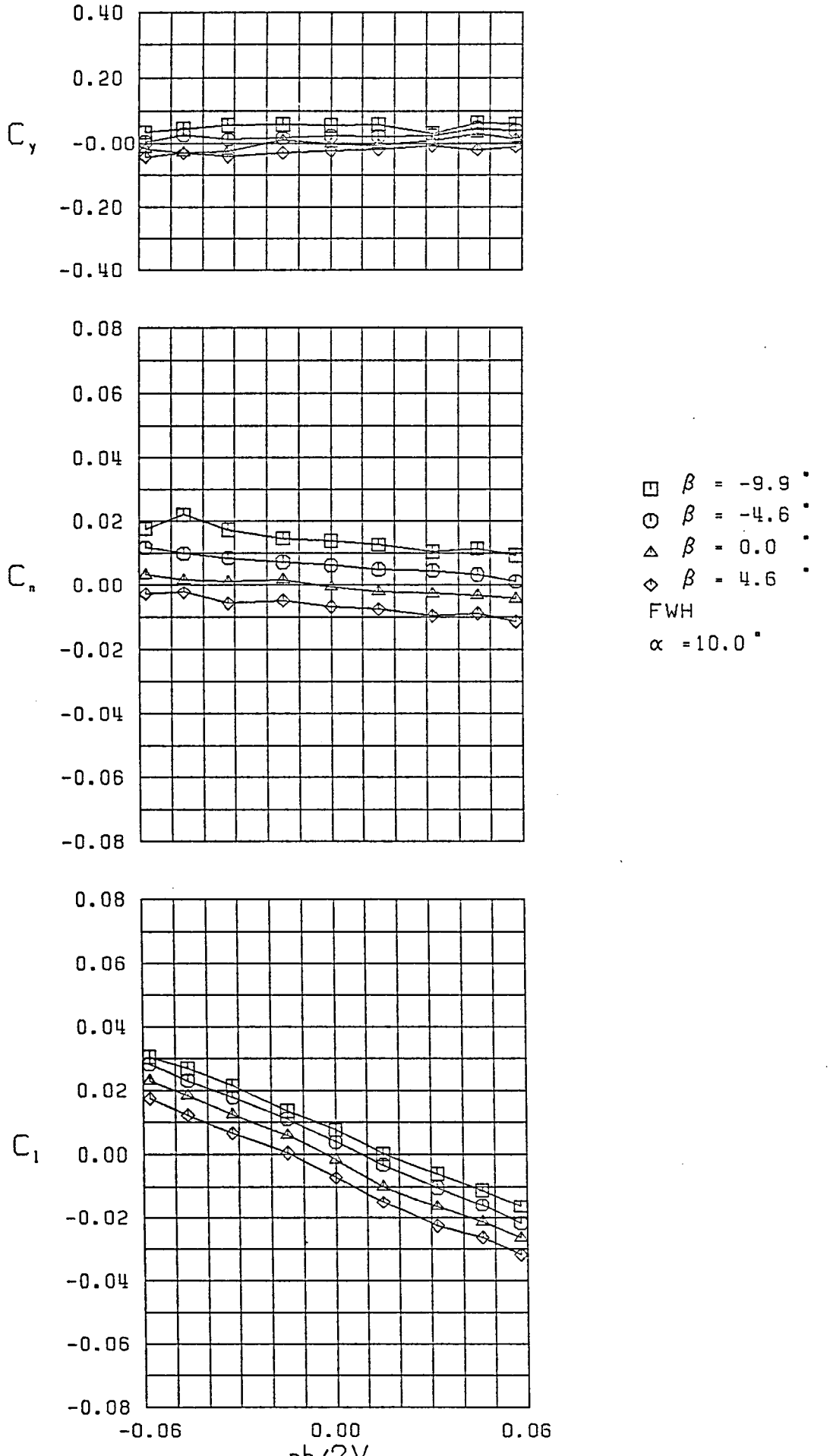

Figure 15 (Continued)

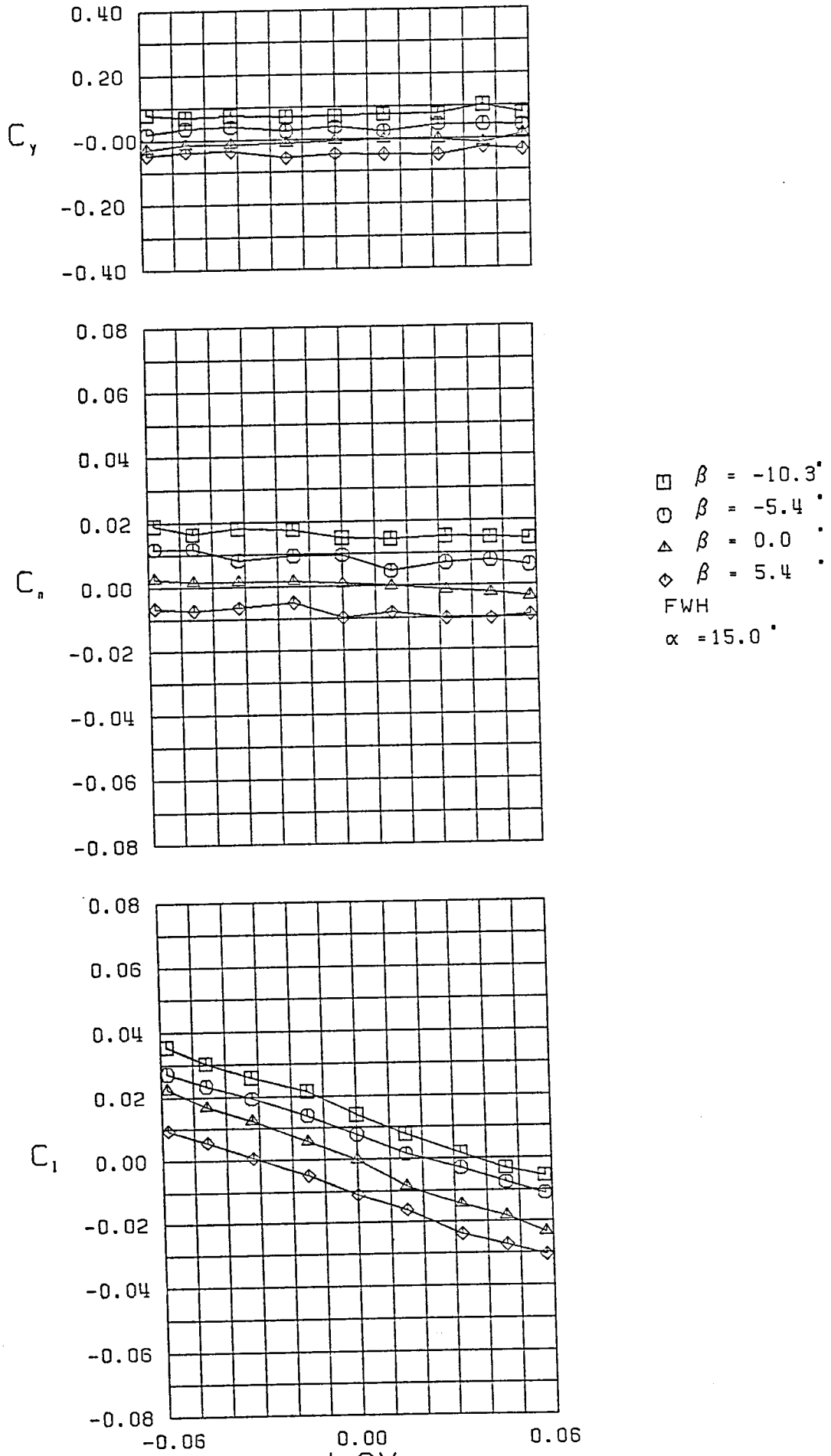

Figure 15 (Continued)

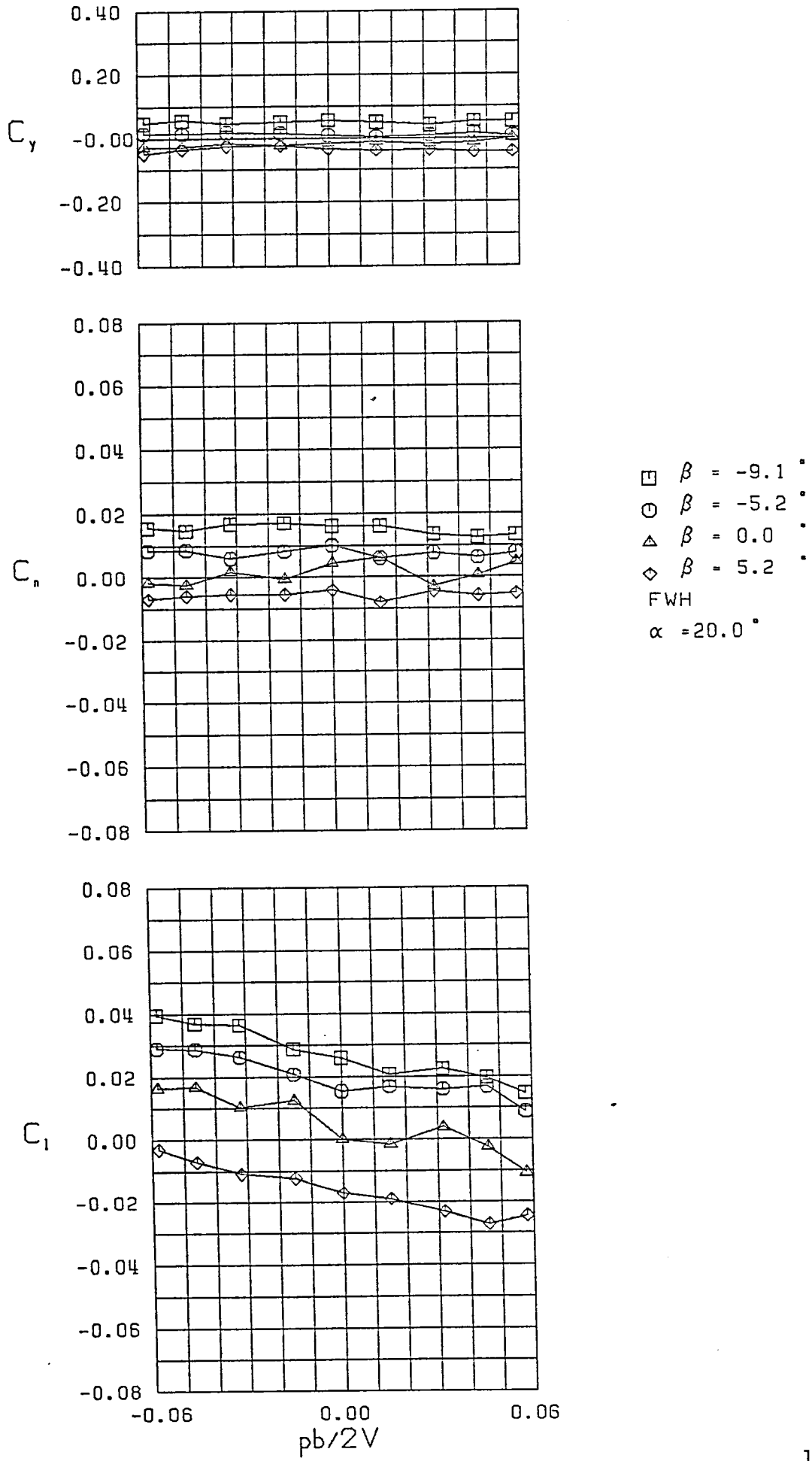

Figure 15 (Continued)

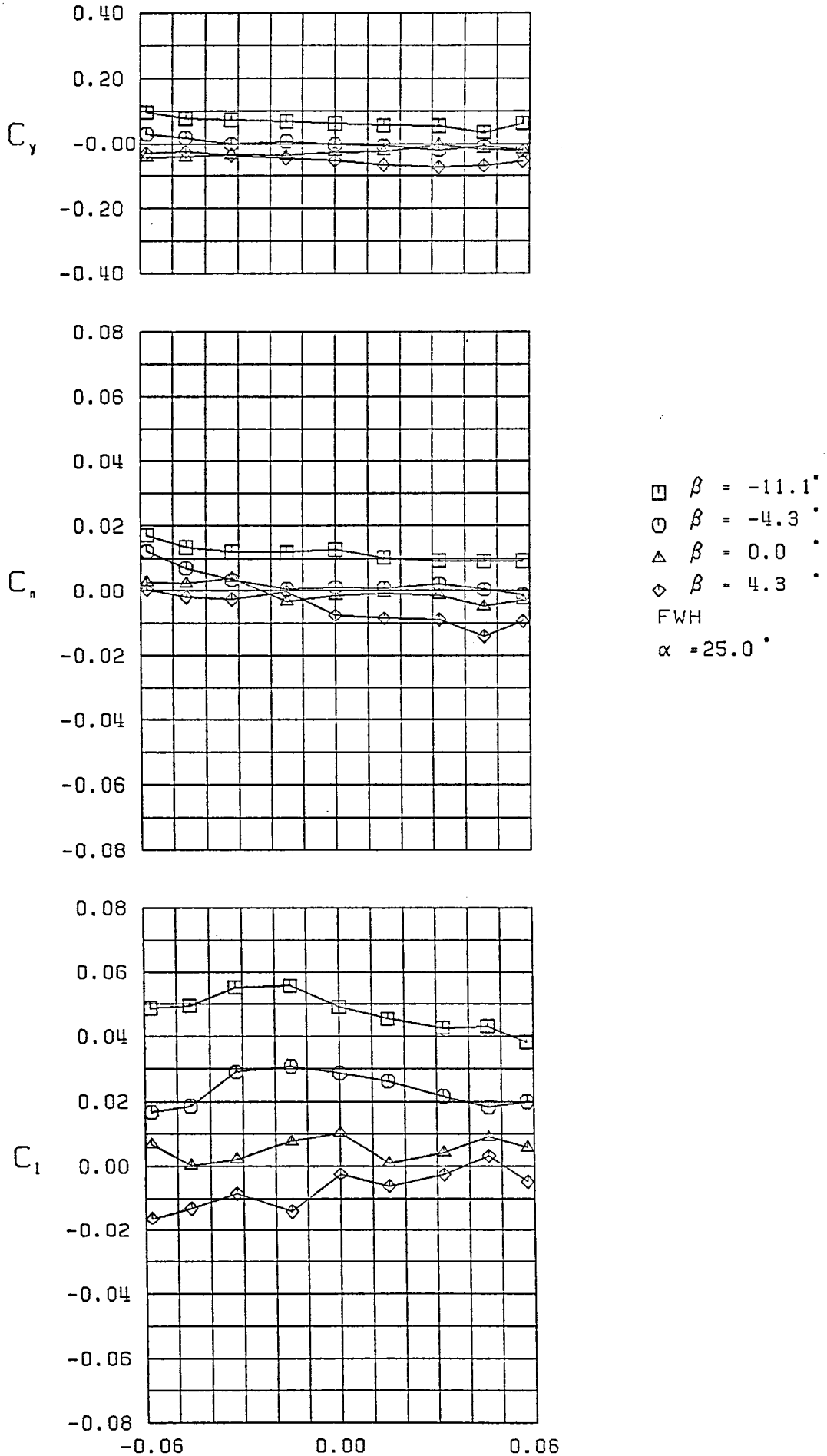

Figure 15 (Continued)

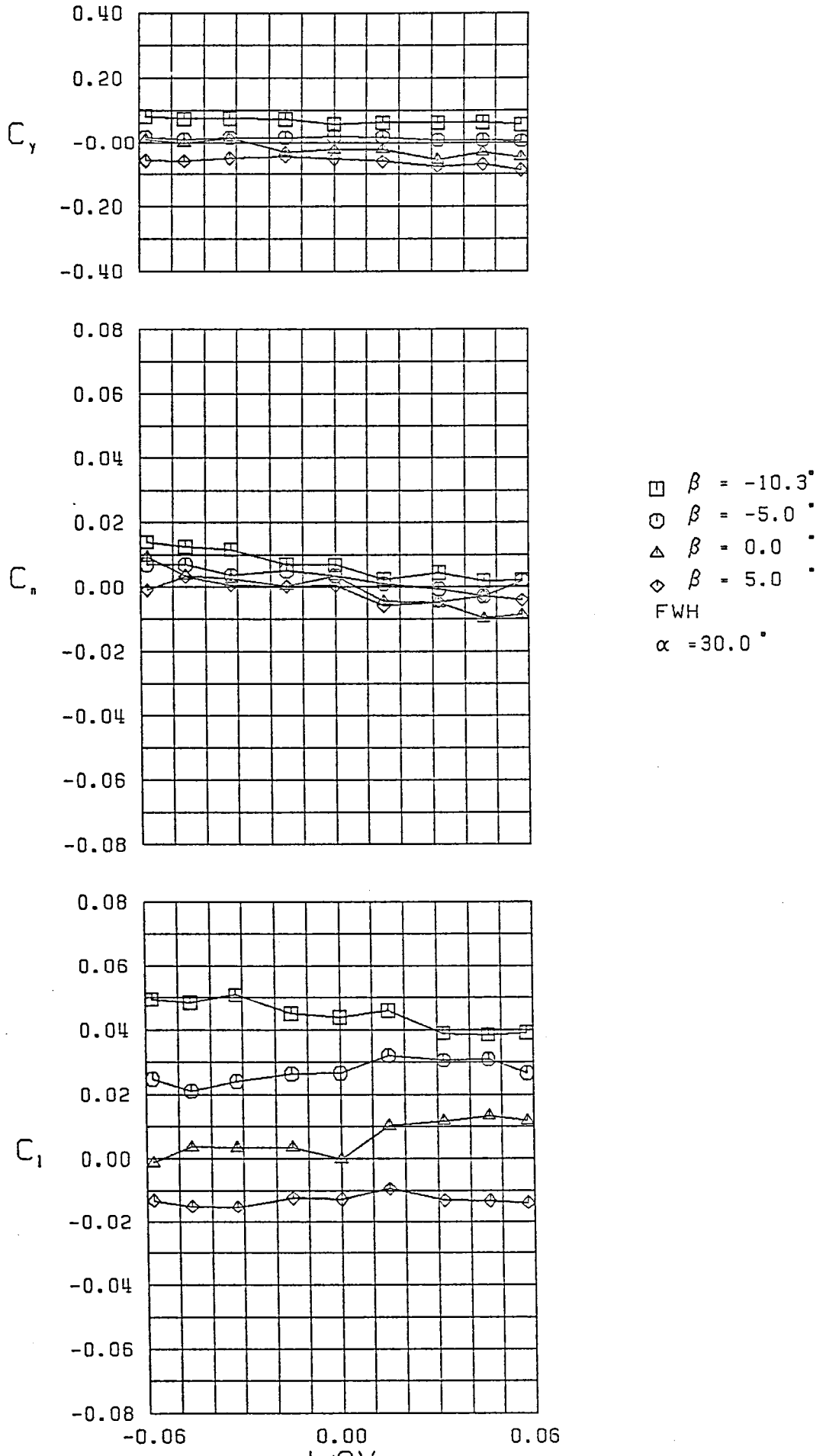

Figure 15 (Continued)

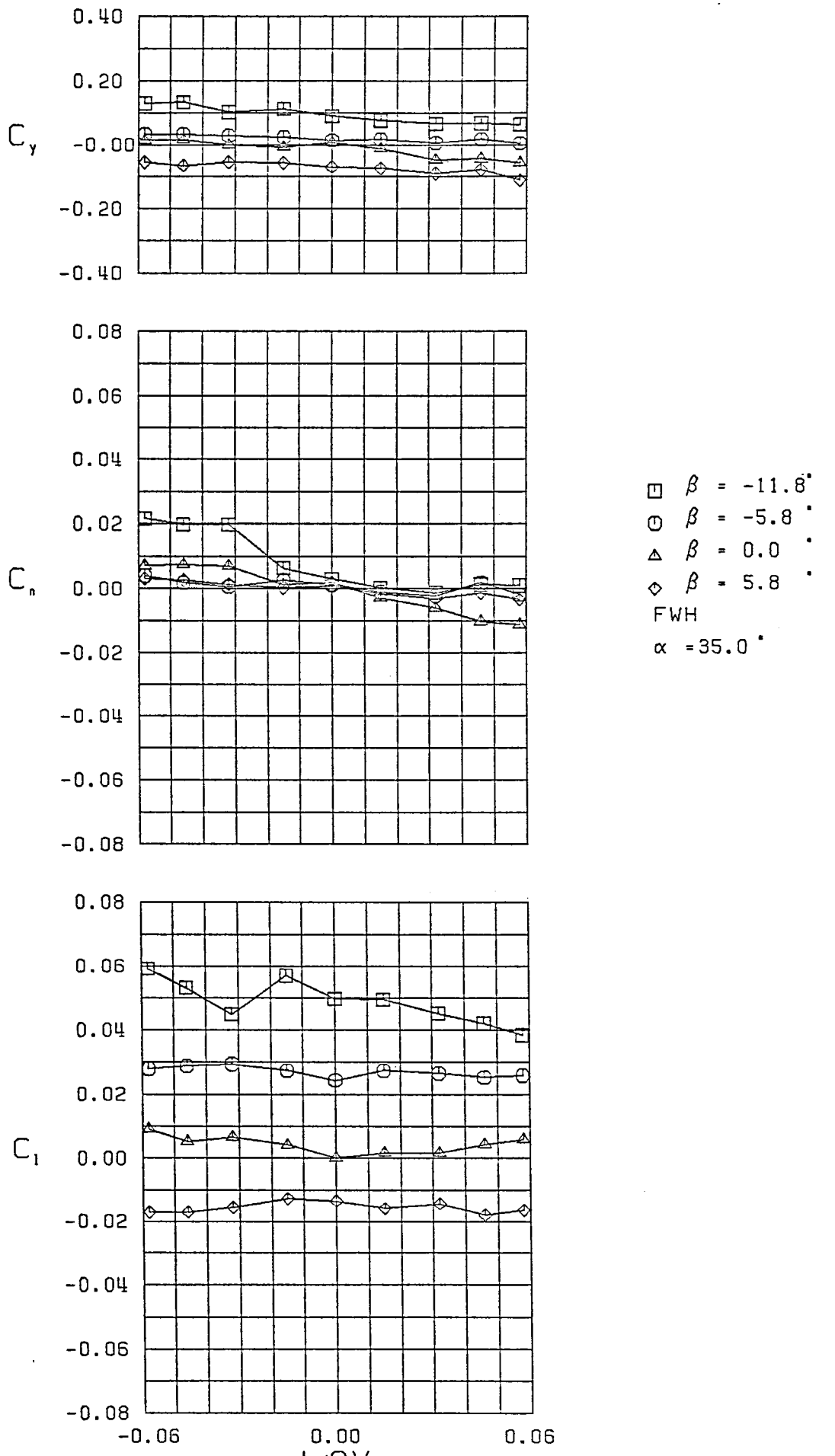

Figure 15 (Continued)

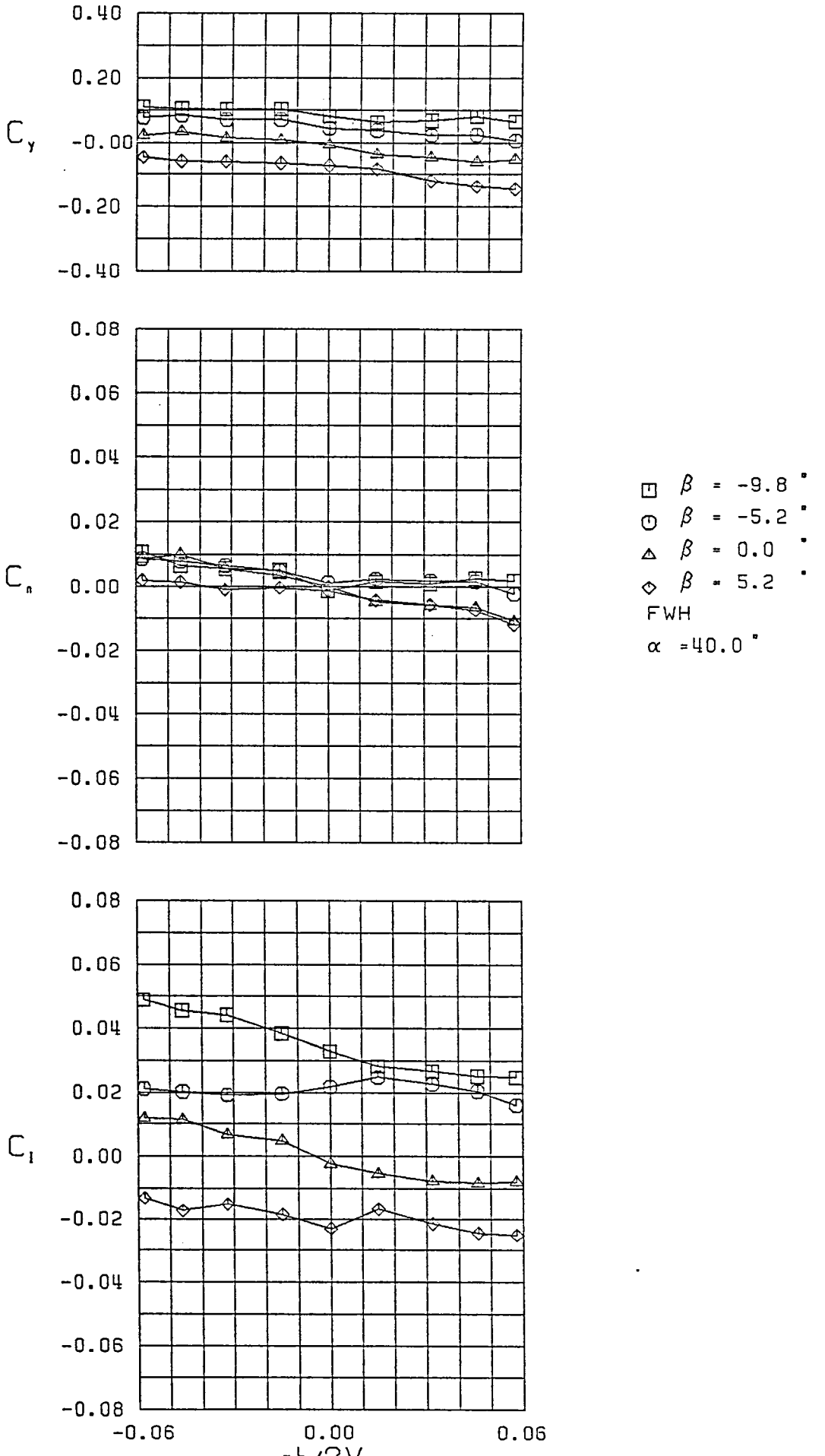

Figure 15 (Continued)

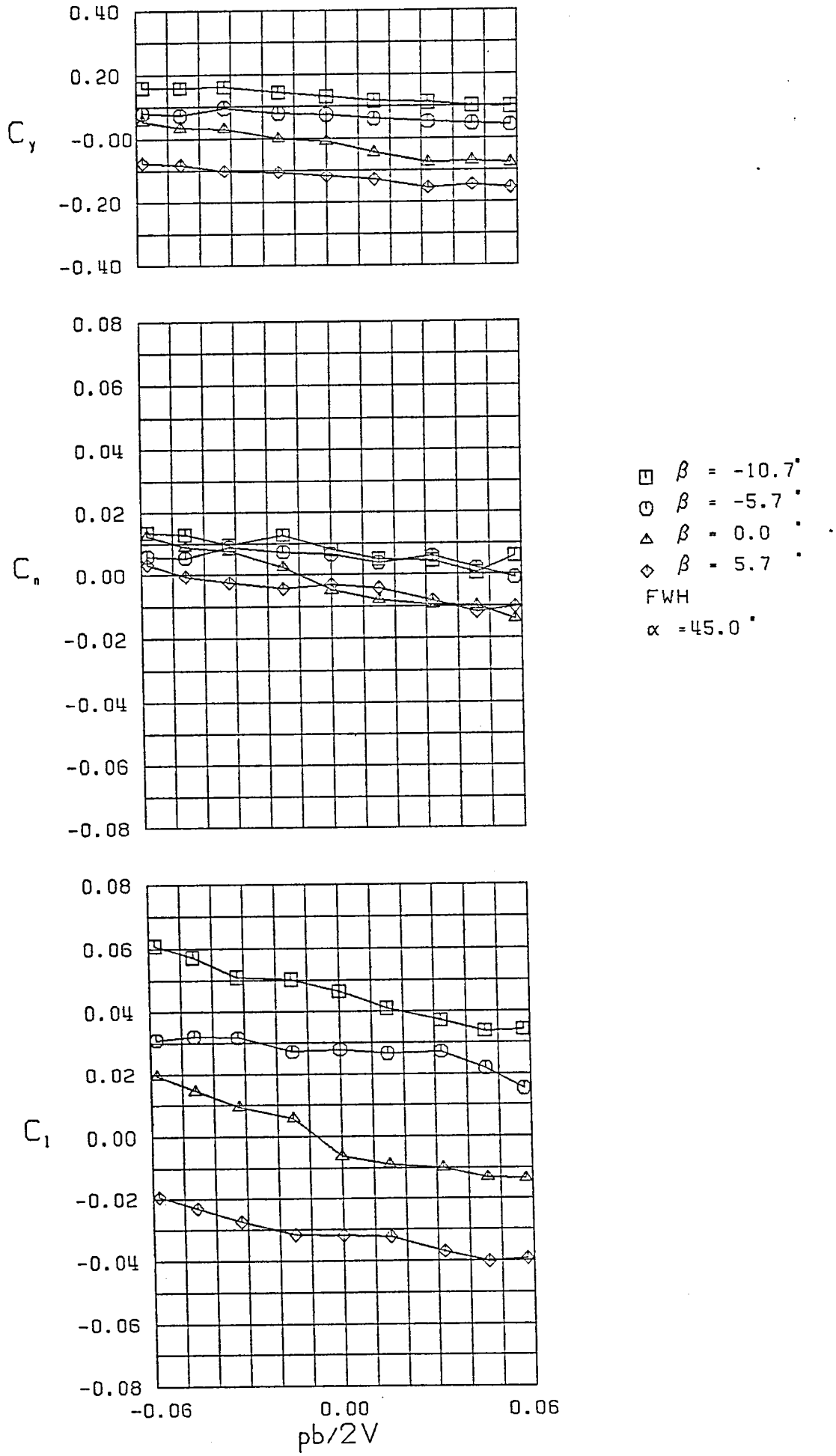

Figure 15 (Continued)

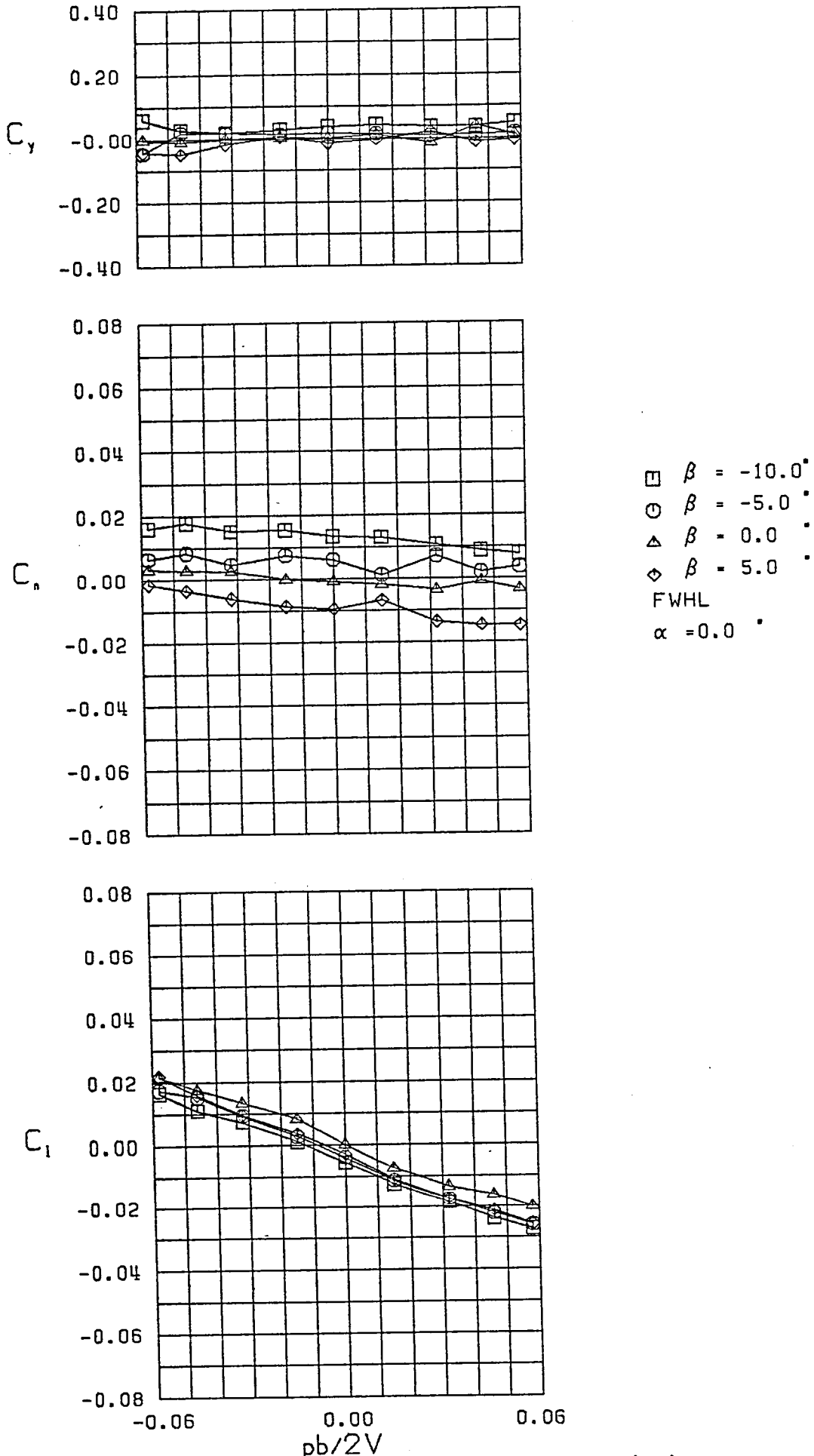

Figure 16 - Variation of Lateral-Directional Characteristics with Roll Rate-Configuration 9

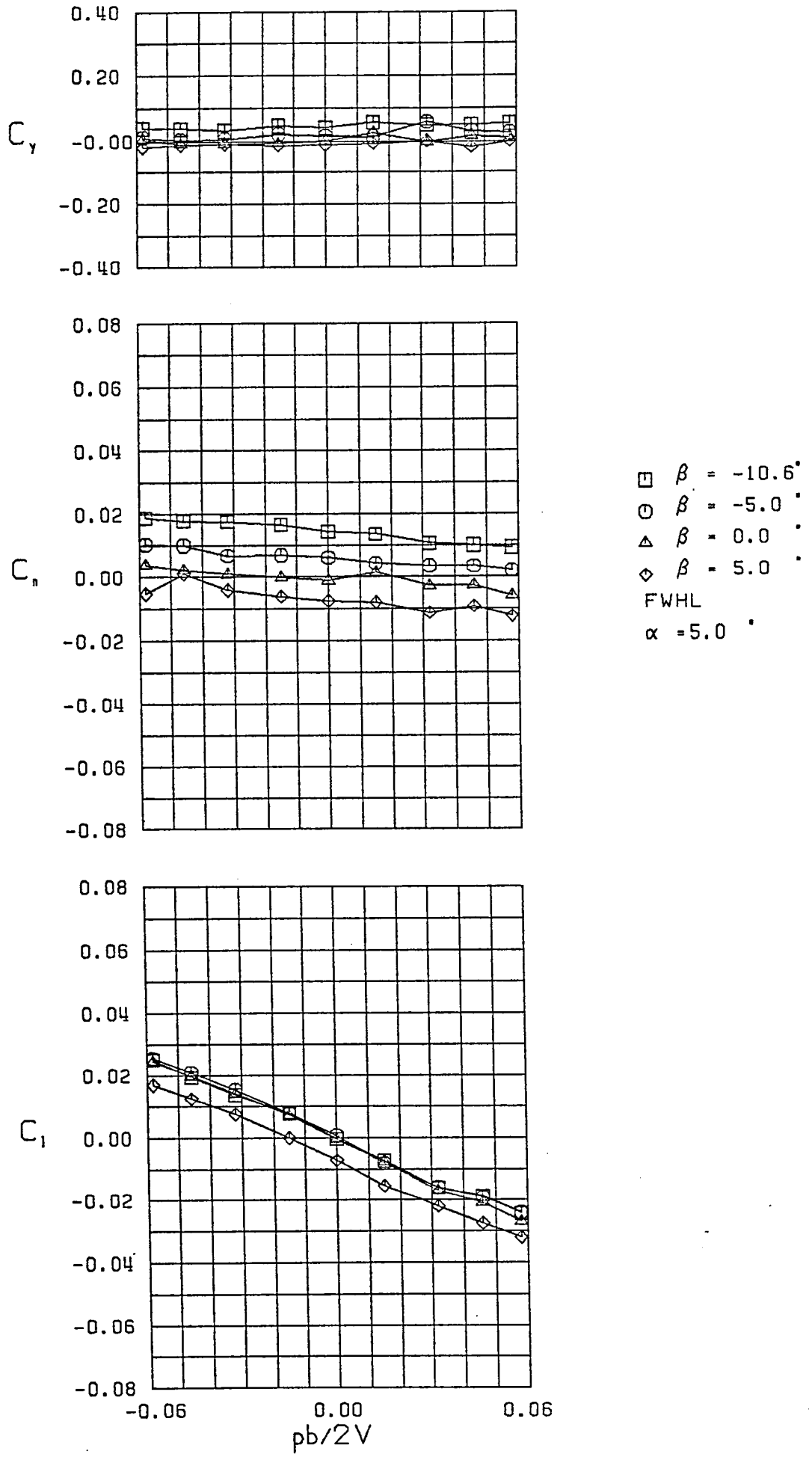

Figure 16 (Continued)

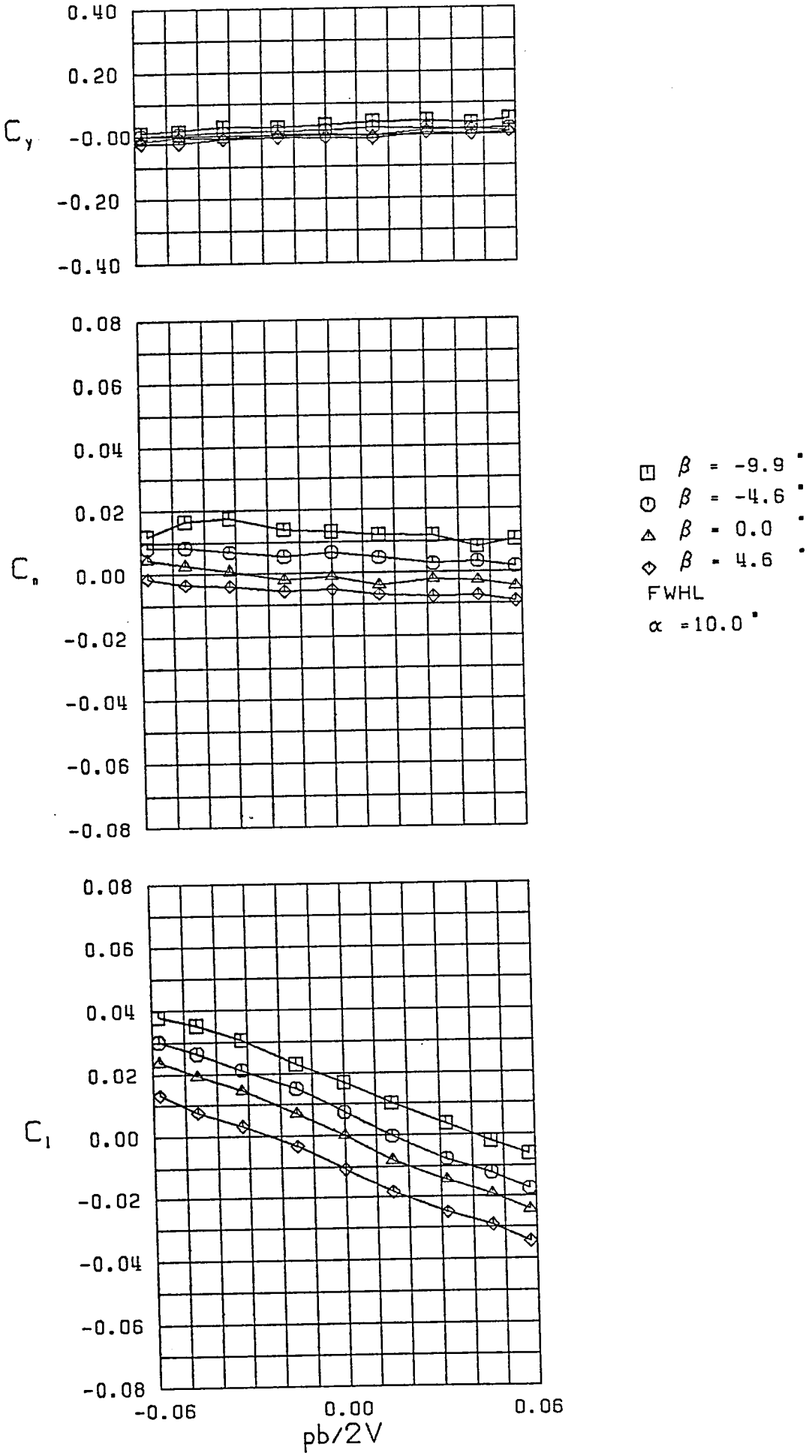

Figure 16 (Continued)

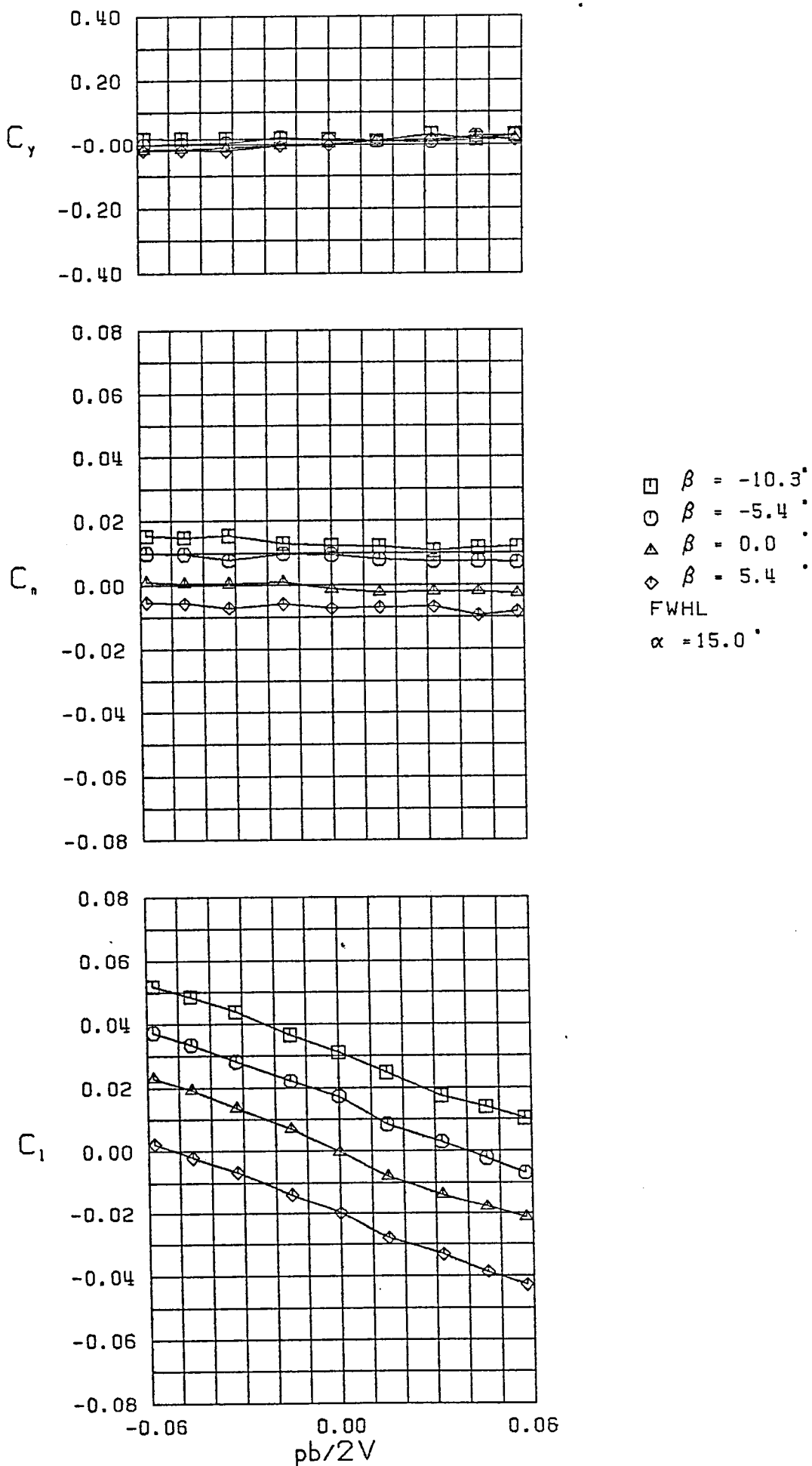

Figure 16 (Continued)

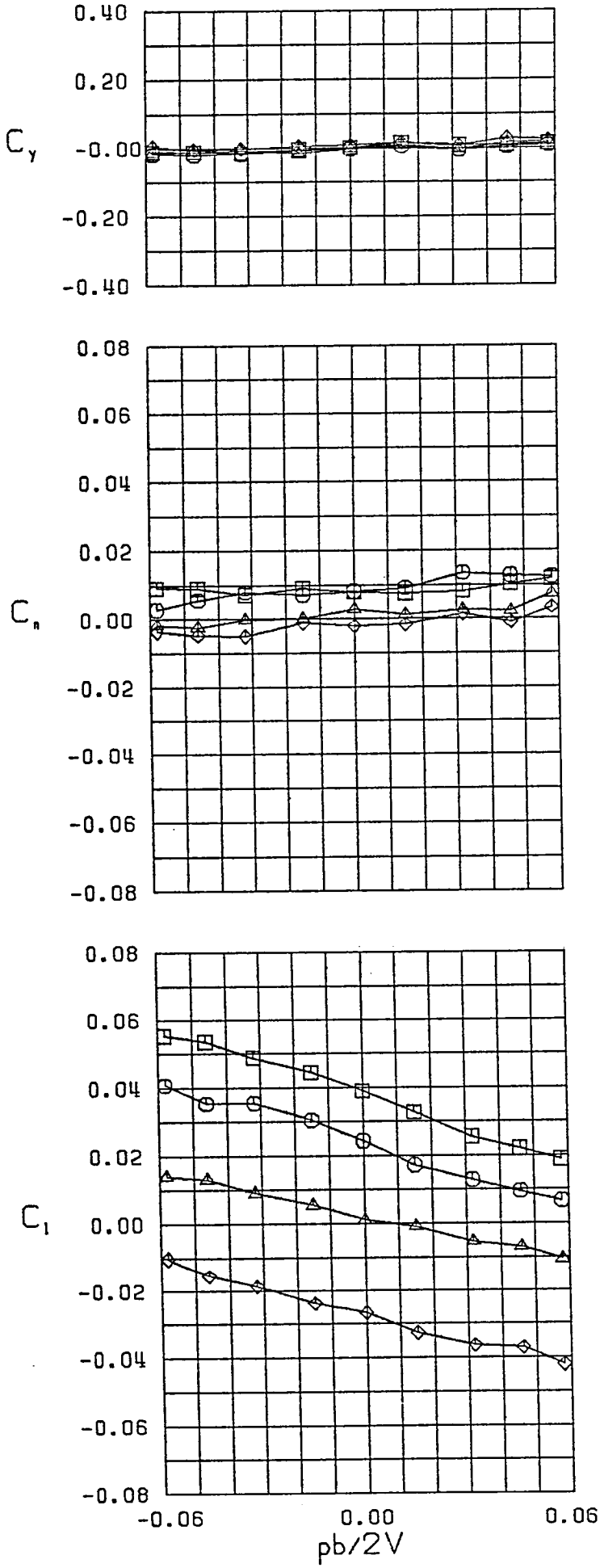

Figure 16 (Continued)

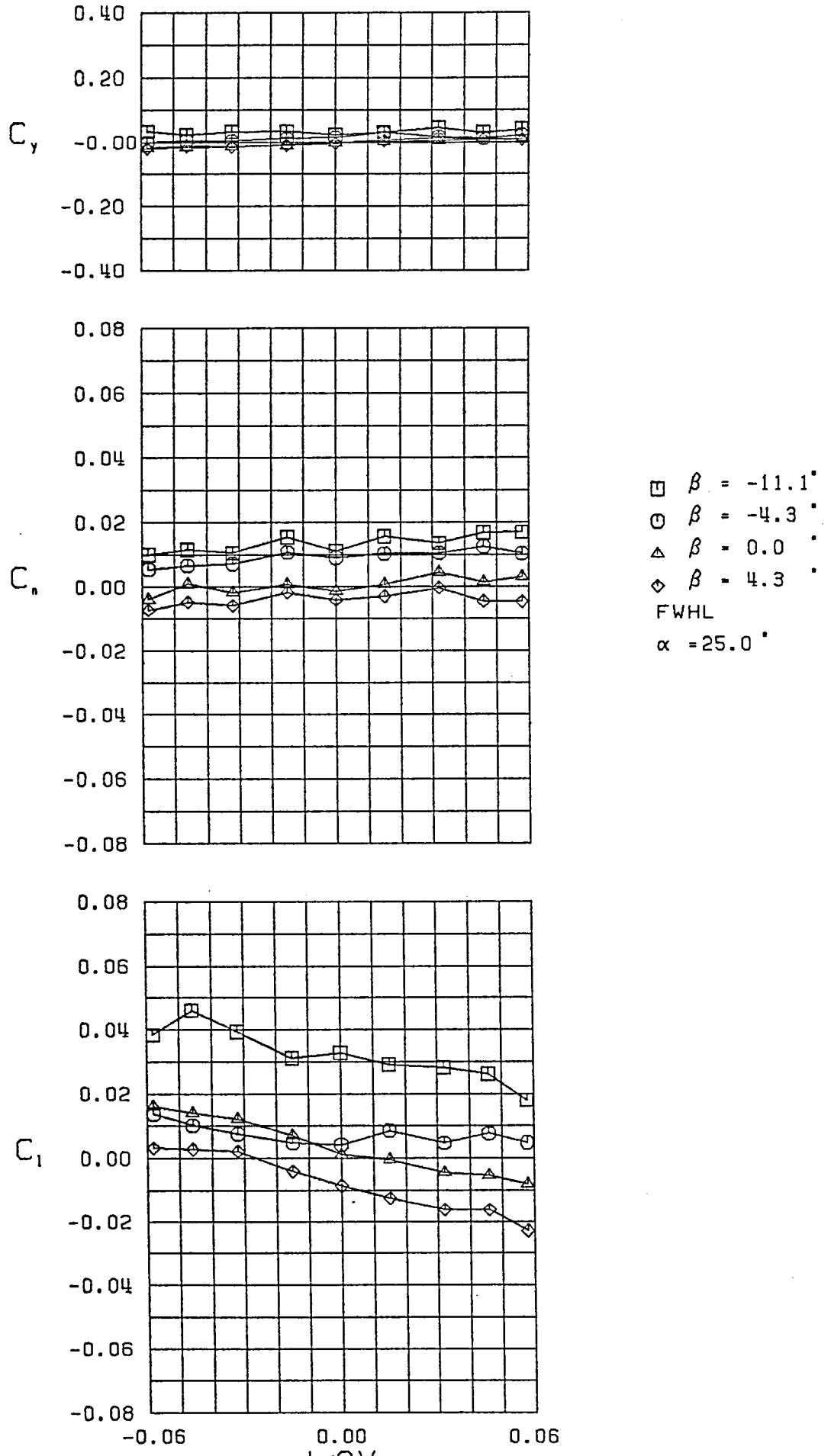

Figure 16 (Continued)

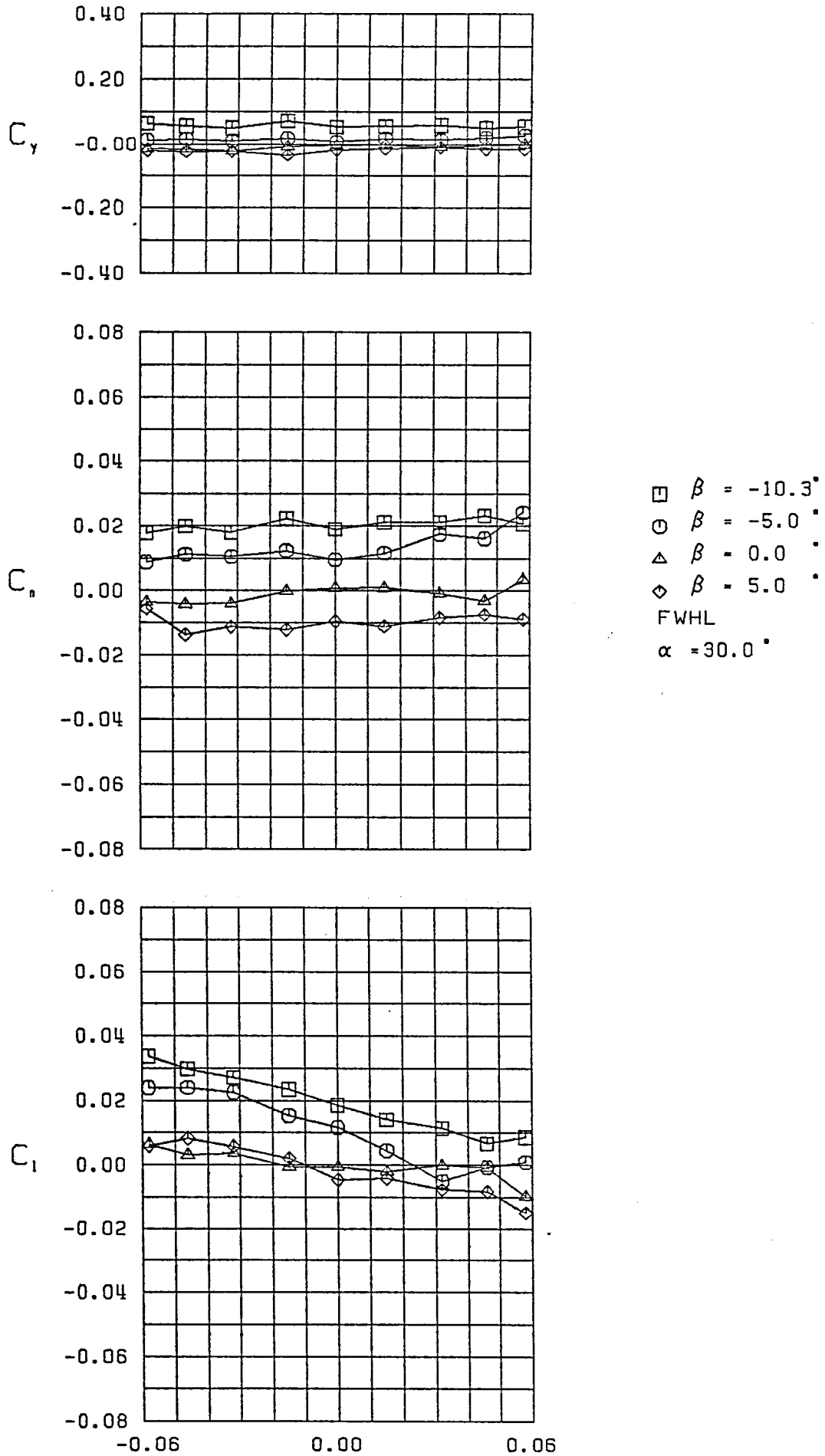

Figure 16 (Continued)

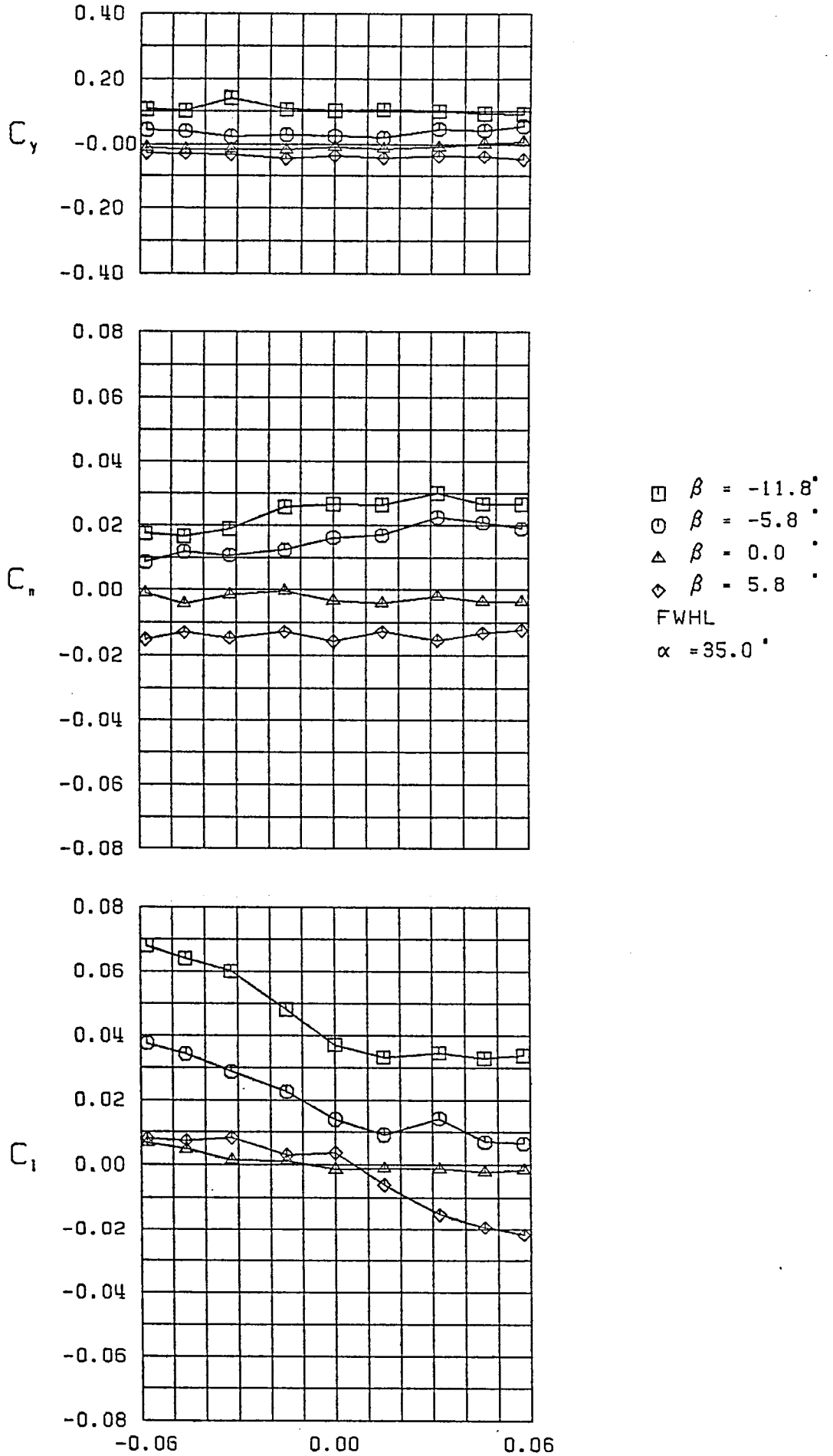

Figure 16 (Continued)

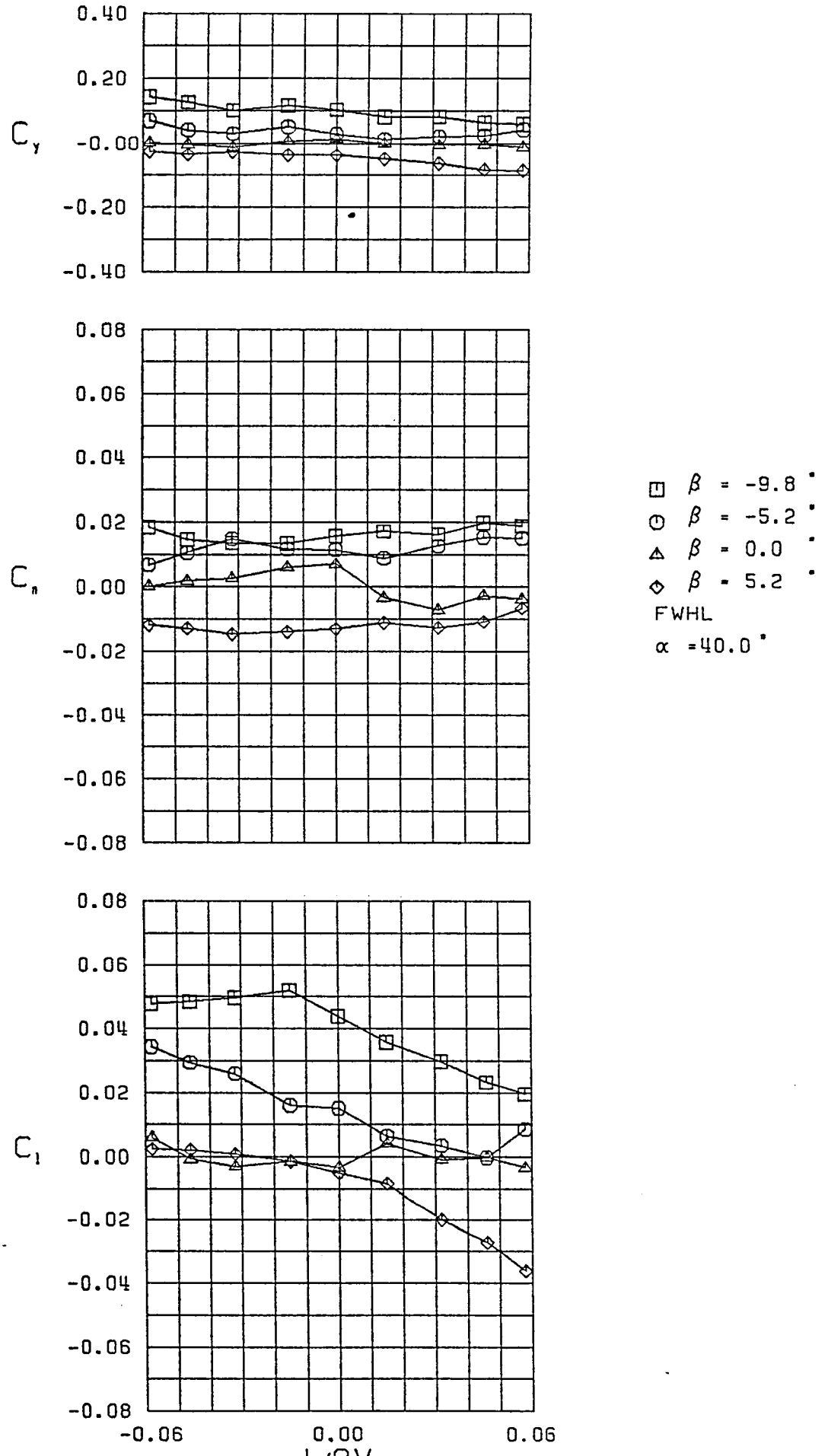

Figure 16 (Continued)

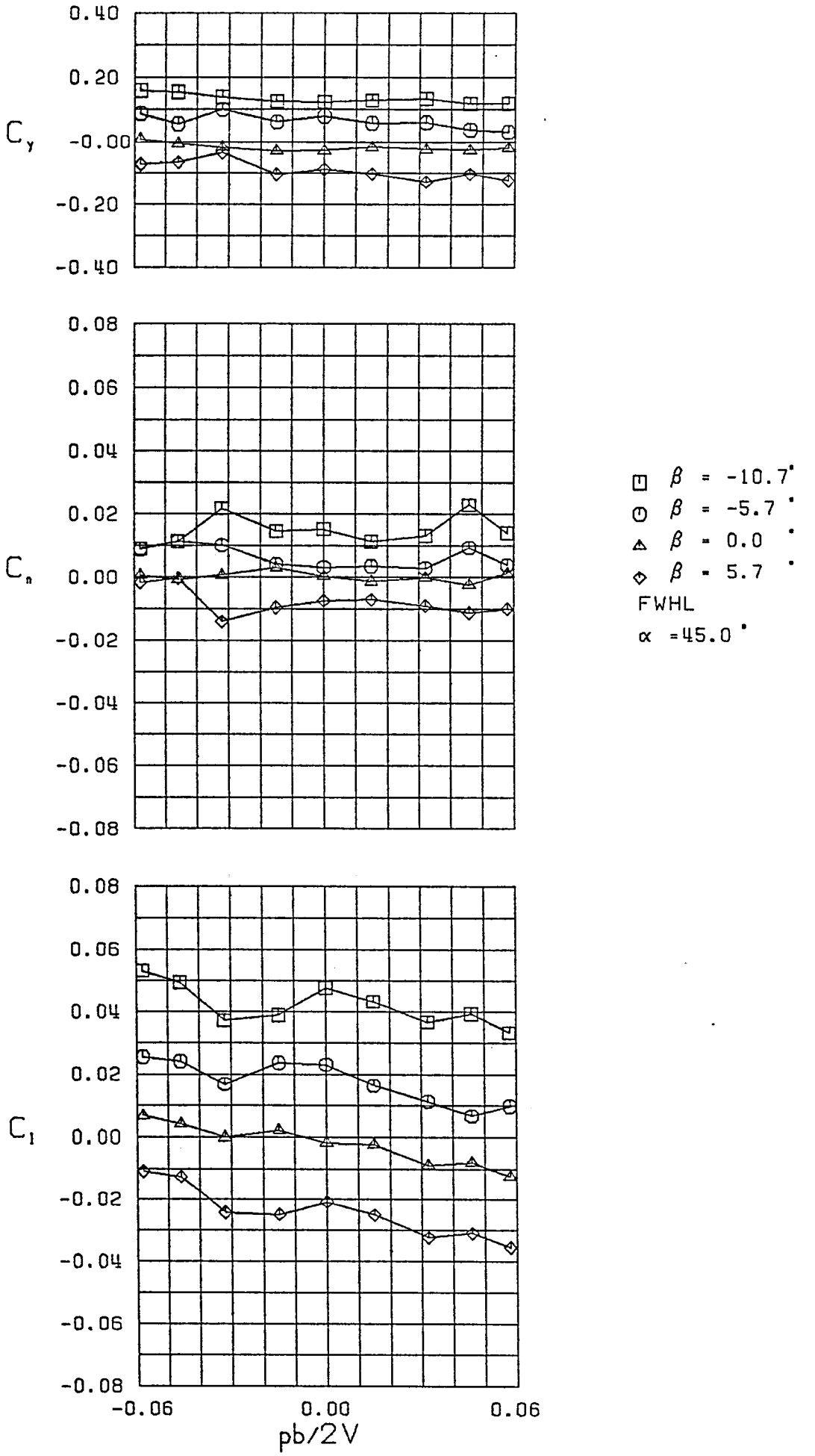

Figure 16 (Continued)

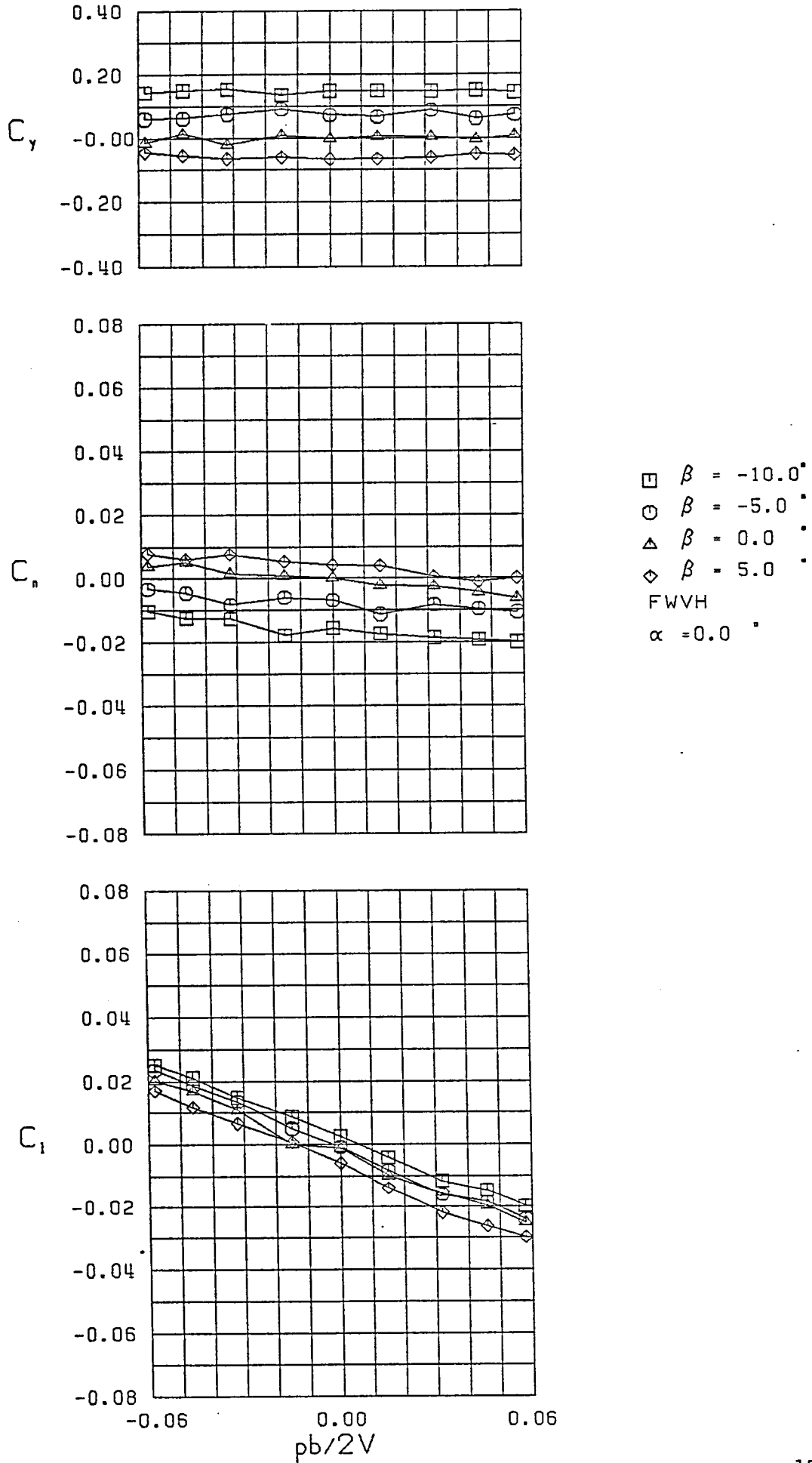

Figure 17 - Variation of Lateral-Directional Characteristics with Roll Rate-Configuration 6

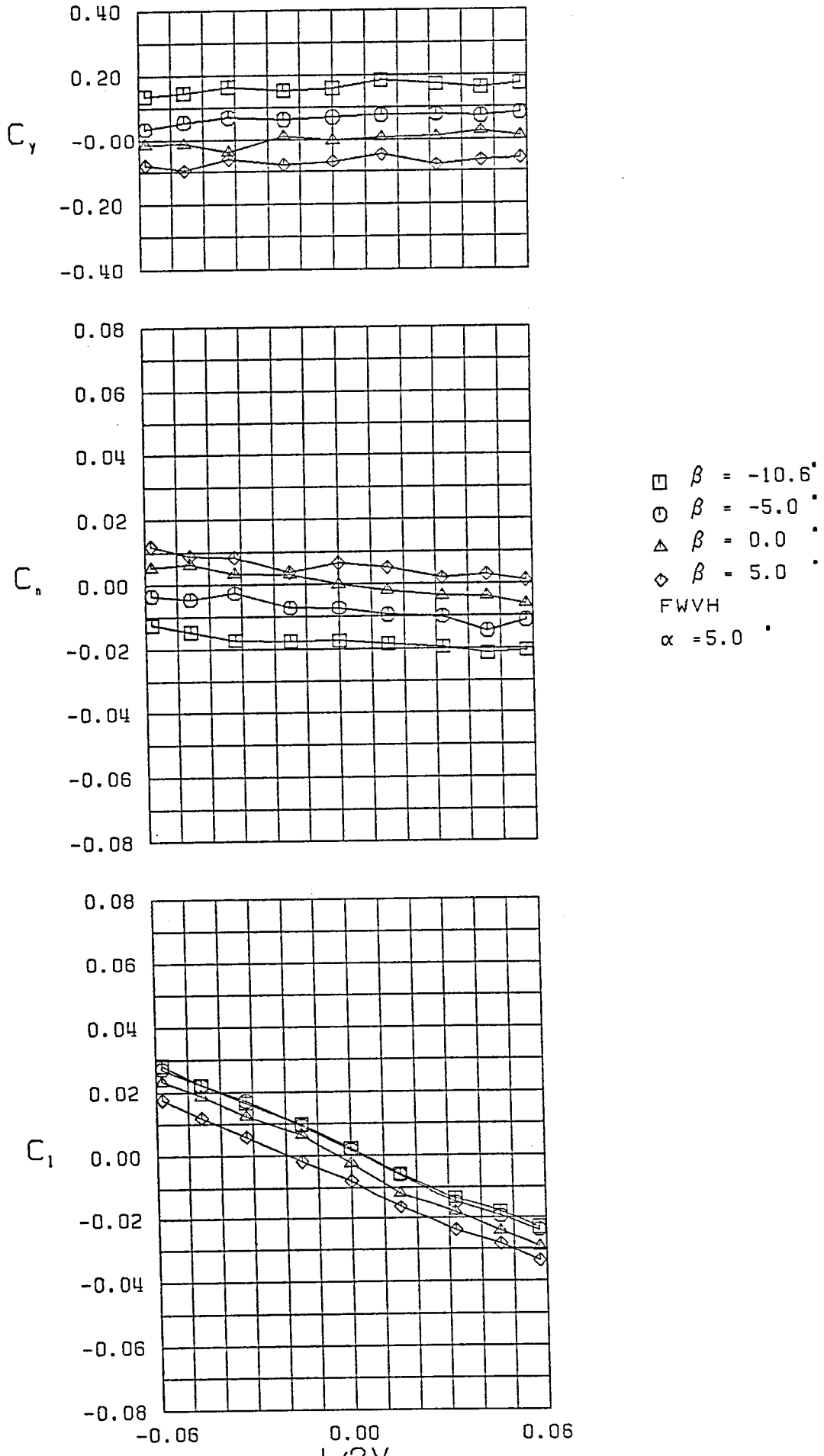

Figure 17 (Continued)

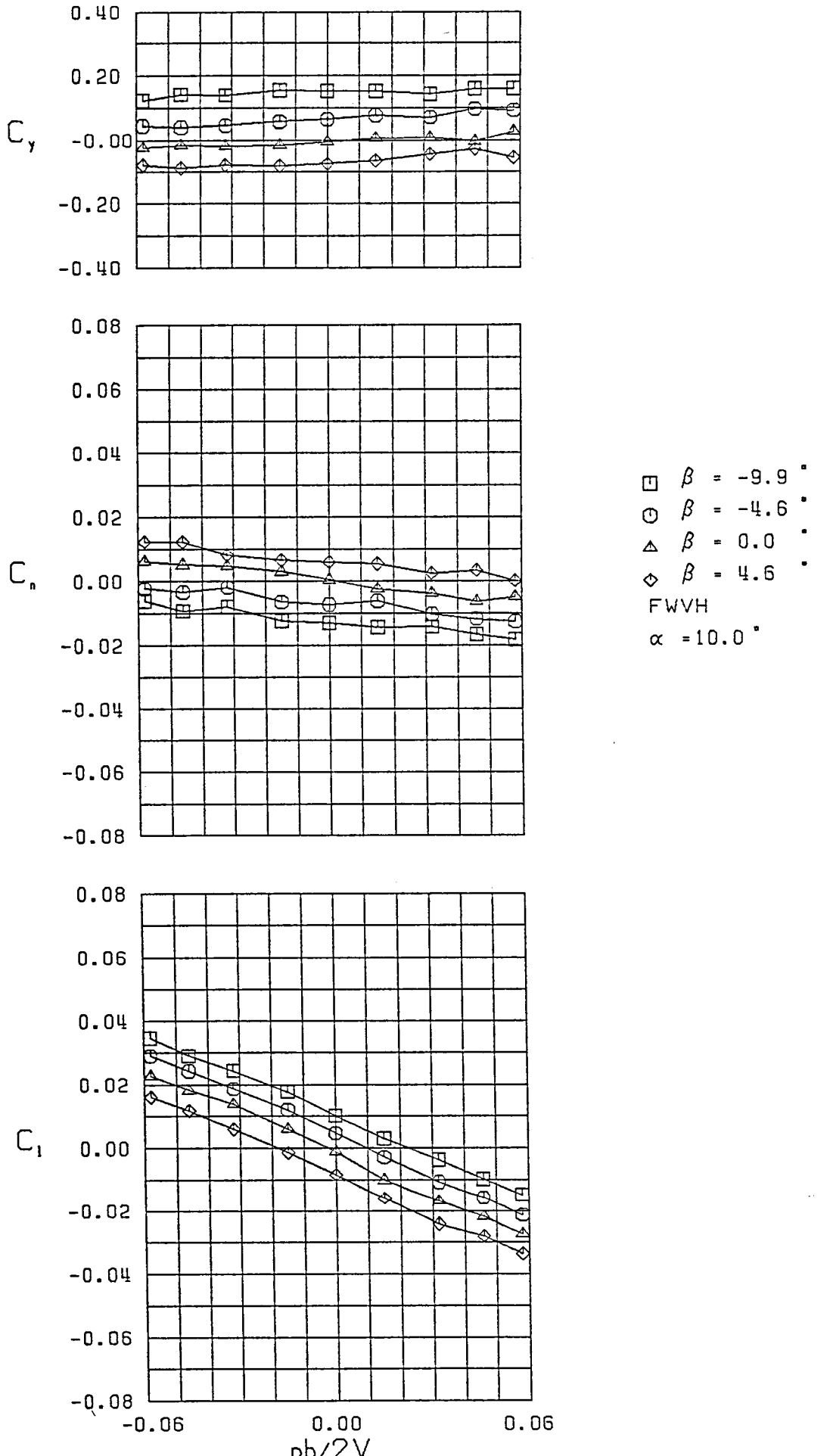

Figure 17 (Continued)

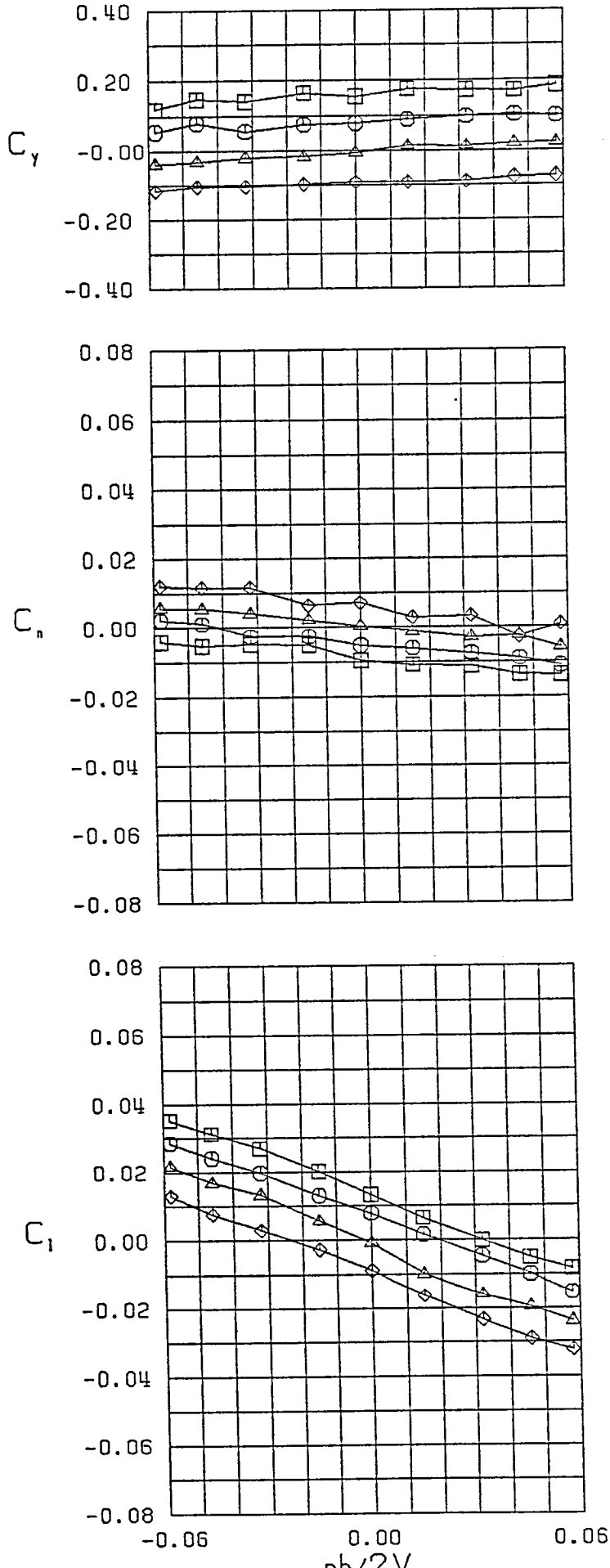

Figure 17 (Continued)

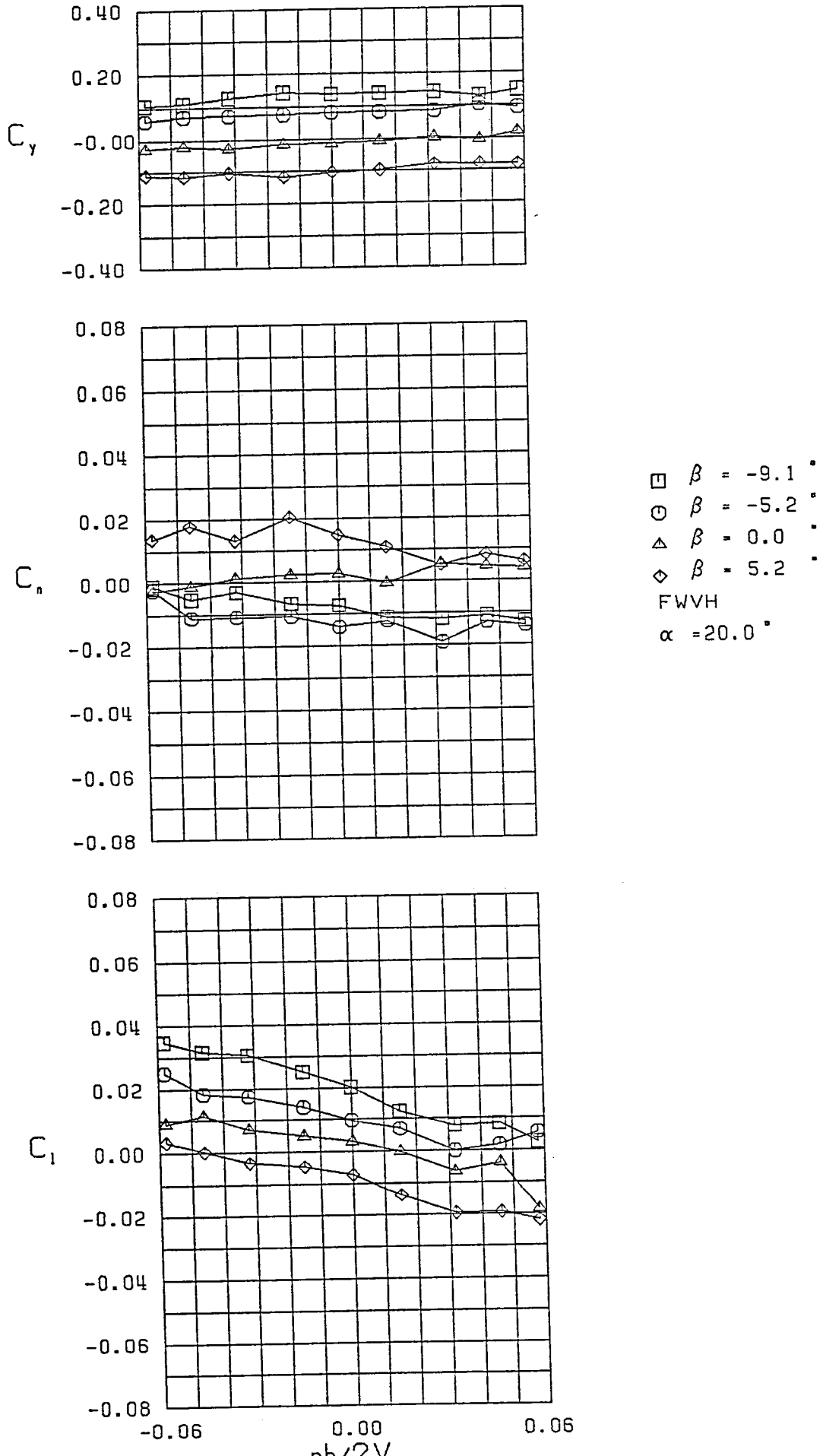

Figure 17 (Continued)

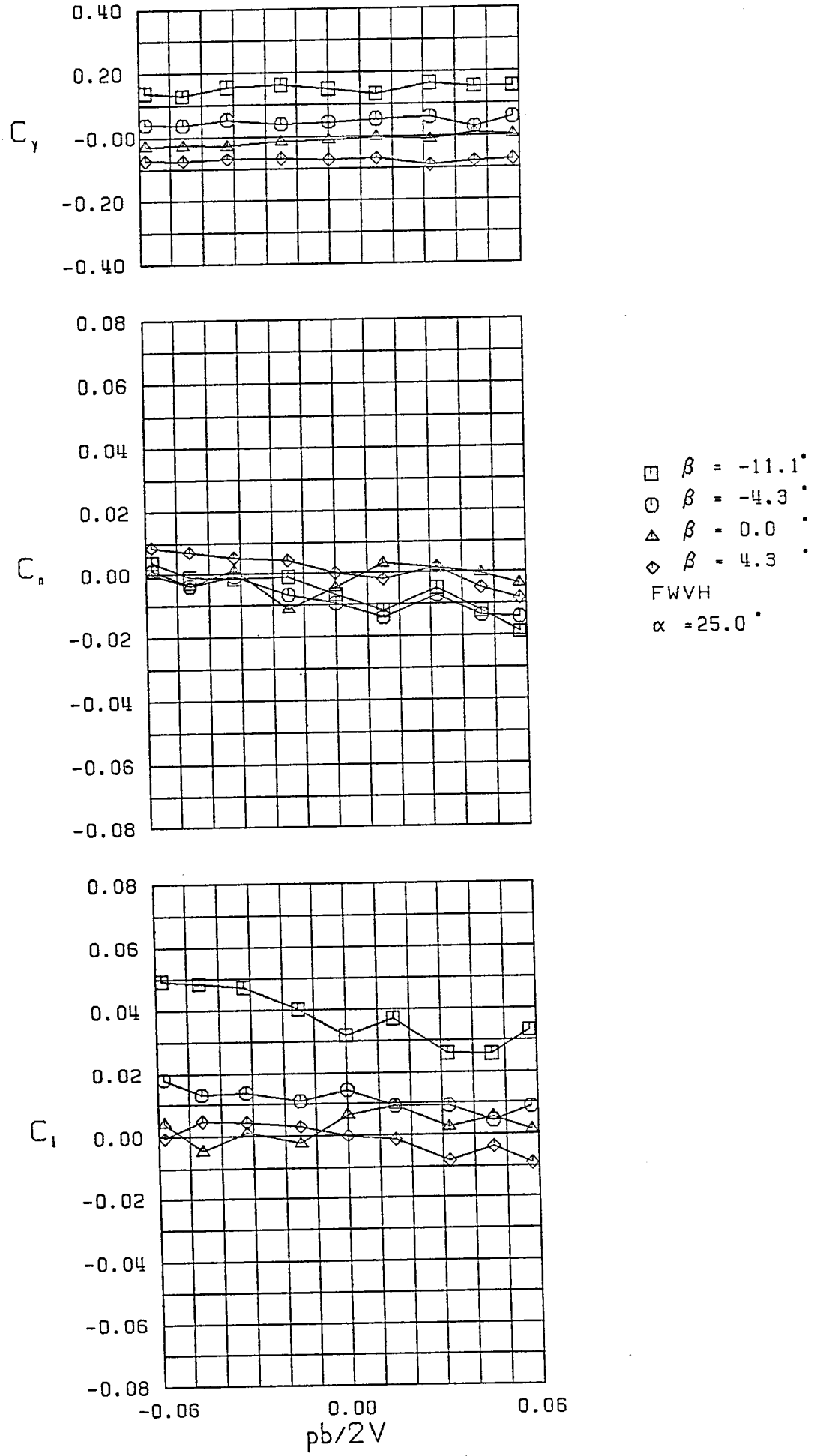

Figure 17 (Continued)

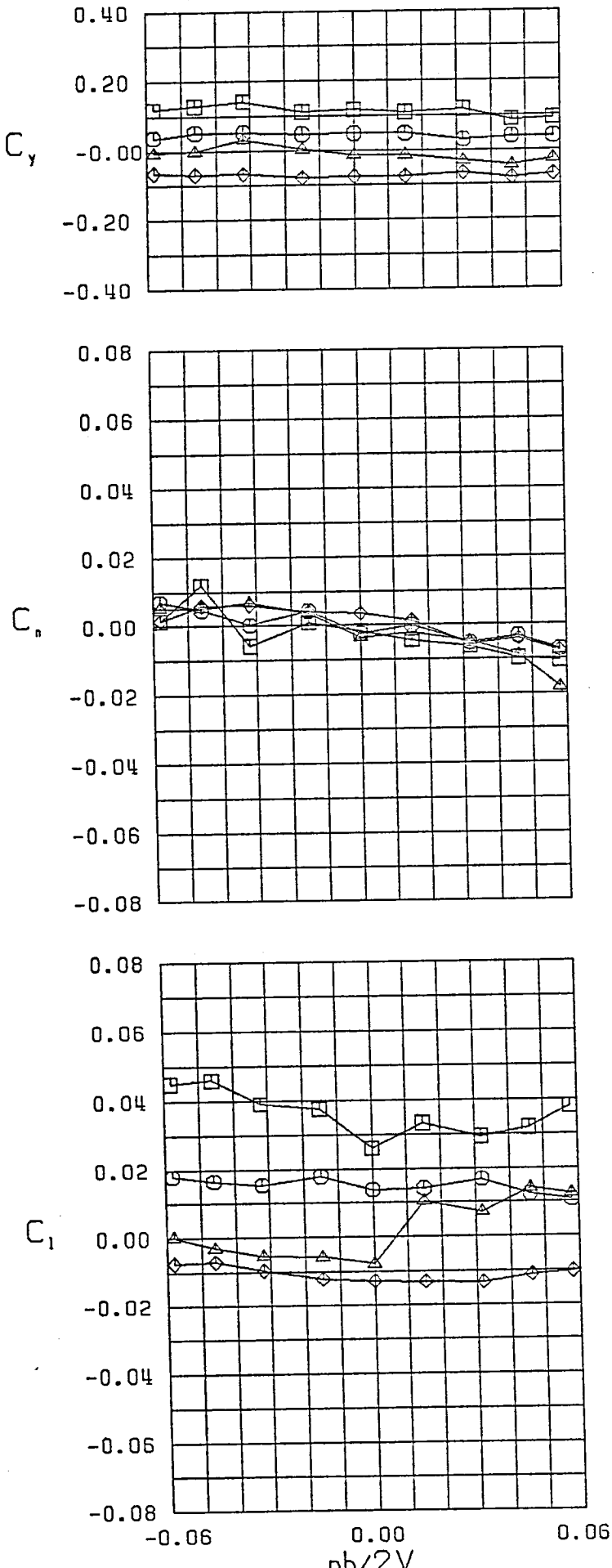

Figure 17 (Continued)

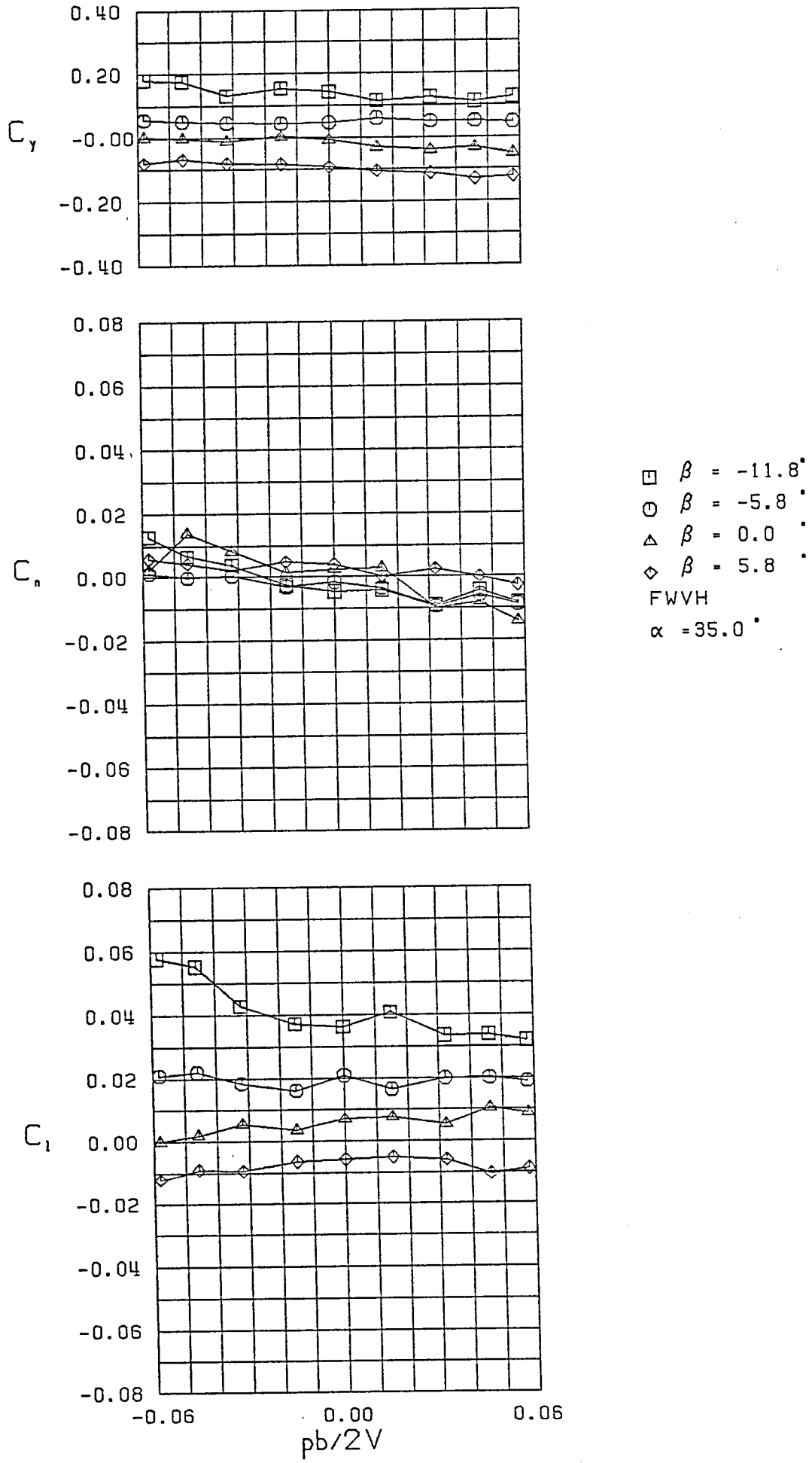

Figure 17 (Continued)

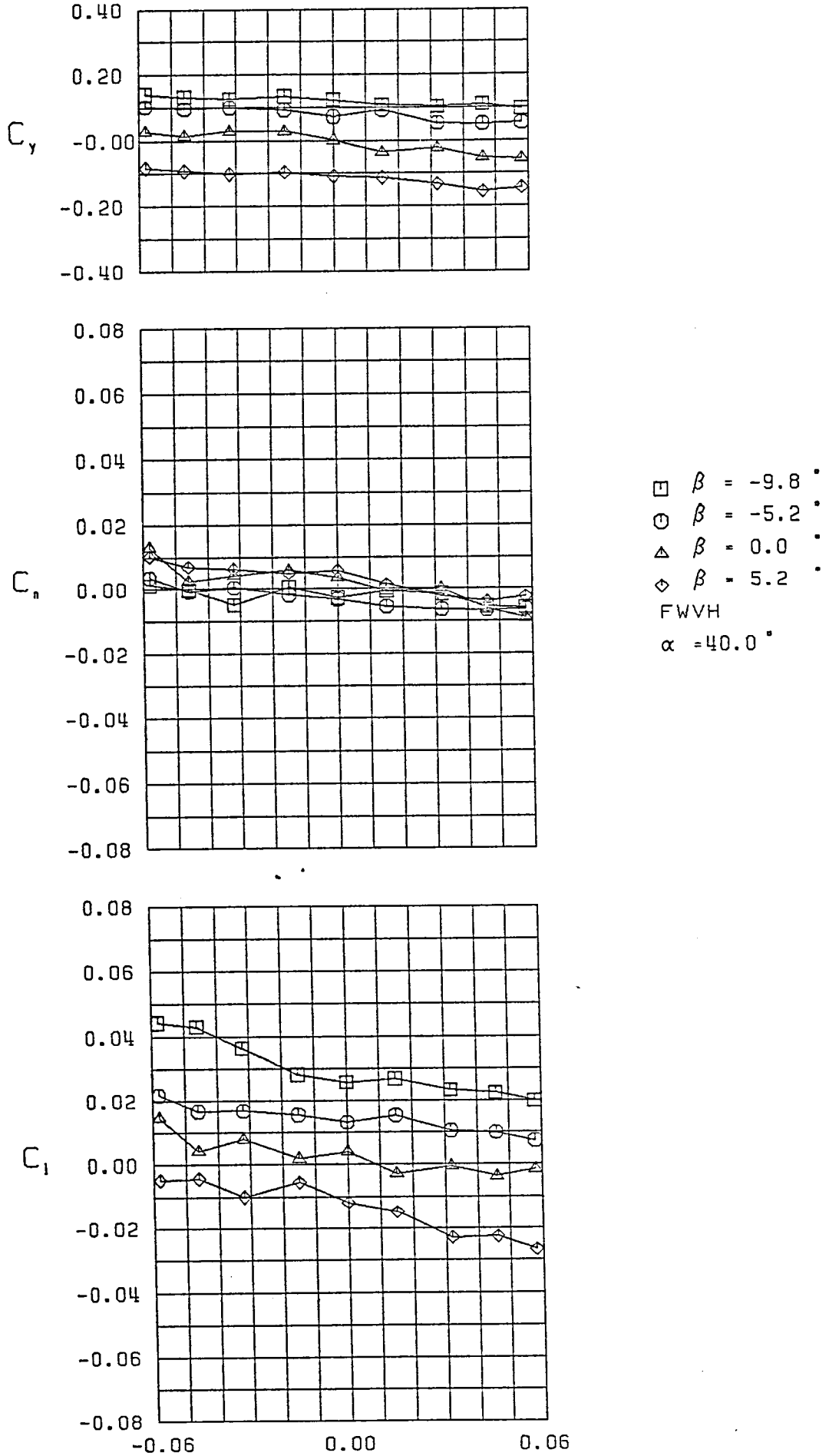

Figure 17 (Continued)

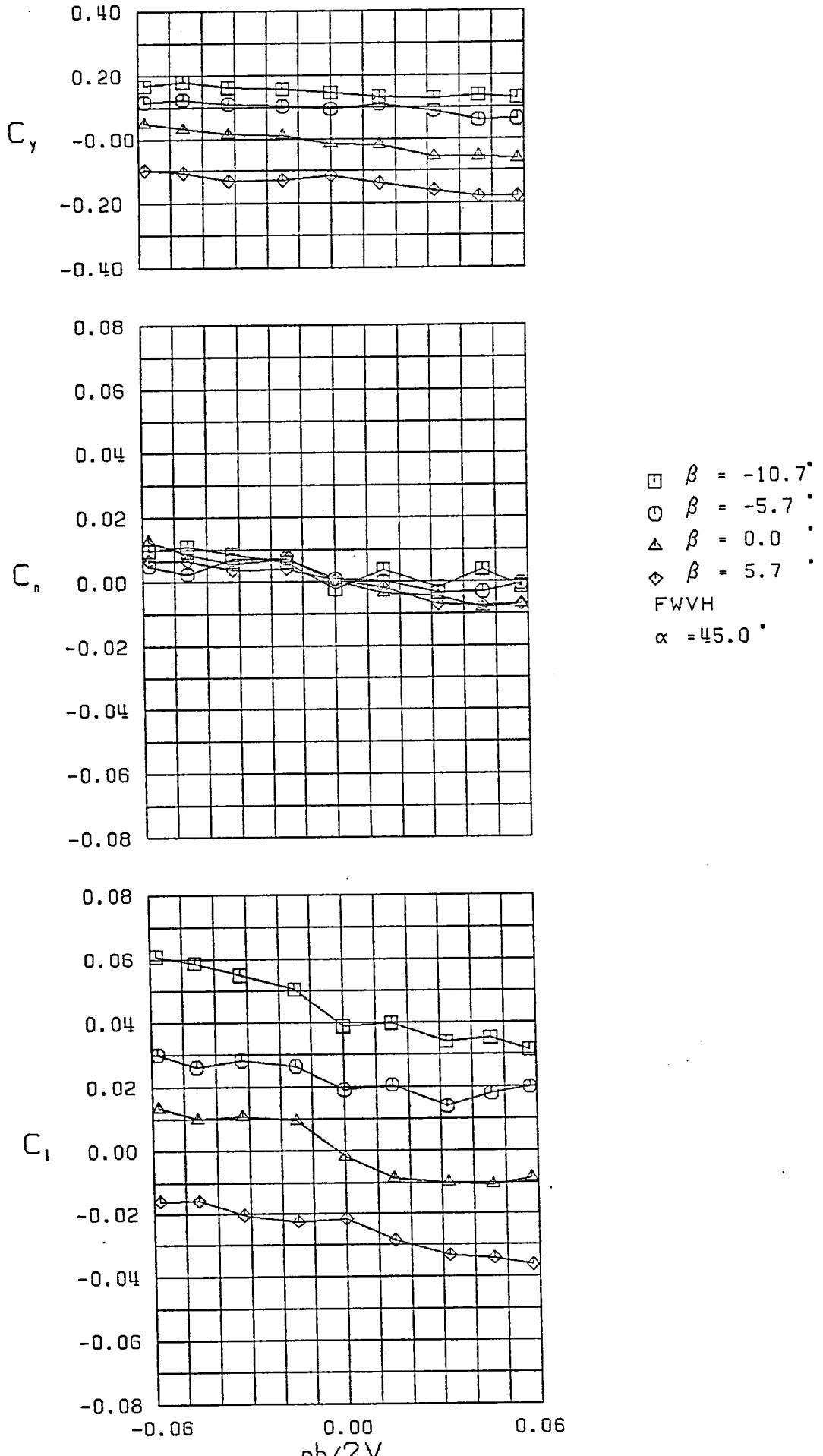

Figure 17 (Continued)

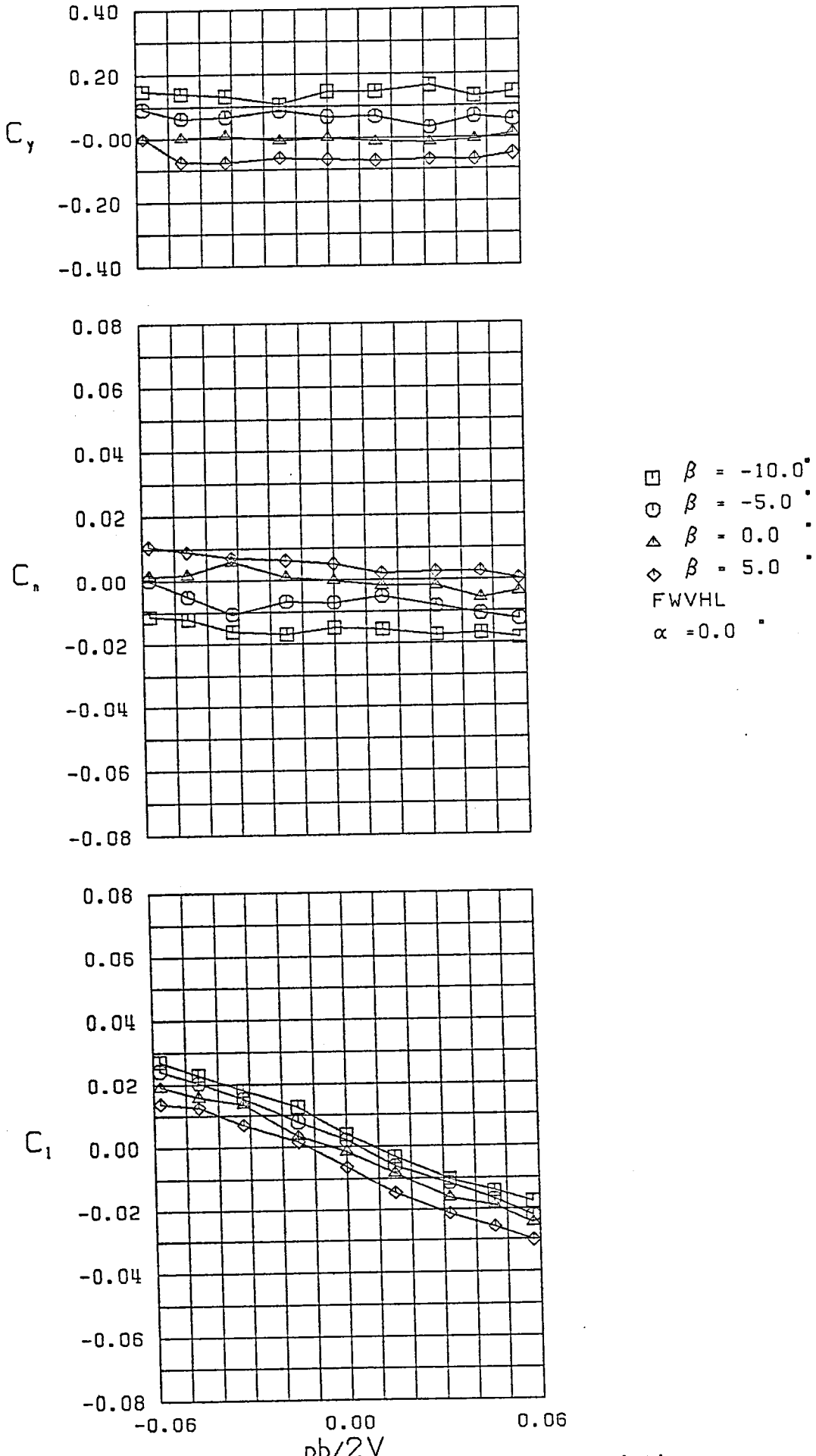

Figure 18 - Variation of Lateral-Directional Characteristics with Roll Rate-Configuration 1

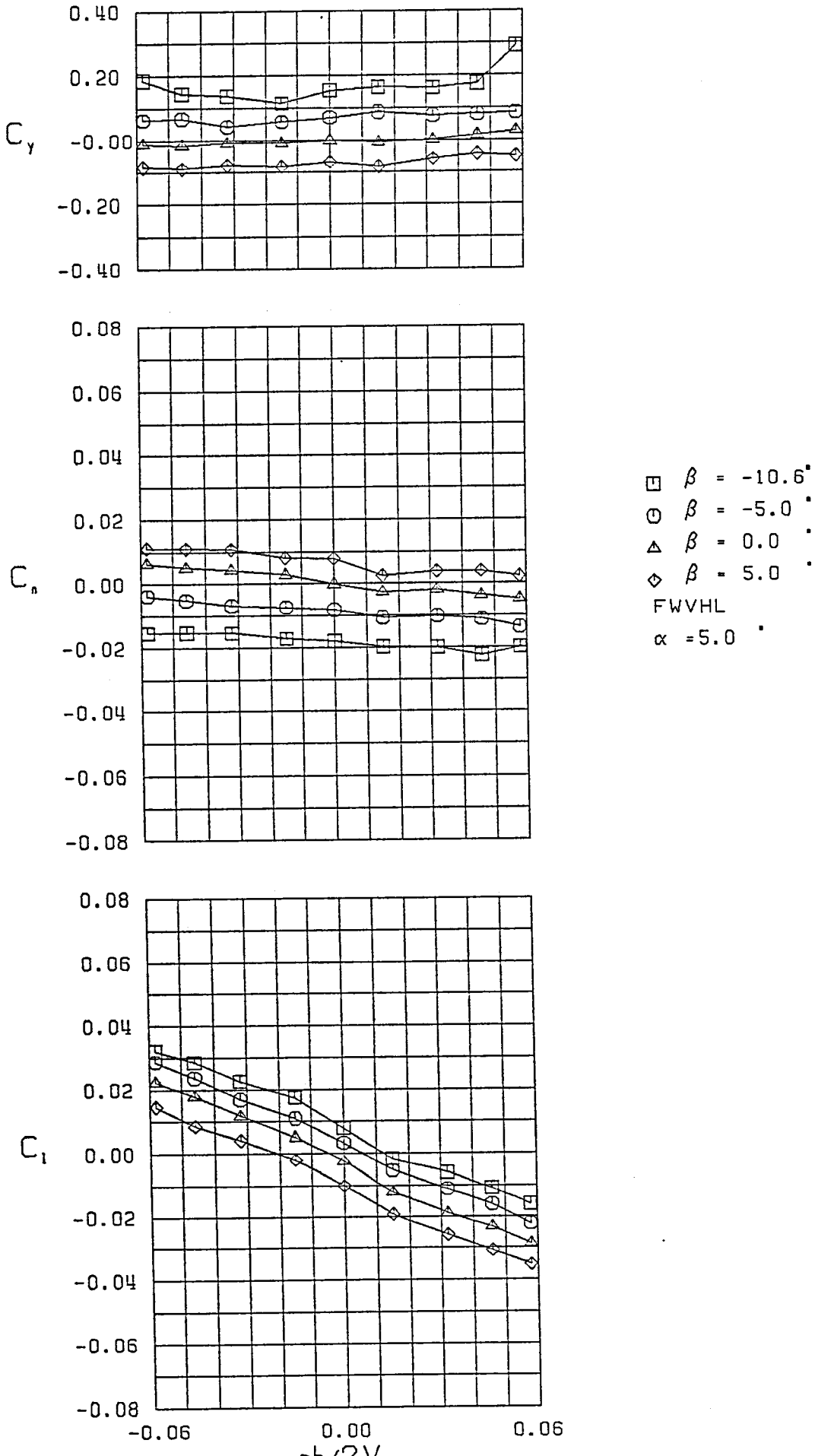

Figure 18 (Continued)

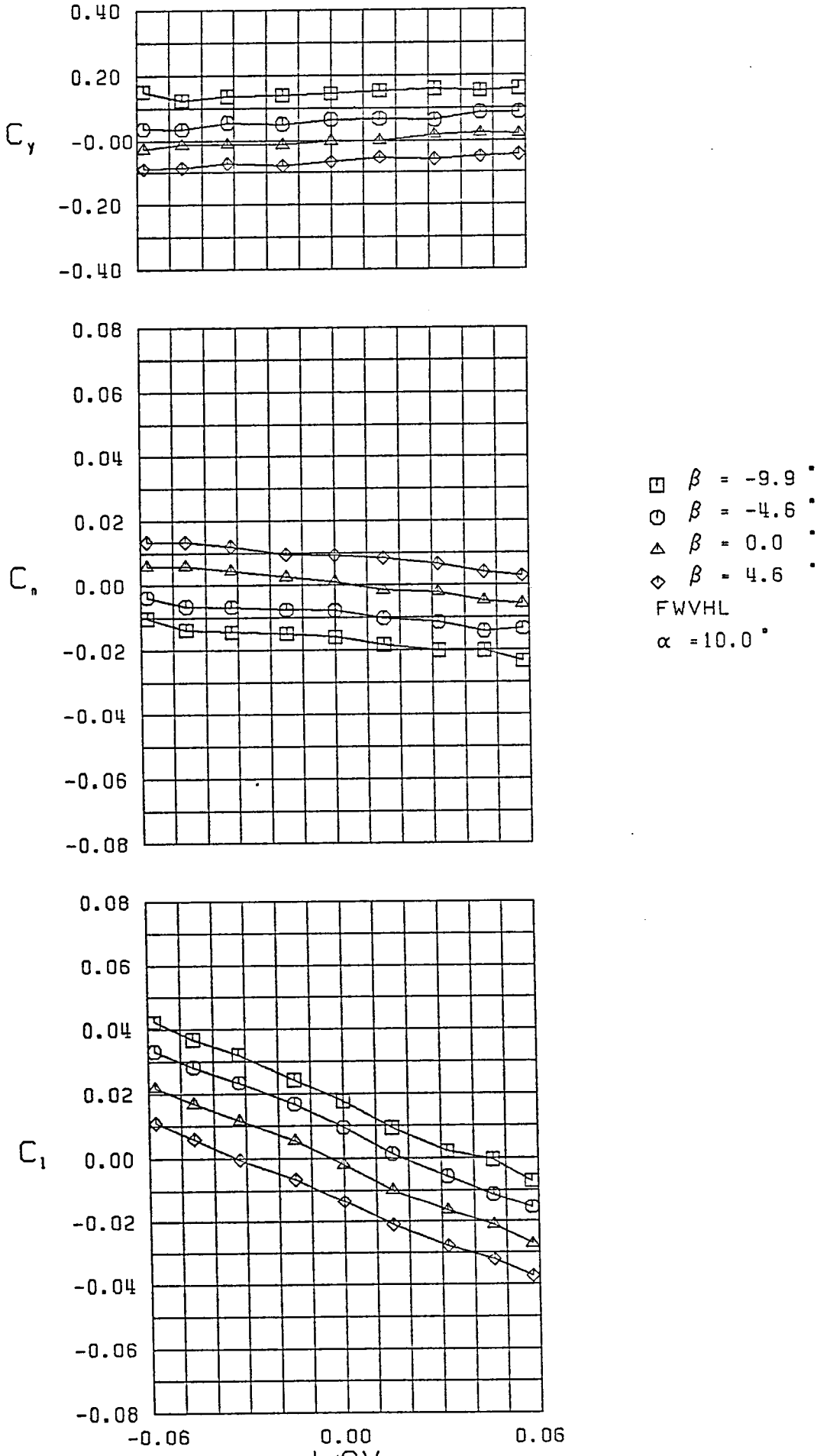

Figure 18 (Continued)

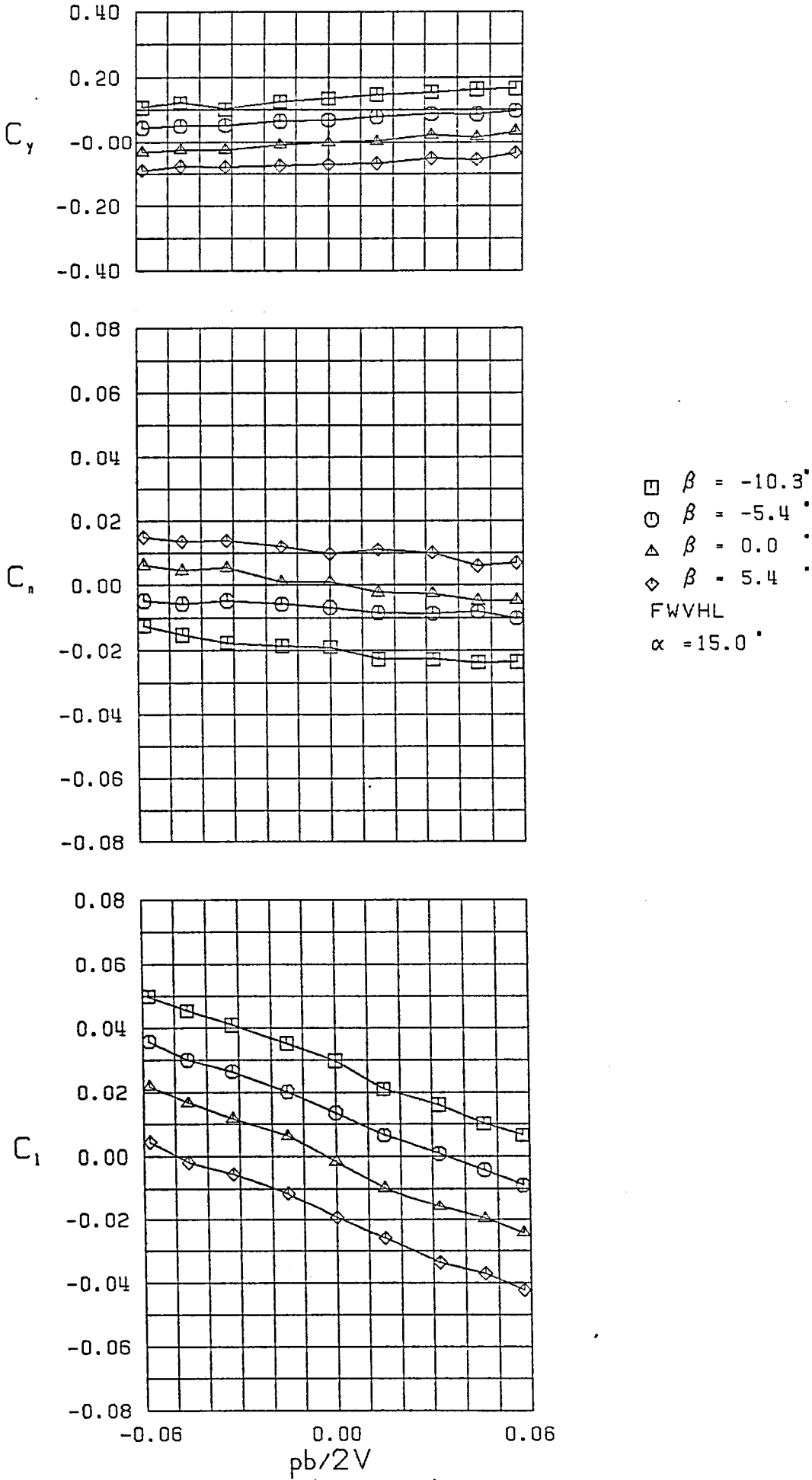

Figure 18 (Continued)

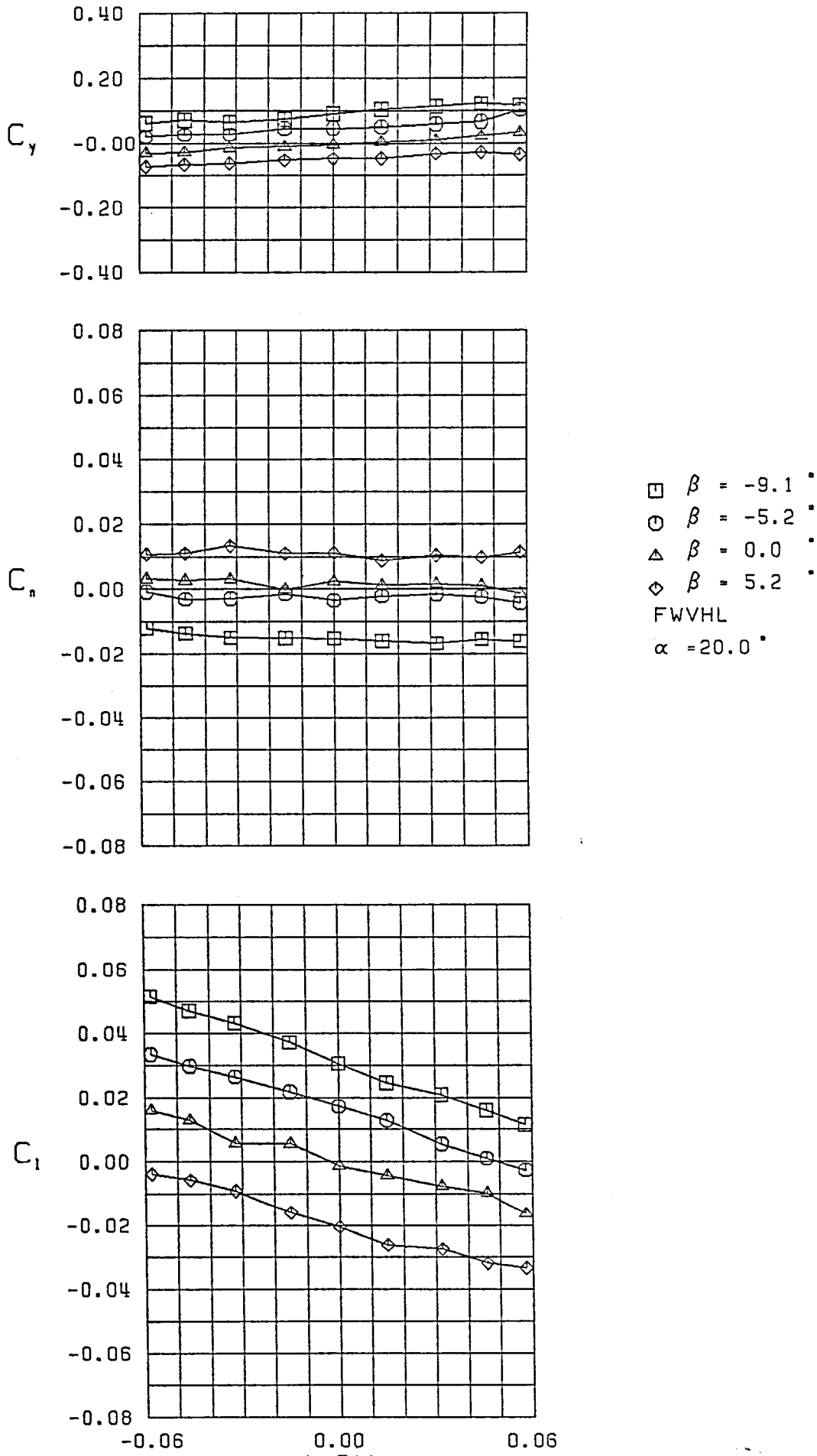

Figure 18 (Continued)

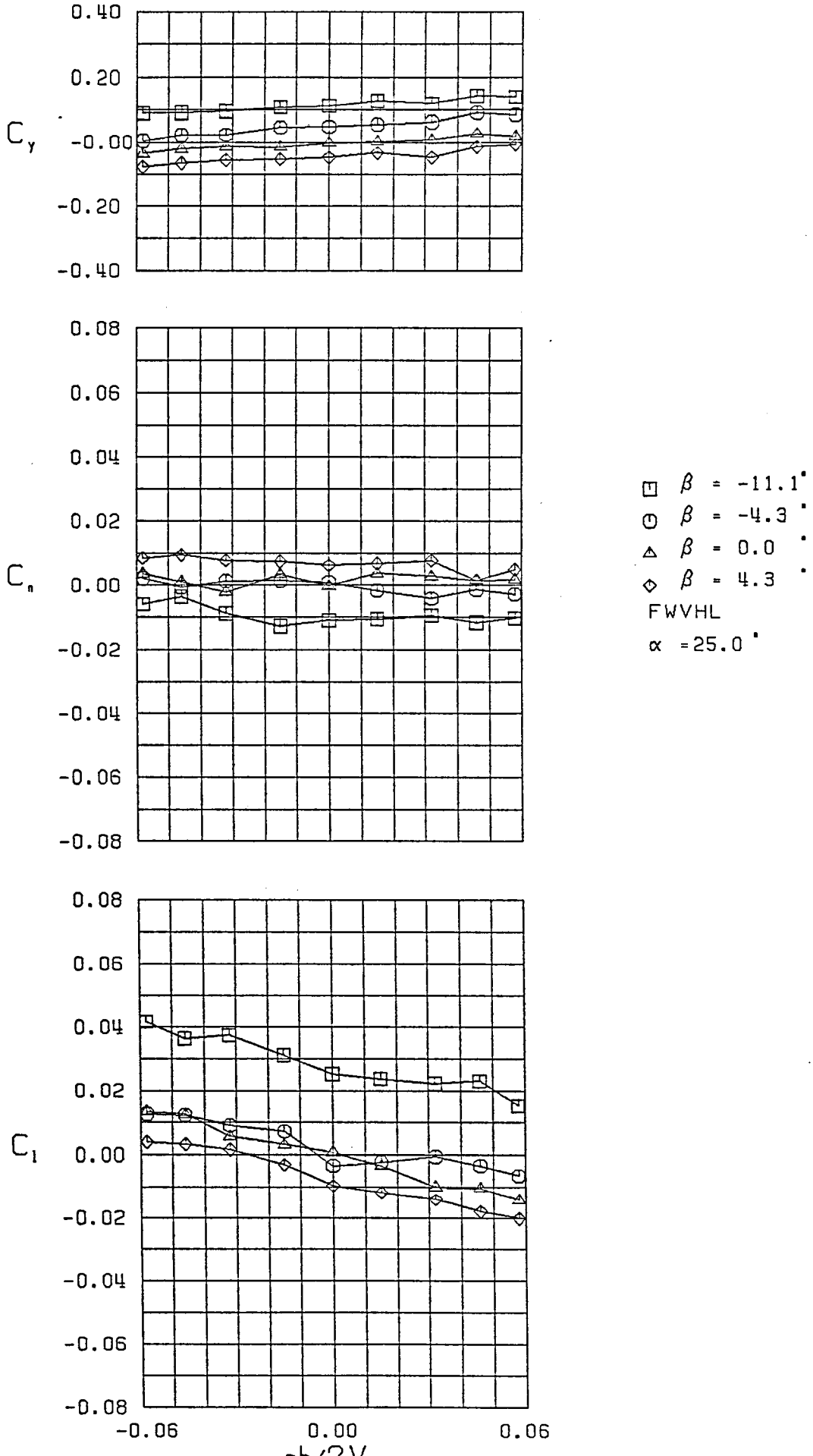

Figure 18 (Continued)

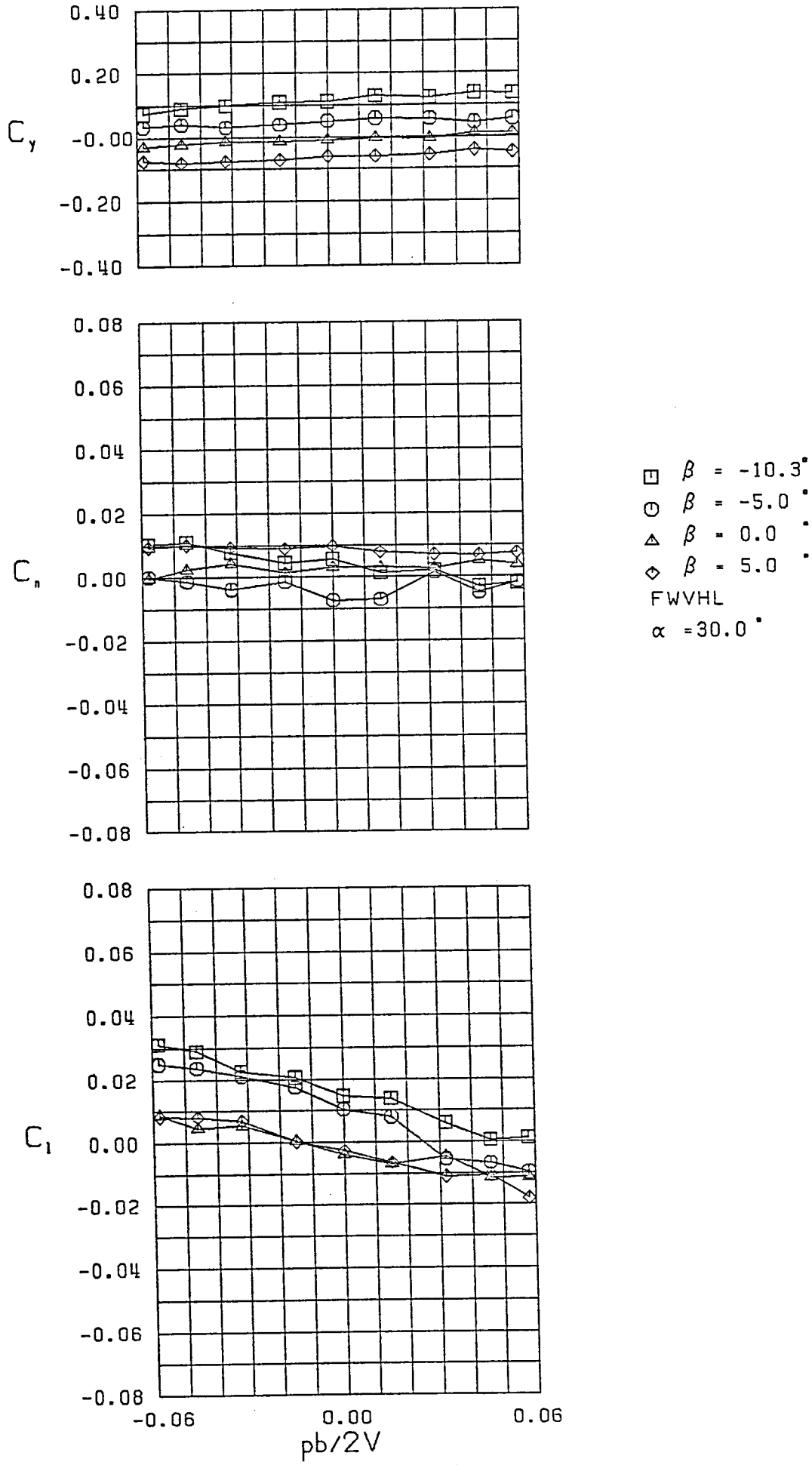

Figure 18 (Continued)

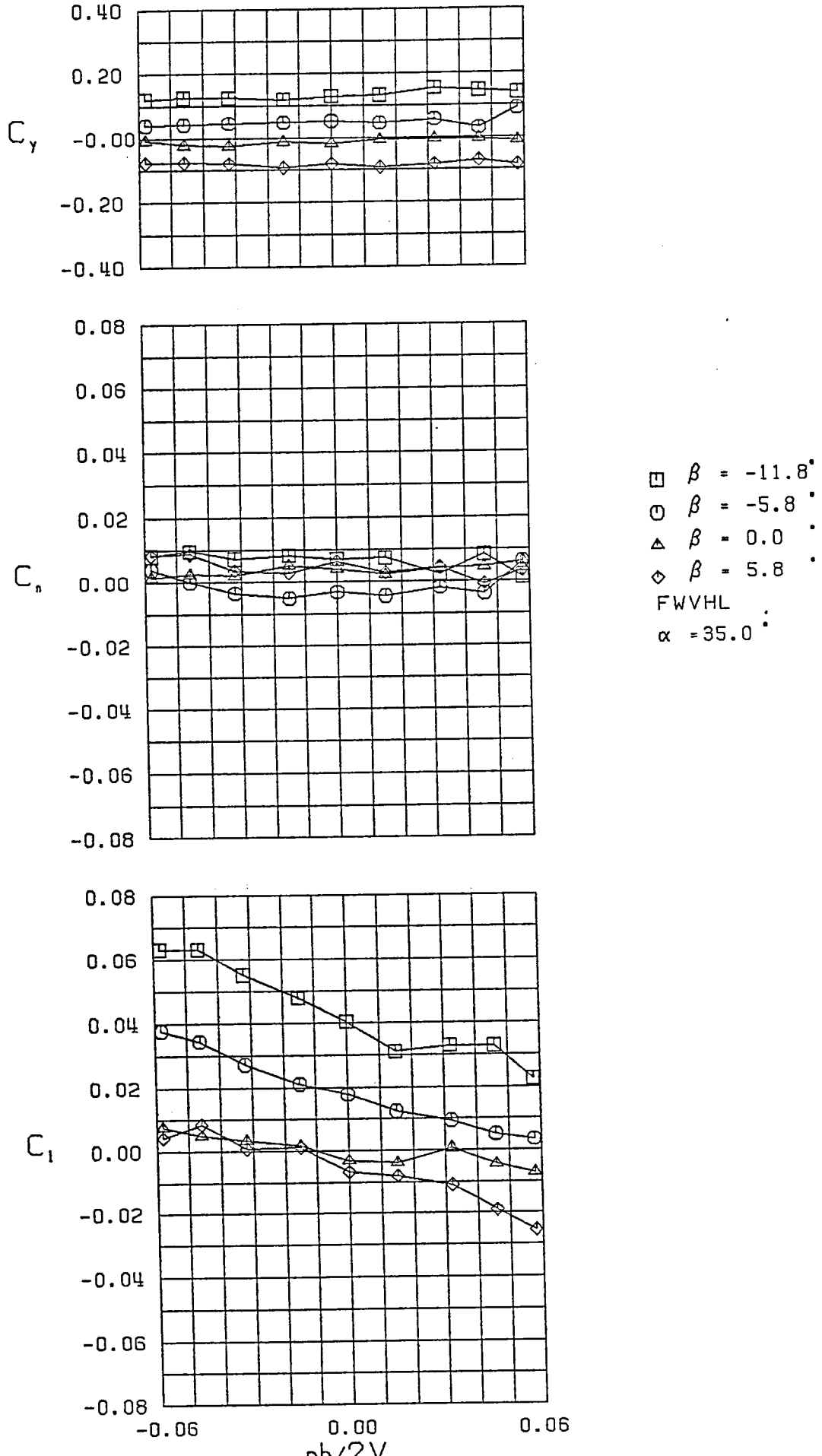

Figure 18 (Continued)

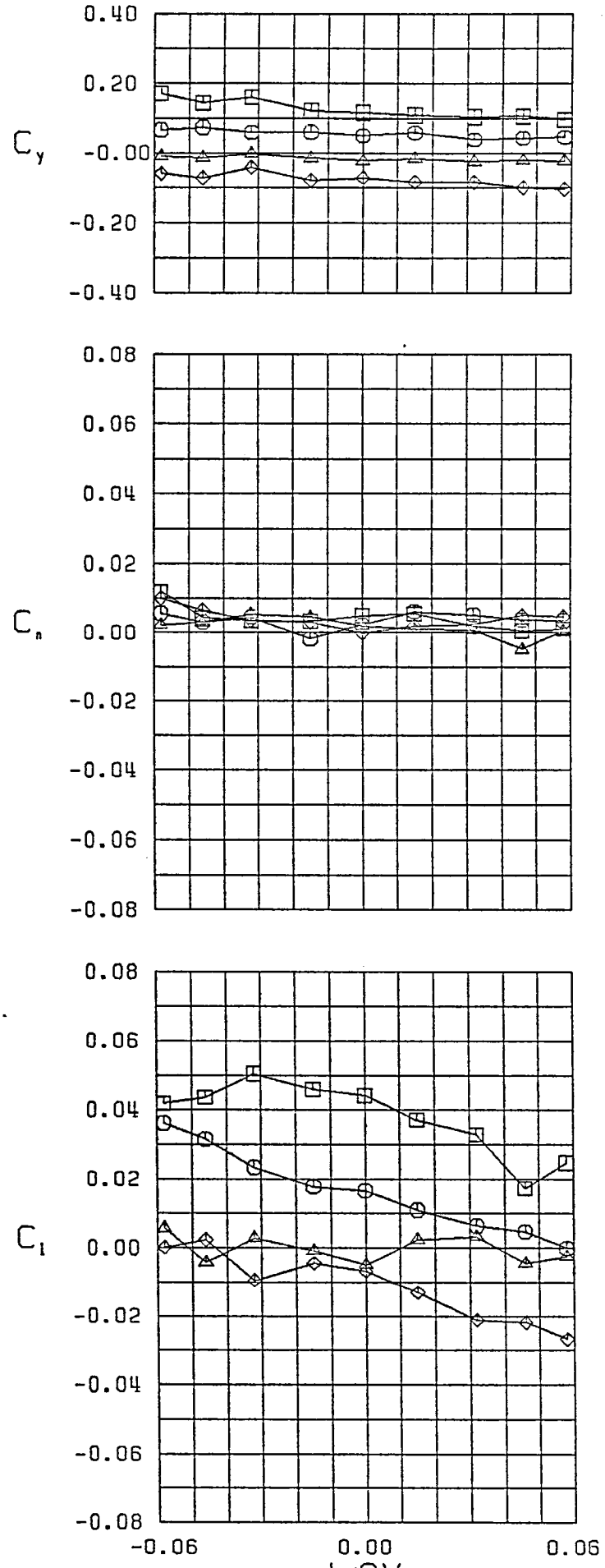

Figure 18 (Continued)

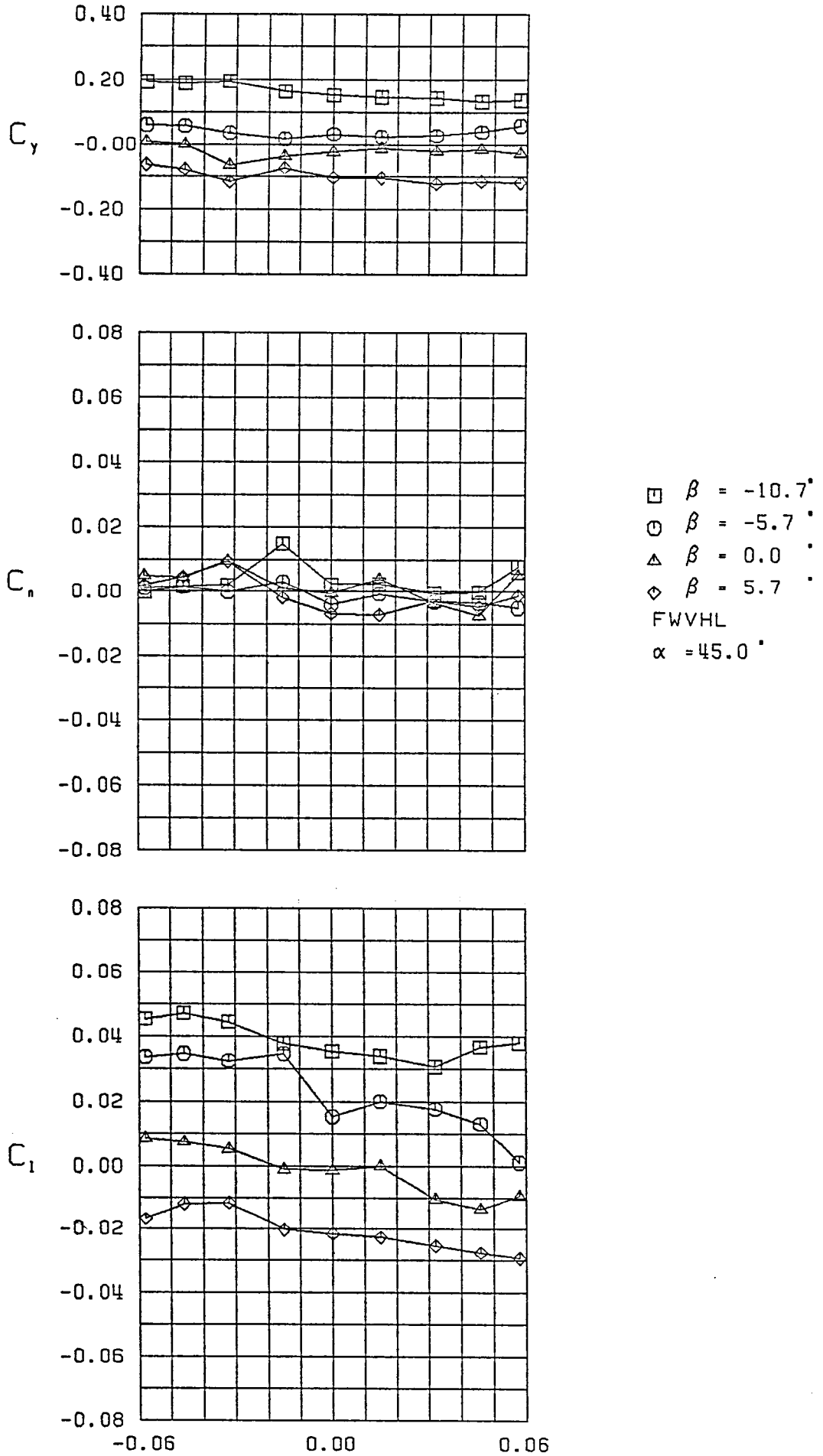

Figure 18 (Continued)

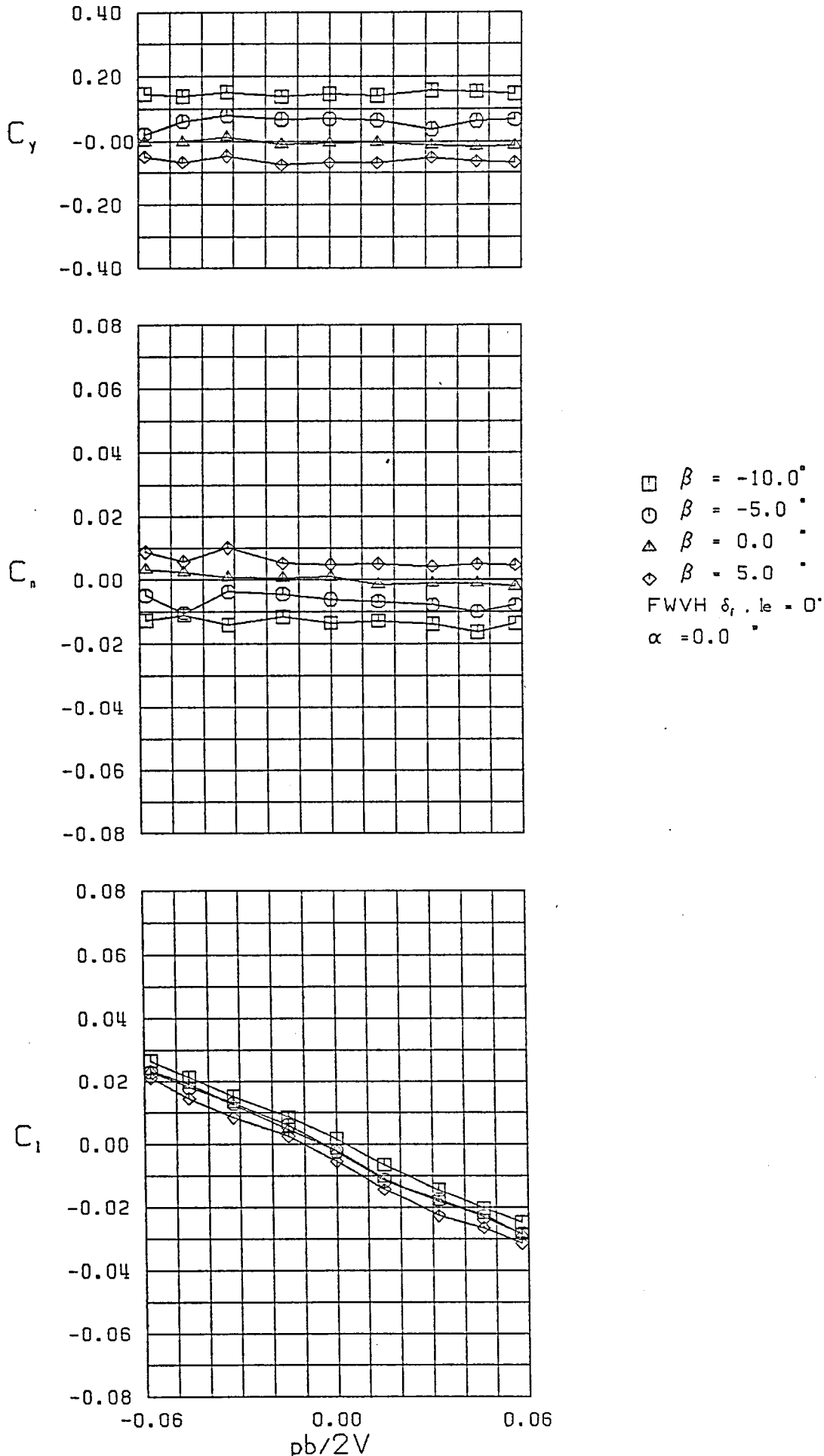

Figure 19 - Variation of Lateral-Directional Characteristics with Roll Rate-Configuration 7

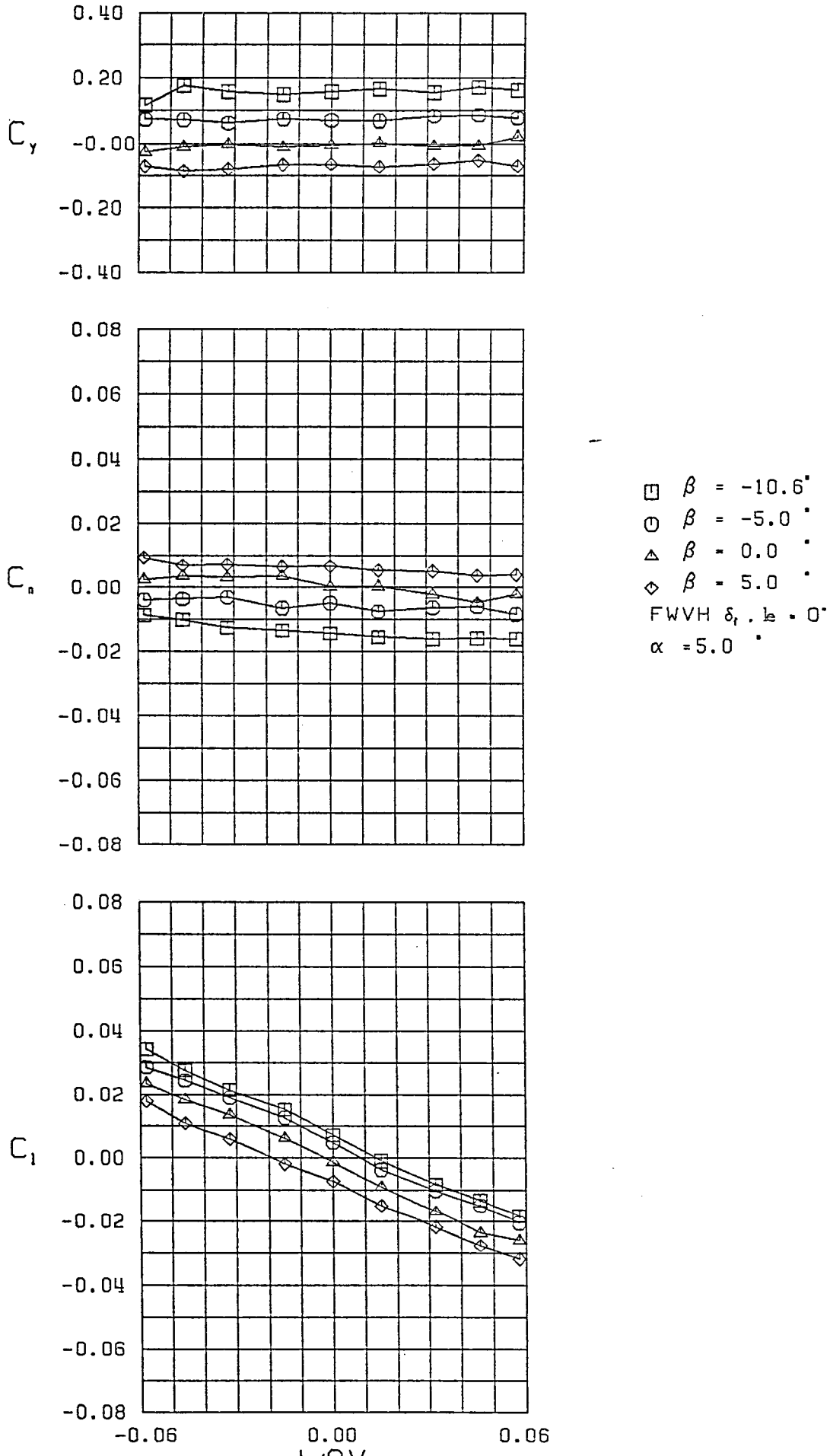

Figure 19 (Continued)

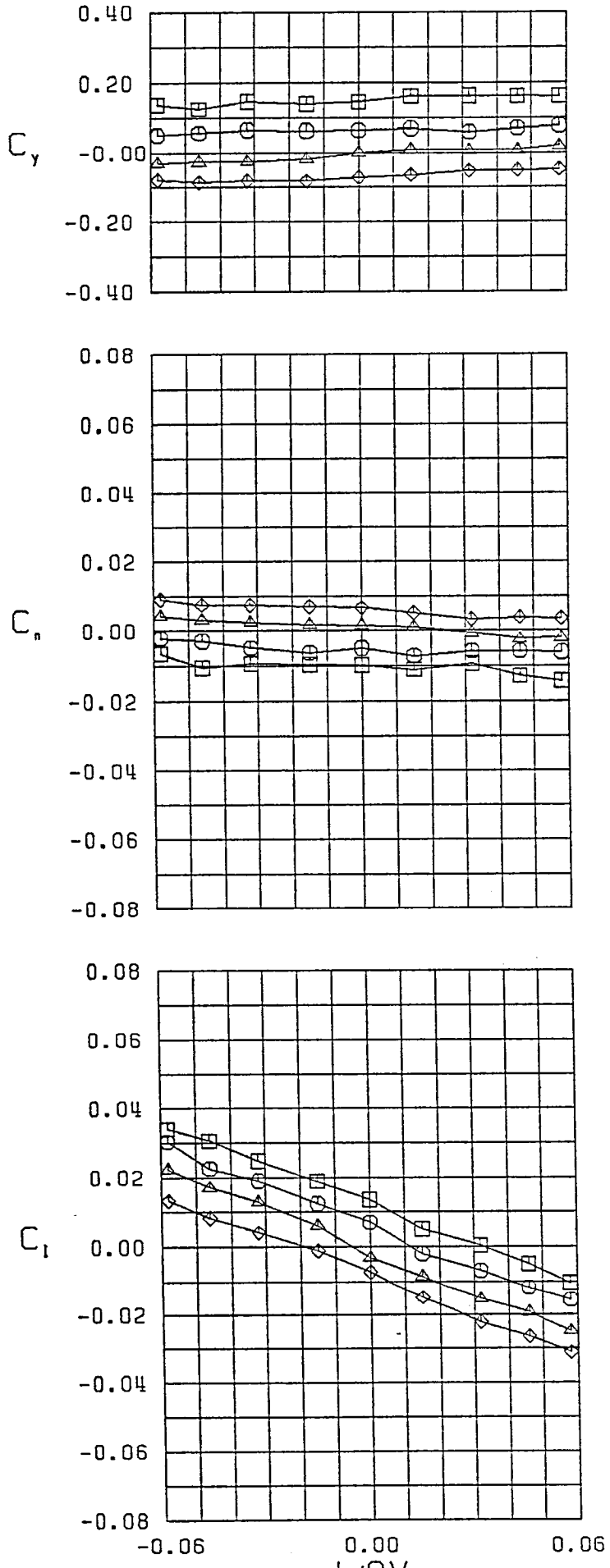

Figure 19 (Continued)

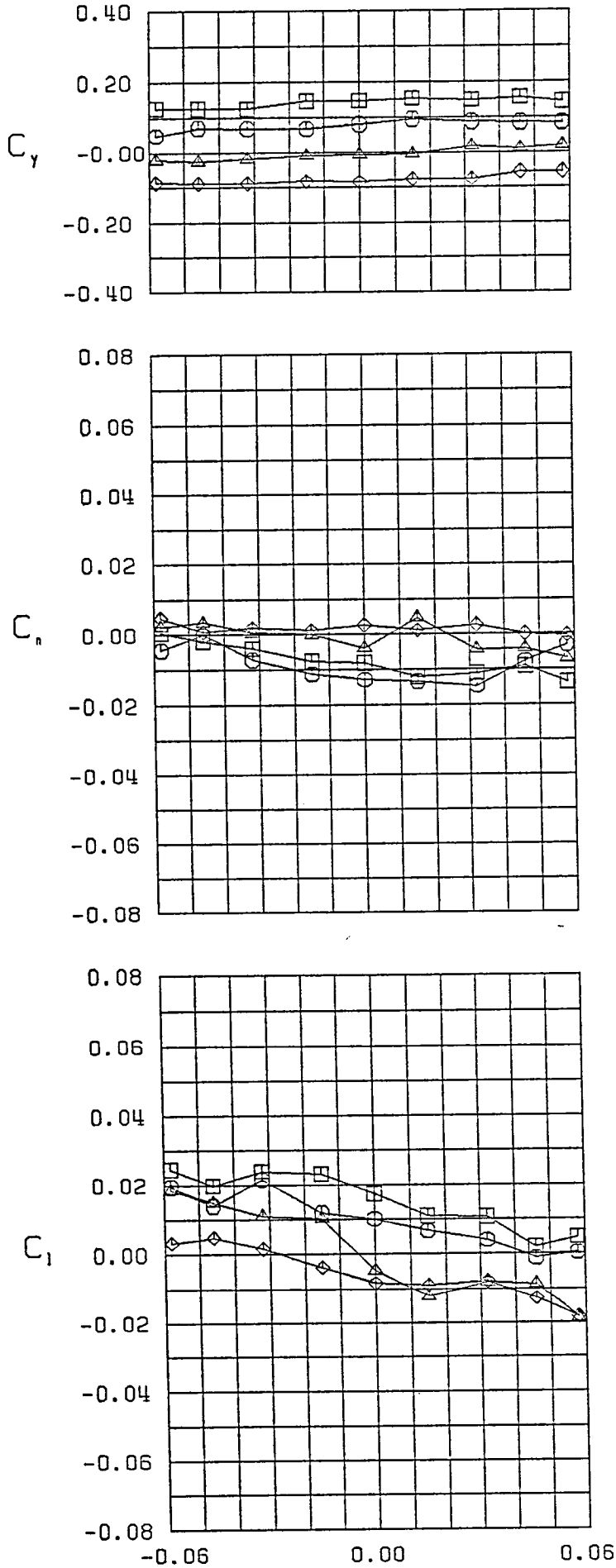

Figure 19 (Continued)

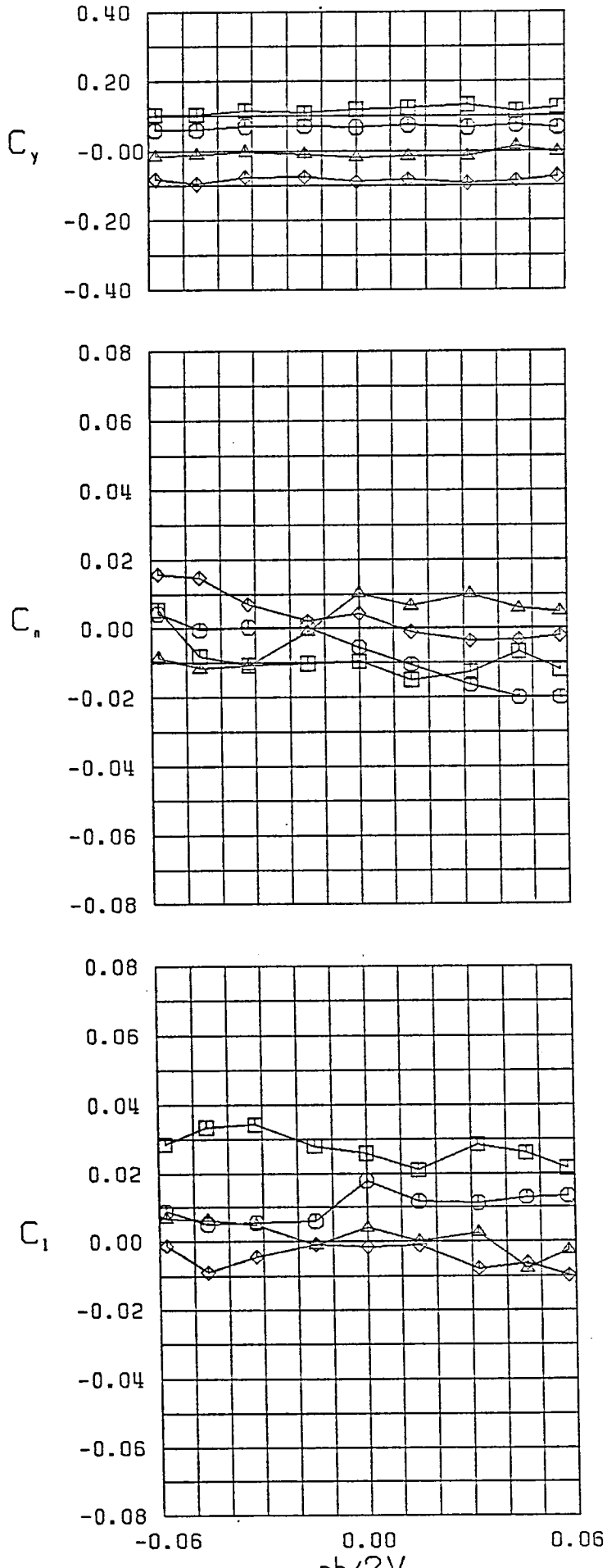

Figure 19 (Continued)

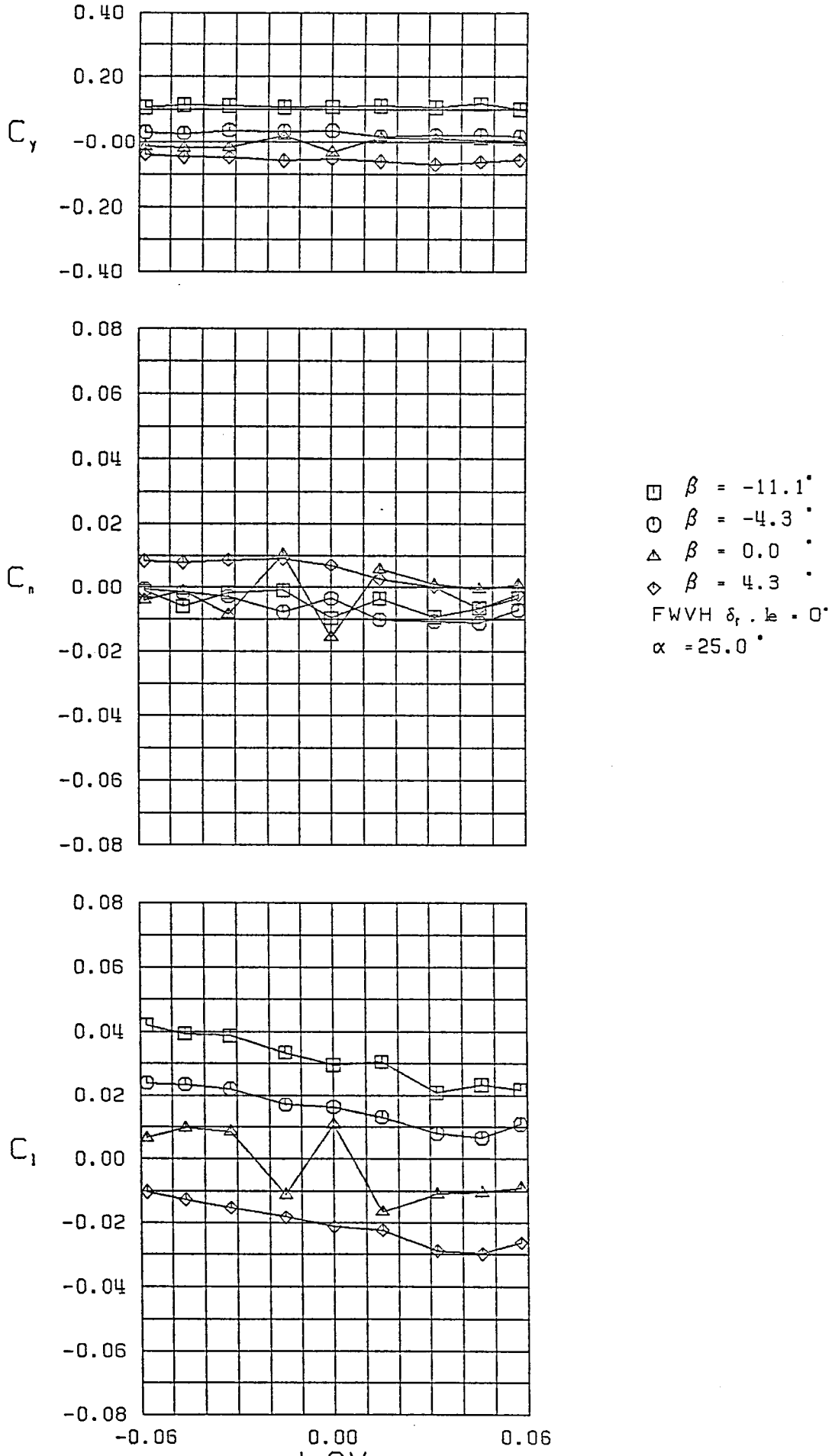

Figure 19 (Continued)

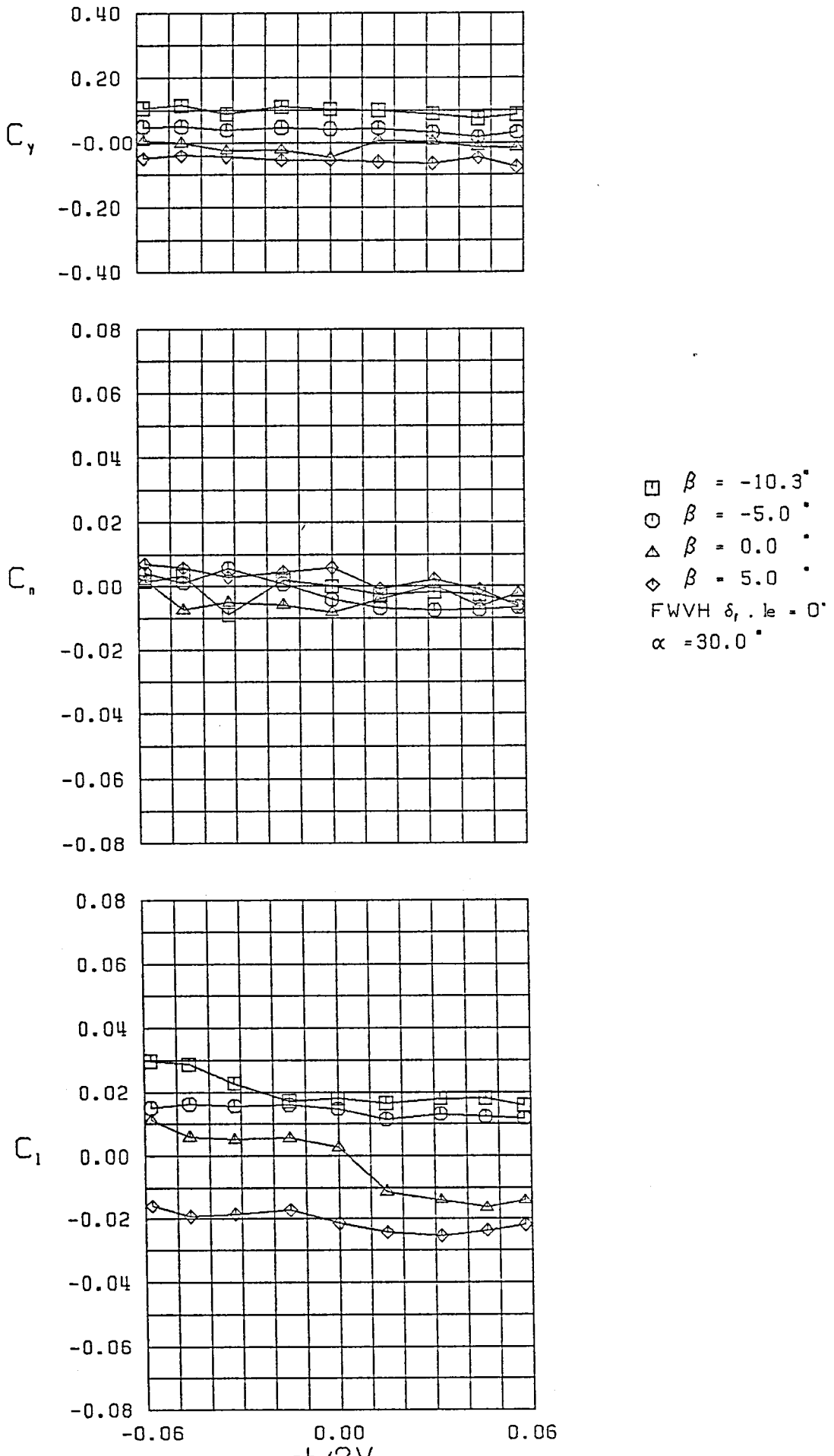

Figure 19 (Continued)

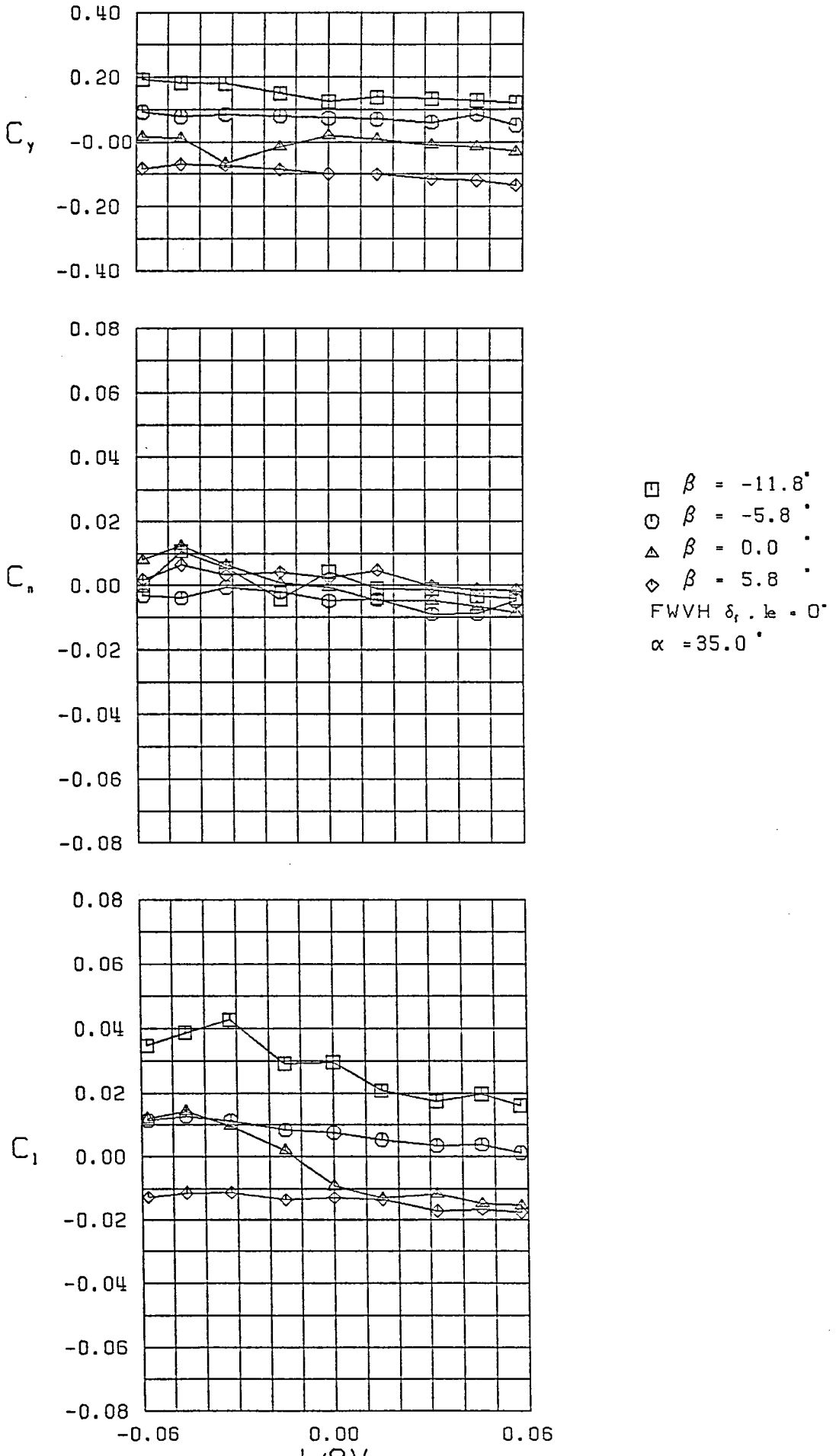

Figure 19 (Continued)

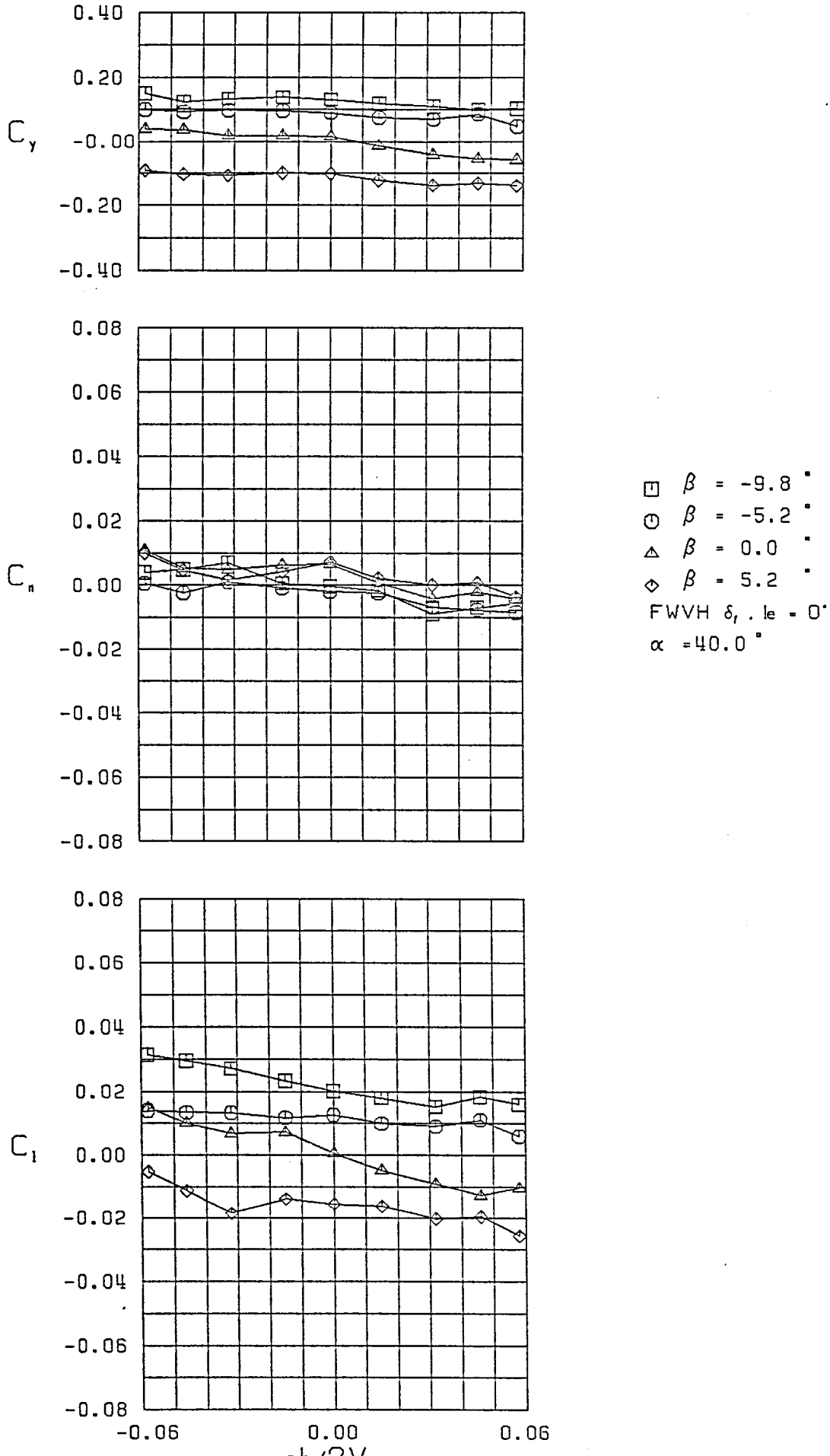

Figure 19 (Continued)

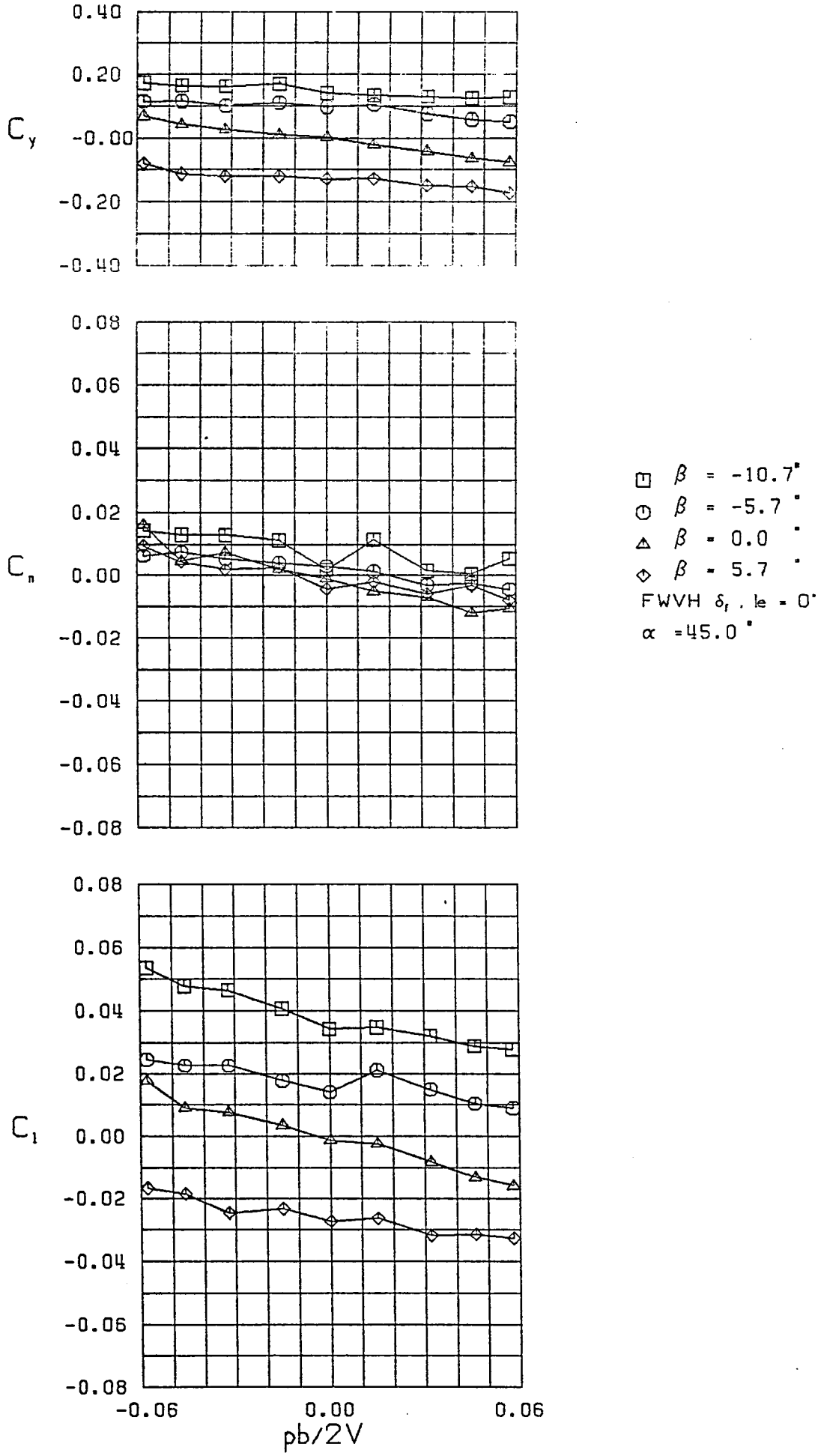

Figure 19 (Continued)

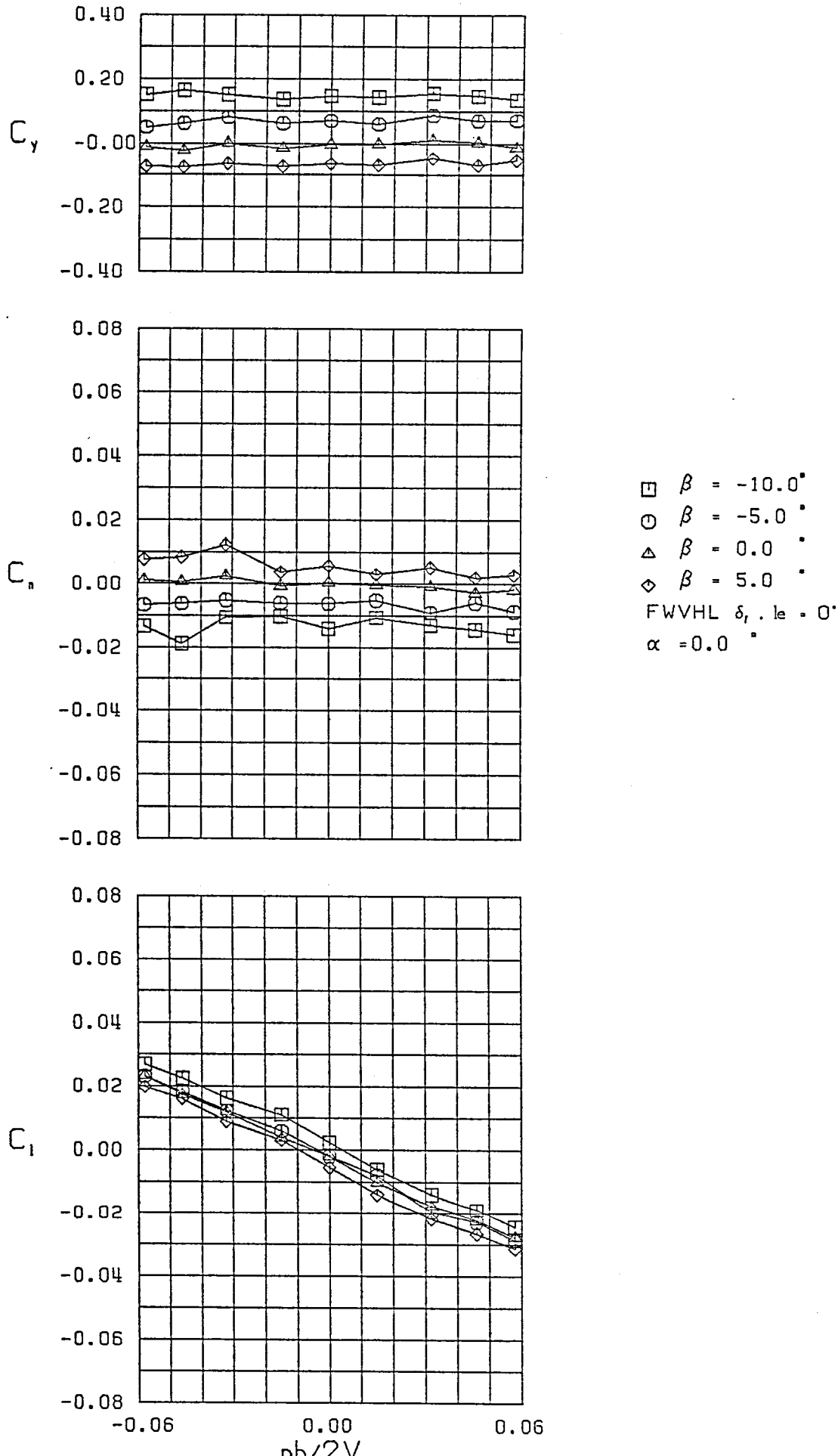

Figure 20 - Variation of Lateral-Directional Characteristics with Roll Rate-Configuration 3

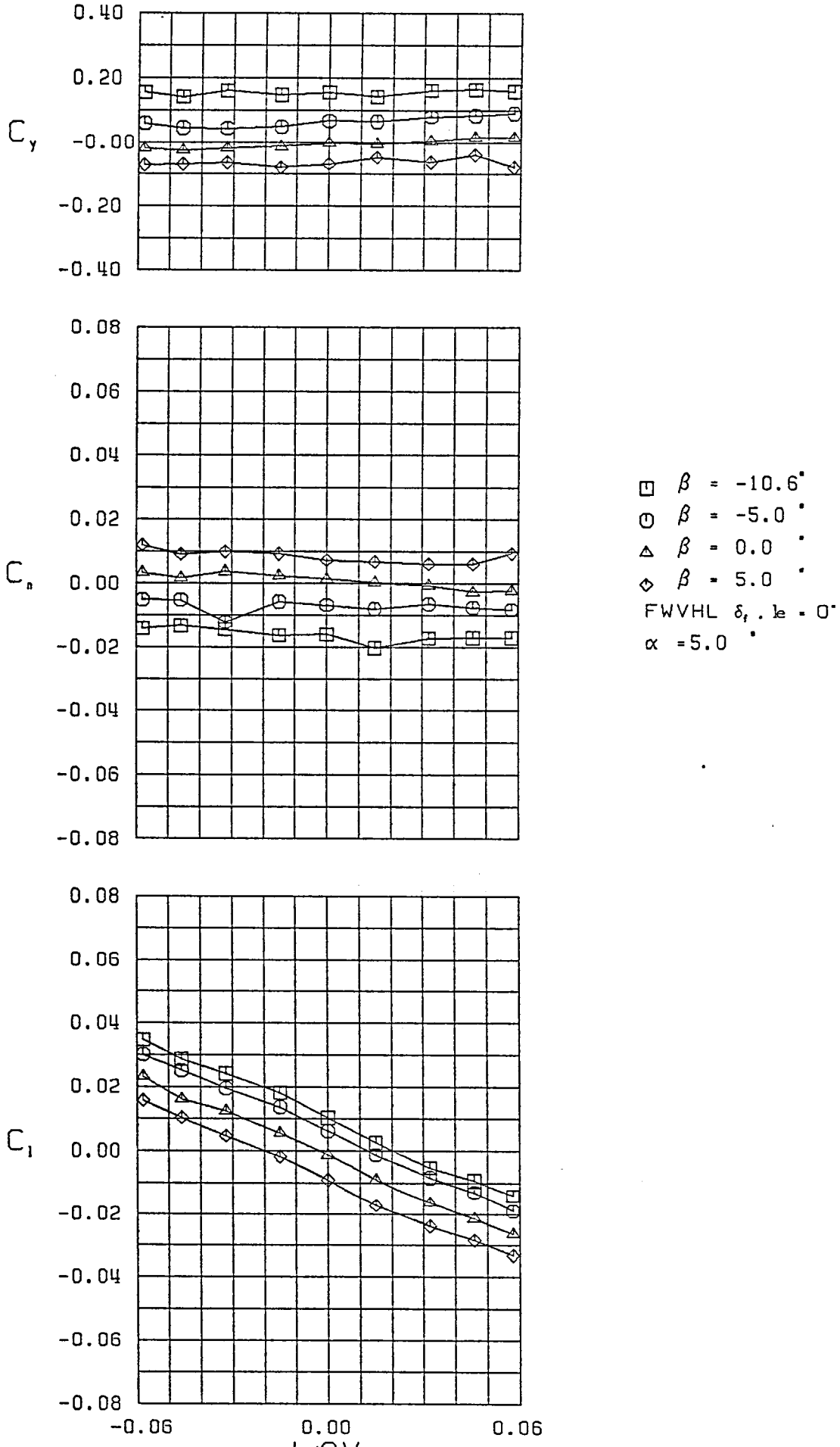

Figure 20 (Continued)

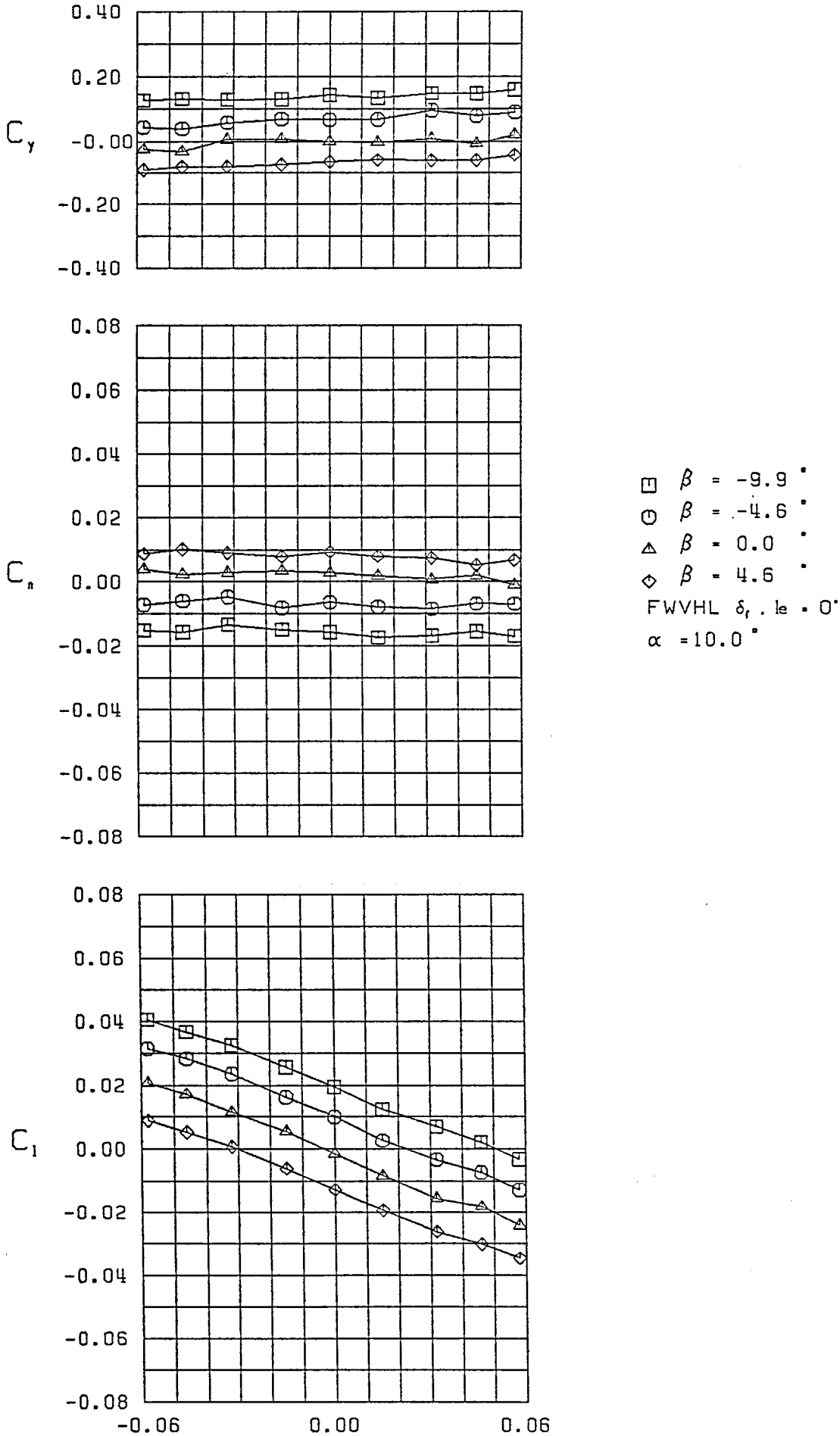

Figure 20 (Continued)

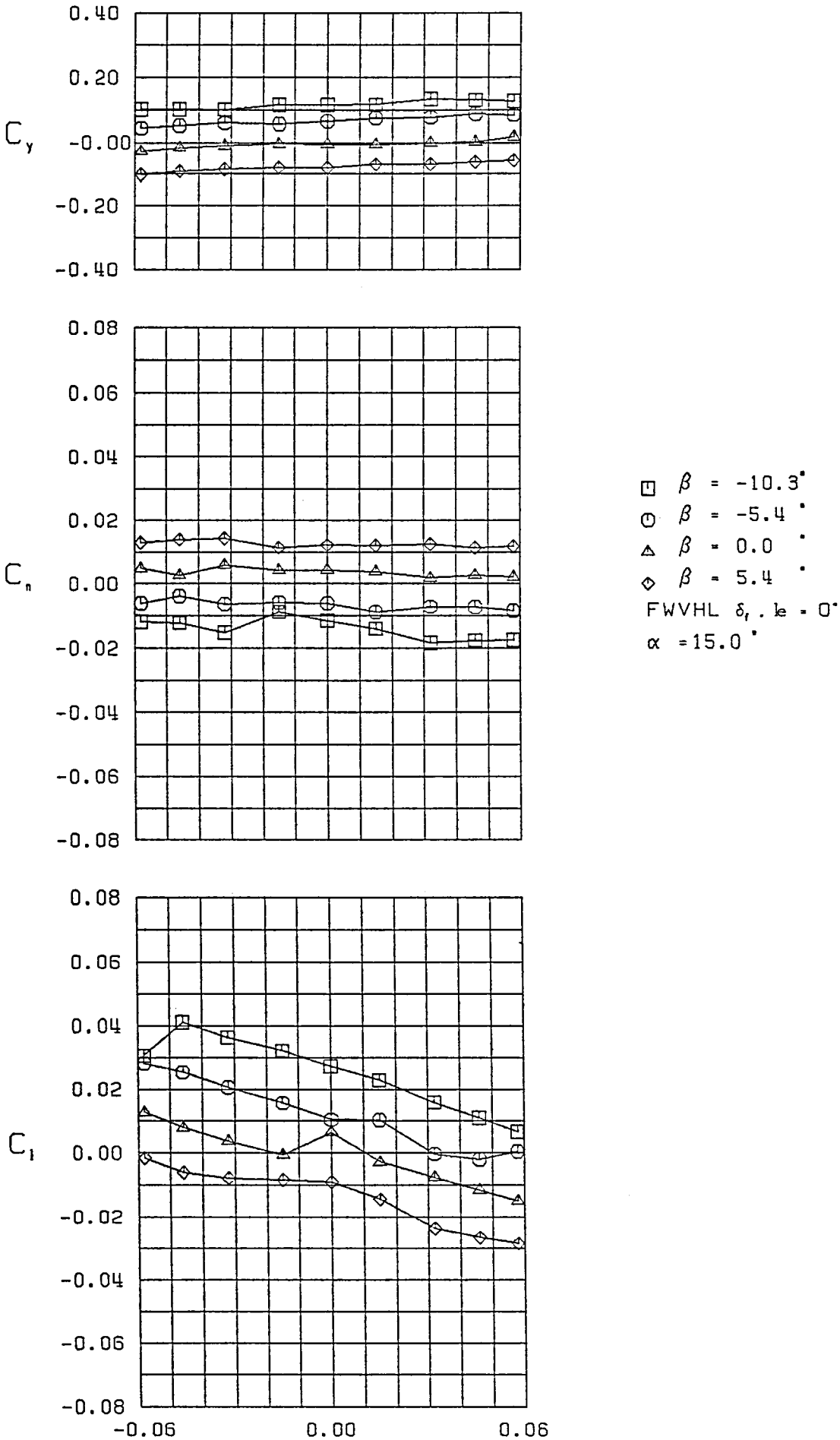

Figure 20 (Continued)

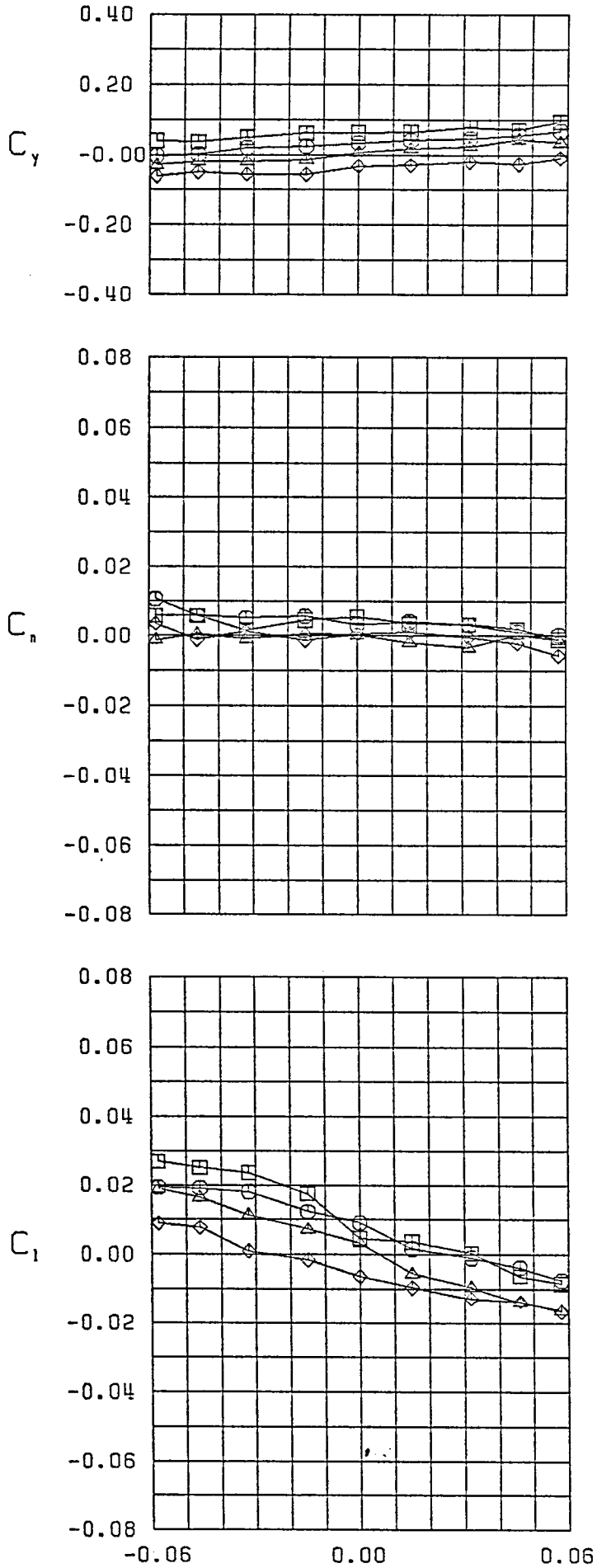

Figure 20 (Continued)

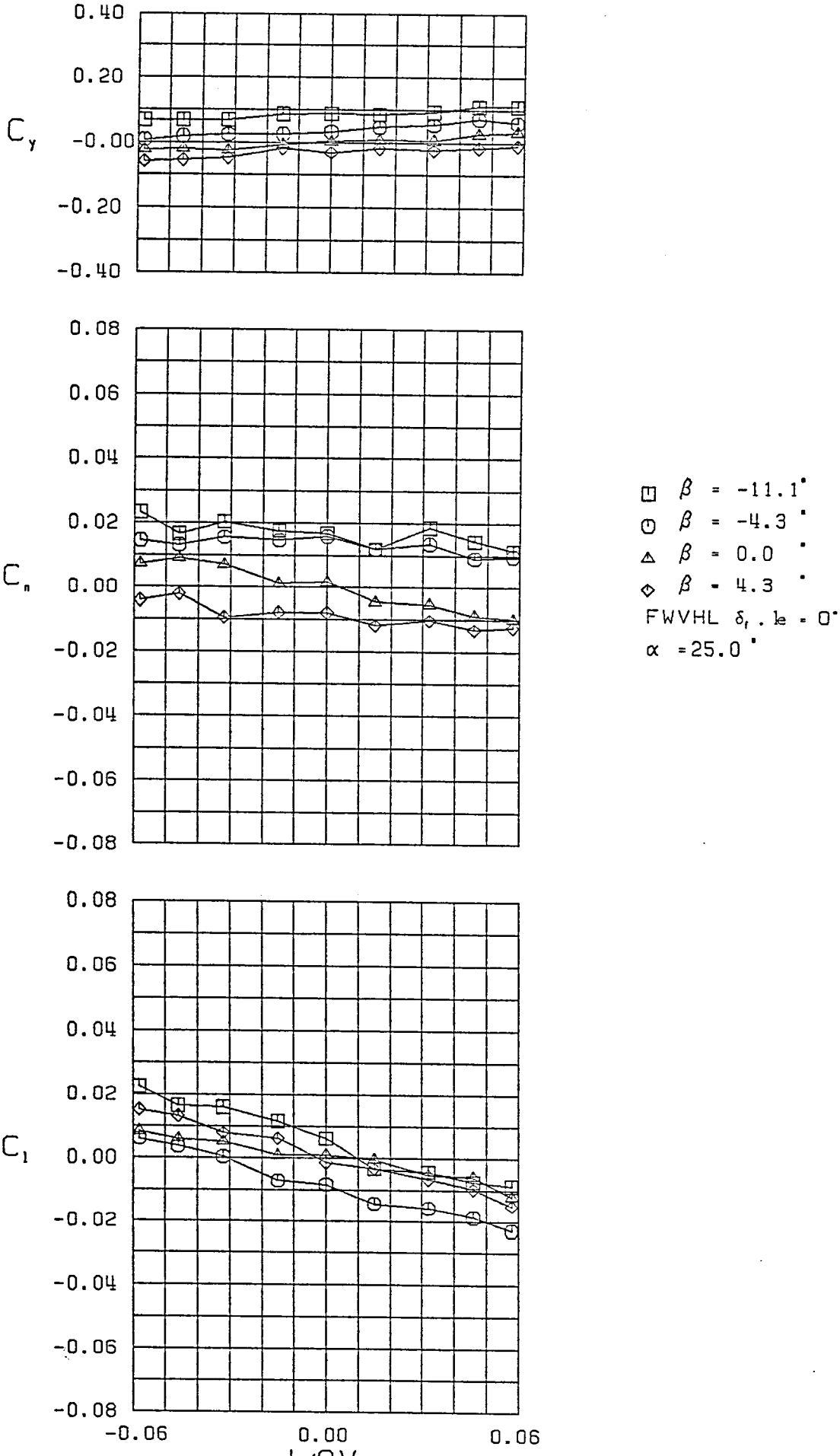

Figure 20 (Continued)

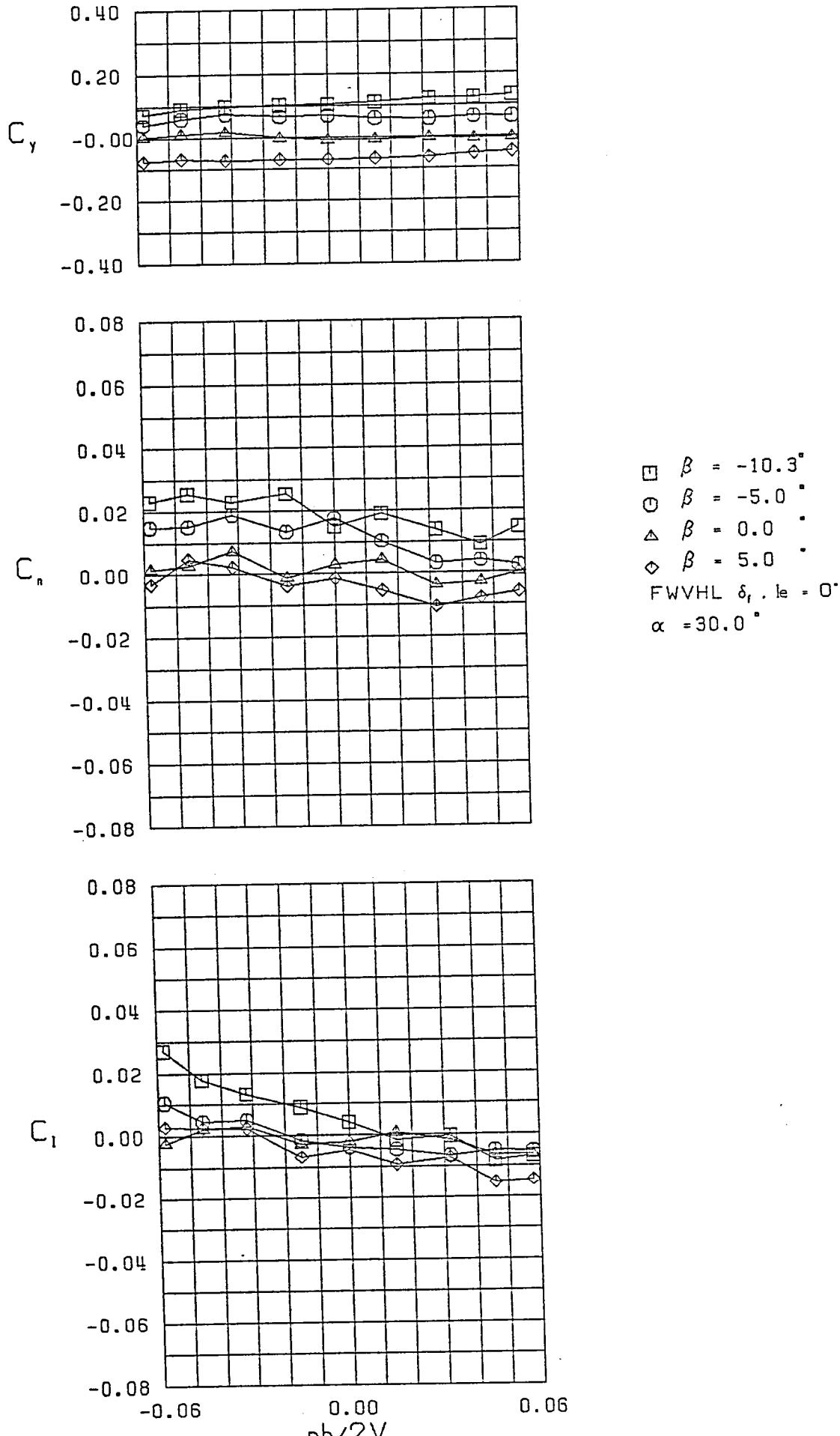

Figure 20 (Continued)

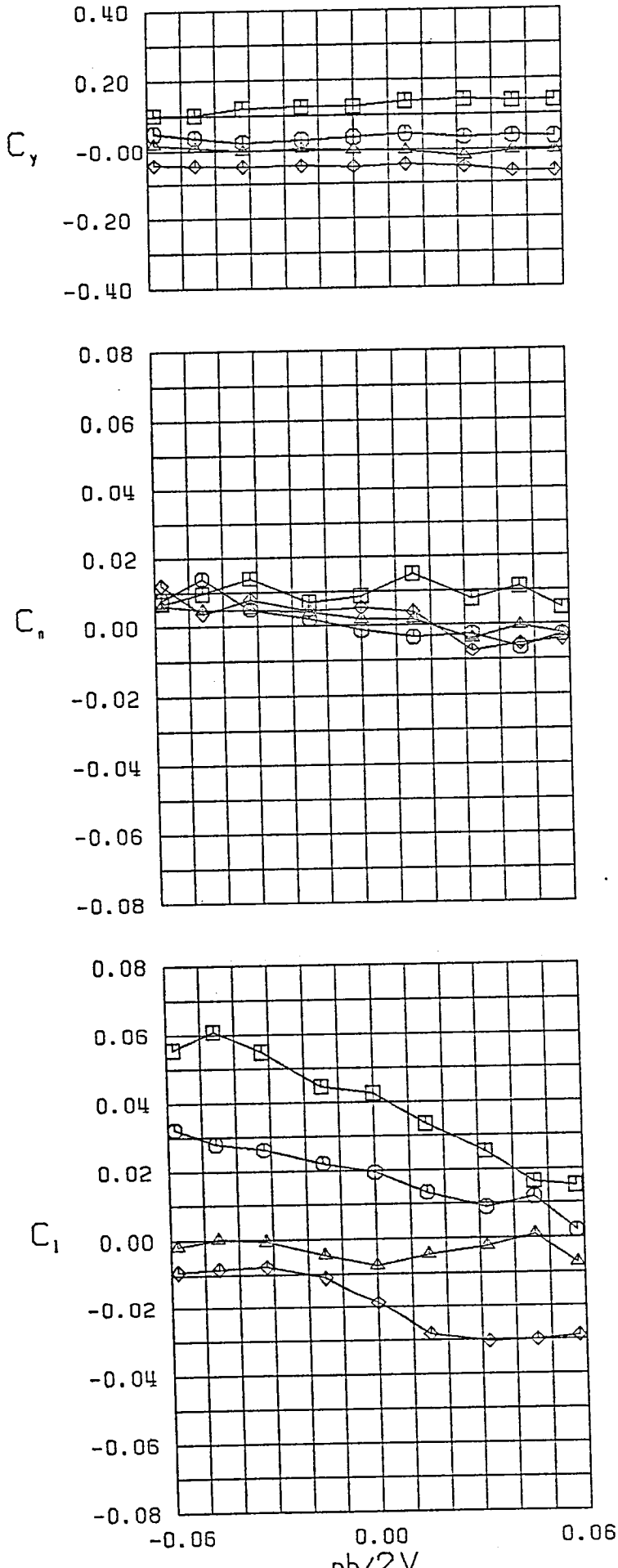

Figure 20 (Continued)

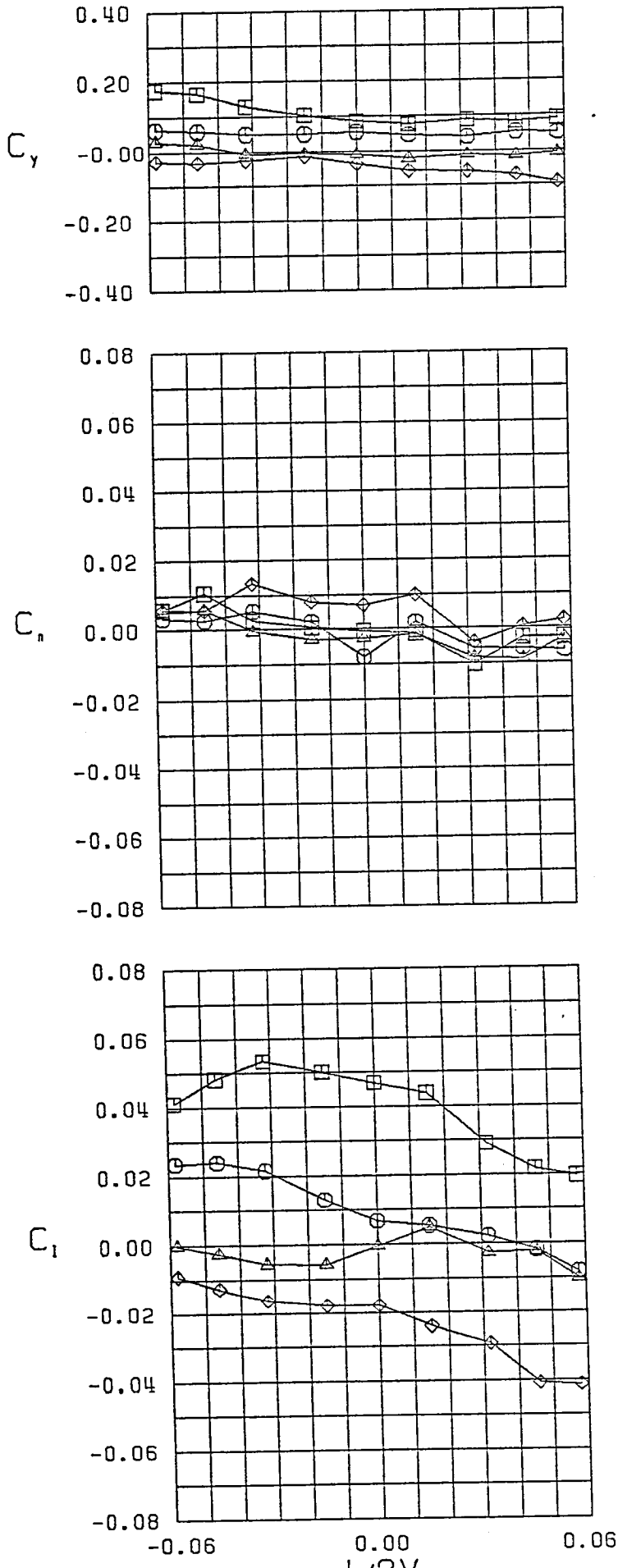

Figure 20 (Continued)

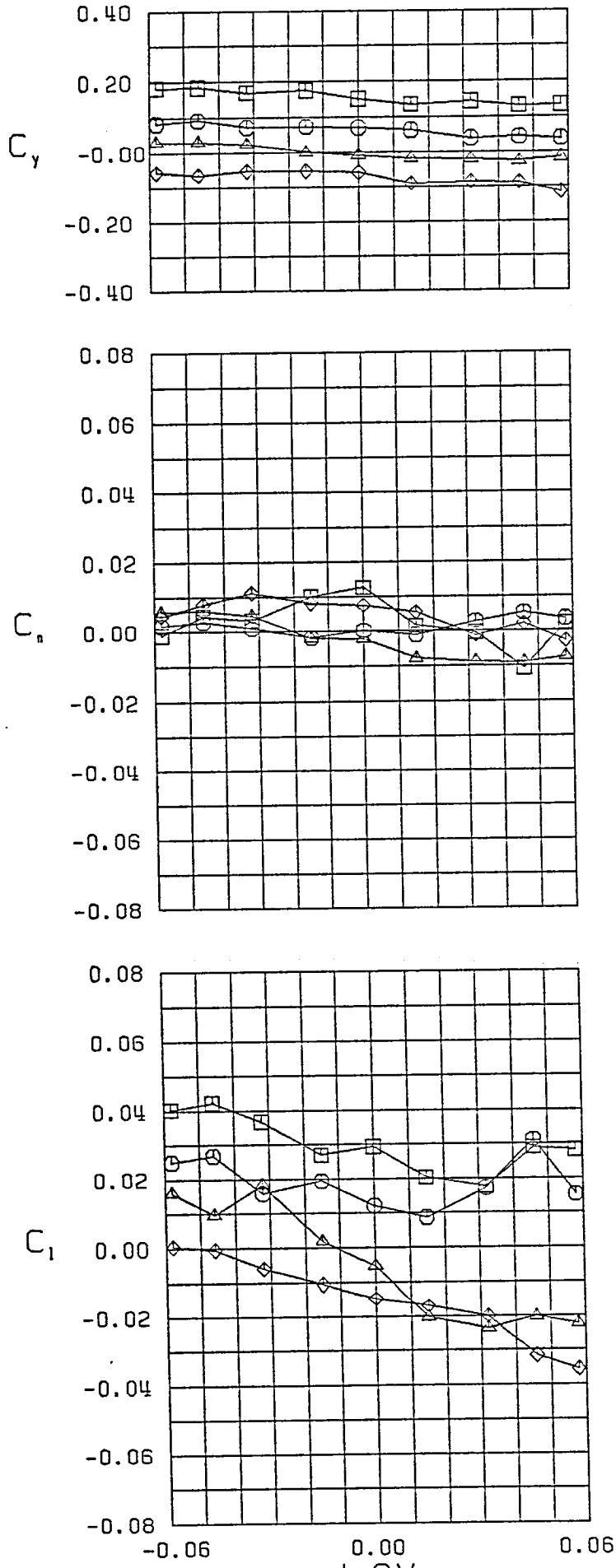

Figure 20 (Continued)

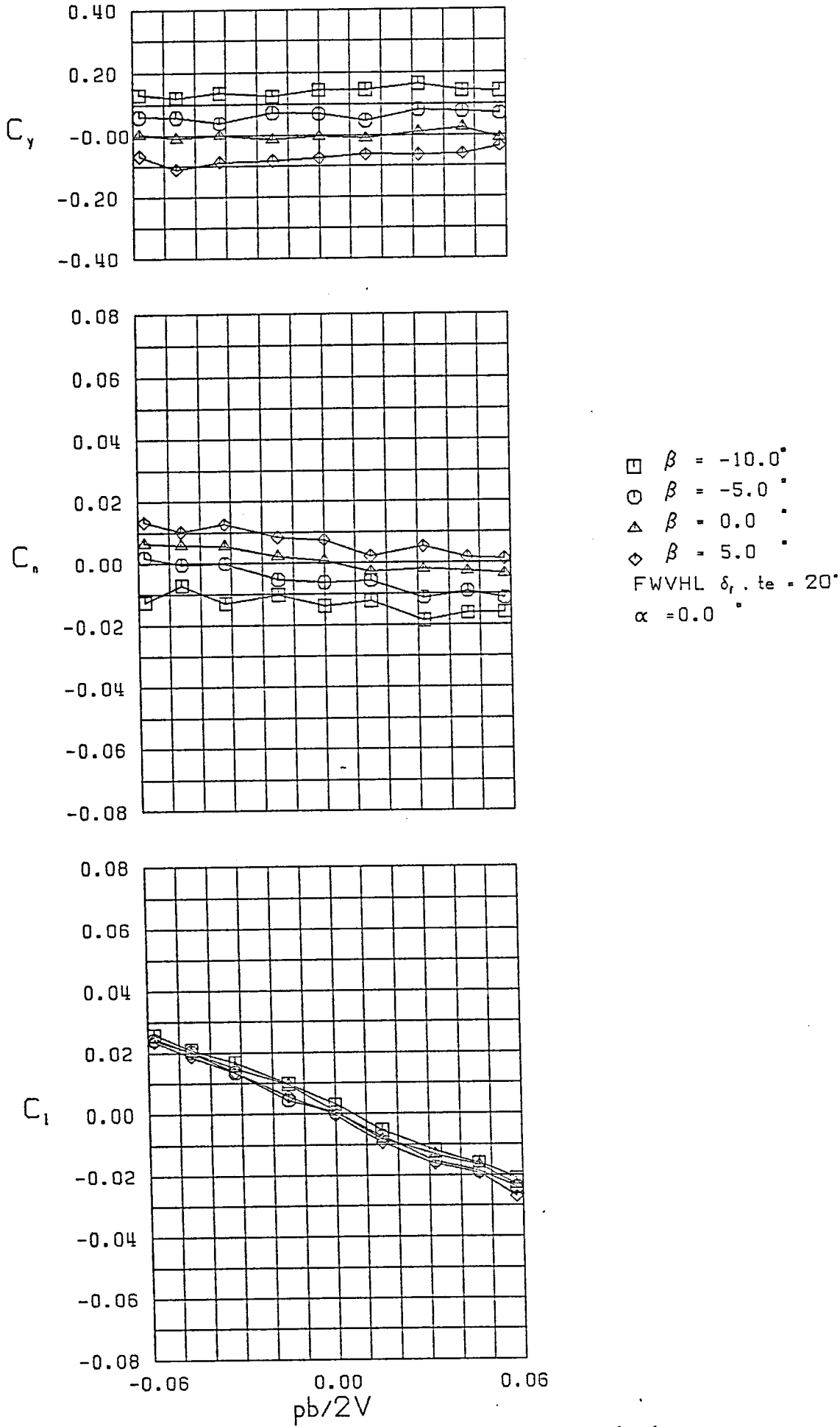

Figure 21 - Variation of Lateral-Directional Characteristics with Roll Rate-Configuration 4

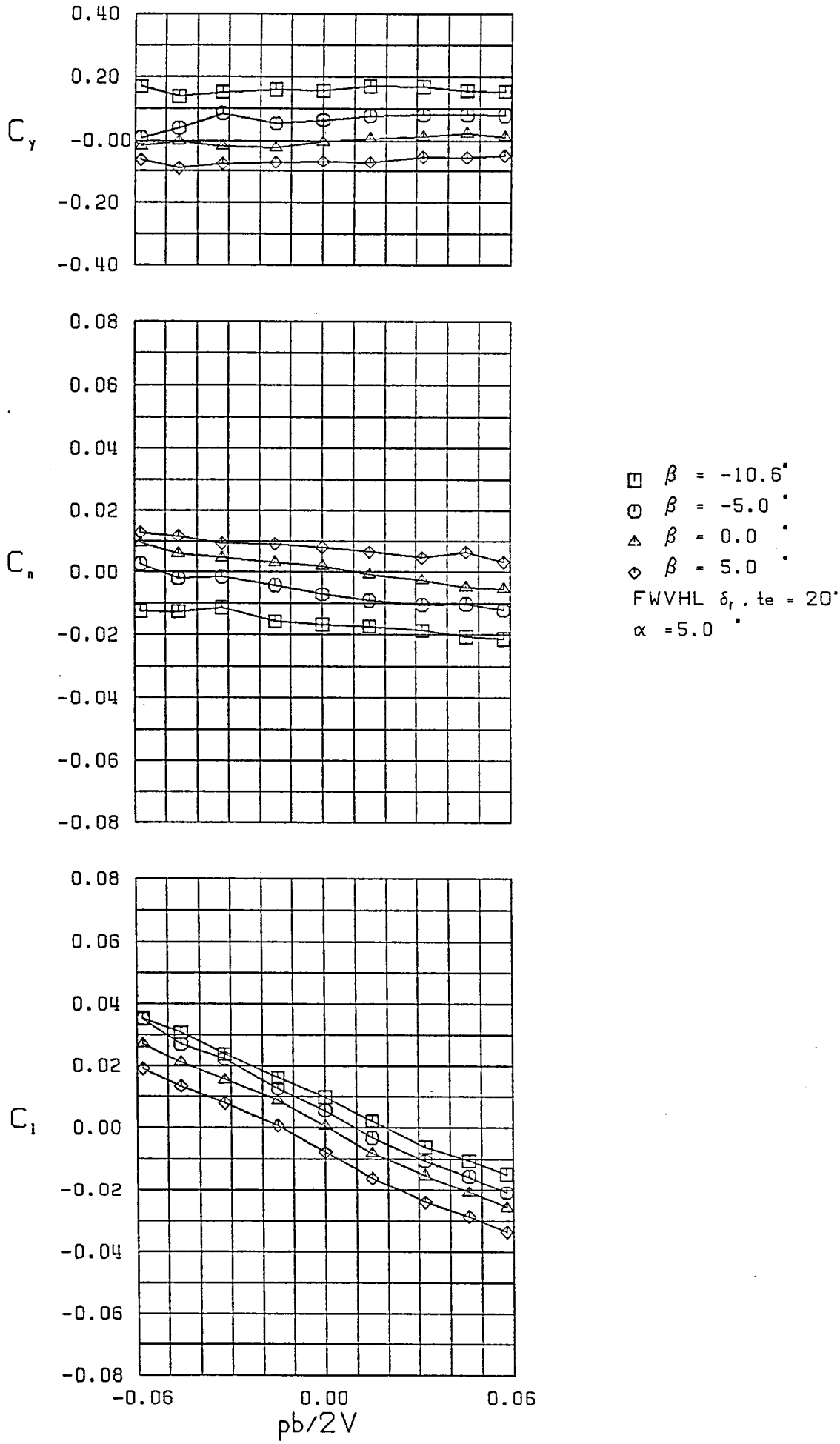

Figure 21 (Continued)

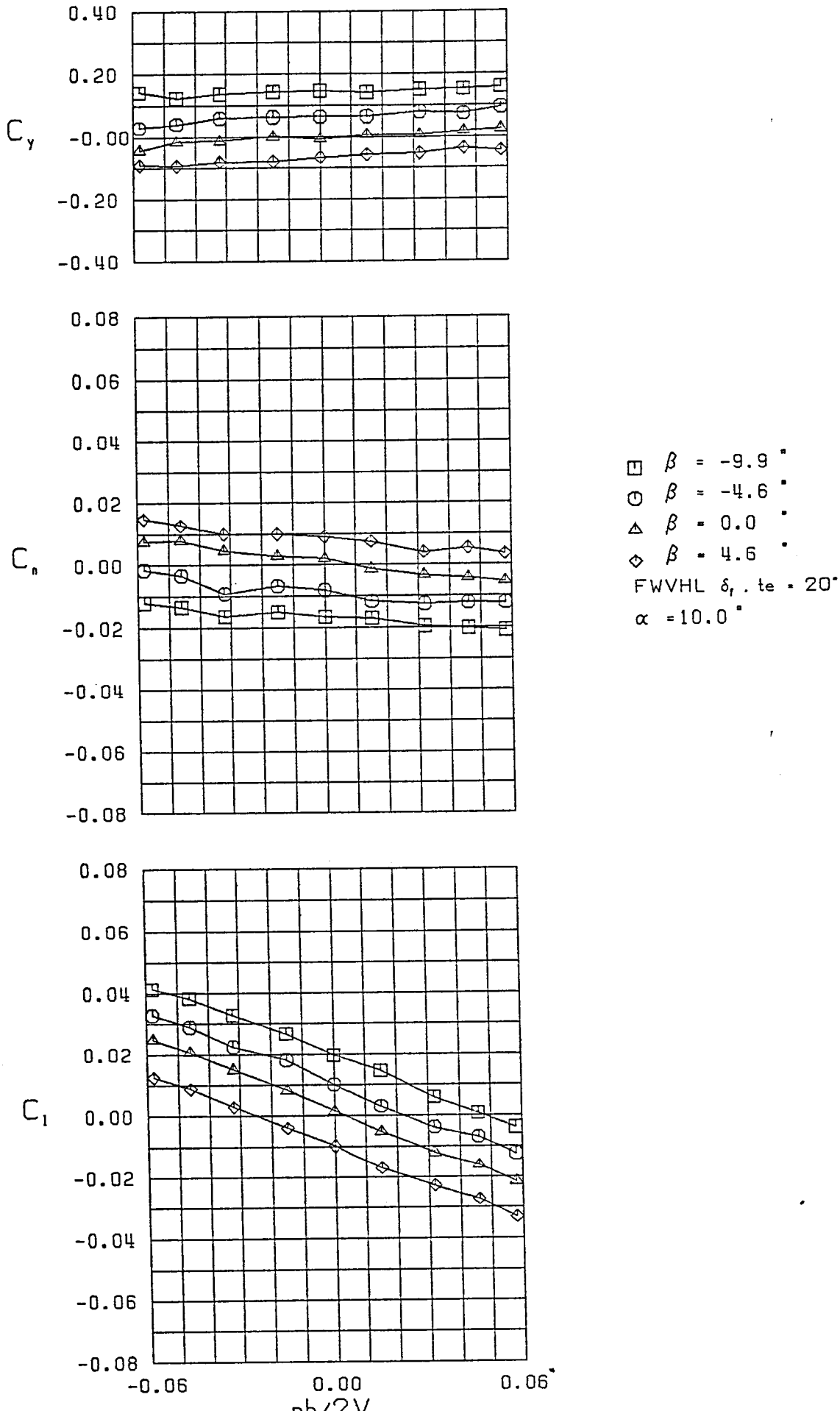

Figure 21 (Continued)

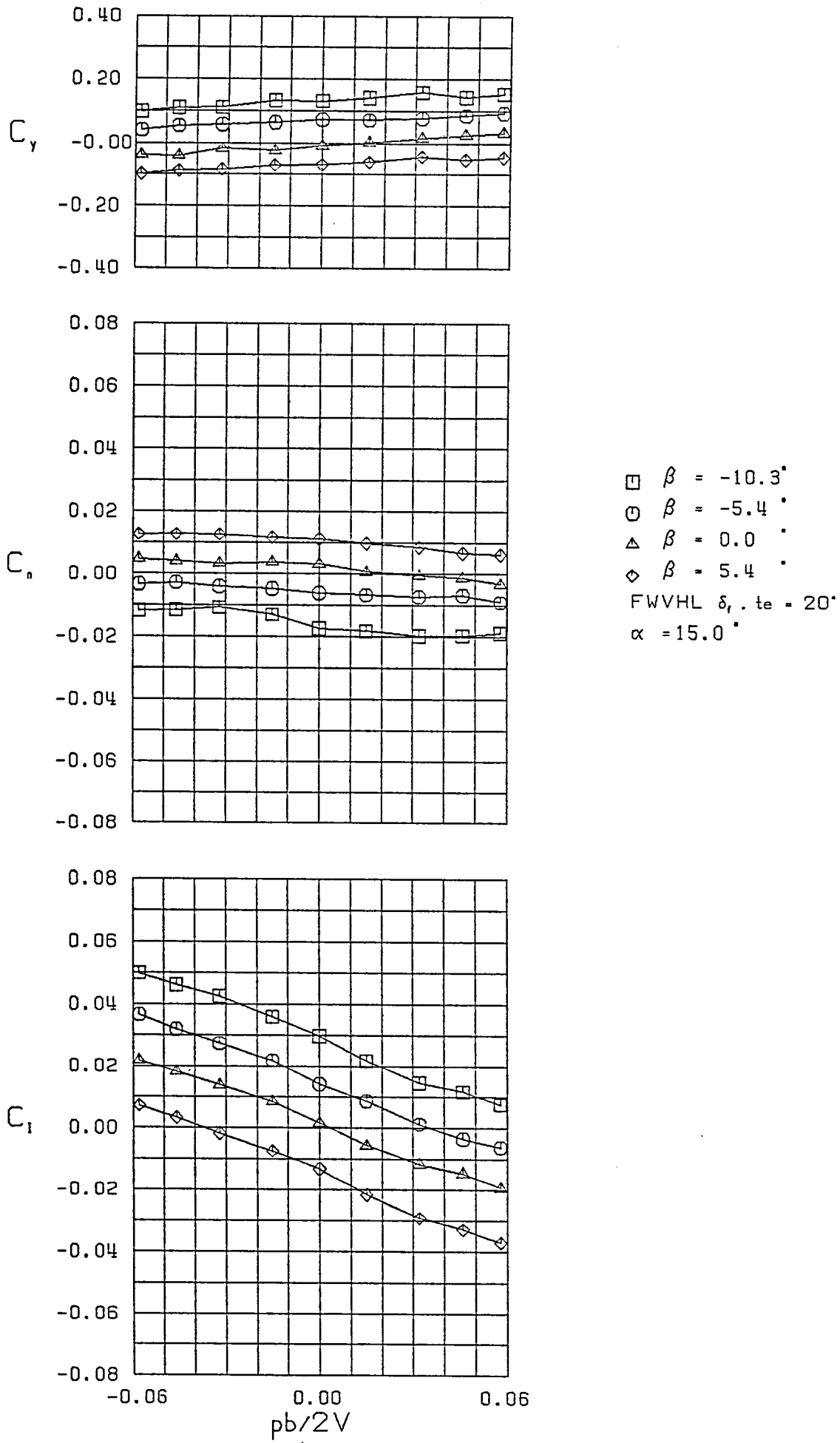

Figure 21 (Continued)

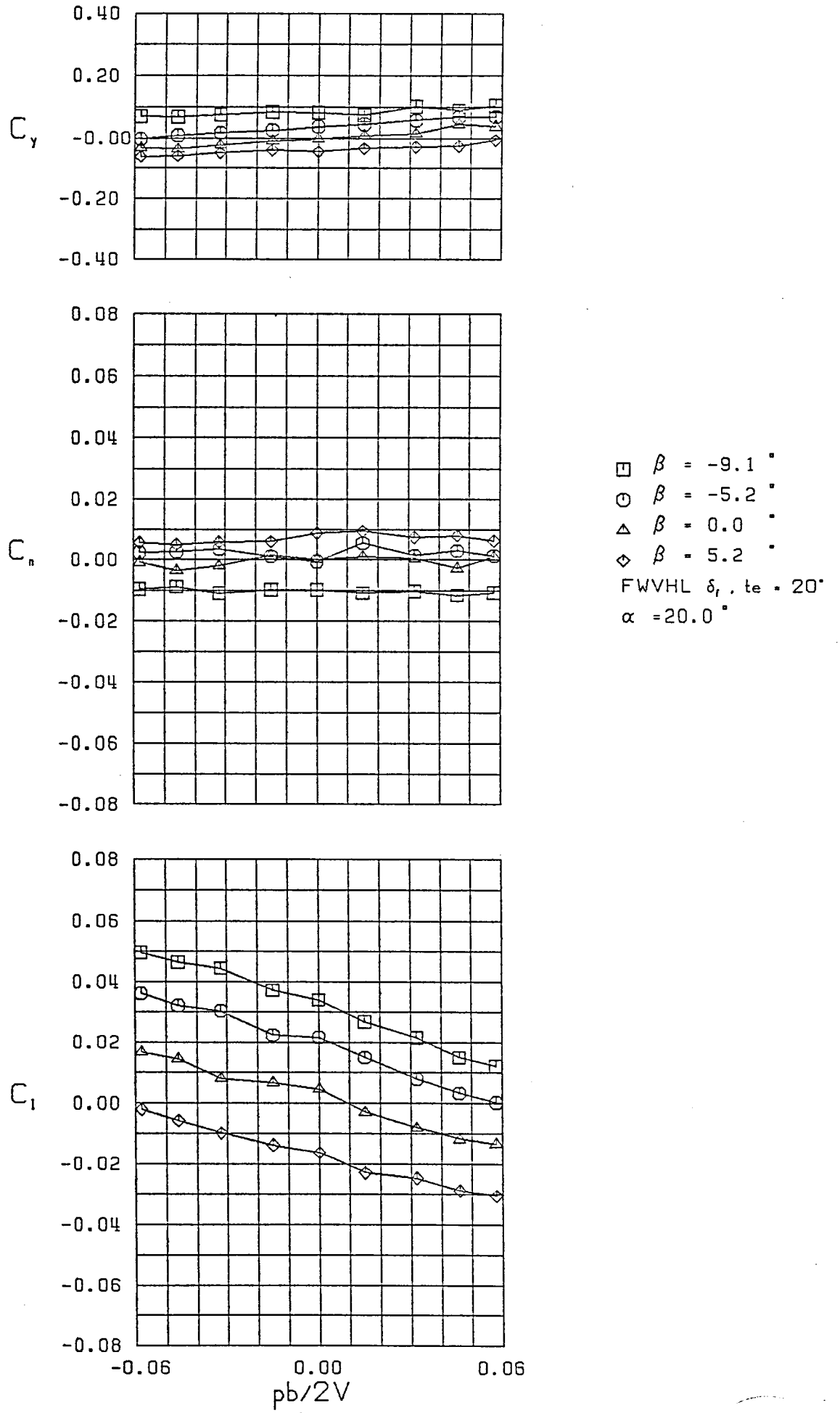

Figure 21 (Continued)

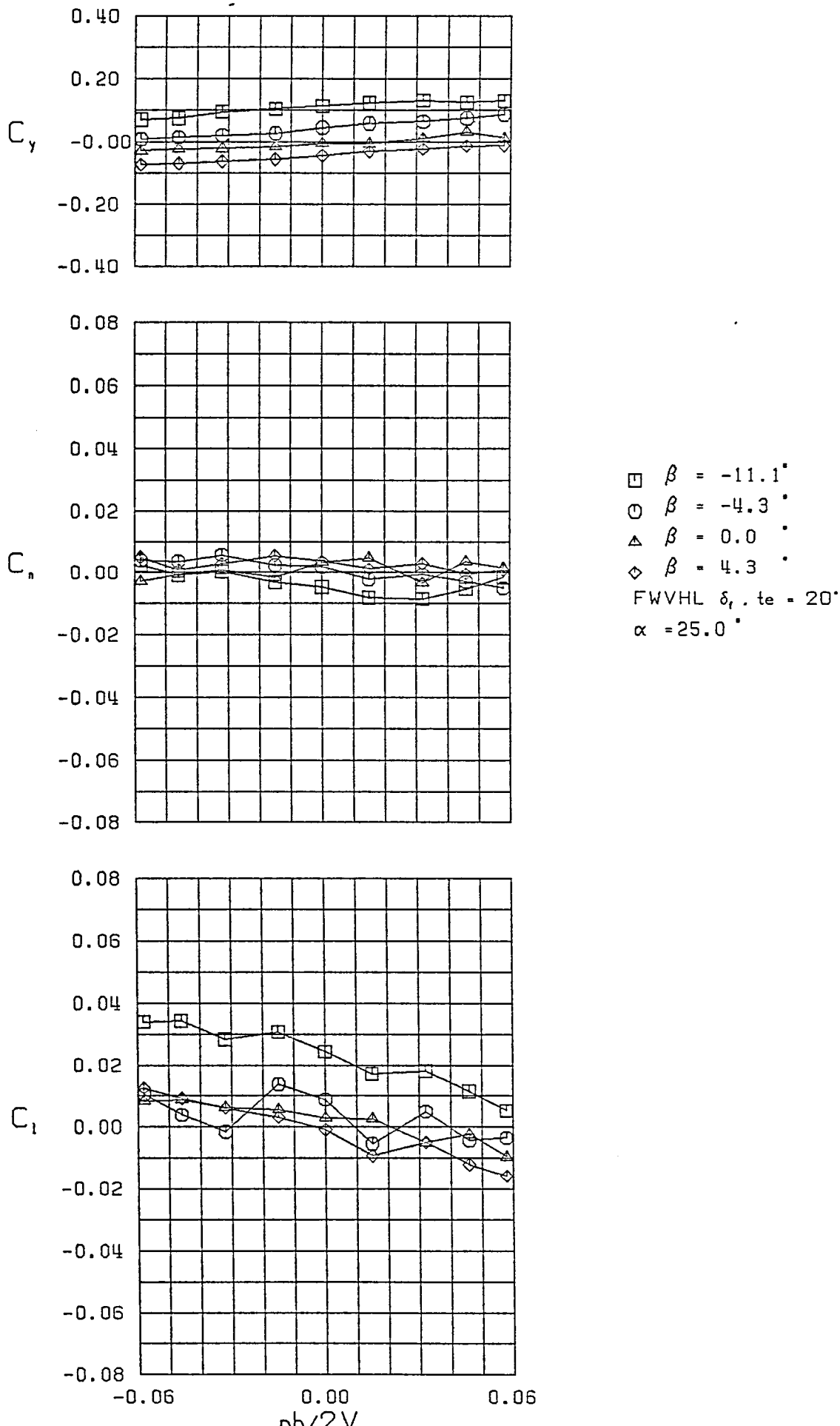

Figure 21 (Continued)

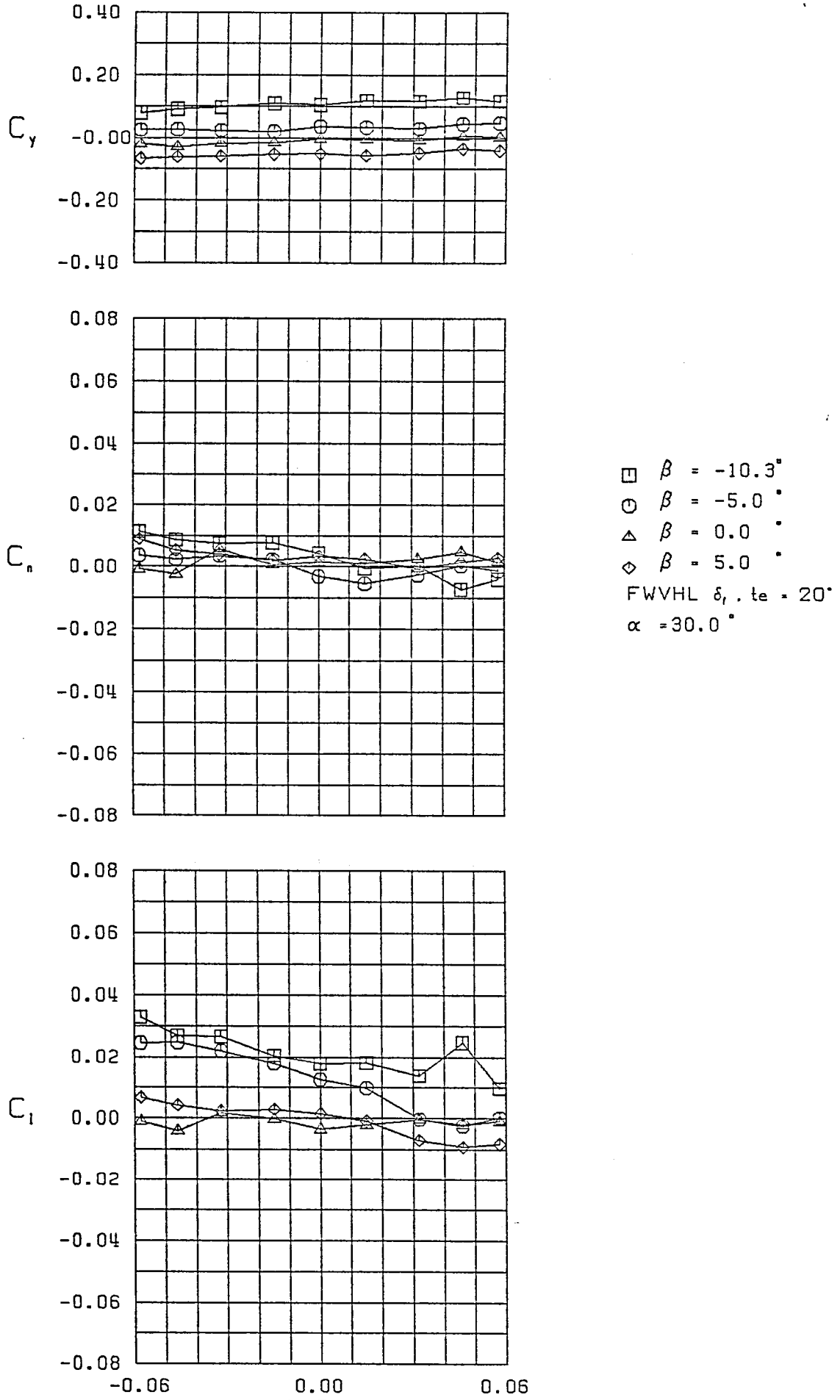

Figure 21 (Continued)

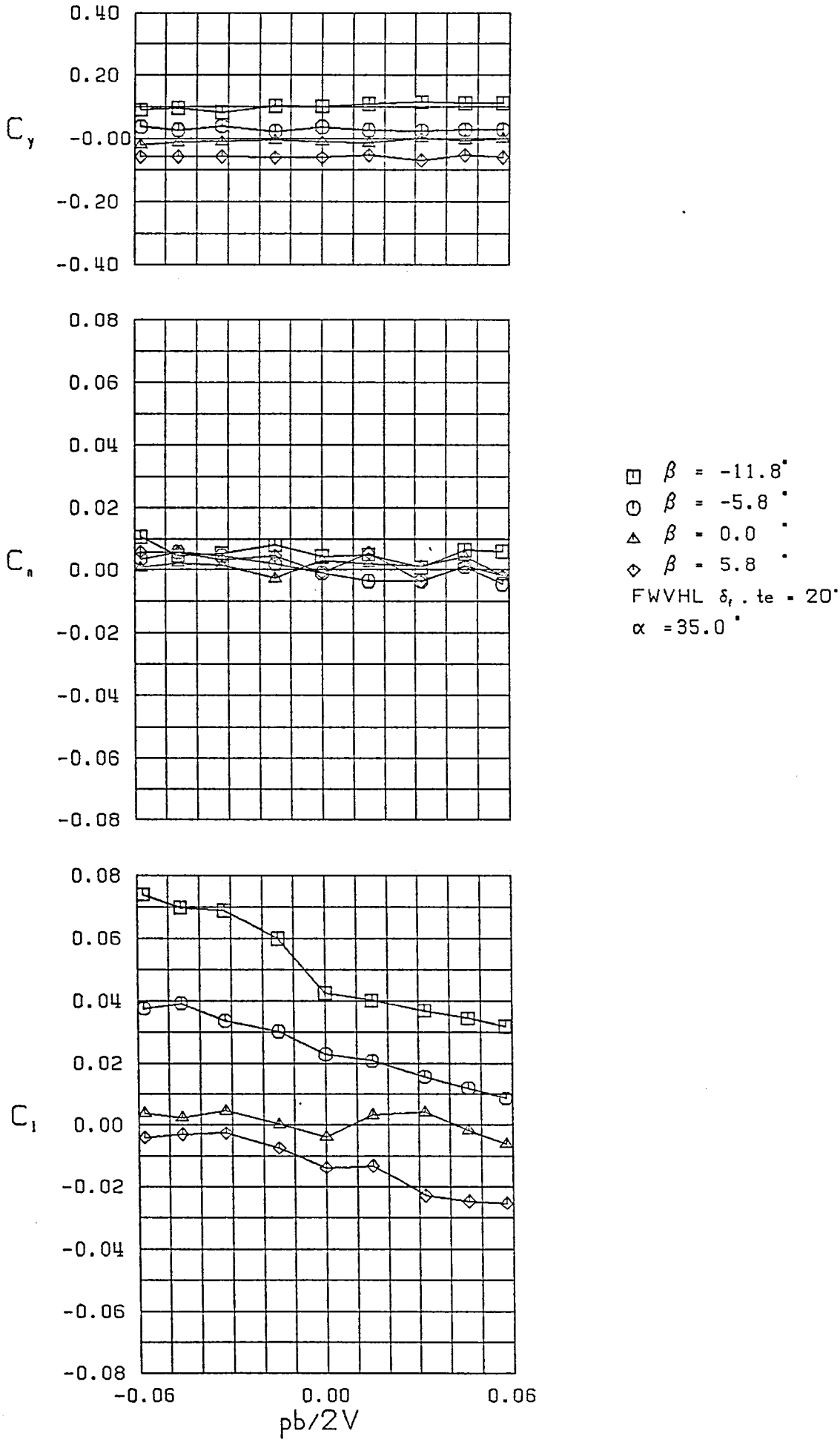

Figure 21 (Continued)

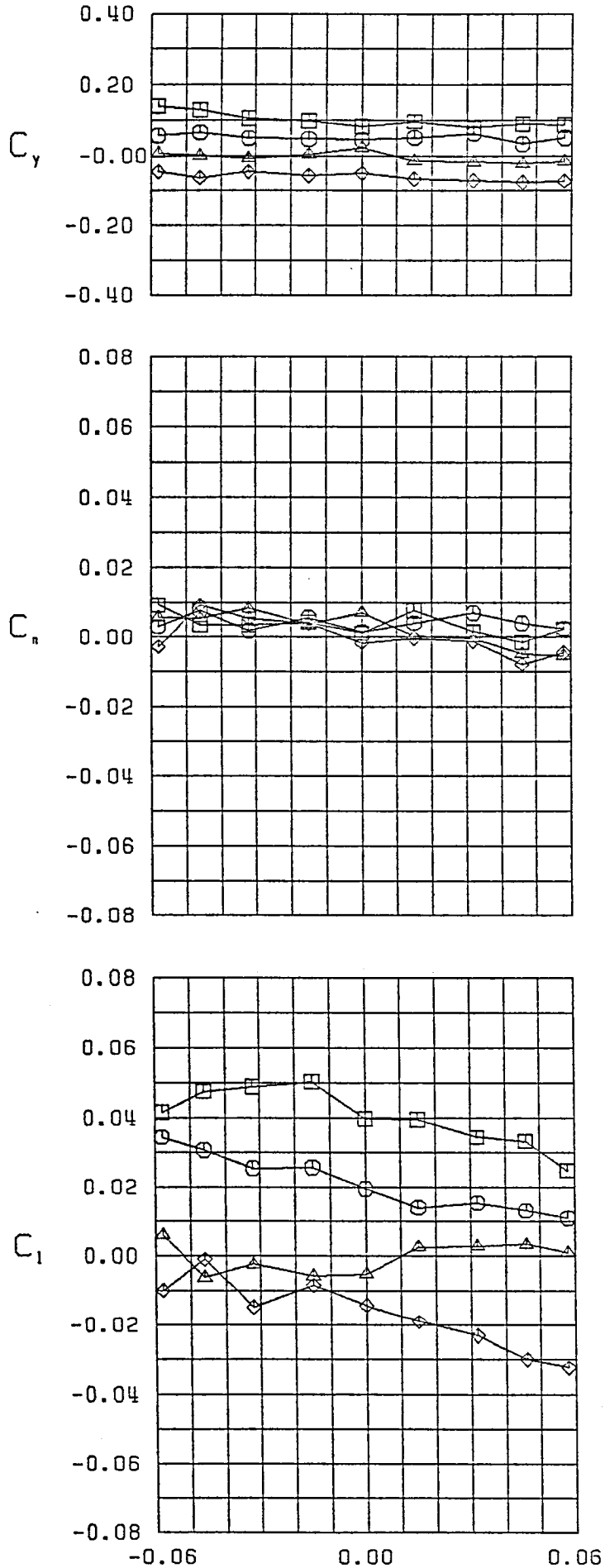

Figure 21 (Continued)

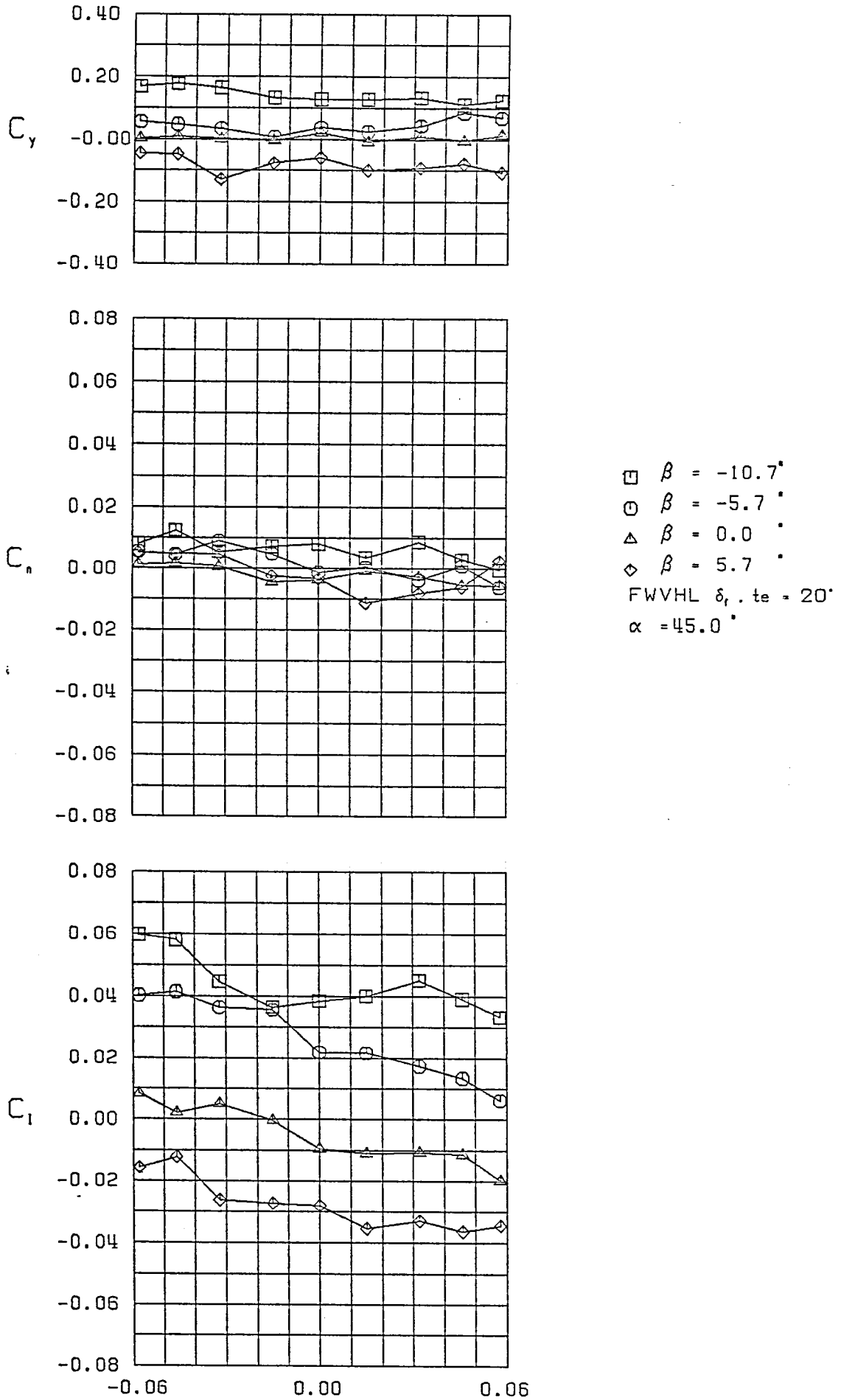

Figure 21 (Continued)

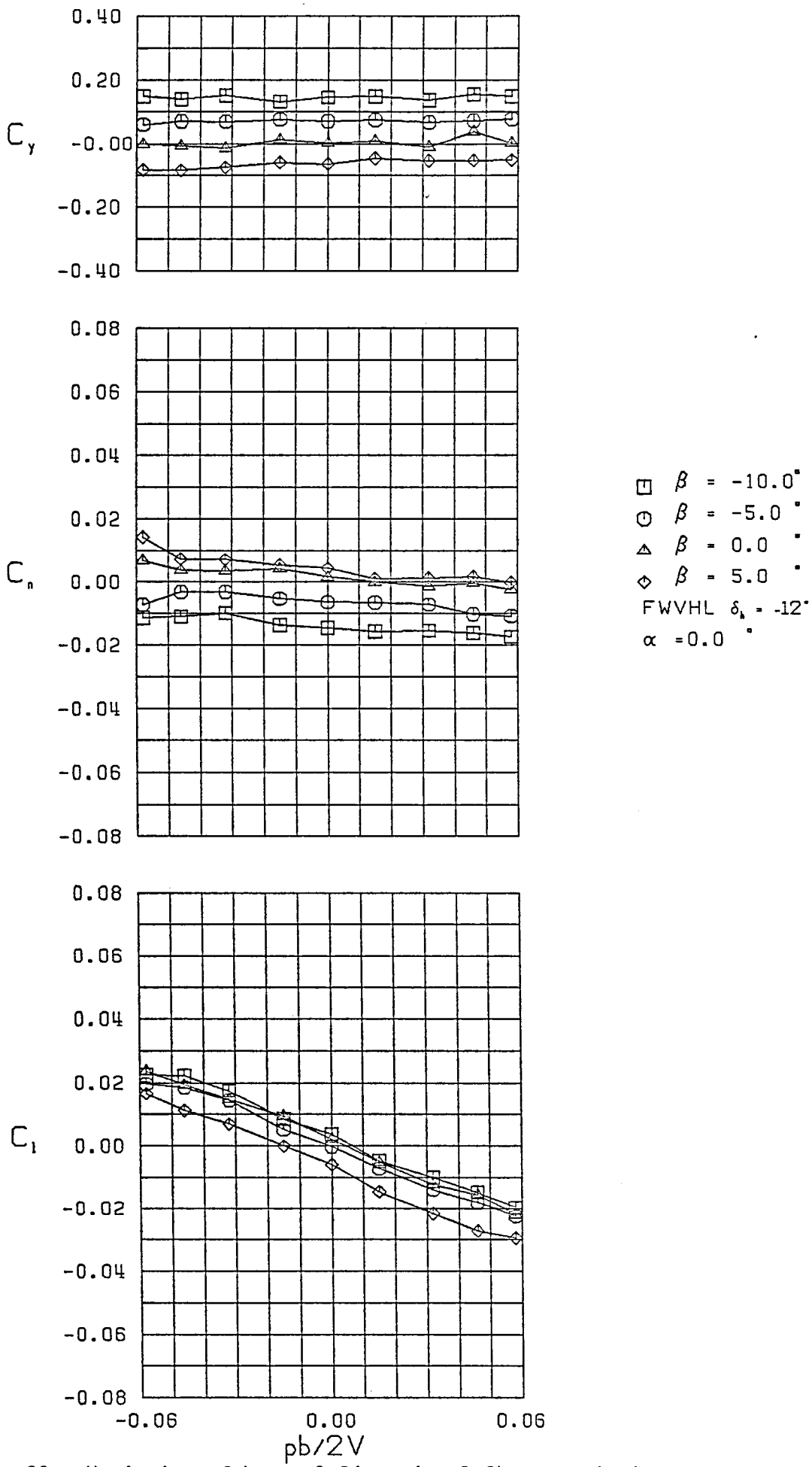

Figure 22 - Variation of Lateral-Directional Characteristics with Roll Rate-Configuration 2

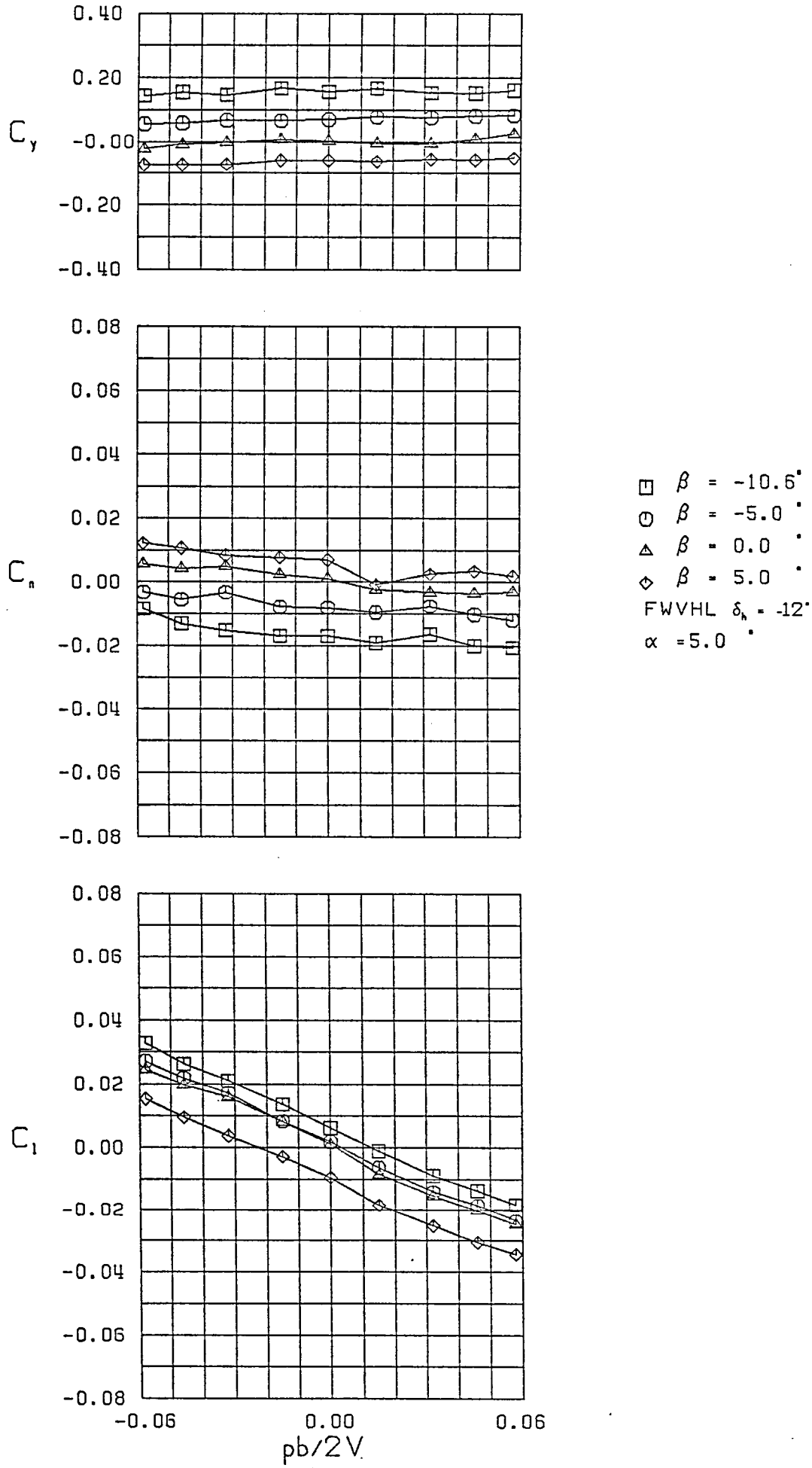

Figure 22 (Continued)

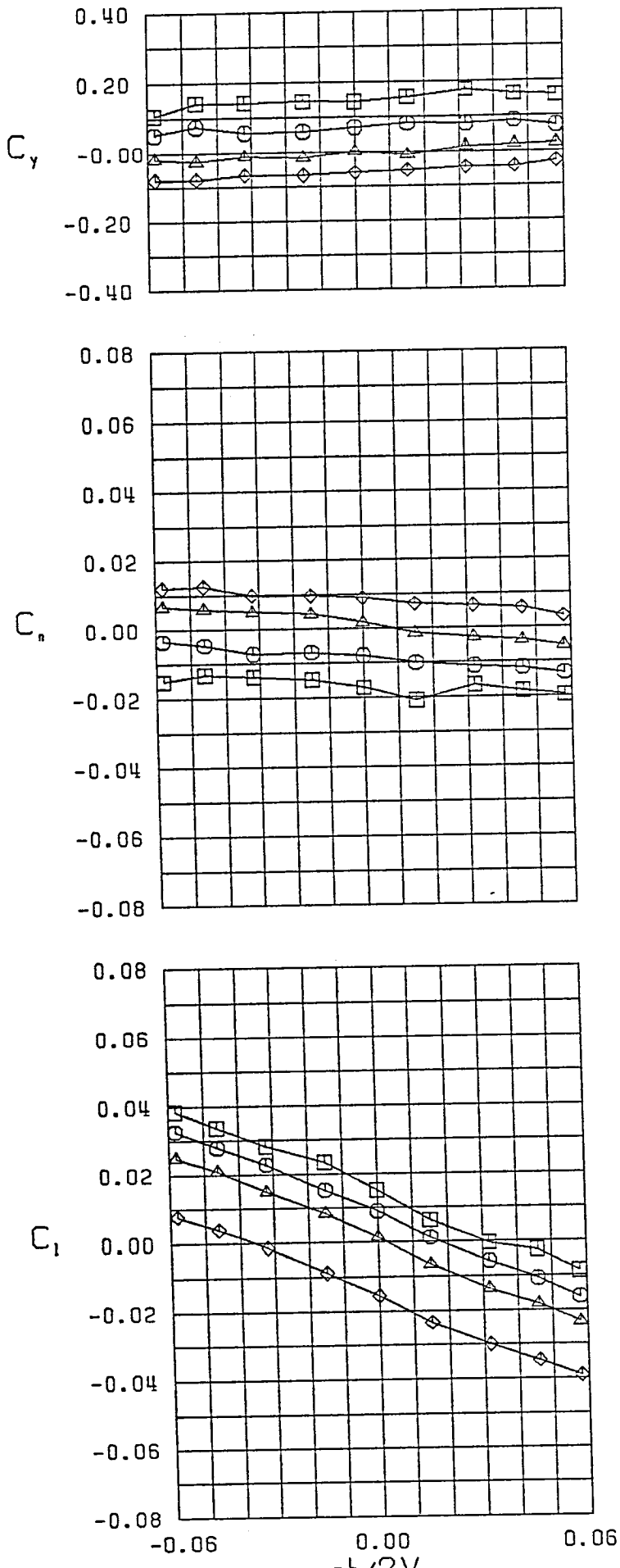

Figure 22 (Continued)

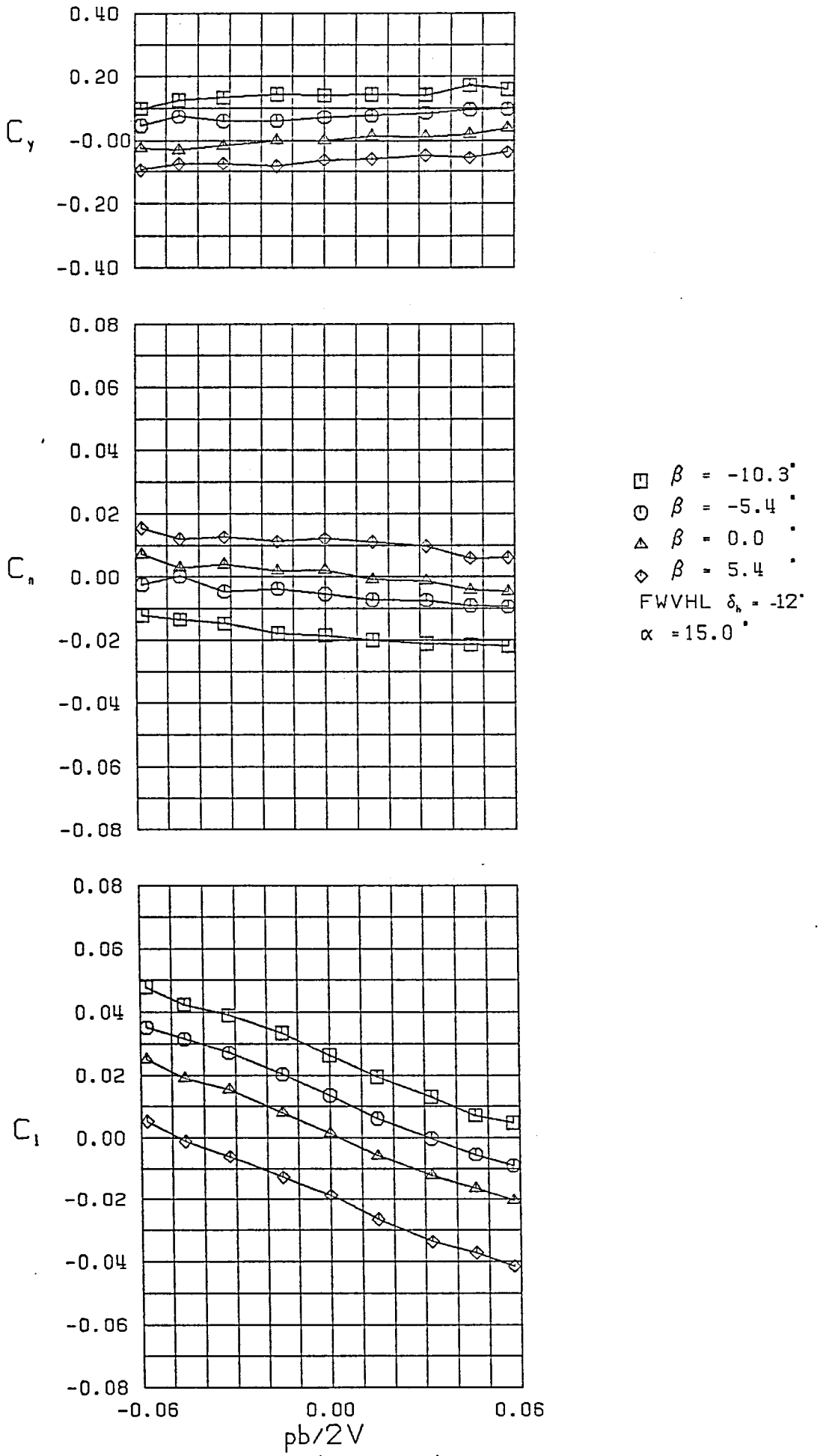

Figure 22 (Continued)

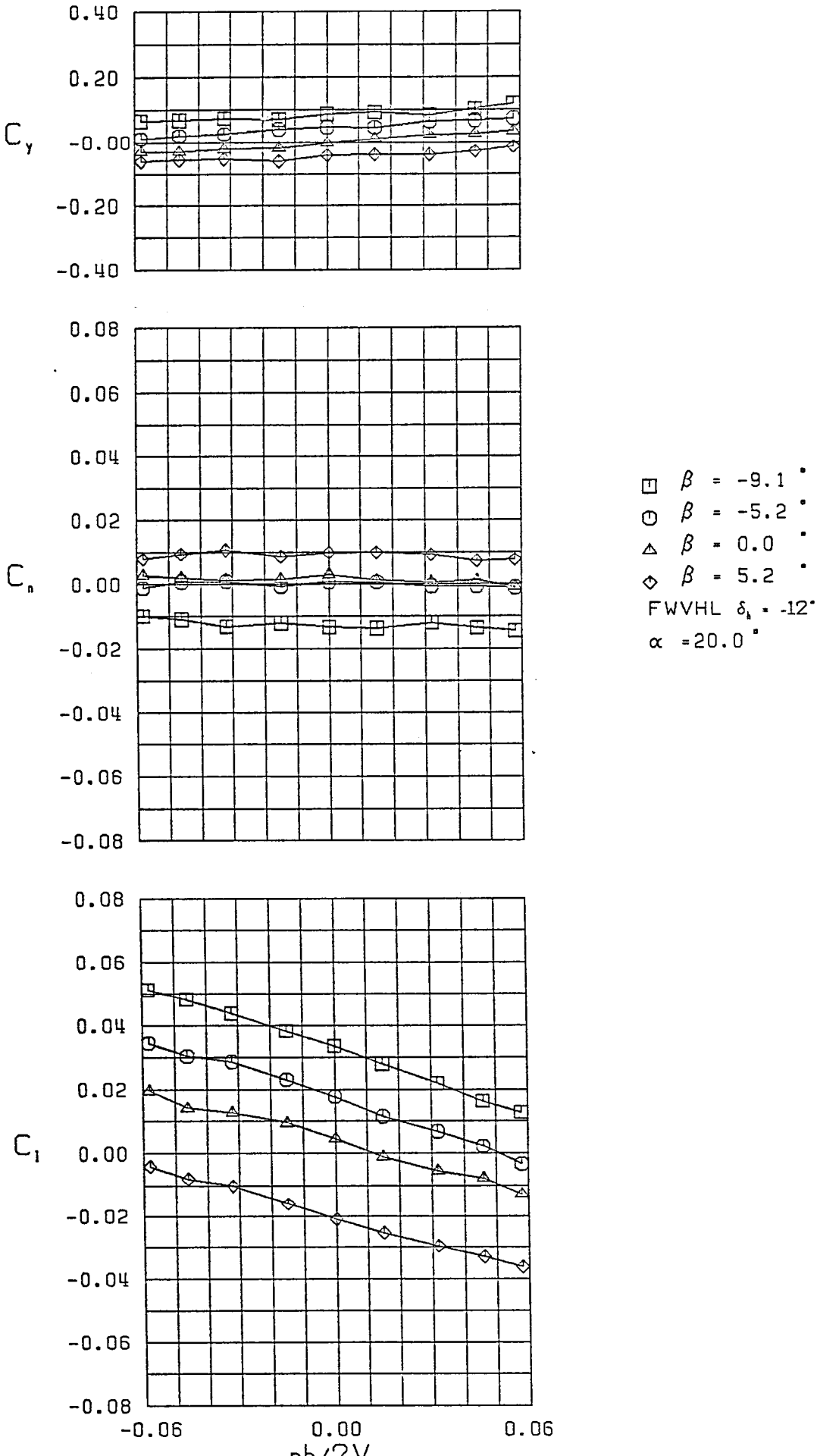

Figure 22 (Continued)

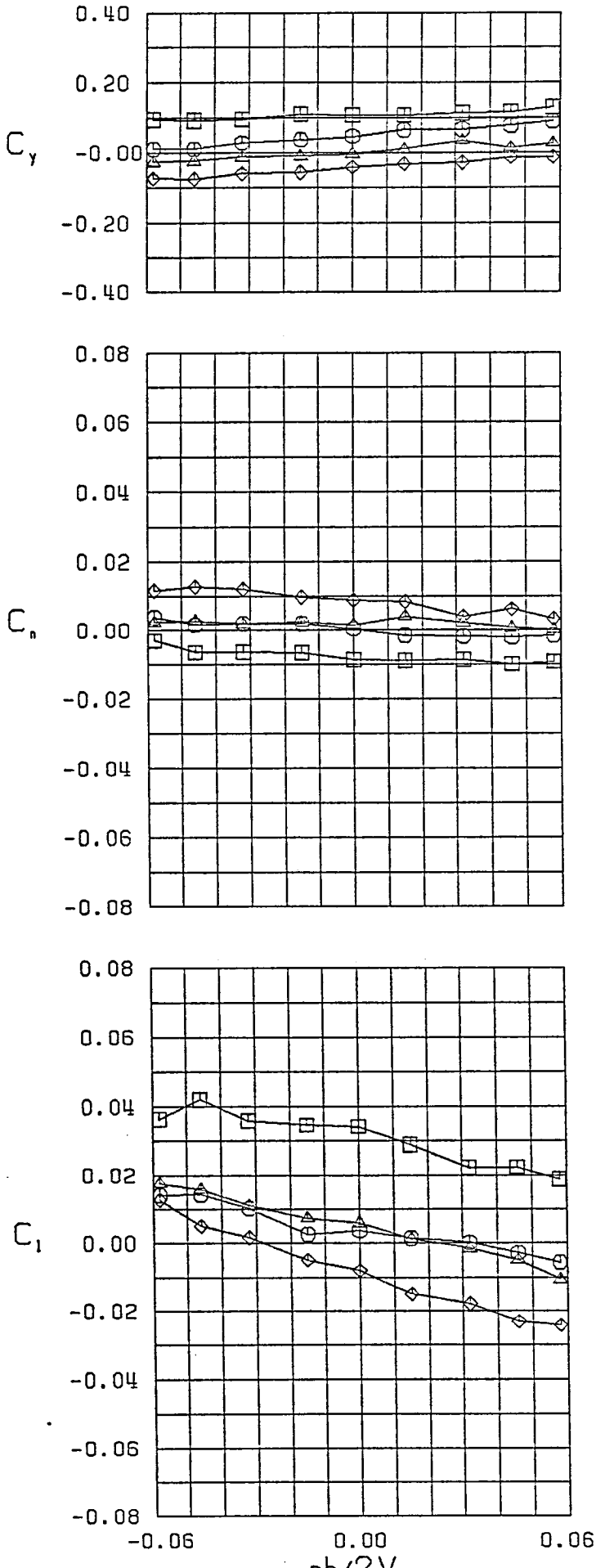

Figure 22 (Continued)

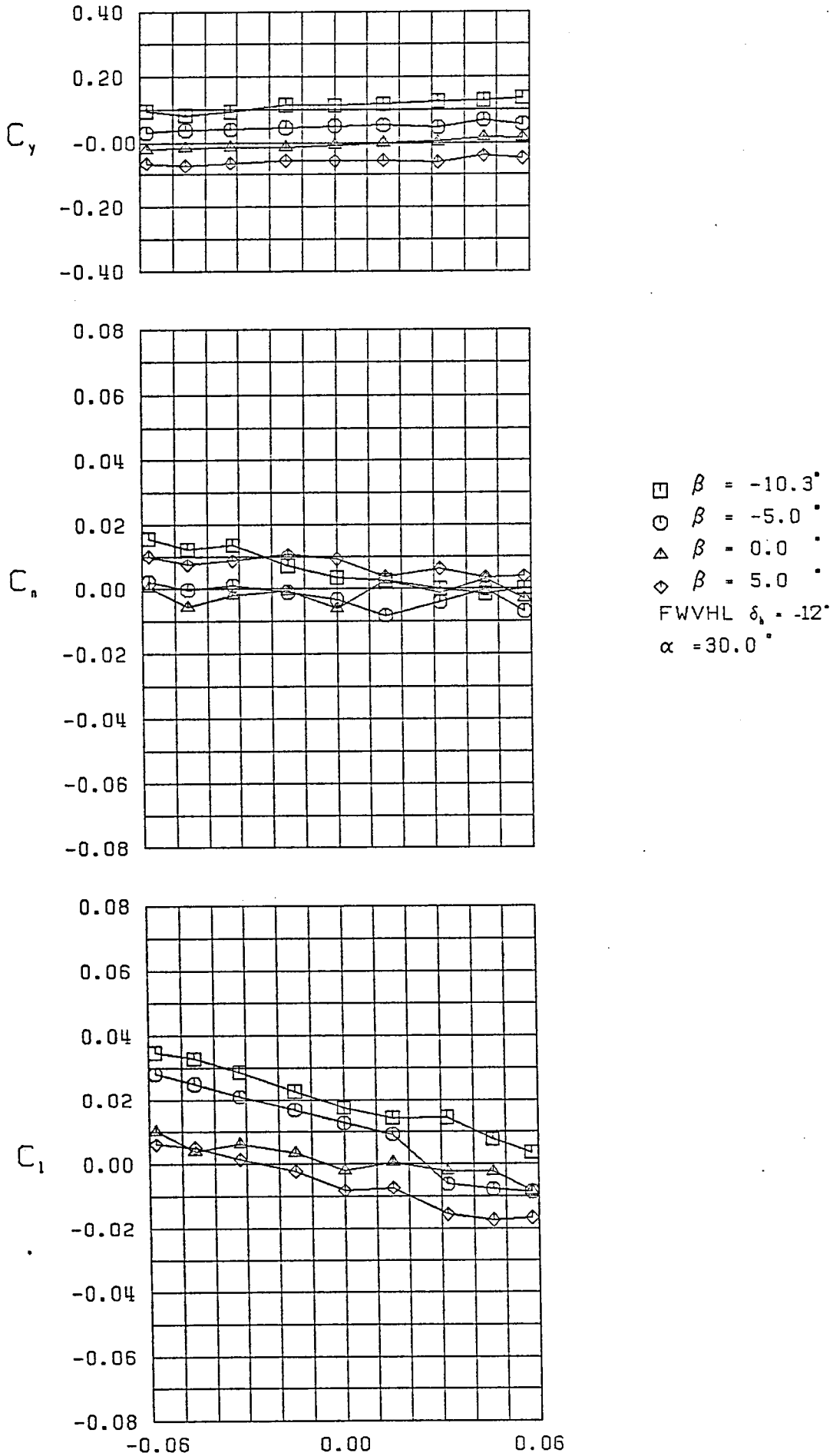

Figure 22 (Continued)

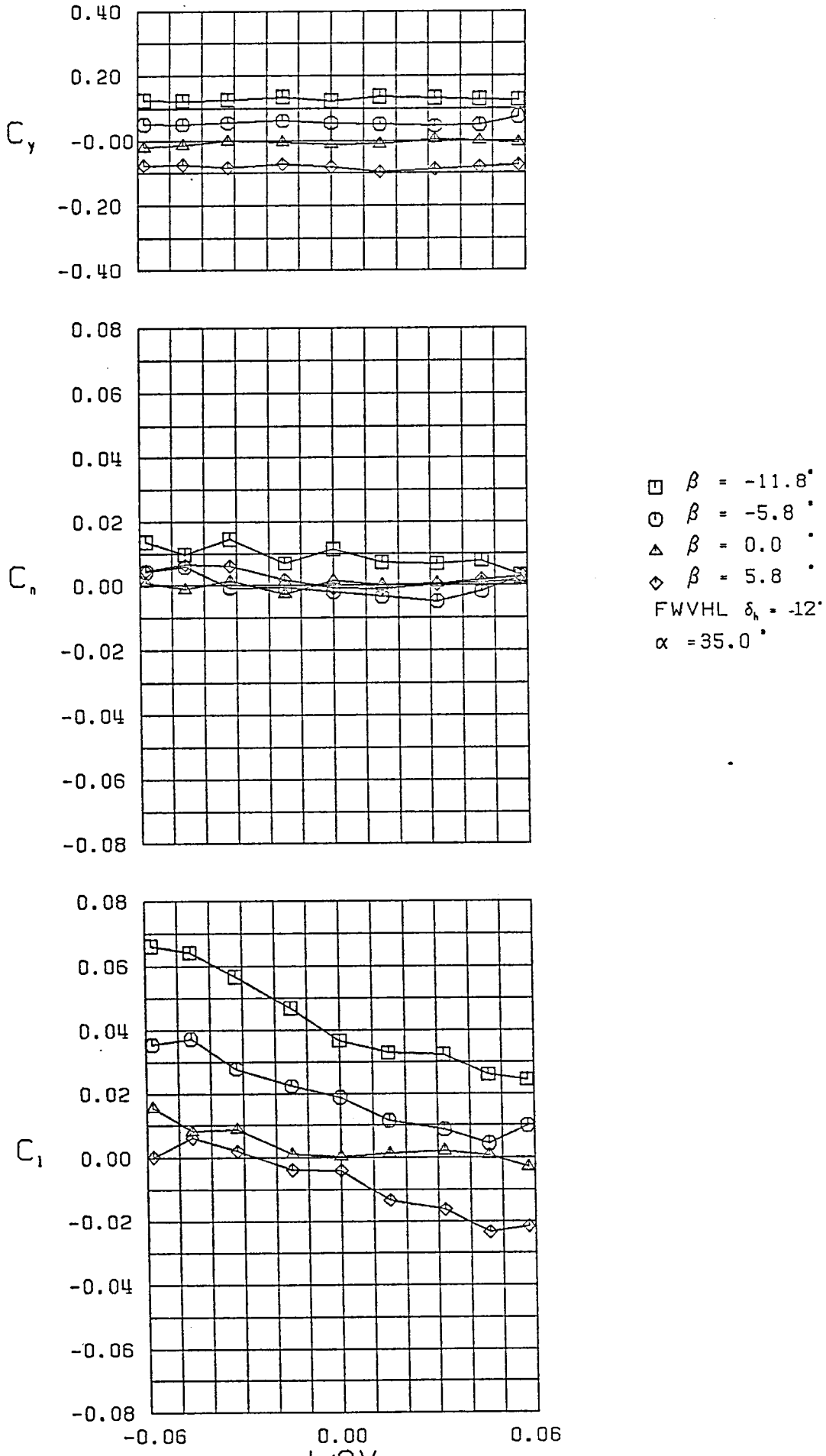

Figure 22 (Continued)

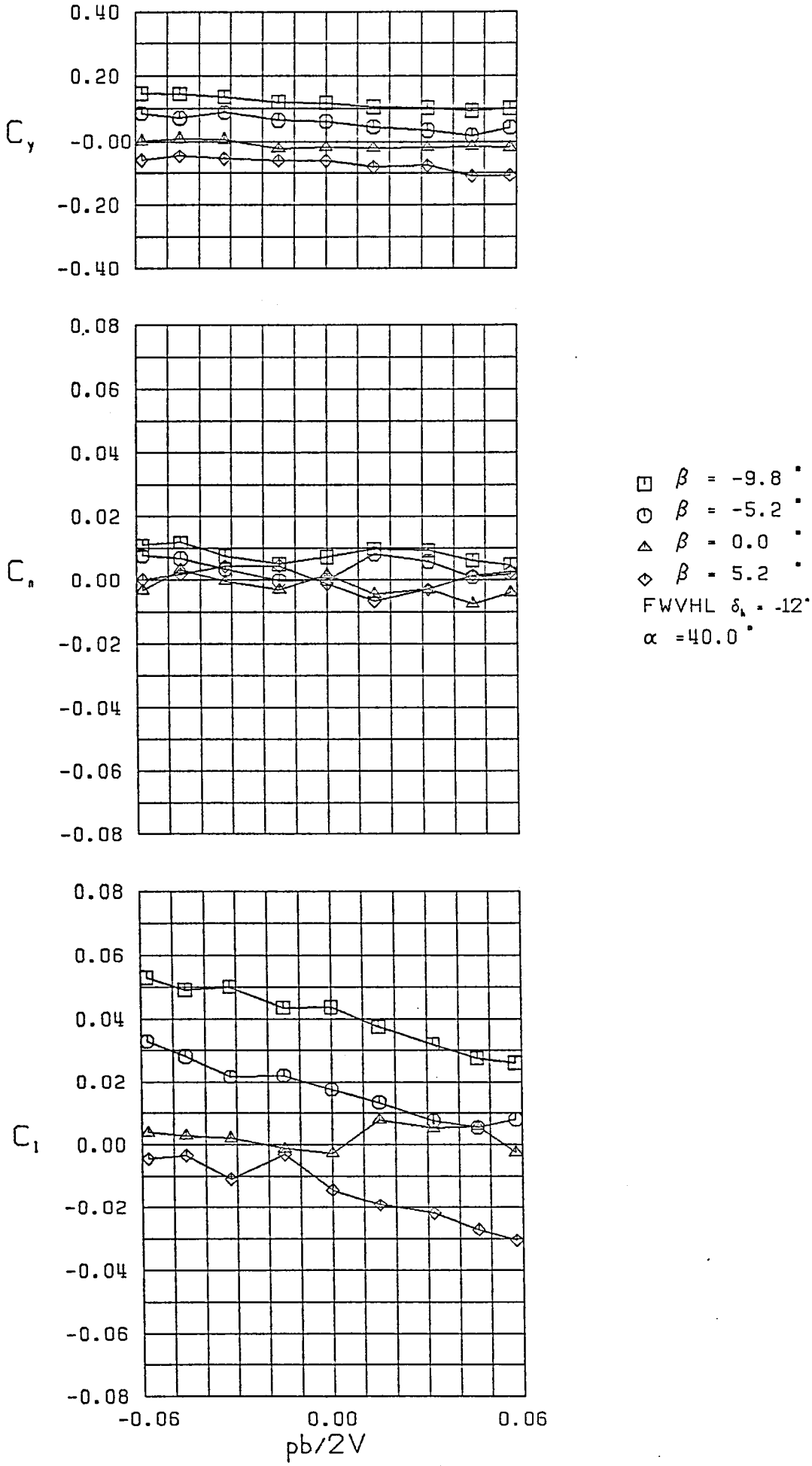

Figure 22 (Continued)

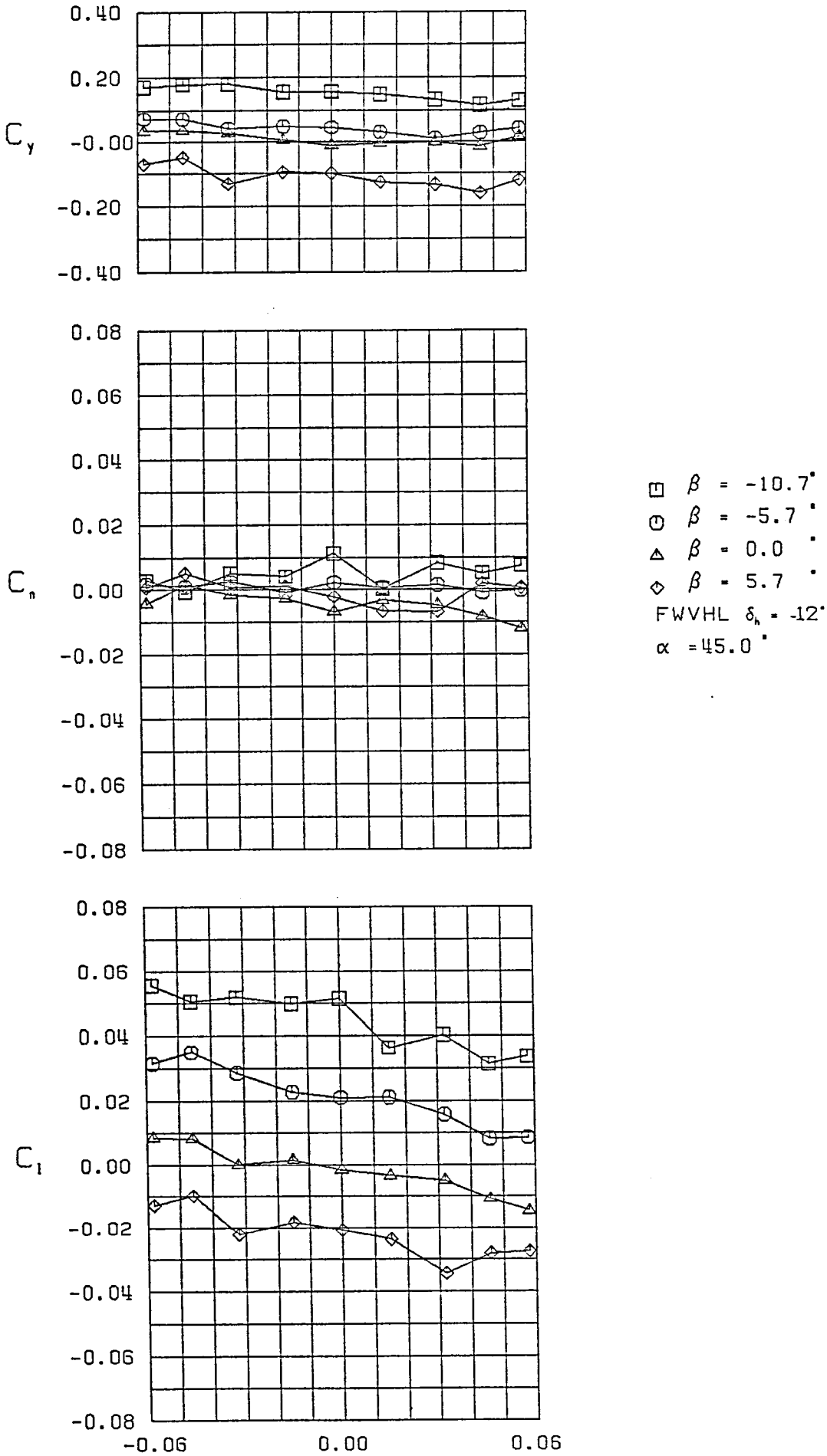

Figure 22 (Continued)

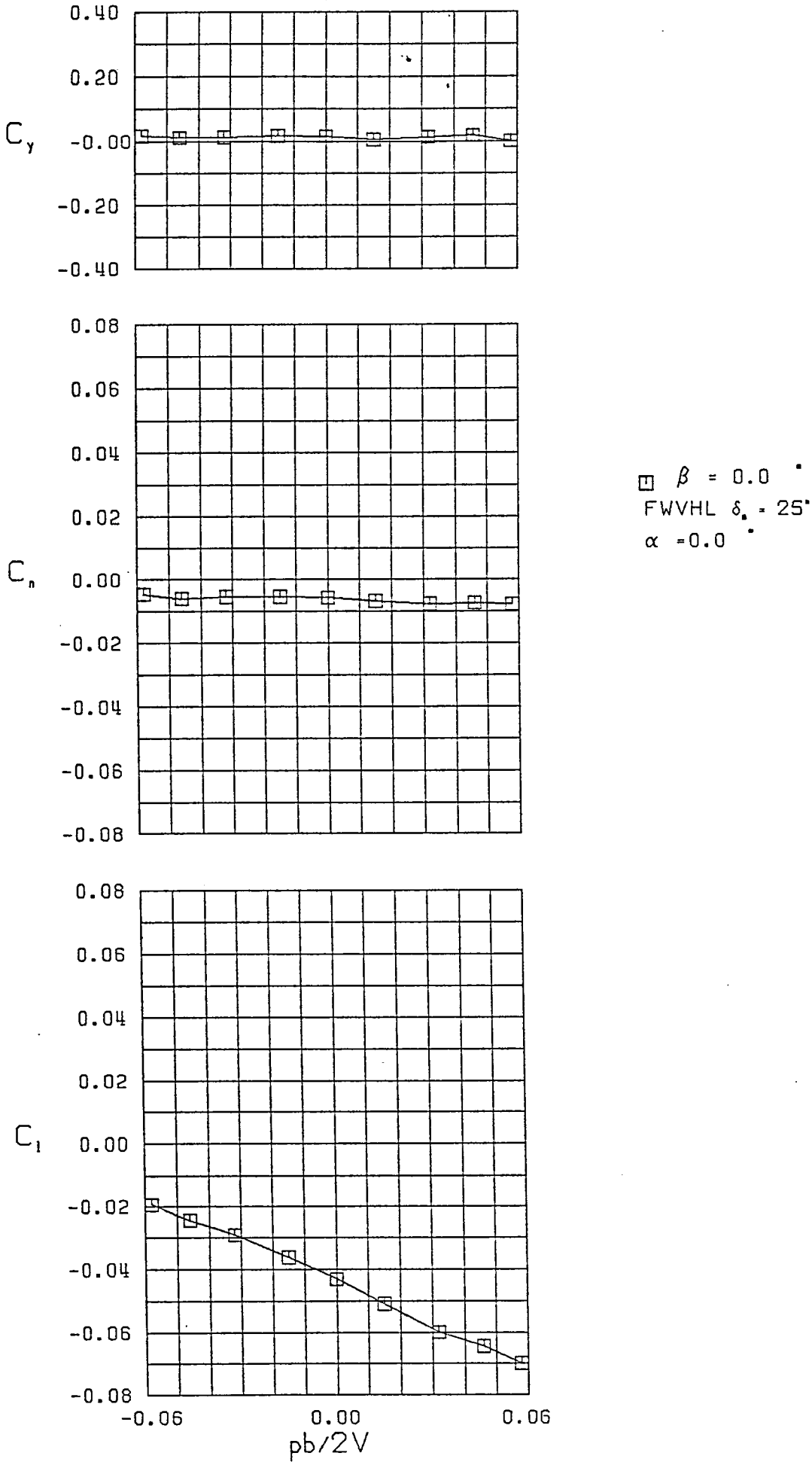

Figure 23 - Variation of Lateral-Directional Characteristics with Roll Rate-Configuration 17

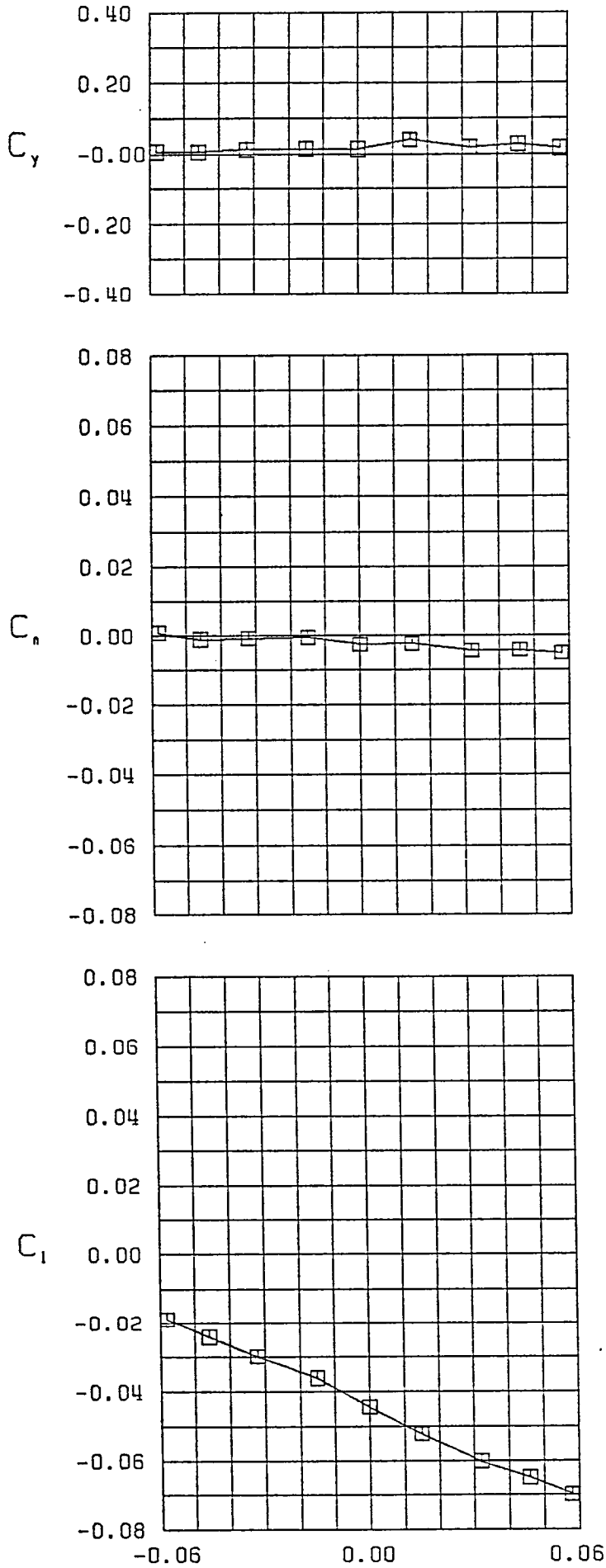

Figure 23 (Continued)

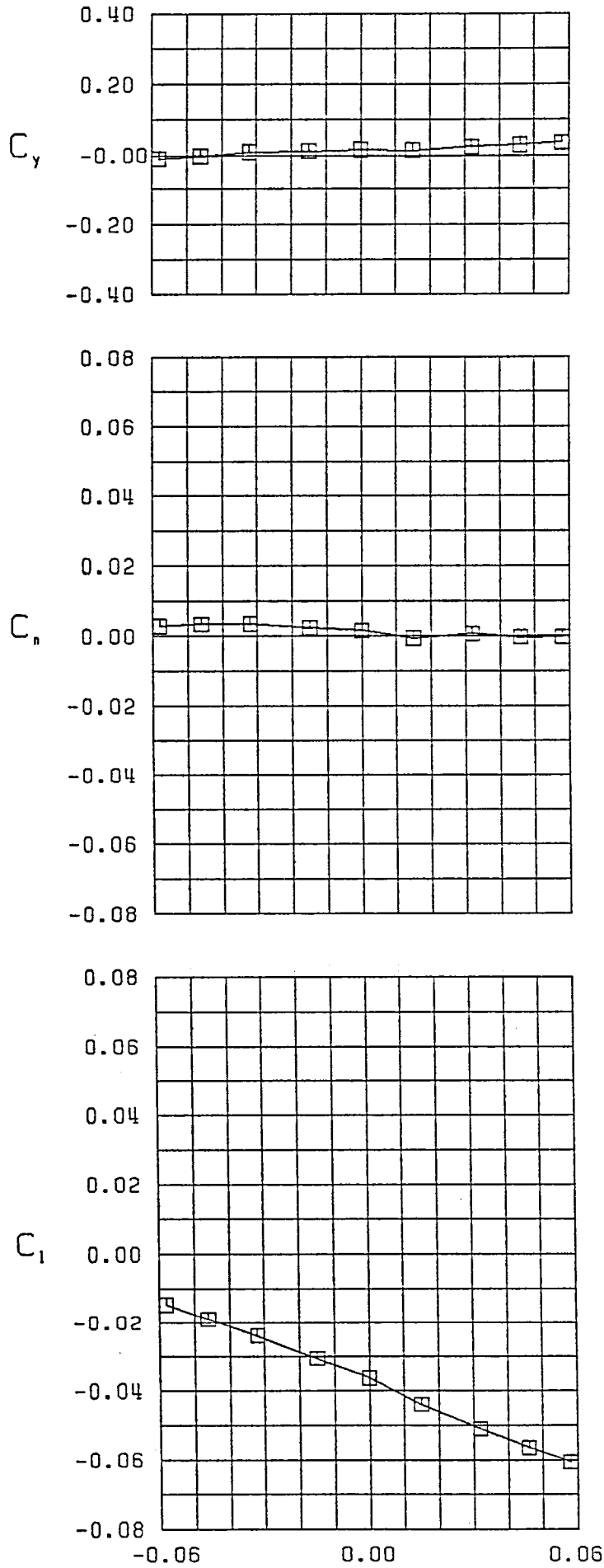

Figure 23 (Continued)

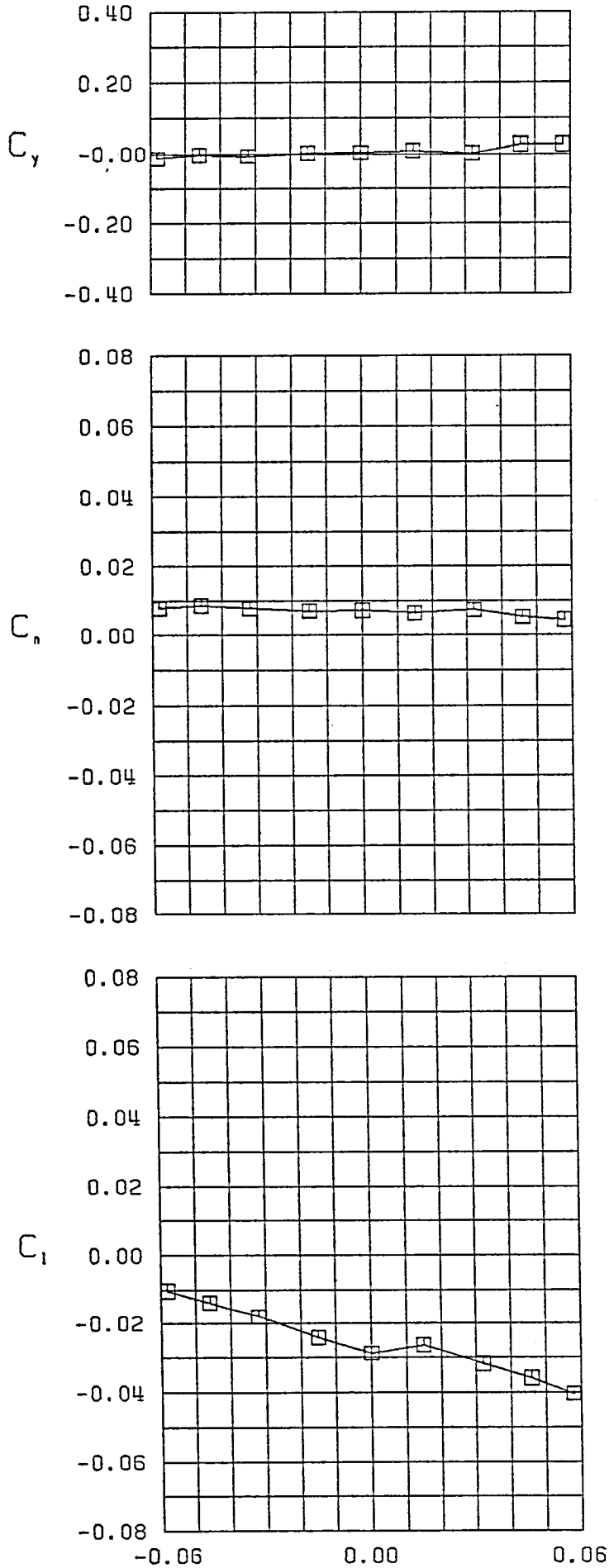

Figure 23 (Continued)

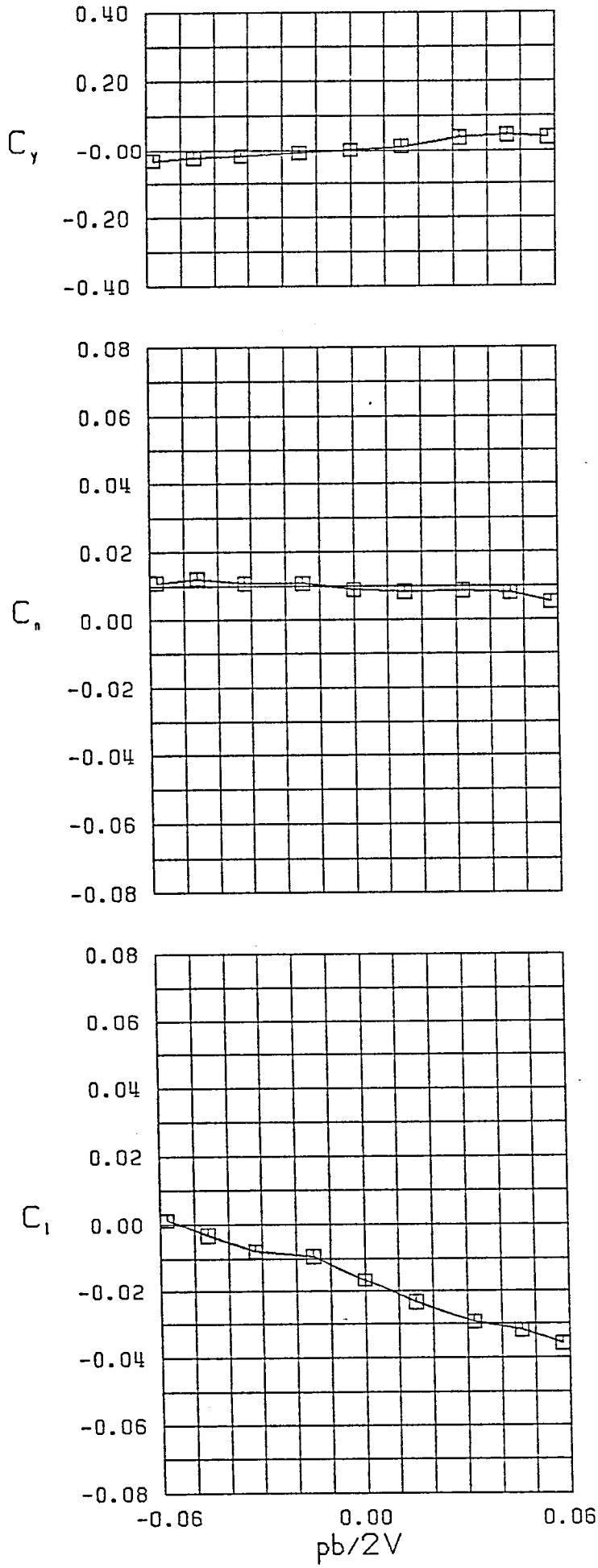

Figure 23 (Continued)

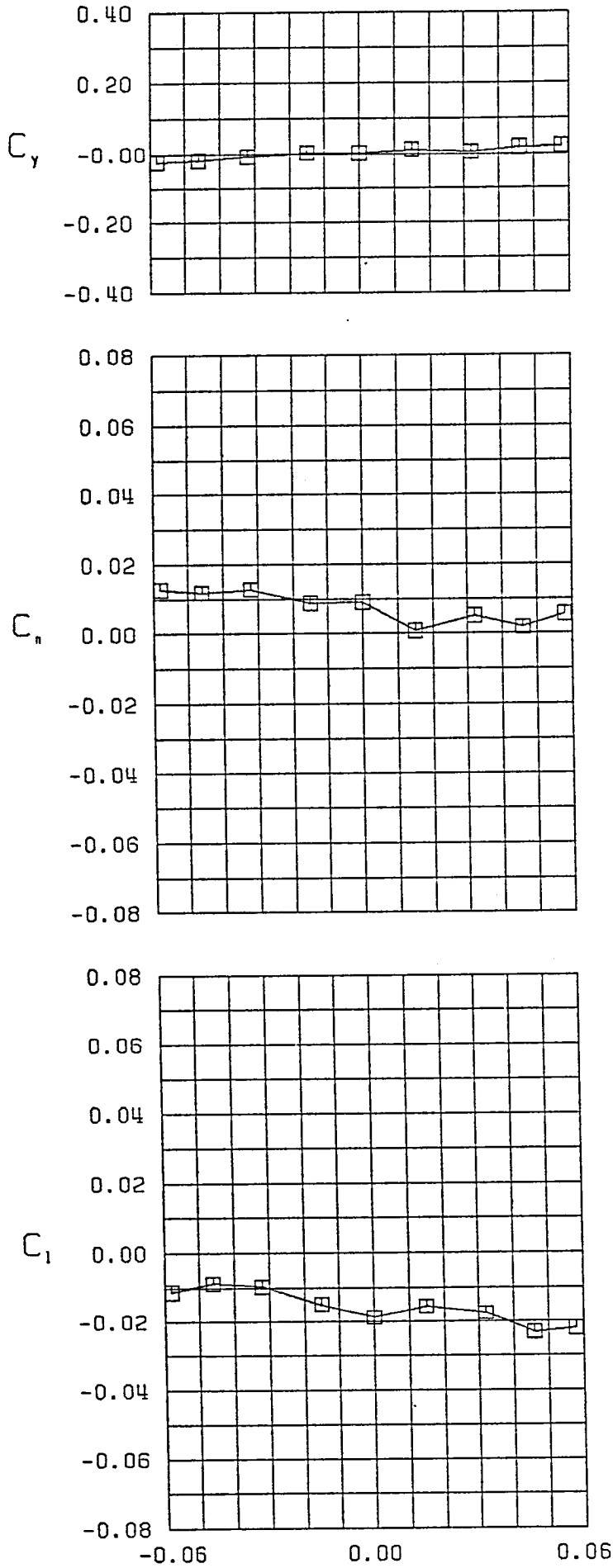

Figure 23 (Continued)

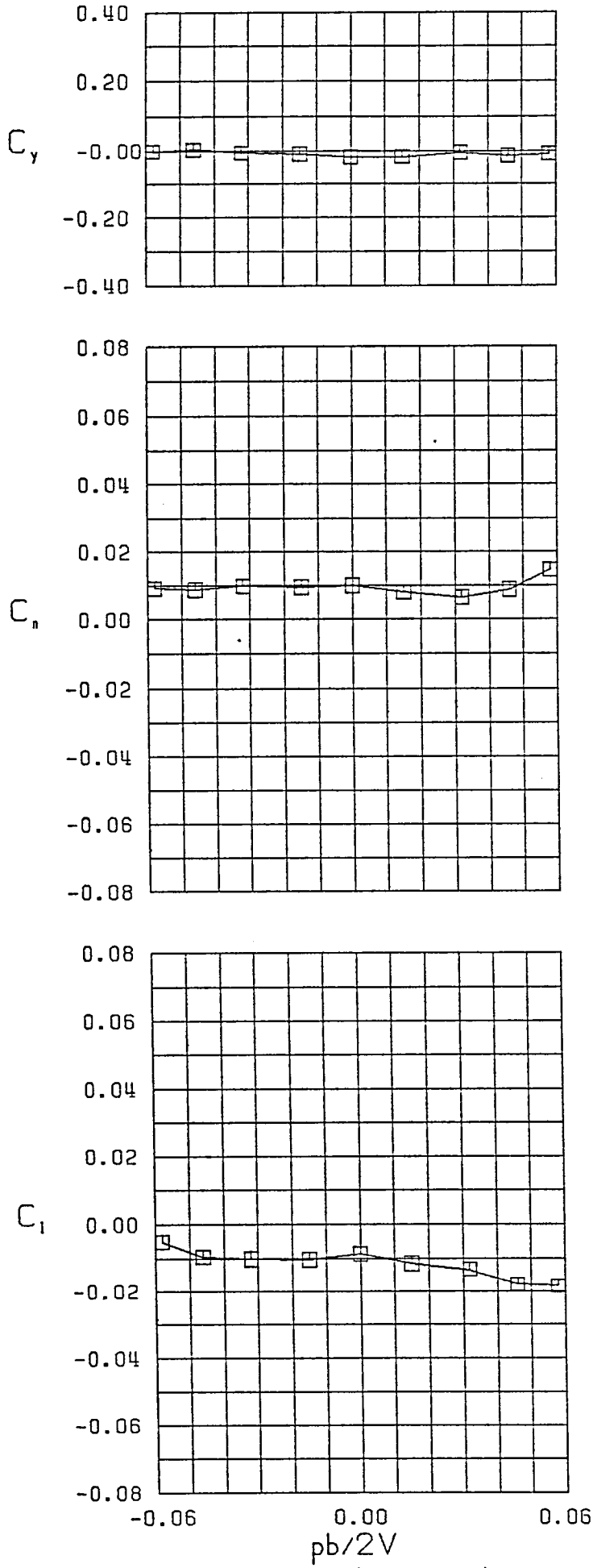

Figure 23 (Continued)

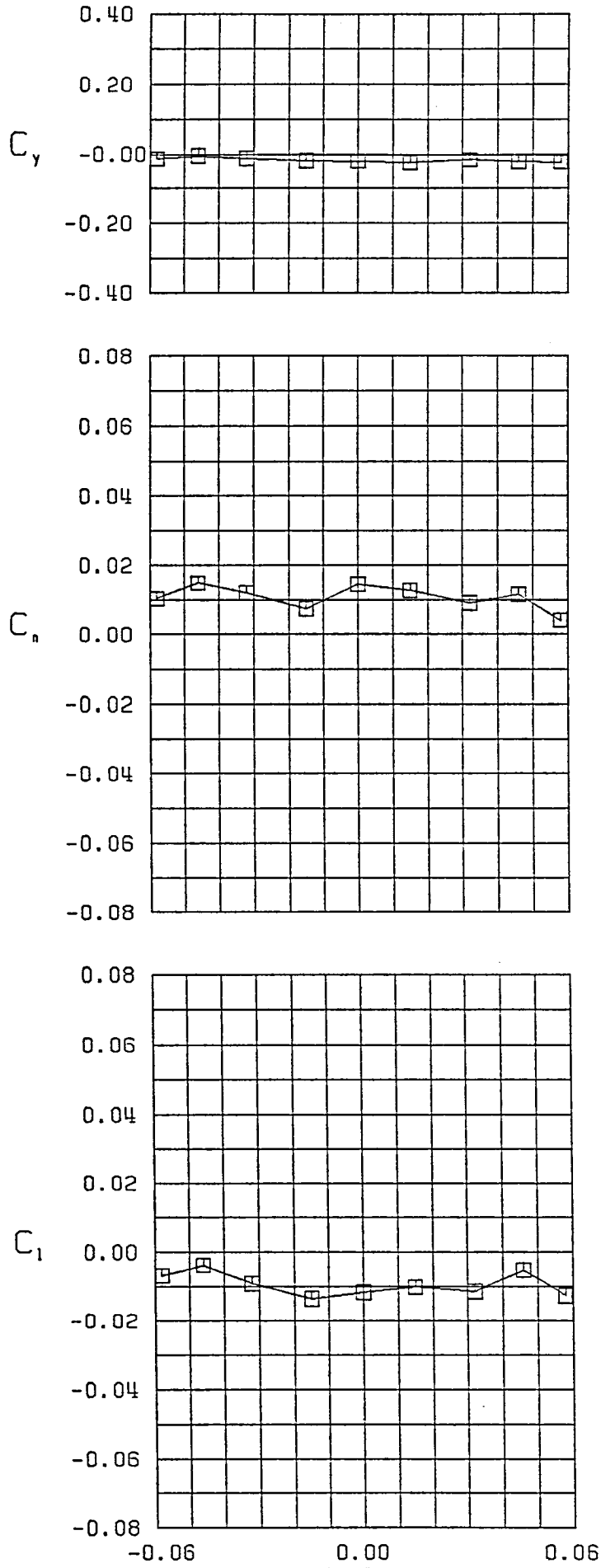

Figure 23 (Continued)

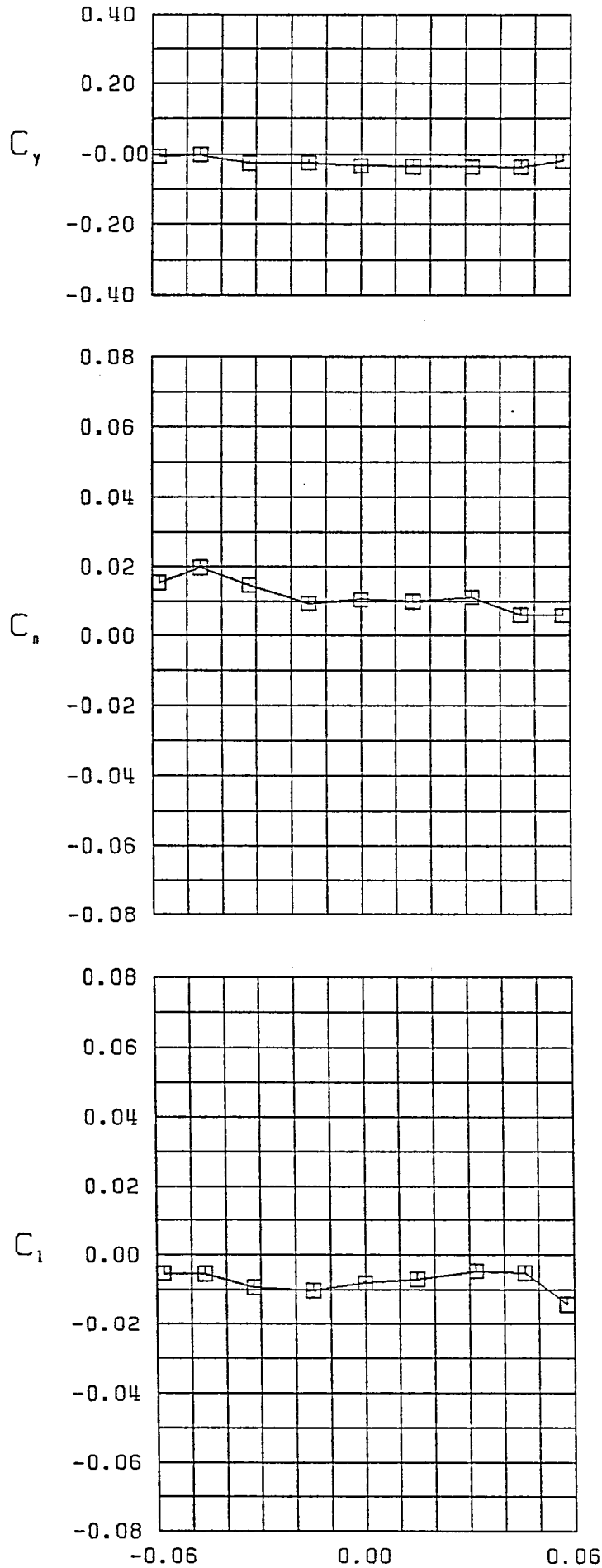

Figure 23 (Continued)

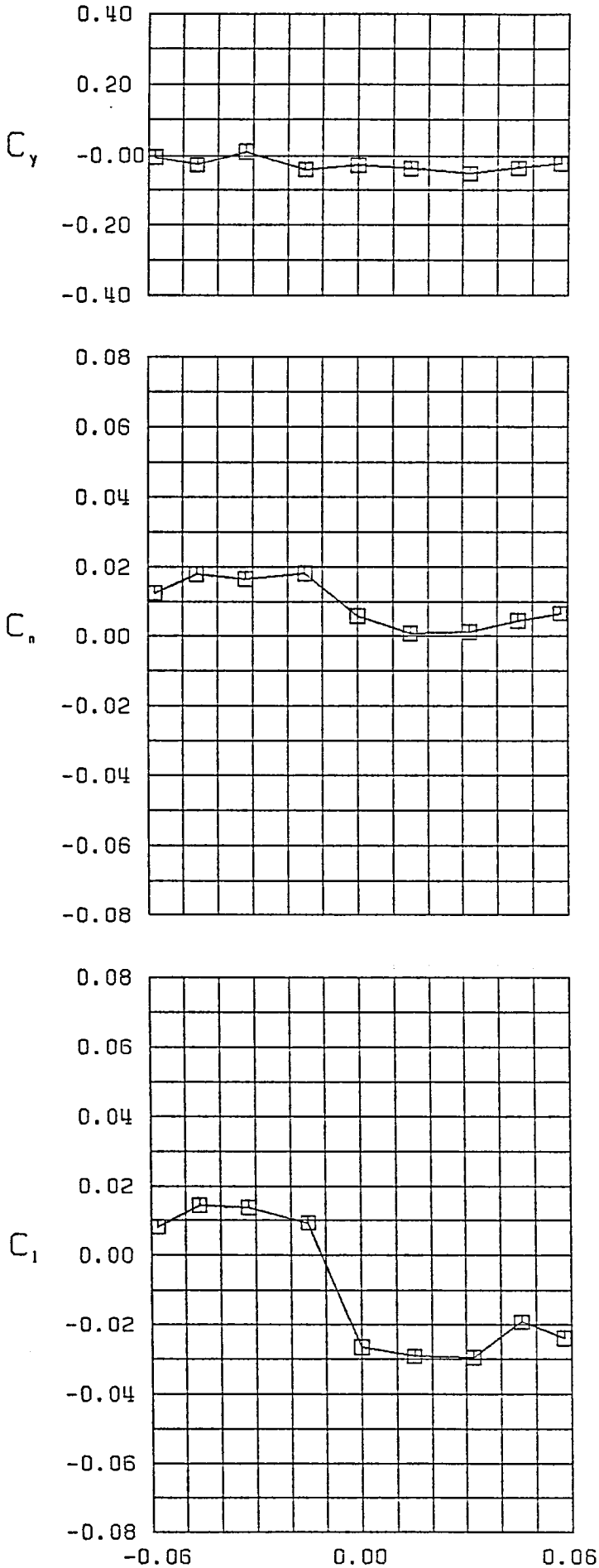

Figure 23 (Continued)

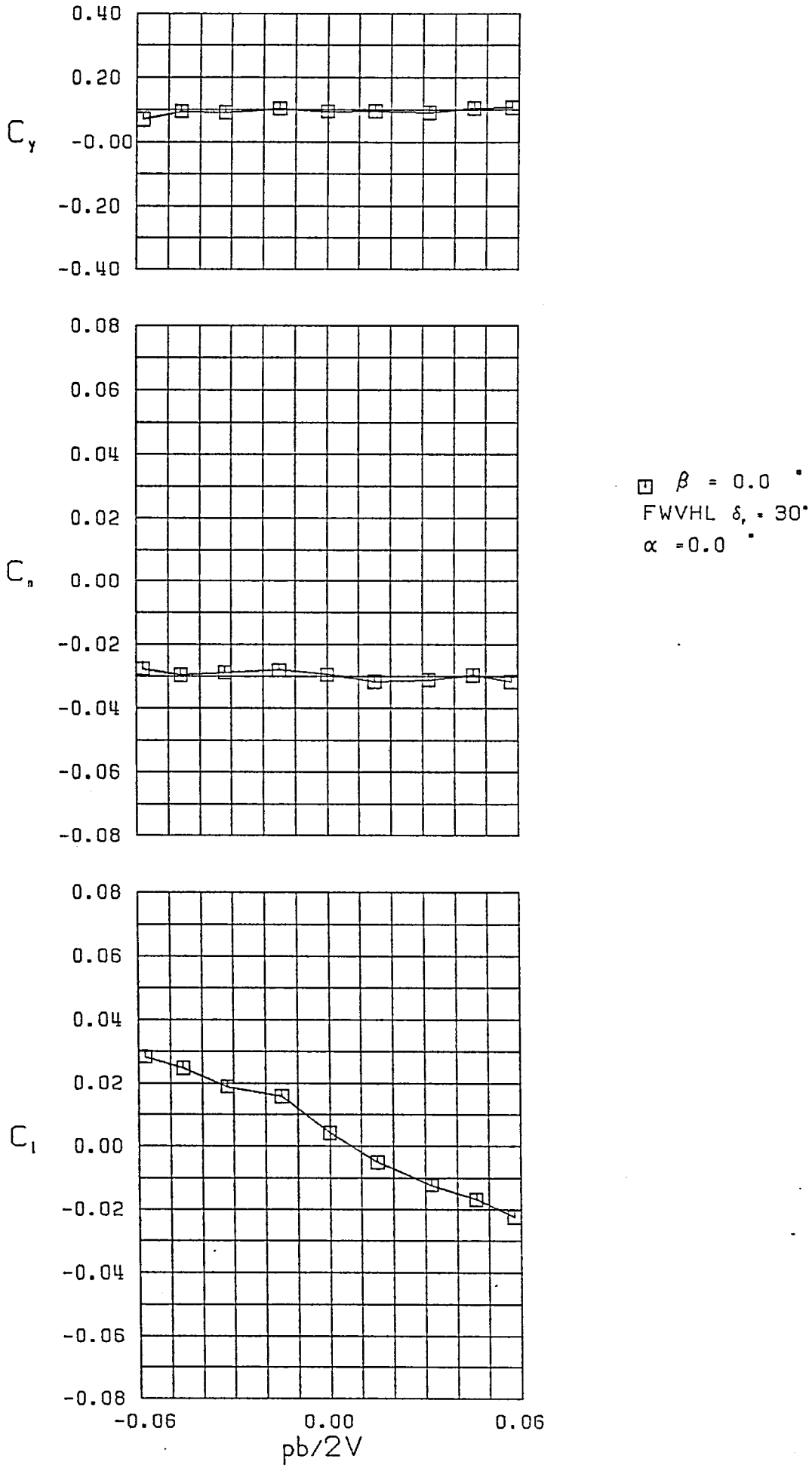

Figure 24 - Variation of Lateral-Directional Characteristics with Roll Rate-Configuration 16

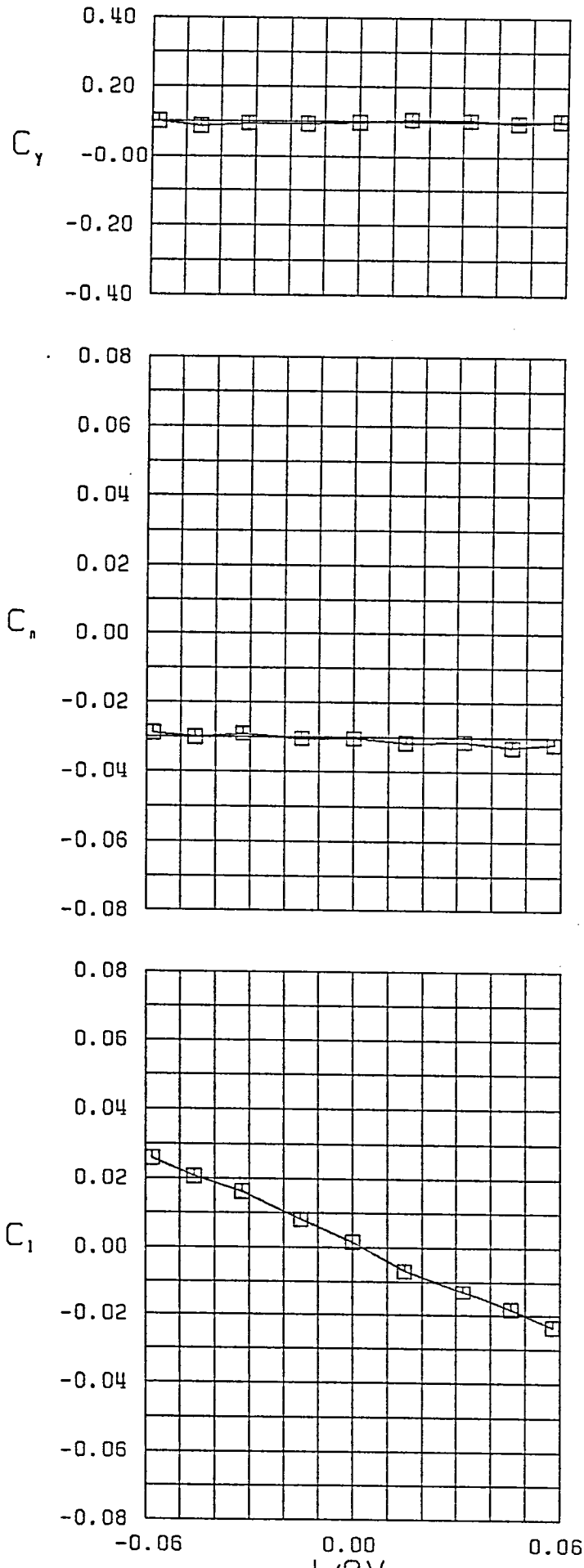

Figure 24 (Continued)

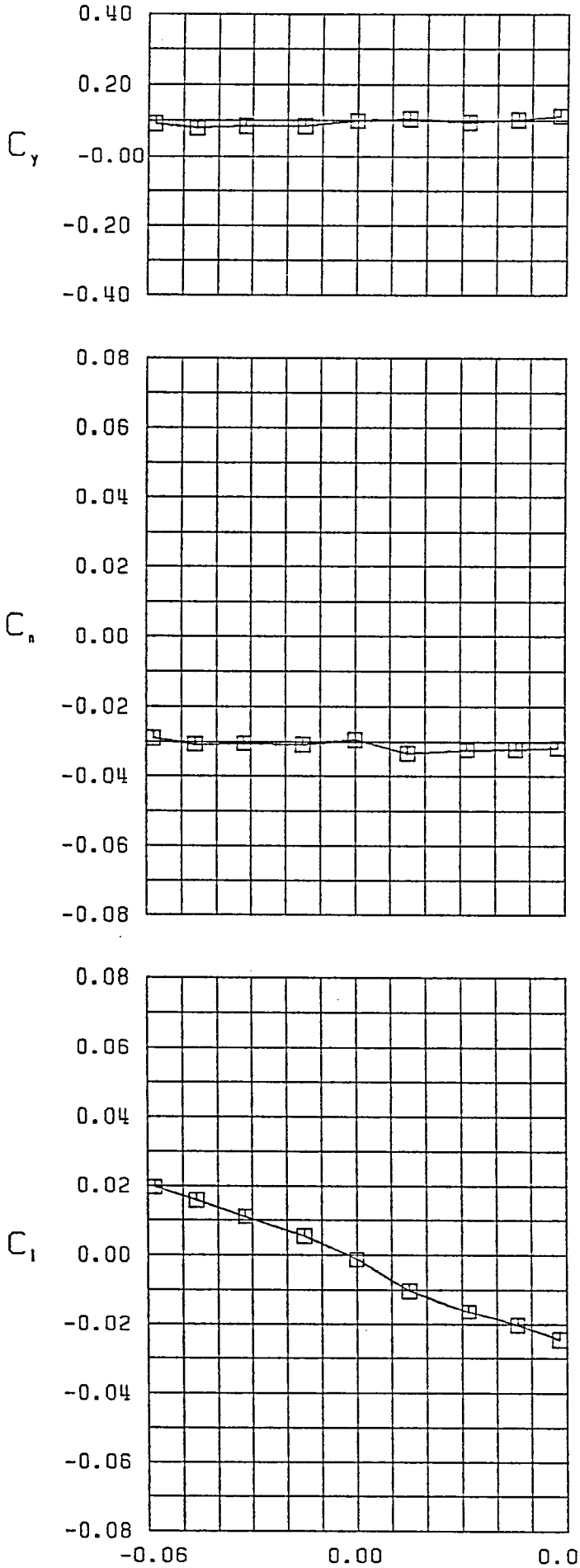

Figure 24 (Continued)

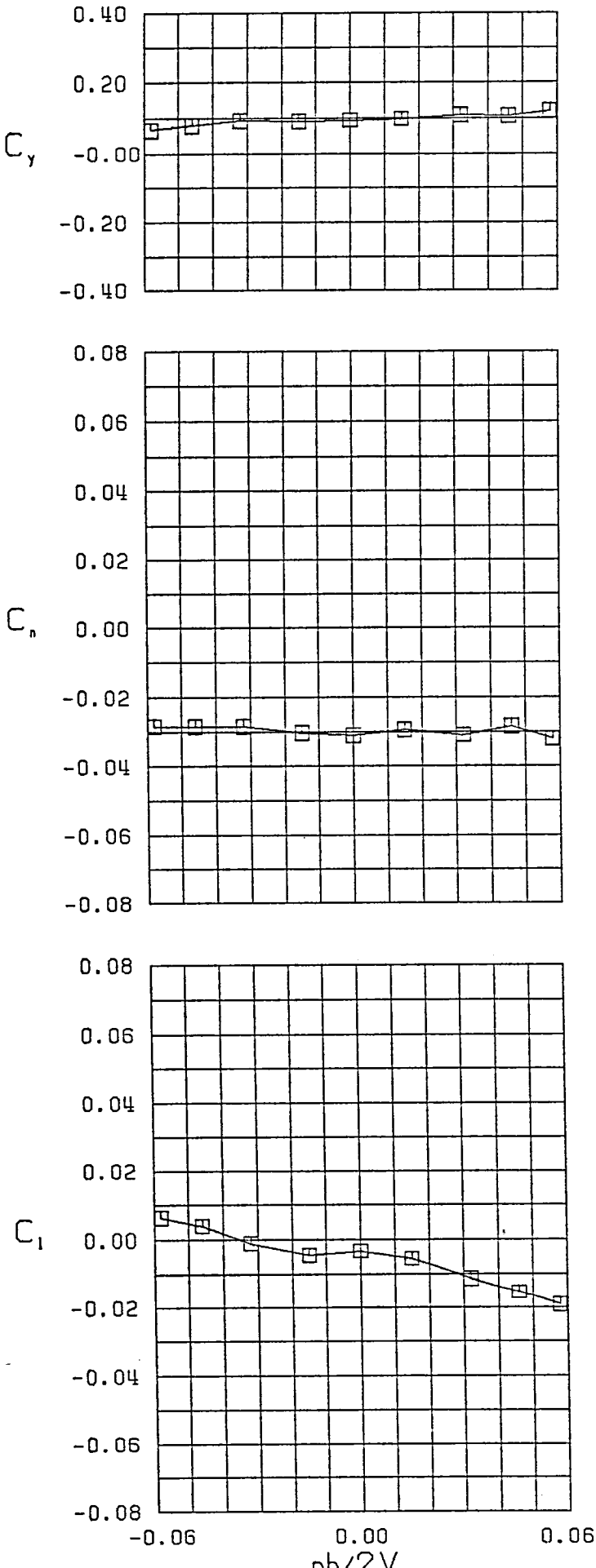

Figure 24 (Continued)

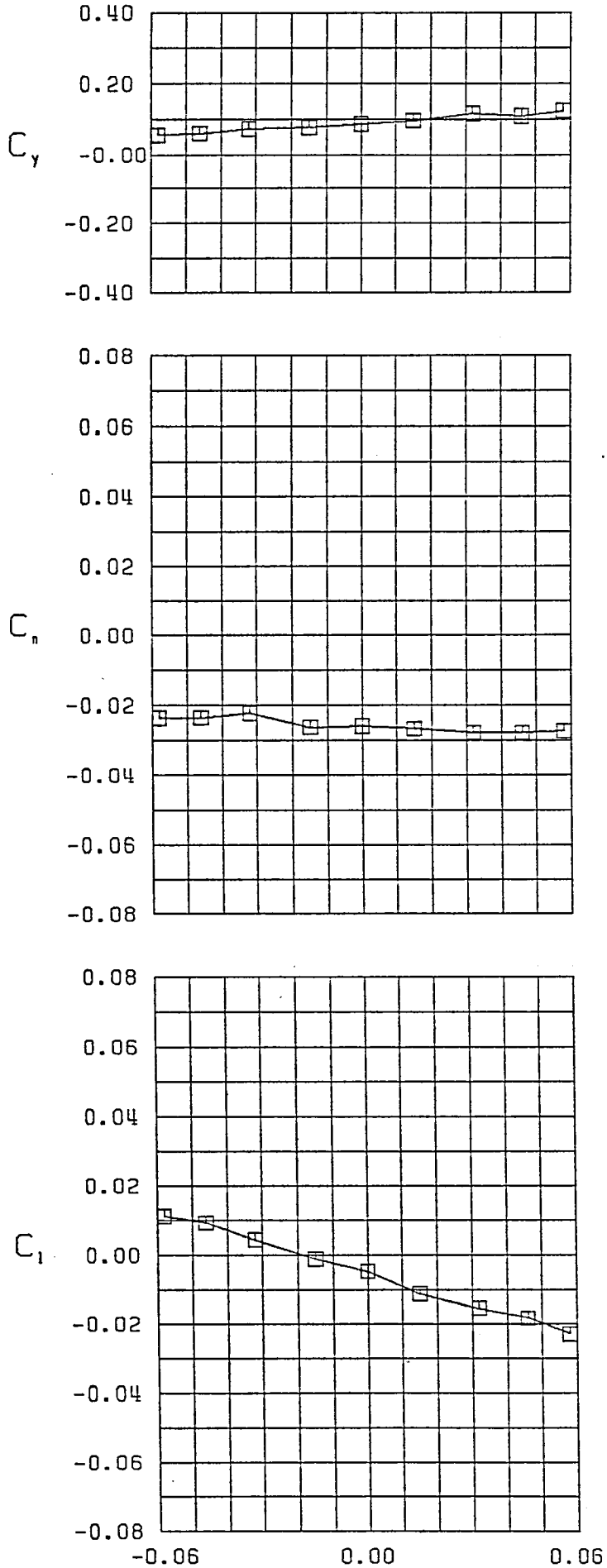

Figure 24 (Continued)

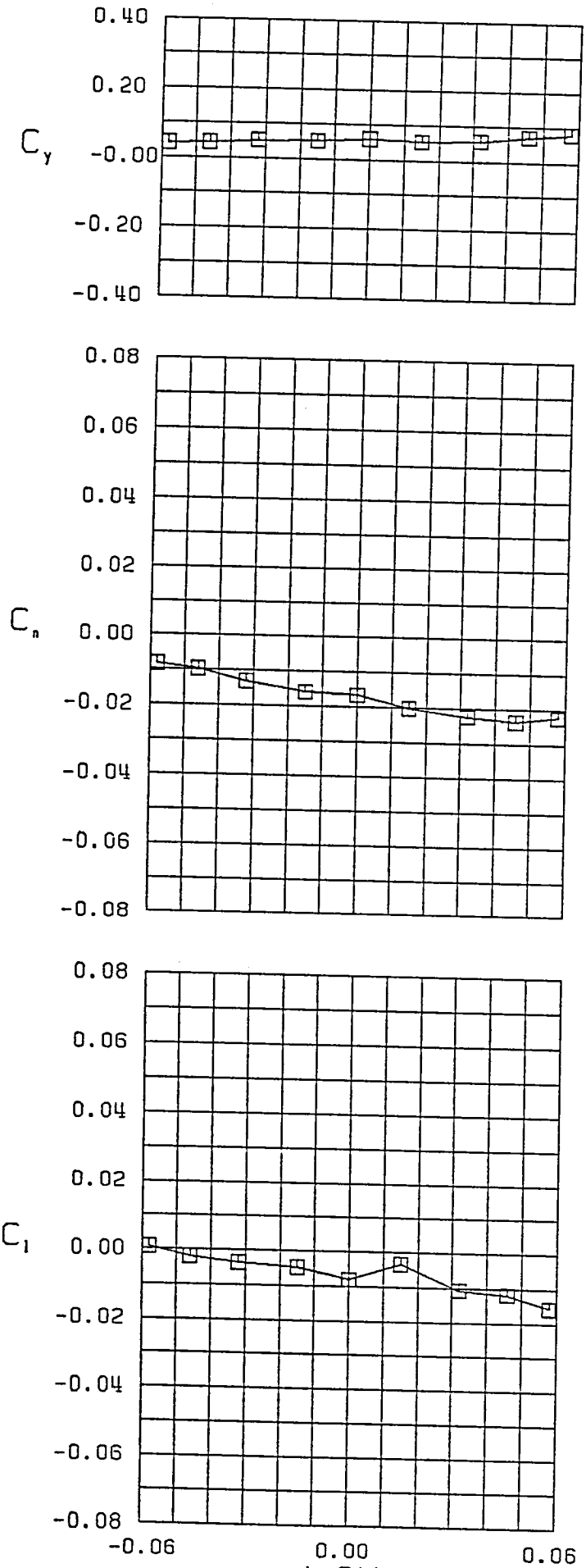

Figure 24 (Continued)

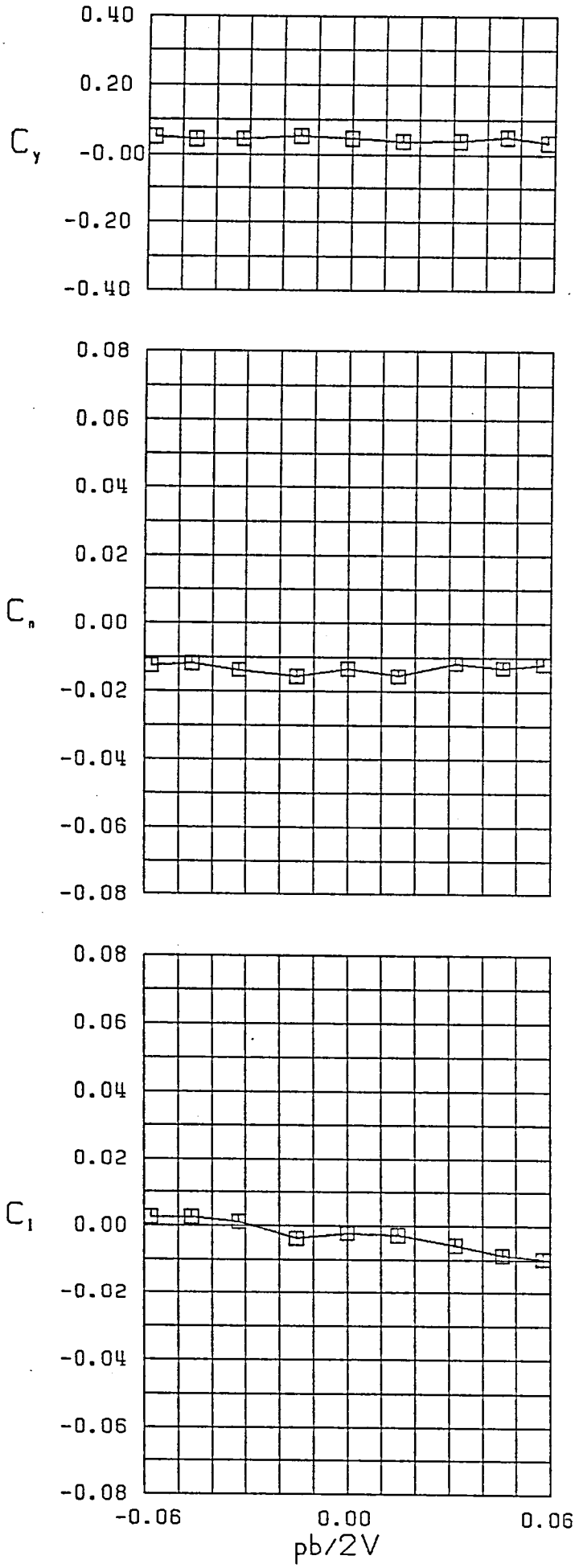

Figure 24 (Continued)

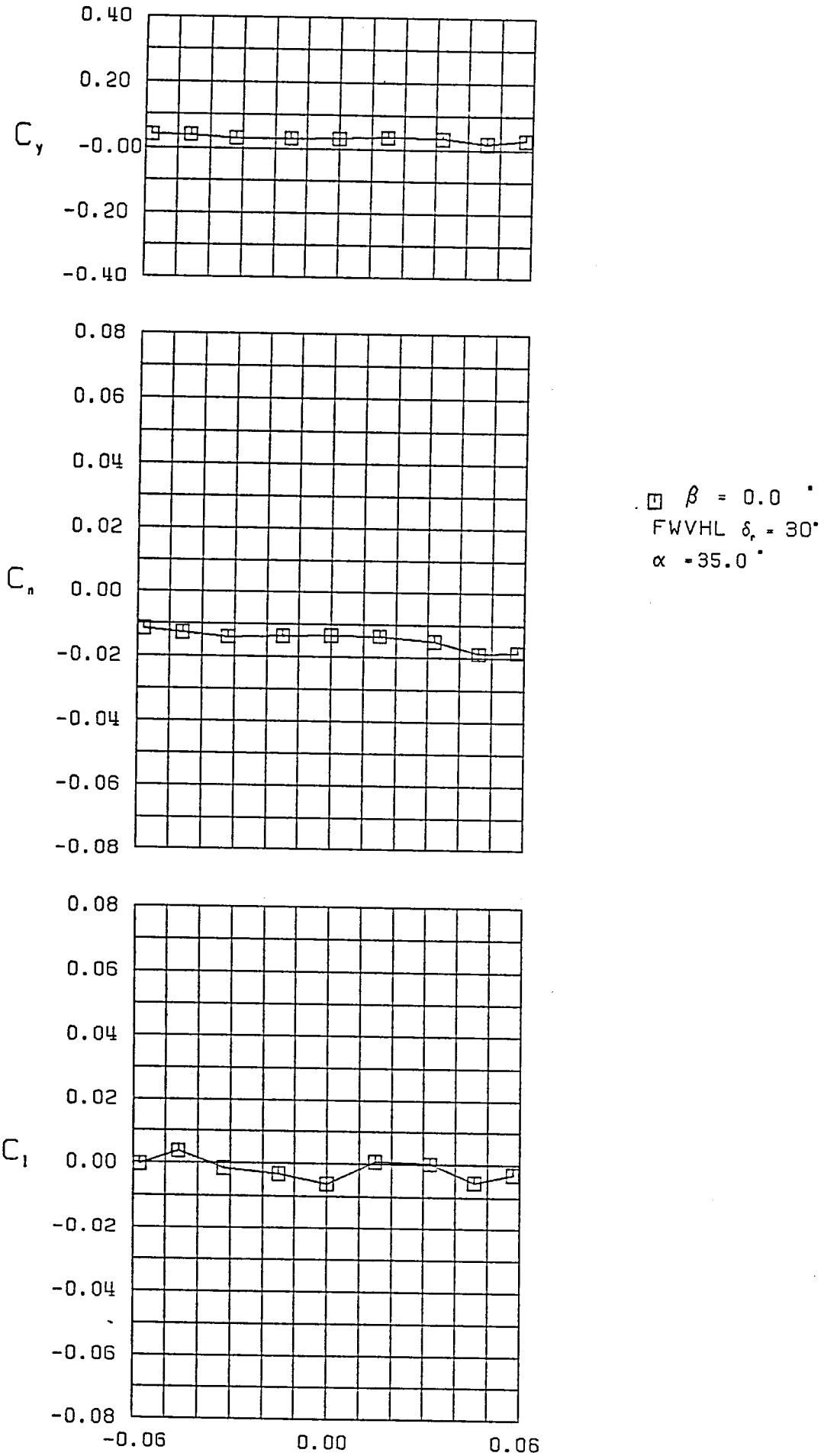

Figure 24 (Continued)

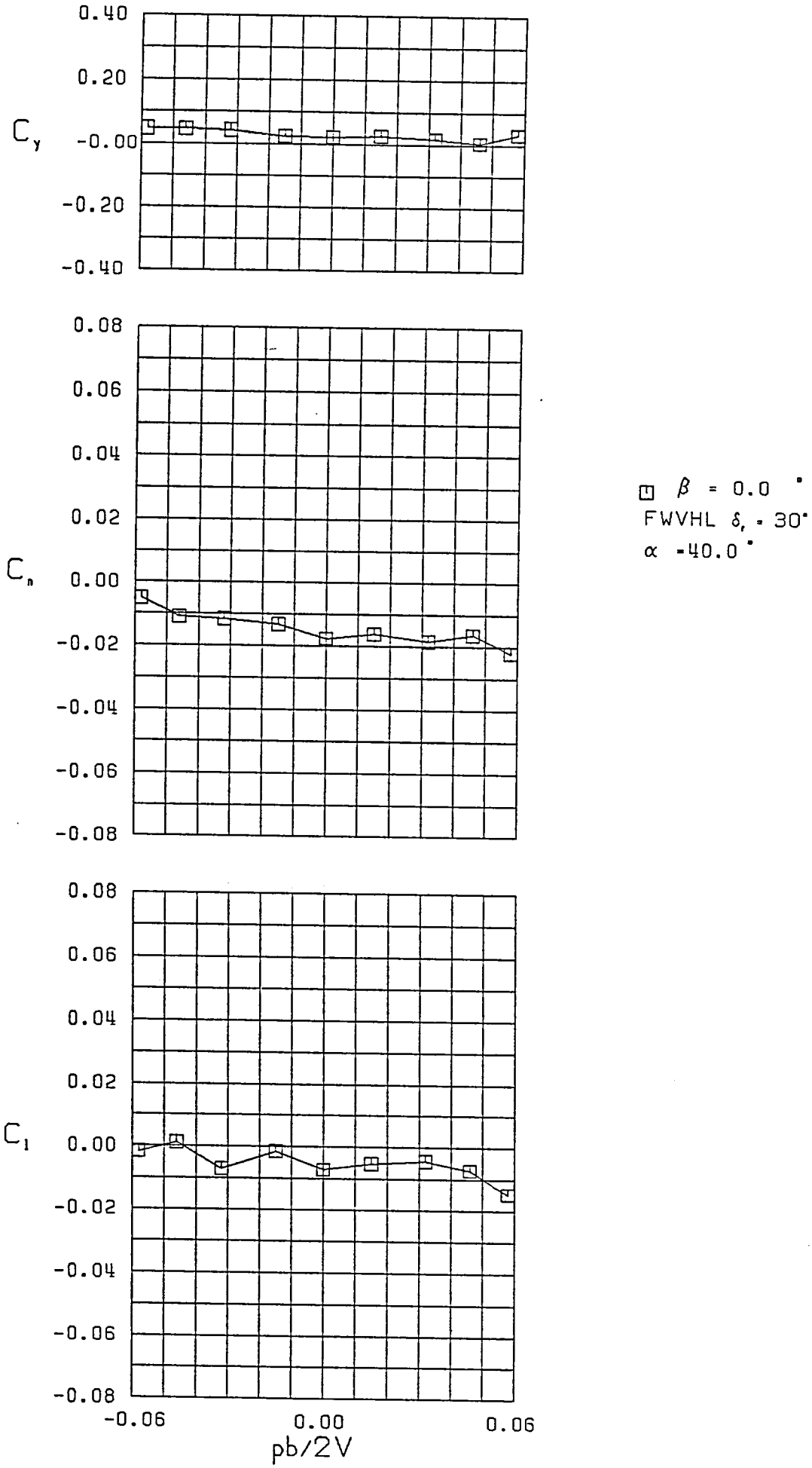

Figure 24 (Continued)

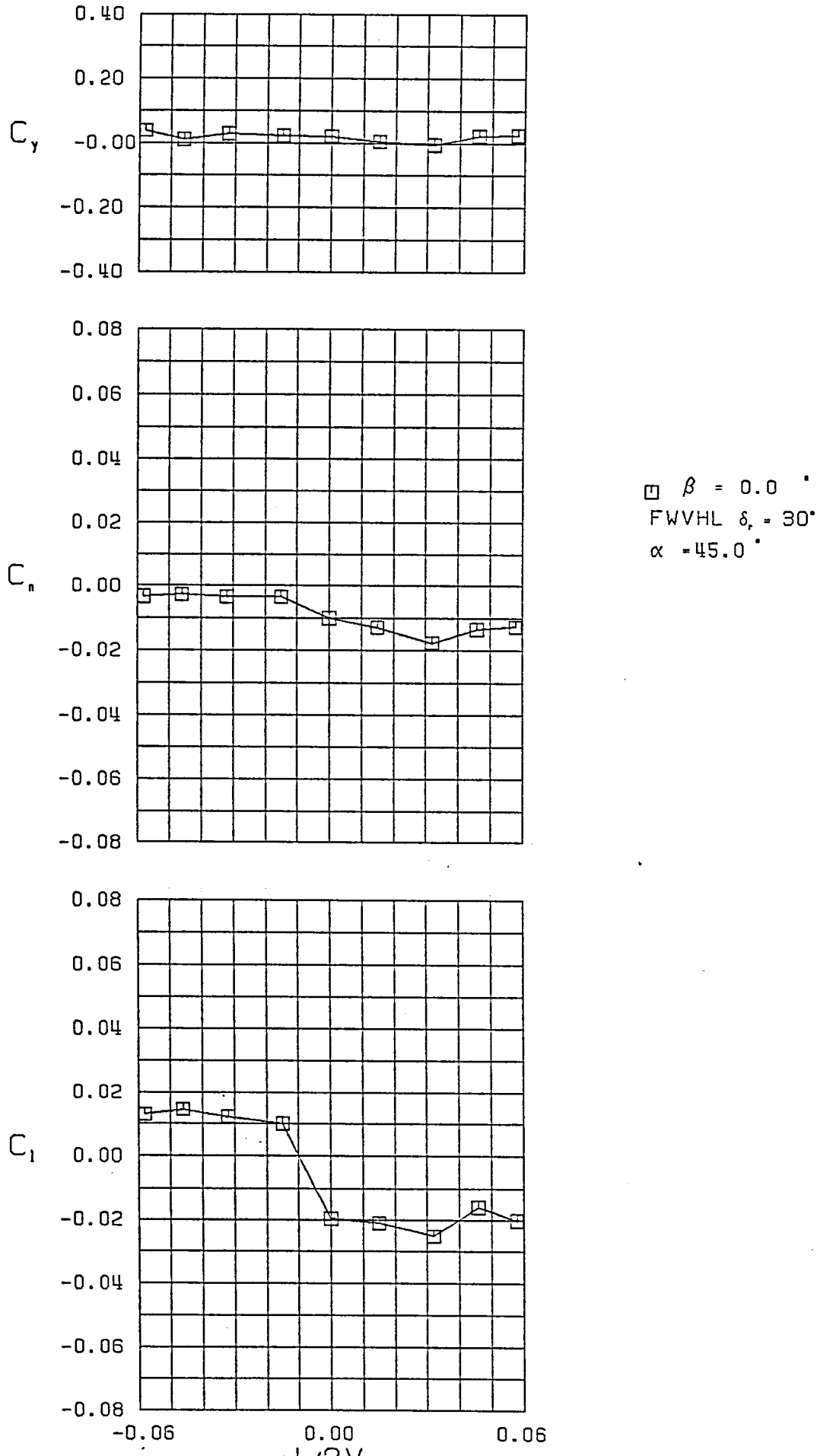

Figure 24 (Continued)

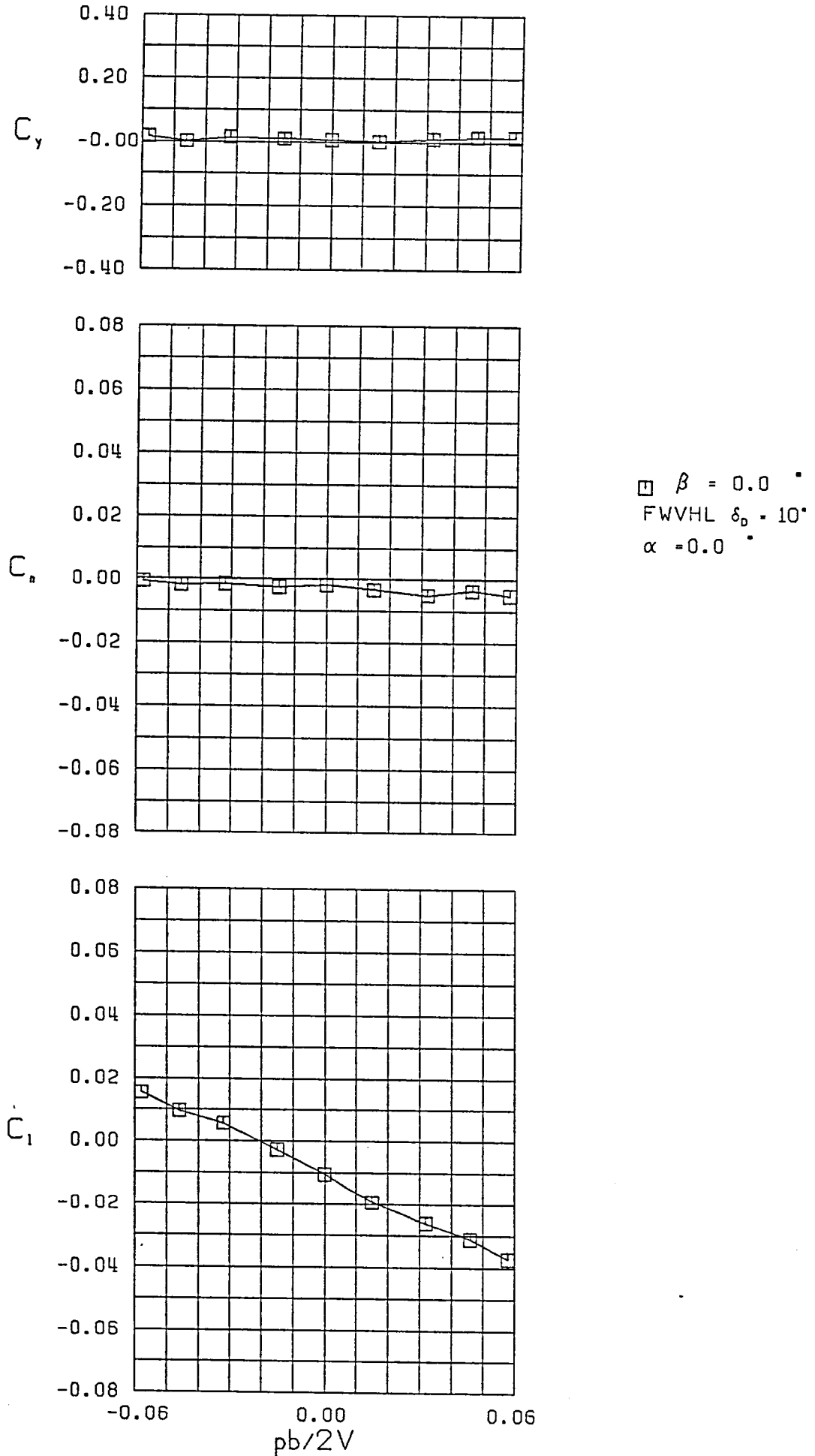

Figure 25 - Variation of Lateral-Directional Characteristics with Roll Rate-Configuration 18

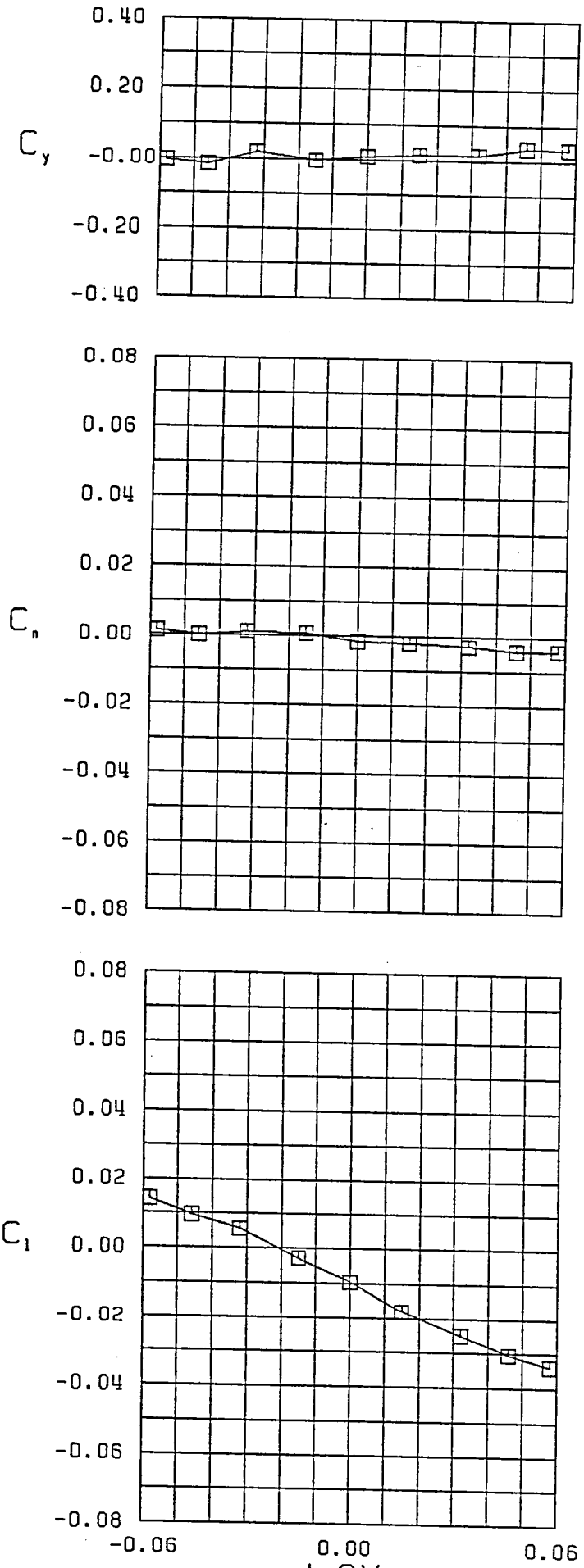

Figure 25 (Continued)

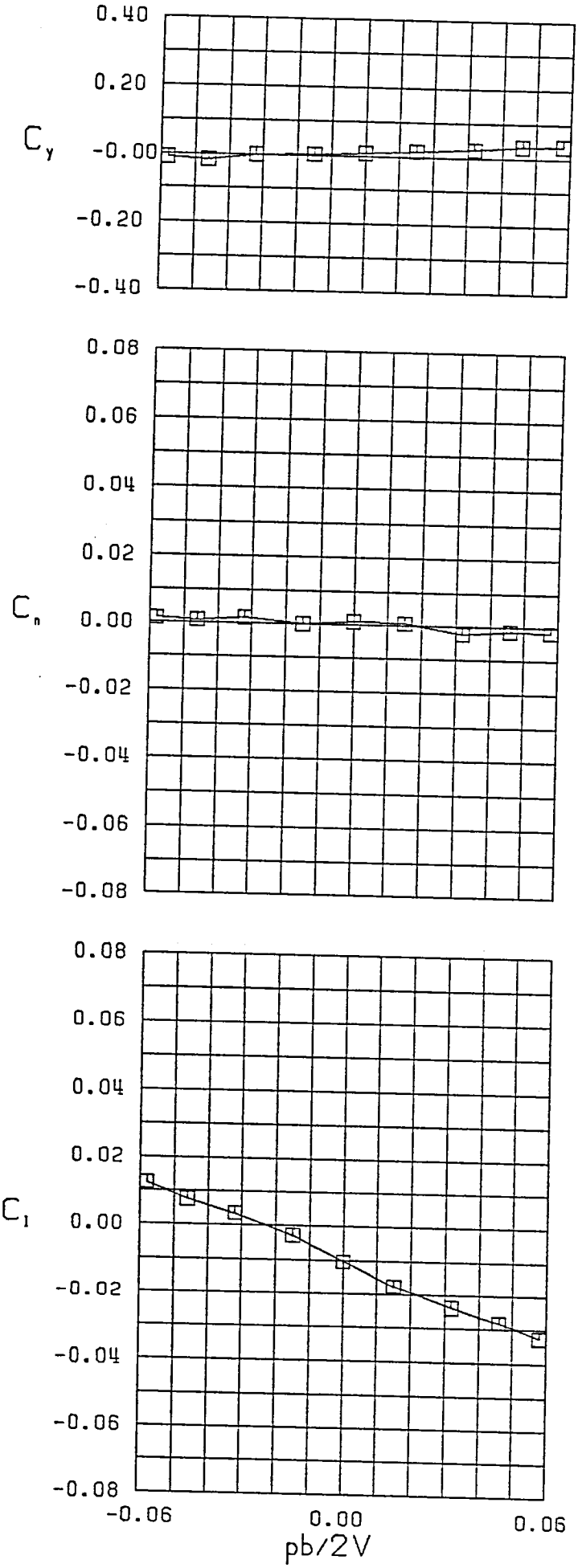

Figure 25 (Continued)

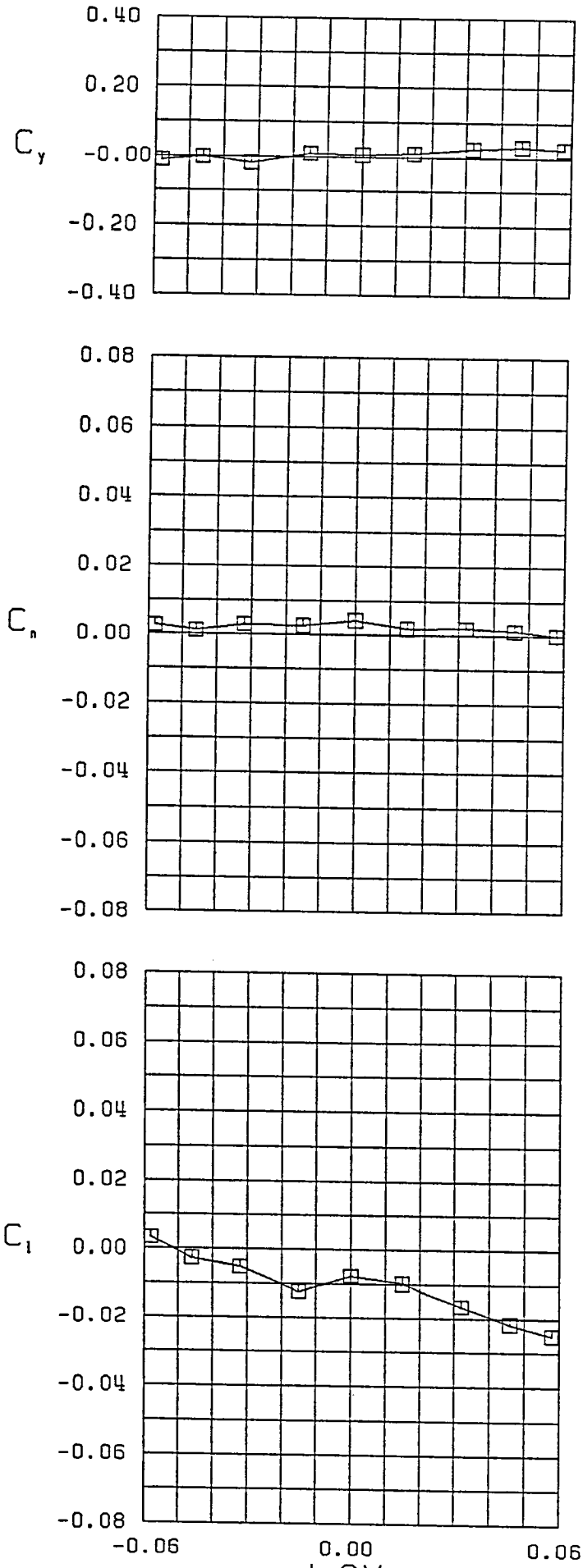

Figure 25 (Continued)

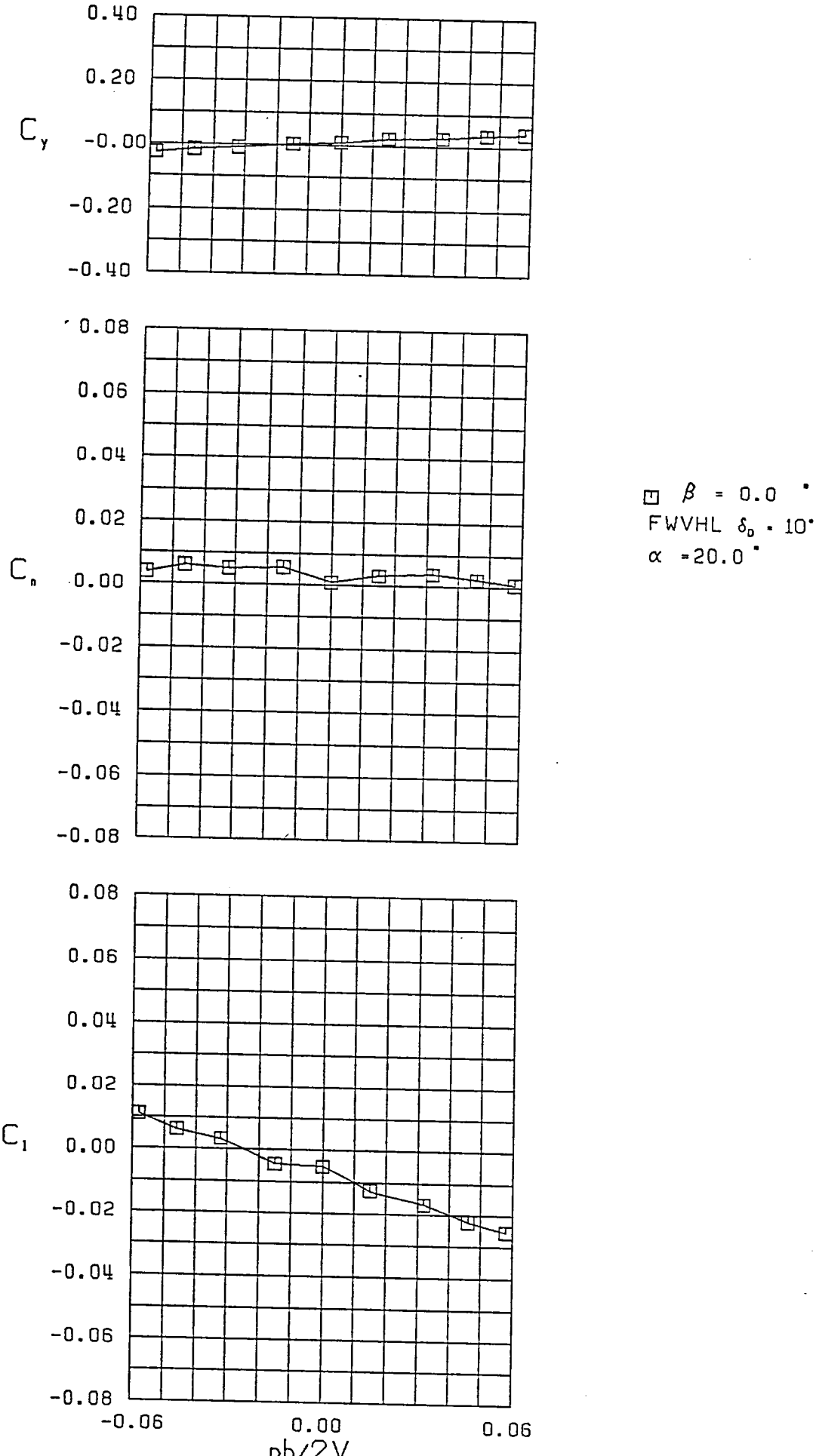

Figure 25 (Continued)

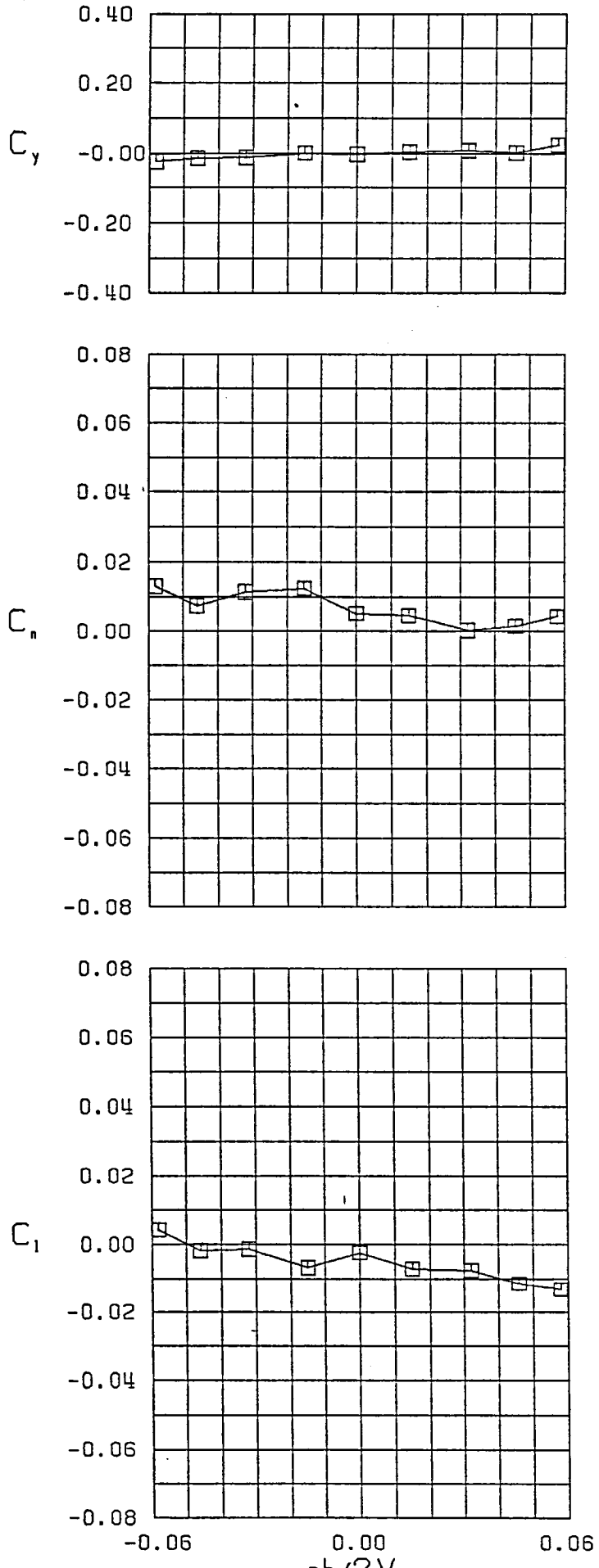

Figure 25 (Continued)

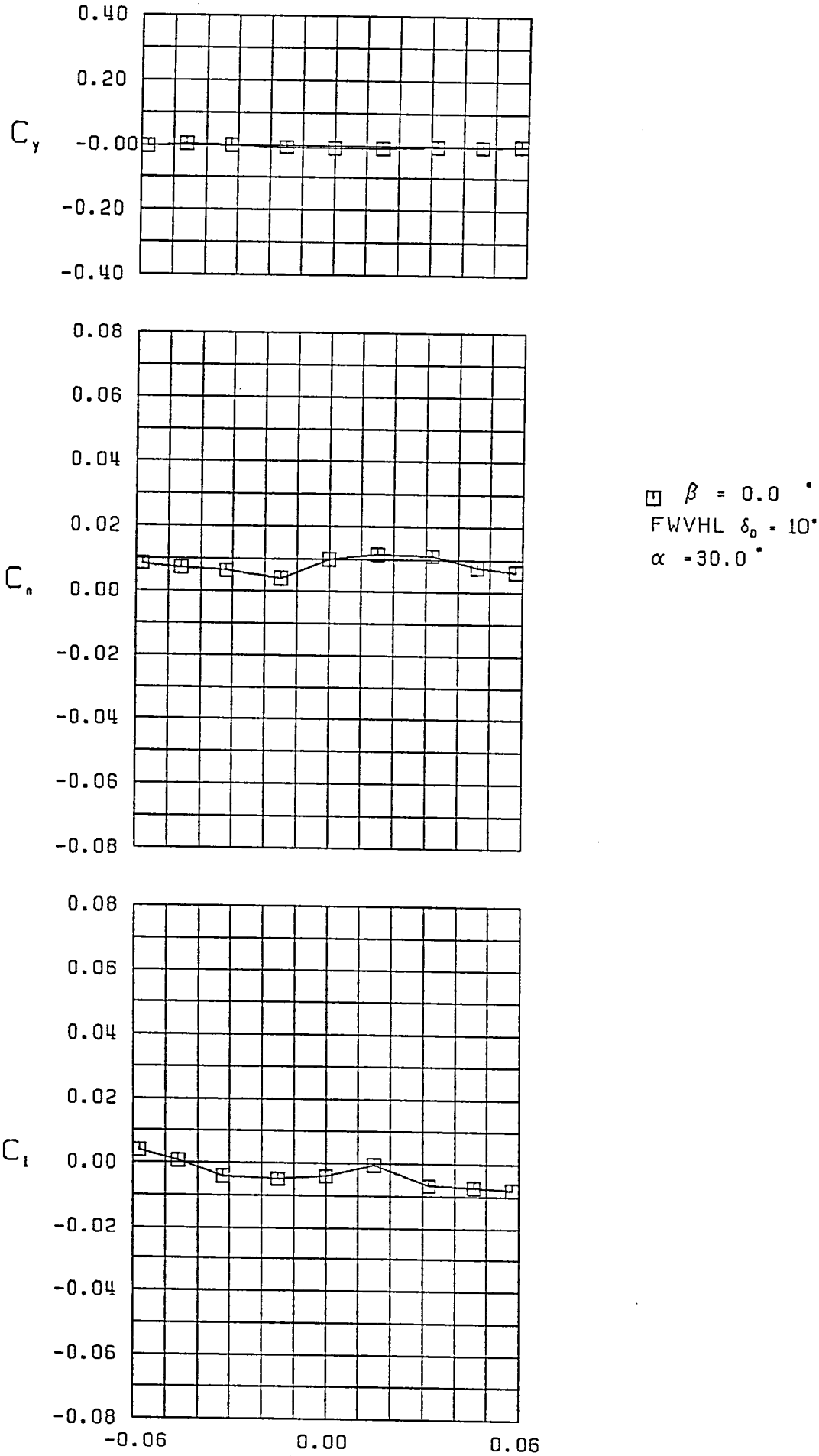

Figure 25 (Continued)

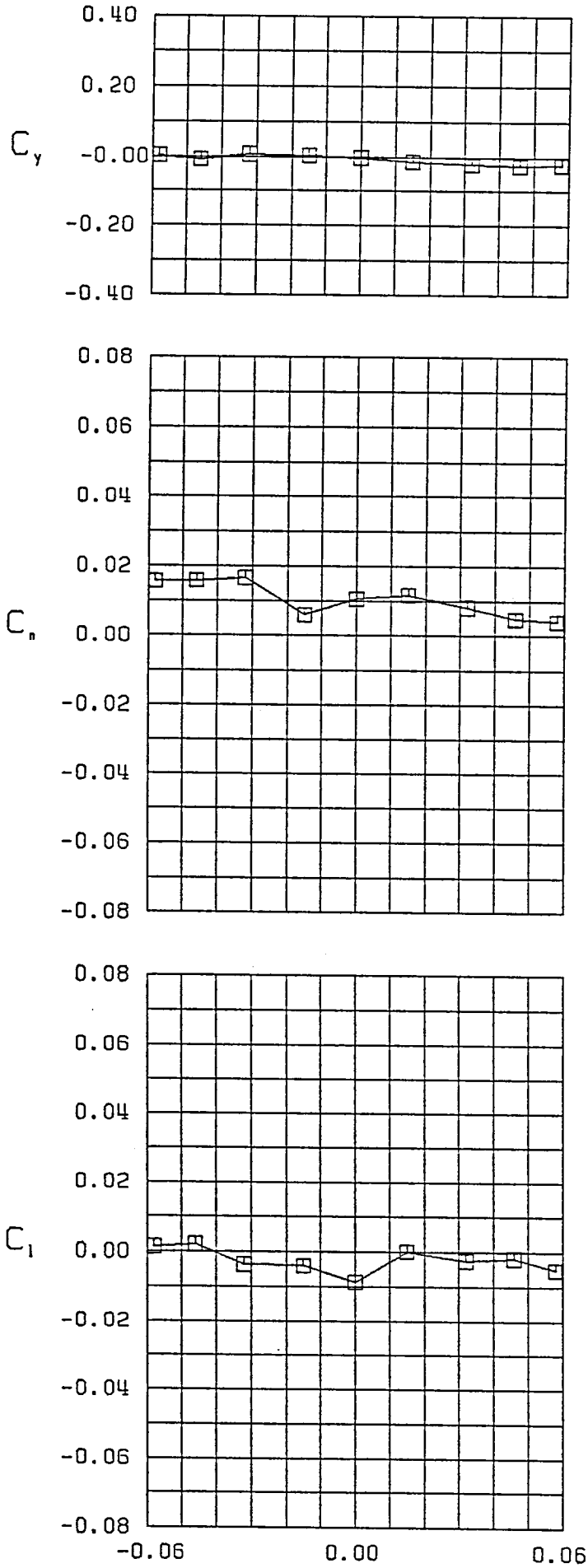

□ β = 0.0 °
FWVHL δ_D = 10°
α = 35.0 °

Figure 25 (Continued)

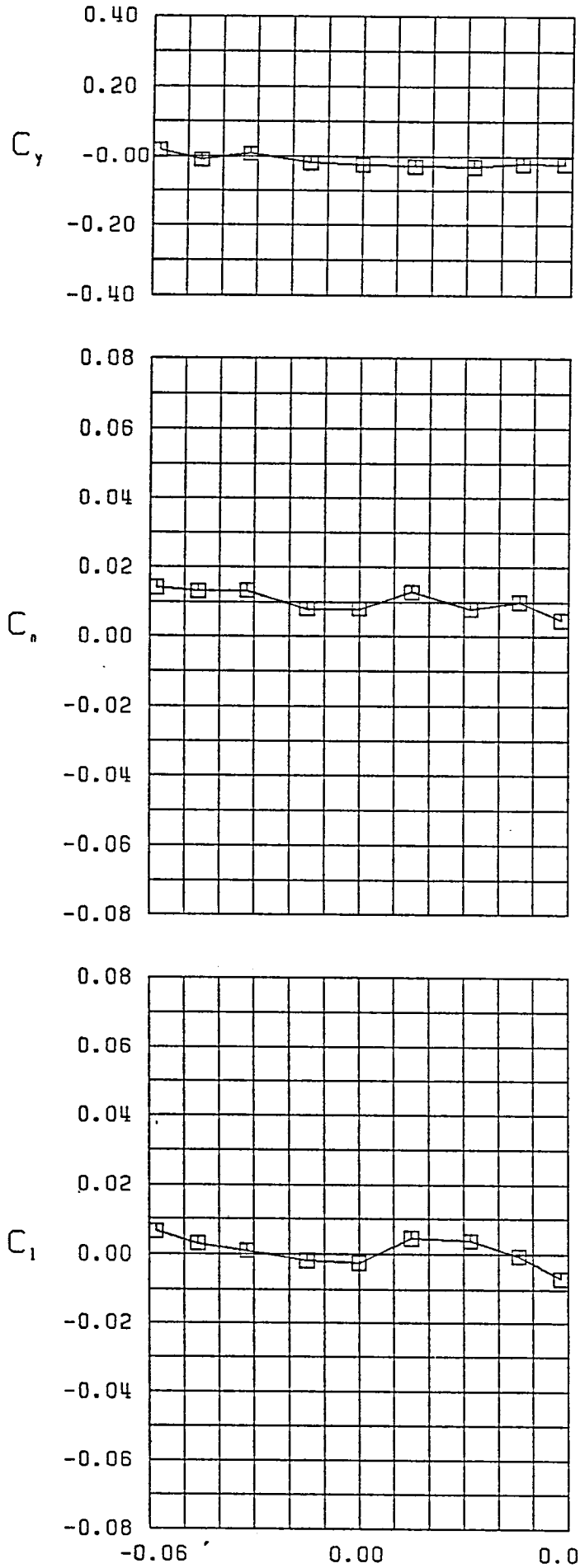

Figure 25 (Continued)

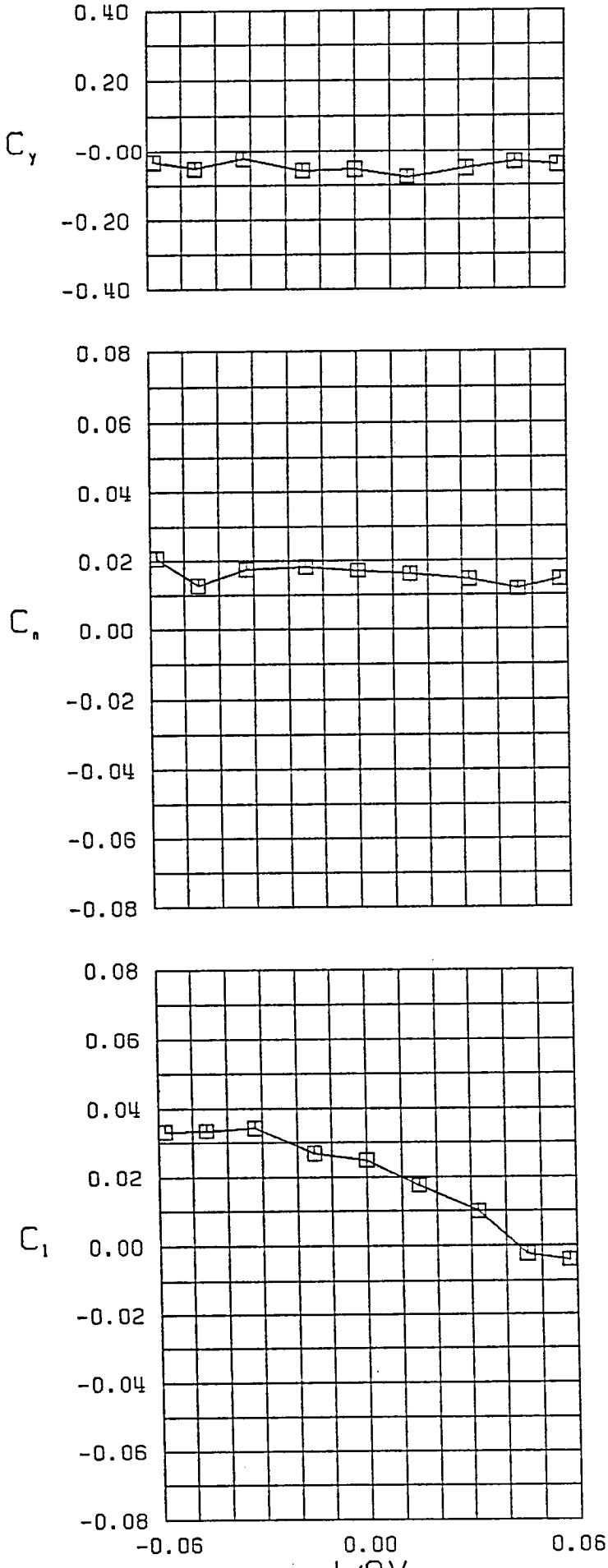

Figure 25 (Continued)